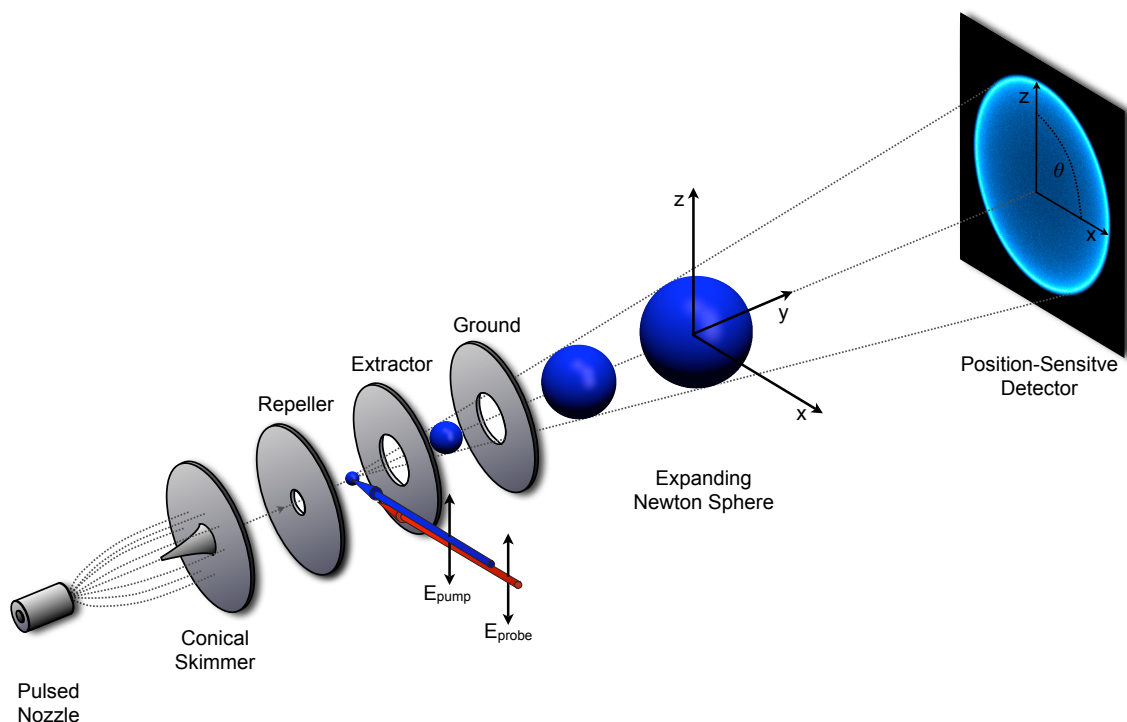


# Ultrafast Radiationless Dynamics of Selected Electronically Excited Aromatic Molecules by Femtosecond Time-Resolved Mass Spectrometry and Photoelectron Imaging



## Dissertation

zur Erlangung des Doktorgrades der  
Mathematisch-Naturwissenschaftlichen Fakultät der  
Christian-Albrechts-Universität zu Kiel

vorgelegt von

**Harald Studzinski**

**Kiel 2007**



## Abstract

The electronic relaxation dynamics of several prototypical aromatic molecules, including benzene, toluene, xylenes, hexafluorobenzene, pyrrole and selected derivatives of pyrrole, were investigated by means of femtosecond time-resolved time-of-flight mass spectrometry (ToF-MS) and femtosecond time-resolved transient photoelectron imaging (PEI). These experiments were setup and characterized in this thesis.

Benzene molecules were excited to the  $S_1$  state by one-photon absorption at  $\lambda_{pump} = 258$  nm and to the  $S_2$  state by two-photon absorption at  $\lambda_{pump} = 387$  nm. The excited state decays were monitored by multi-photon ionization, probing with  $\lambda_{probe} = 775$  nm. Biexponential fits to the transient parent mass signals gave two decay constants, which were respectively,  $\tau_1 = 0.04$  and  $\tau_2 > 150$  ps for  $S_1$  excited benzene and  $\tau_1 = 0.02$  and  $\tau_2 > 1.12$  ps for  $S_2$  excited benzene. Additional information on the vibronic dynamics were observed by (1+1)- and (3+3)-PEI, where a vibrational progression originating from the  $\nu_1$  and  $\nu_6$  modes was observed.

ToF-MS experiments on the derivatives toluene and all three xylenes show results similar to those of benzene. However, their dynamics were significantly faster.

The excited state decays of the  $S_2$  ( $\pi\pi^*$ ) and the  $S_3$  ( $\pi\pi^*$ ) states of hexafluorobenzene were investigated using excitation wavelengths of  $265$  nm  $\geq \lambda_{pump} \geq 217$  nm and an ionization wavelength at  $\lambda_{probe} = 775$  nm. The observed decays exhibit two decay times ( $\tau_1 = 0.54$  ps to 0.10 ps and  $\tau_2 = 493$  ps to 4.67 ps), superimposed by a damped coherent oscillation ( $\tau_D = 1.18$  ps to 0.36 ps,  $\tilde{\nu}_{osc} = 94$  cm $^{-1}$  to 107 cm $^{-1}$ ).  $\tau_2$  showed a strong dependence on the pump wavelength and decreased over the whole excitation range by a factor of 100. The coherent oscillation originated from vibrational motion in the optically “dark”  $S_1$  state, reached from the  $S_2$  state with  $\tau_1 \leq 1$  ps through a conical intersection.

The heteroaromatic molecule pyrrole was excited to the  $1^1B_2(\pi\pi^*)$  state by one-photon absorption at  $\lambda_{pump} = 219$  nm and to the  $2^1A_1(\pi\pi^*)$  state by two-photon absorption at  $\lambda_{pump} = 387$  nm. The decays of these states were probed by multi-photon absorption at  $\lambda_{probe} = 775$  nm. Monoexponential fits revealed a decay time  $\tau_1 = 0.38$  ps for the  $B_2$  state and  $\tau_1 = 0.06$  ps for the  $A_1$  state. The  $1^1B_2(\pi\pi^*)$  state of pyrrole was also studied by PEI using a (1+1’)-REMPI scheme ( $\lambda_{pump} = 219$  nm and  $\lambda_{probe} = 258$  nm). Three electron bands were observed, with  $E_{el}^{\#1} = 3\,100$  cm $^{-1}$ ,  $E_{el}^{\#2} = 12\,425$  cm $^{-1}$  and  $E_{el}^{\#3} = 17\,150$  cm $^{-1}$ . The latter two bands showed a vibronic progression of  $\approx 1000$  cm $^{-1}$ . Several methyl-substituted derivatives of pyrrole gave similar time constants, but the PEI results for *N*-methylpyrrole showed interesting differences owing to the higher stability of its  $\pi\sigma^*$  state.

## Zusammenfassung

Die elektronische Relaxationsdynamik verschiedener prototypischer Aromaten, wie Benzol, Toluol, Xylol, Hexafluorbenzol, Pyrrol sowie einiger Derivate des Pyrrols, wurde mittels Femtosekunden-zeitaufgelöster Flugzeit-Massenspektrometrie (ToF-MS) und Femtosekunden-zeitaufgelöster Photoelektronen-Spektroskopie (PEI) untersucht. Diese Experimente wurden in der vorliegenden Arbeit aufgebaut und charakterisiert.

Benzol wurde mit  $\lambda_{pump} = 258$  nm in den  $S_1$ -Zustand und bei  $\lambda_{pump} = 387$  nm in den  $S_2$ -Zustand angeregt. Deren Dynamik wurde durch Mehrphotonen-Ionisation mit einem Analysepulse bei  $\lambda_{probe} = 775$  nm abgefragt. Die transienten Signale konnten jeweils durch zwei abklingende Exponentialfunktionen beschrieben werden, wobei  $\tau_1 = 0.04$  und  $\tau_2 > 150$  ps für den  $S_1$ -Zustand und  $\tau_1 = 0.02$  und  $\tau_2 > 1.12$  ps für den  $S_2$ -Zustand gefunden wurden. Zusätzliche Informationen über die vibronischen Energie-Zustände wurden durch (1+1)- und (3+3)-PEI erhalten. Hier wurde eine Schwingungsprogression, die durch die Normalschwingungen  $\nu_1$  und  $\nu_6$  verursacht wird, beobachtet.

ToF-MS Experimente an den Benzol-Derivaten Toluol und allen drei Xylole lieferten ähnliche Ergebnisse, wobei allerdings eine schnellere Dynamik beobachtet wurde.

Die elektronische Deaktivierung des  $S_2$ - und des  $S_3$ -Zustandes von Hexafluorbenzol wurde mit Anregungswellenlängen zwischen  $265 \text{ nm} \geq \lambda_{pump} \geq 217$  nm und einer Ionisierungswellenlänge von  $\lambda_{probe} = 775$  nm untersucht. Die beobachteten transienten Signale setzten sich aus zwei Abklingkomponenten ( $\tau_1 = 0.54 - 0.10$  ps und  $\tau_2 = 493 - 4.67$  ps) zusammen, die von einer gedämpften Oszillation ( $\tau_D = 1.18$  ps  $- 0.36$  ps,  $\tilde{\nu}_{osc} = 94 \text{ cm}^{-1} - 107 \text{ cm}^{-1}$ ) überlagert wurden. Nur  $\tau_2$  zeigte eine deutliche Abhängigkeit von der Anregungswellenlänge und variierte über den gesamten Anregebereich um etwa einen Faktor 100. Die kohärent angeregte Oszillation wird über eine Schwingung im optisch "dunklen"  $S_1$ -Zustand hervorgerufen, der durch eine konische Durchschneidung mit dem  $S_1$ -Zustand erreicht wird.

Pyrrol wurde bei  $\lambda_{pump} = 219$  nm in den  $1^1B_2(\pi\pi^*)$ -Zustand und durch Zwei-Photonen-Absorption bei  $\lambda_{pump} = 387$  nm in den  $2^1A_1(\pi\pi^*)$ -Zustand angeregt. Die Abnahme des transienten Massensignals wurde durch Mehrphotonen-Ionisation bei  $\lambda_{probe} = 775$  nm verfolgt. Über eine monoexponentielle Datenanpassung wurde die Abklingzeit zu  $\tau_1 = 0.38$  ps für den  $B_2$ -Zustand und zu  $\tau_1 = 0.06$  ps für den  $A_1$ -Zustand bestimmt. Der  $1^1B_2(\pi\pi^*)$ -Zustand von Pyrrol wurde außerdem mit PEI untersucht, wobei ein (1+1')-REMPI-Schema mit  $\lambda_{pump} = 219$  nm und  $\lambda_{probe} = 258$  nm angewendet wurde. Drei Elektronen-Banden bei  $E_{el}^{\#1} = 3100 \text{ cm}^{-1}$ ,  $E_{el}^{\#2} = 12425 \text{ cm}^{-1}$  und  $E_{el}^{\#3} = 17150 \text{ cm}^{-1}$  wurden beobachtet. Die zwei zuletzt genannten Banden zeigten eine Schwingungsprogression mit  $\approx 1000 \text{ cm}^{-1}$  Energiedifferenz. An *N* oder *C* methylsubstituierte Derivate des Pyrrols besitzen ähnliche Abklingzeiten.

# Contents

<b>1</b>	<b>Introduction</b>	<b>3</b>
<b>2</b>	<b>Experimental Chapter</b>	<b>9</b>
2.1	Time-of-Flight Mass Spectrometry (ToF-MS) . . . . .	9
2.1.1	Basics of Time-of-Flight Mass Spectrometry . . . . .	9
2.1.1.1	Mass Resolution of a ToF-MS . . . . .	11
2.1.1.2	Space Defect and Space Focussing . . . . .	12
2.1.1.3	Energy Defect and Energy Focussing . . . . .	14
2.1.2	Experimental Setup for Time-of-Flight Mass Spectroscopy . .	16
2.1.2.1	Vacuum Equipment . . . . .	16
2.1.2.2	Sample Preparation . . . . .	17
2.1.2.3	Pulsed Nozzle, Molecular Beam, and Flight Conditions	18
2.1.2.4	Ion Lens Assembly . . . . .	18
2.1.2.5	Detector and Data Acquisition . . . . .	19
2.1.2.6	Achieved Mass Resolution . . . . .	21
2.1.2.7	Timing of the Components . . . . .	22
2.1.3	Data Analysis of Transient Mass Spectra . . . . .	24
2.2	Photoelectron Imaging . . . . .	25
2.2.1	Introduction to Photoelectron Imaging . . . . .	25
2.2.1.1	Energy Conservation in Isolated Molecules . . . . .	26
2.2.1.2	Koopmans' Theorem . . . . .	27
2.2.1.3	Photoelectron Angular Distribution . . . . .	28
2.2.2	Technical Design . . . . .	30
2.2.2.1	Shielding of Static and Dynamic Magnetic Fields . .	30
2.2.2.2	Position Sensitive Detector . . . . .	31
2.2.2.3	Reproduction Scale of the Camera System . . . . .	32
2.2.2.4	Temporal Sequence of the Experiment . . . . .	33
2.2.3	Projection and Reconstruction of the 3D Electron Distribution	35
2.2.3.1	Introduction to the Inversion Methods . . . . .	35
2.2.3.2	Polar Basis Function Expansion (pBASEX) . . . . .	37
2.2.3.3	Projected-Landweber Method (PL) . . . . .	38
2.2.3.4	Comparison of pBASEX and PL . . . . .	39
2.3	Femtosecond Pump-Probe Laser System . . . . .	46
2.3.1	The Ti:Sa Laser System . . . . .	46
2.3.2	Nonlinear Optics and Optical Light Conversion Processes . . .	47
2.3.2.1	Multi-Photon Absorption . . . . .	47
2.3.2.2	Optical Kerr-Effect and Group Velocity Dispersion .	47

---

2.3.2.3	Frequency Conversion . . . . .	48
2.3.3	Schemes for Tunable Light Generation . . . . .	49
2.3.3.1	Second Harmonic Generation . . . . .	49
2.3.3.2	Third Harmonic Generation . . . . .	50
2.3.3.3	Tunable Light Source: Non-Collinear Optical Para- metric Amplification . . . . .	51
2.3.3.4	Frequency Doubling of a NOPA . . . . .	52
2.3.3.5	Sum Frequency Generation of NOPA Output and Fundamental or SHG of the Fundamental . . . . .	52
<b>3</b>	<b>Results and Discussion</b>	<b>55</b>
3.1	Benzene . . . . .	56
3.1.1	Introduction . . . . .	56
3.1.2	Experimental . . . . .	58
3.1.3	Results . . . . .	59
3.1.3.1	Time-Resolved ToF Mass Spectrometry . . . . .	59
3.1.3.2	Transient Photoelectron Imaging . . . . .	62
3.1.4	Discussion . . . . .	69
3.1.5	Conclusion and Summary . . . . .	70
3.2	Toluene and <i>o</i> -, <i>m</i> -, <i>p</i> -Xylene . . . . .	71
3.2.1	Introduction . . . . .	71
3.2.2	Experimental Setup . . . . .	73
3.2.3	Results . . . . .	74
3.2.3.1	Time-resolved ToF Mass Spectrometry . . . . .	74
3.2.4	Discussion . . . . .	78
3.2.5	Conclusion and Summary . . . . .	79
3.3	Hexafluorobenzene . . . . .	80
3.3.1	Introduction . . . . .	80
3.3.2	Experimental Setup . . . . .	81
3.3.3	Computational Methods . . . . .	82
3.3.4	Results . . . . .	83
3.3.4.1	DFT and TDDFT Calculations . . . . .	83
3.3.4.2	Time-Resolved ToF Mass Spectrometry . . . . .	88
3.3.5	Discussion . . . . .	91
3.3.6	Conclusion and Summary . . . . .	98
3.4	Pyrrrole . . . . .	99
3.4.1	Introduction . . . . .	99
3.4.2	Experimental Setup . . . . .	102
3.4.3	Computational Methods . . . . .	103
3.4.4	Results . . . . .	103
3.4.4.1	DFT Calculations . . . . .	103
3.4.4.2	Time-Resolved ToF Mass Spectrometry . . . . .	107
3.4.4.3	Transient Photoelectron Imaging . . . . .	109

---

3.4.5	Discussion . . . . .	113
3.4.6	Conclusion and Summary . . . . .	116
3.5	<i>N</i> -Methylpyrrole, and <i>2,4</i> -, and <i>2,5</i> -Dimethylpyrrole . . . . .	117
3.5.1	Introduction . . . . .	117
3.5.2	Experimental Setup . . . . .	118
3.5.3	Results for <i>N</i> -Methylpyrrole . . . . .	119
3.5.3.1	Time-Resolved ToF Mass Spectrometry . . . . .	119
3.5.3.2	Transient Photoelectron Imaging . . . . .	120
3.5.4	Results for <i>2,4</i> - and <i>2,5</i> -Dimethylpyrrole . . . . .	123
3.5.4.1	Time-Resolved ToF Mass Spectrometry . . . . .	123
3.5.5	Discussion . . . . .	124
3.5.5.1	<i>N</i> -Methylpyrrole . . . . .	124
3.5.5.2	<i>2,4</i> - and <i>2,5</i> -Dimethylpyrrole . . . . .	125
3.5.6	Conclusion and Summary . . . . .	125
<b>4</b>	<b>Summary</b>	<b>127</b>
<b>5</b>	<b>Appendix</b>	<b>129</b>
5.1	Technical Drawings and Photographs . . . . .	129
5.1.1	ToF Mass Spectrometry and Photoelectron Imaging Setup . . . . .	129
5.2	Control Programs . . . . .	137
5.2.1	Time-Resolved ToF Mass Spectrometry . . . . .	137
5.2.2	Transient Photoelectron Imaging . . . . .	139
5.3	Data Evaluation . . . . .	141
5.3.1	Fit of Transient Mass Spectra with Mathematica . . . . .	141
5.3.2	Inversion of 2D Projections with pBasex . . . . .	146
5.3.3	Energy Calibration of the PE Distributions . . . . .	150
5.3.3.1	By Maximum Electron Kinetic Energy . . . . .	150
5.3.3.2	By Over Threshold Ionization . . . . .	153
	<b>Bibliography</b>	<b>155</b>
	<b>Acknowledgment</b>	<b>167</b>
	<b>Curriculum Vitae</b>	<b>169</b>
	<b>Eidesstattliche Erklärung</b>	<b>171</b>





## List of Figures

1.1	Avoided Crossing and Conical Intersection . . . . .	4
1.2	Molecular Structures of the Investigated Molecules . . . . .	5
1.3	Schematic Drawing of the Time-of-Flight Mass Spectrometry Setup . . . . .	6
1.4	Schematic Drawing of the Photoelectron Imaging Setup . . . . .	7
2.1	Schematic Time-of-Flight Mass Spectrometer . . . . .	10
2.2	Scheme: Mass Resolution of a ToF-MS . . . . .	11
2.3	Wiley-McLaren Space Focussing . . . . .	13
2.4	Energy Focussing: Behavior of Ions with Different Velocities in an Electric Field . . . . .	14
2.5	Trajectories of Ions with Excess Recoil Energy in Different Directions . . . . .	15
2.6	Detection Loss because of Bad Energy Focussing . . . . .	15
2.7	Schematic Drawing of the Experimental Setup for Time-of-Flight Mass Spectrometry . . . . .	16
2.8	Sample Preparation and Cluster Control . . . . .	17
2.9	Translational Energy Distribution Before and After Adiabatic Expansion . . . . .	19
2.10	Ion Lens Assembly . . . . .	20
2.11	Schematic Drawing of the "Multi-Channel Plate" Detector Assembly . . . . .	20
2.12	Mass Resolution of the ToF Mass Spectrometer . . . . .	21
2.13	Timing of the ToF-MS Components . . . . .	22
2.14	Visualization of the Timing . . . . .	23
2.15	Electronic Dynamics in the Excited States: Jablonski Diagram . . . . .	25
2.16	Koopmans' Type I Correlation . . . . .	28
2.17	Koopmans' Type II Correlation . . . . .	28
2.18	Schematic Sphere in a Cartesian Coordinate System . . . . .	29
2.19	Schematic Drawing of the PEI Detector Assembly . . . . .	32
2.20	Determination of the Camera Reproduction Scale . . . . .	33
2.21	Trigger Contacts for the PEI Experiment . . . . .	34
2.22	Timing of the PEI Experiment . . . . .	34
2.23	Simulated and Experimental Test Images . . . . .	39
2.24	Slices of the Reconstructed Simulated Image . . . . .	41
2.25	Radial Distributions of the Reconstructed Test Images . . . . .	41
2.26	Values of the Anisotropy Parameters for the Reconstructed Simulated Test Image . . . . .	42
2.27	Slices of the Reconstructed Experimental Image . . . . .	43

---

2.28	Radial Distributions of the Experimental Test Image for pBASEX and PL . . . . .	44
2.29	Ti:Sa Laser Scheme . . . . .	46
2.30	Overview of the applied Light Conversion Processes . . . . .	50
2.31	THG Setup . . . . .	51
2.32	Setup for SHG of the NOPA Output . . . . .	52
2.33	Setup for SFG of NOPA Output and SHG . . . . .	53
3.1	UV Spectrum of Benzene . . . . .	56
3.2	Benzene Potential Energy Curves . . . . .	57
3.3	Mass Spectrum of Benzene . . . . .	59
3.4	Benzene Excitation Scheme . . . . .	60
3.5	Transient Mass Spectra of Benzene . . . . .	61
3.6	PEI One Color Results of Benzene . . . . .	63
3.7	PEI Excitation Scheme of Benzene at $\lambda = 258$ nm. . . . .	64
3.8	Time-Resolved Two-Color PEIs on Benzene . . . . .	65
3.9	Time-Resolved Photoelectron Kinetic Energy Release . . . . .	67
3.10	UV Spectrum of Toluene . . . . .	71
3.11	Comparision of UV Spectra from Benzene, Toluene, <i>o</i> -, <i>m</i> -, and <i>p</i> -Xylene . . . . .	72
3.12	Toluene Excitation Scheme ( $S_1$ and $S_2$ ). . . . .	74
3.13	Time-Resolved ToF-MS Results Probing the $S_1$ and $S_2$ States of Toluene. . . . .	75
3.14	Time-Resolved ToF-MS Results for Toluene, <i>o</i> -Xylene, <i>m</i> -Xylene and <i>p</i> -Xylene Exciting into the $S_2$ State. . . . .	76
3.15	UV Absorption and Fluorescence Spectra of Hexafluorobenzene . . . . .	80
3.16	Electron Density Distribution of Hexafluorobenzene and Benzene in Comparison . . . . .	83
3.17	State Energy and Character of the Molecular Orbitals of Hexafluorobenzene . . . . .	84
3.18	Vertical Excitation Energies of Hexafluorobenzene . . . . .	85
3.19	Calculated Geometries for Hexafluorobenzene . . . . .	86
3.20	$E_{2u}$ Vibrational Modes of Hexafluorobenzene in the Ground State . . . . .	87
3.21	Hexafluorobenzene Pump-probe Excitation Scheme . . . . .	88
3.22	Time-Resolved ToF-MS Results Over a Broad Excitation Range for Hexafluorobenzene . . . . .	89
3.23	Hexafluorobenzene Decay Rates Plotted Against Excitation Wavelength. . . . .	91
3.24	Modeled Potential Curves and Deactivation Mechanisms for Photo-Excited Hexafluorobenzene in the First $\pi\pi^*$ state. . . . .	92
3.25	Modeled Potential Curves and Deactivation Mechanisms for Photo-Excited Hexafluorobenzene in the Second $\pi\pi^*$ state. . . . .	93

---

3.26	Coherent Excitation of Multiple Vibronic Levels . . . . .	94
3.27	Schematic Explanation for the Coherent Oscillation Observed for Hexafluorobenzene . . . . .	95
3.28	Coherent Electron Transfer in Hexafluorobenzene . . . . .	96
3.29	Coherent Wavepacket Revival in Hexafluorobenzene . . . . .	97
3.30	UV Spectrum of Pyrrole . . . . .	99
3.31	Electron Density Distribution of the $\sigma^*$ Orbital in Pyrrole . . . . .	100
3.32	<i>N-H</i> Stretching Potential Curves Calculated for Pyrrole . . . . .	101
3.33	Calculated Infrared Spectra of Neutral and Ionic Pyrrole . . . . .	105
3.34	Pump Probe Excitation Scheme for the ToF-MS Measurements on Pyrrole . . . . .	107
3.35	Time-Resolved ToF-MS Results on Pyrrole . . . . .	108
3.36	PE Image Correction . . . . .	109
3.37	Summary of the PEI Results on Pyrrole . . . . .	110
3.38	Background Corrected Transient PE Distributions for Pyrrole . . . . .	111
3.39	Discussion of the Pyrrole Results on the Basis of the Calculated Po- tential Surfaces . . . . .	113
3.40	Schematic Relaxation Mechanism of Pyrrole after $^1B_2$ Excitation: 1st Model . . . . .	114
3.41	Schematic Relaxation Mechanism of Pyrrole after $^1B_2$ Excitation: 2nd Model . . . . .	115
3.42	UV Absorption Spectrum of Pyrrole Compared to its Derivatives . . . . .	117
3.43	Transient ToF-MS Results on <i>N</i> -Methylpyrrole . . . . .	119
3.44	Summary of the PEI Results on <i>N</i> -Methylpyrrole . . . . .	121
3.45	Transient PE Distributions of <i>N</i> -Methylpyrrole . . . . .	122
3.46	Time-Resolved ToF-MS Measurements on <i>2,4</i> - and <i>2,5</i> -Dimethylpyrrole	123
3.47	Schematic Relaxation Mechanism of <i>N</i> -Methylpyrrole after Excita- tion to the Lower Excited Electronic States . . . . .	124
5.1	Technical Drawing: ToF-MS/PEI Chamber . . . . .	130
5.2	Technical Drawing: Nozzle Mount . . . . .	131
5.3	Technical Drawing: Ion Lens Assembly . . . . .	132
5.4	Technical Drawing: Cooling Trap . . . . .	133
5.5	Technical Drawing: Flight Tube . . . . .	134
5.6	Technical Drawing: ToF-MS and PEI Detectors . . . . .	135
5.7	Photographs: ToF Mass Spectrometer . . . . .	136
5.8	LabView ToF-MS: Front Panel . . . . .	137
5.9	LabView ToF-MS: Menu “Delay”. . . . .	138
5.10	LabView ToF-MS: Menu “Measurement”. . . . .	138
5.11	LabView PEI: Front Panel . . . . .	139
5.12	LabView PEI: Take Background Image . . . . .	140
5.13	LabView PEI: Peak Detection . . . . .	140

---

5.14	Mathematica Fit: Initialization . . . . .	141
5.15	Mathematica Fit: Initialization - Part 2 . . . . .	142
5.16	Mathematica Fit: Import Data . . . . .	143
5.17	Mathematica Fit: Start the Fit . . . . .	143
5.18	Mathematica Fit: Plotting the Fit Results . . . . .	144
5.19	Mathematica Fit: Results are Prepared for Export . . . . .	145
5.20	Mathematica Fit: Export Results . . . . .	145
5.21	pBASEX: Open Image . . . . .	146
5.22	pBASEX: Order of the Anisotropy Parameters . . . . .	147
5.23	pBASEX: Image Centering . . . . .	148
5.24	pBASEX: Inversion . . . . .	148
5.25	pBASEX: Saving the Results . . . . .	149
5.26	Matematica PEI Calibration: Initialization . . . . .	150
5.27	Matematica PEI Calibration: Calculations . . . . .	151
5.28	Matematica PEI Calibration: Batch Processing . . . . .	152
5.29	Matematica PEI Calibration: Over Threshold Ionization . . . . .	153
5.30	Matematica PEI Calibration: Calculations and Export . . . . .	154

## List of Tables

2.1	Parameters of the Simulated Test Image . . . . .	40
2.2	Anisotropy Parameters of the Reconstructed Simulated Image . . . . .	43
2.3	Anisotropy Parameters of the Reconstructed Experimental Image . . . . .	44
2.4	Computational Time Expanse: pBasex vs. PL . . . . .	45
3.1	One-color PEI Results for Benzene at $\lambda = 258$ nm . . . . .	66
3.2	Time-Resolved Two-Color PEI Results on Benzene . . . . .	66
3.3	Red Shifts of Absorption Bands by Methylation in Toluene . . . . .	73
3.4	TD-Calculations on Hexafluorobenzene . . . . .	85
3.5	$E_{2u}$ Vibrational Coupling Frequencies of the Ground and Excited States of Hexafluorobenzene . . . . .	87
3.6	Fit Results for the Transient Mass Decay Data of Hexafluorobenzene . . . . .	88
3.7	Frequencies of the $a_2$ and $b_1$ Symmetry Vibrational Coupling Modes for Pyrrole . . . . .	104
3.8	Symmetries of the Coupling Modes for the $\pi\pi^* \rightarrow \pi\sigma^*$ Conical Intersections in Pyrrole . . . . .	106
3.9	Electronic Spectrum of Pyrrole: DFT versus CASPT2 . . . . .	106
3.10	Results of the Time-Resolved Measurements on Pyrrole . . . . .	109
3.11	PEI Anisotropy Parameters for the Pyrrole Measurements . . . . .	112
3.12	Fit Results of the Time-Resolved ToF-MS Measurements on <i>N</i> -Methylpyrrole . . . . .	120
3.13	Fit Results of the Time-Resolved PEI Measurements for <i>N</i> -Methylpyrrole . . . . .	122



# 1 Introduction

The understanding of the interplay between structure, dynamics, and function has been the focus in the realms of the scientific world for a long time. With the invention of the first (ruby) laser by Maiman [1] in 1960, the hunt for short laser pulses began. 14 years later, Ippen [2] succeeded in generating the first ultrashort pulses with a duration of several hundred femtoseconds (femto  $\hat{=}$   $10^{-15}$  s) and, by that, the frontier was pushed further to the direct investigation of nuclear motions. The progress in the generation of ultrashort laser pulses and the invention of the pump/probe technique formed the foundation for the development of “femtochemistry” and “femtobiology”. A. H. Zewail and his workgroup were forerunners in this field and were honored with the Nobel Prize Zewail in 1999 [3, 4, 5]. Since the late 1980s, their work inspired a multiplicity of people bringing a new depth of knowledge in fundamental problems such as the dynamics of inter- and intramolecular vibrational redistribution [6, 7, 8], the breaking and making of bonds [9, 10, 11], and important elementary processes, e.g. electron and proton transfer reactions [12, 13, 14, 15] and electronic relaxation [7]. Outstanding examples are the unraveling of the photochemical mechanisms for photosynthesis, vision [16], and the explanations for the exceptionally high photostability of the deoxyribonucleic acid (DNA) and its incorporated building blocks [17], the DNA bases adenine, guanine, cytosine, and thymine.

Of special interest were and are the mechanisms for internal conversion (IC) of electronically excited polyatomic molecules into vibrational modes of lower electronic levels and the ground state. These mechanisms were controversially discussed in the literature for a long time, but now the concept of conical intersections as driving force is generally accepted [18, 13]. A conical intersection is a crossing in the nuclear coordinate space with a topology of a double cone at the confluence of two Born-Oppenheimer potential energy surfaces [19]. The following conditions have to be fulfilled in order to form a CI between potential energy surfaces: (1) The crossing potential energy surfaces (electronic states) have to belong to different symmetry species, otherwise a crossing is forbidden (non-crossing rule [20, 21]). (2) Conical intersections can only occur in molecules which consist of more than two atoms. A two-atom system has only one degree of freedom (the nuclear distance), therefore conditions (3) and (4) below cannot be fulfilled. The result is an avoided crossing.[22] (3) The potential energy surfaces have to become isoenergetic (degenerate) at one point along a specific reaction coordinate. This coordinate could be bond stretching, bending, or twisting. (4) The symmetry of the initial (starting) wave function has

to be conserved throughout the crossing into the product state. This is granted by vibrational coupling modes of appropriate symmetry. Examples of avoided crossing and conical intersection are illustrated in Figure 1.1.

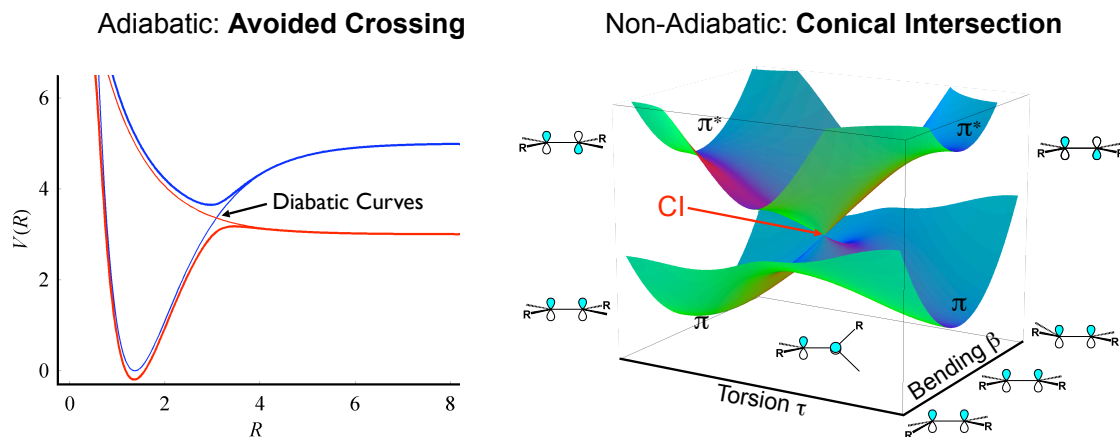


**Figure 1.1:** An avoided crossing is shown on the left, the adiabatic limit of a diatomic molecular system. Polyatomic systems can form conical intersections at the crossing of two potential energy surfaces. The potential energy surfaces on the right schematically demonstrate the photochemical cis/trans isomerization of ethylene through a conical intersection [23].

In the past, it was shown theoretically [24, 25] and experimentally [26, 27] that optically “dark”  $\sigma^*$  states often serve as a sort of “lightning conductor” for the deactivation of photo-excited polyatomic molecules, and do connect different excited states with the ground state by CIs.

This thesis concentrates on studies of photo-initiated ultrafast dynamics in isolated molecules that involve optically dark  $(\pi)\sigma^*$  transitions in their electronic relaxation process. The molecules studied are benzene, its derivatives toluene, *o*-, *m*-, *p*-xylene, and hexafluorobenzene, pyrrole and its methylated derivatives *N*-methylpyrrole, *2,4*-, and *2,5*-dimethylpyrrole. The chemical structure of these molecules are shown in Figure 1.2.

Benzene is the prototypical aromatic molecule and the essential structure of numerous biologically important compounds in nature. The most characteristic feature is the delocalized  $\pi$ -electron system, which leads to a remarkably reduced reactivity of the ground state. Hence, it is even more astonishing that electronically excited benzene is highly reactive. Many industrial products are made from or contain benzene rings, *e.g.*, gasoline, polymers, plastics, rubbers, dyes, lubricants, detergents, drugs, explosives and pesticides. Toluene and xylenes are simple derivatives of benzene, which have not yet been fully studied regarding the photophysical



and photochemical dynamics.

From earlier spectroscopic [28] and photophysical [29, 30] studies of the fluorinated benzenes ( $C_6F_nH_m; n + m = 6$ ), it is known that the spectral absorption and emission features, as well as the lifetimes of the fluorescence, depend strongly on the number of fluorine atoms.  $C_6F_nH_m$  with four or less F atoms,  $n = 1 - 4$ , exhibit structured  $S_1 \leftarrow S_0$  absorption and fluorescence spectra, strong fluorescence, and nanosecond fluorescence lifetimes, whereas those with five or more F atoms display structureless absorption and excitation spectra [28], very weak fluorescence [29, 30], and biexponential fluorescence decay with picosecond and nanosecond lifetimes [31]. These differences suggest that the nature of the lowest excited singlet state may be different for the two classes of compounds, despite the previous  $\pi\pi^*$  assignment of the  $S_1$  states for all fluorinated benzenes [28].

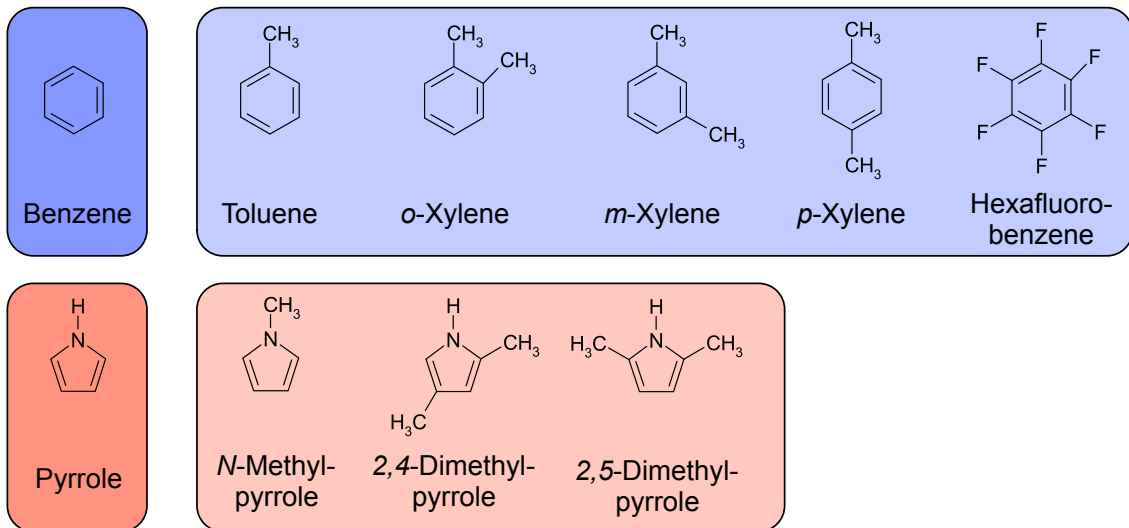


**Figure 1.2:** Chemical structures of the investigated molecules.

The relatively small molecule pyrrole possesses a structural analogy with several organic molecules. The pyrrole framework and similar heteroaromatic rings are contained, *e.g.*, in the amino acids histidine and tryptophane [32, 33], as well as in the nucleobases, which are the carriers of our genetic code and thus the elements of the DNA [25]. Already a single damaged molecule could potentially induce a mutation and lead to cancer. Nevertheless, all bases absorb in the high energy ultraviolet spectrum. It is known that the bases exhibit an intrinsic protection mechanism to dissipate absorbed photon energy without taking profound damage [17], *e.g.*, through ring opening or other structural changes. Because of the low fluorescence quantum yields of  $\phi < 10^{-4}$ , the mechanism has to be non-radiative. Other organic molecules, like the amino acids, show a similar photostability.

The electronic structures of the respective hetero rings have been assumed to be responsible for the deactivation process. Additionally, pyrrole is used to synthesize biologically active agents [24], pesticides, organic polymers and organo-metallic magnets [34].

In this work, femtosecond time-resolved experiments were developed to study the nonadiabatic molecular dynamics of the abovementioned molecules and some of their derivatives under collision-free conditions in supersonic molecular beams. Two methods were employed: time-resolved mass spectrometry (ToF-MS) and transient photoelectron imaging (PEI). Together with femtosecond pumping and probing these methods offer a complementary view of the electronic dynamics and can yield physical insight leading to deeper understanding.

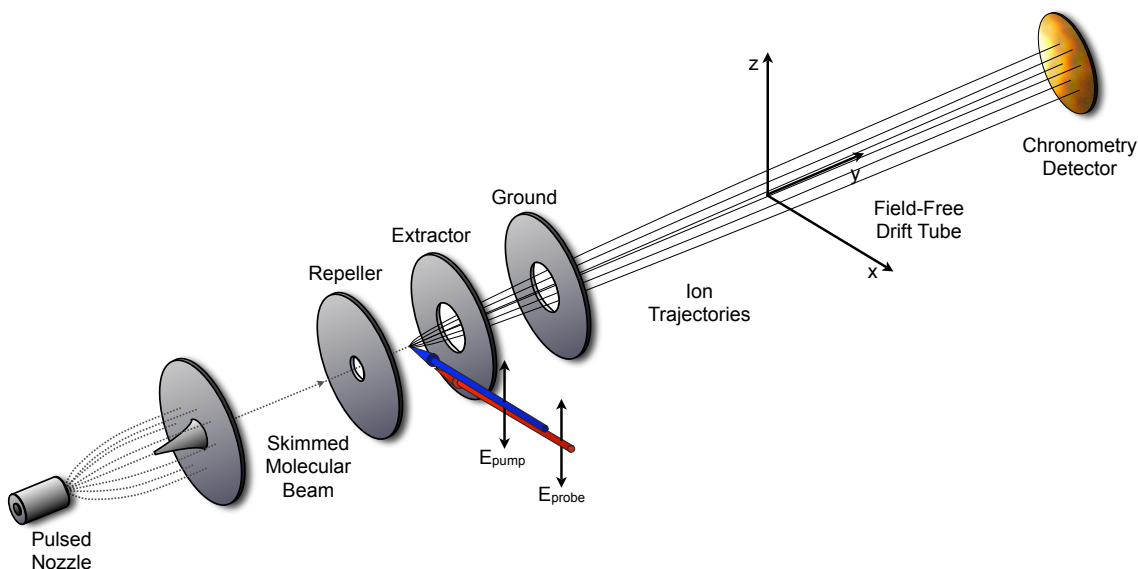


**Figure 1.3:** Schematic drawing of the time-of-flight mass spectrometry setup.

Time-resolved time-of-flight mass spectrometry in combination with ultrashort pulses is an ideal technology to determine the lifetimes of electronically excited states and has the additional ability to elucidate nuclear motions. The principle is schematically shown in Figure 1.3. The investigated molecules are adiabatically cooled in a pulsed molecular beam. The beam passes a skimmer to remove all molecules having velocity components perpendicular to the main direction of propagation. Within the ion lens assembly, between the repeller and extractor plates, the molecular beam is crossed by the pump and probe laser pulses. The dynamics of the excited electronic states are determined by time-delaying the probe pulse. Only if the combined energies of the pump and probe exceed the ionization threshold, the sample can be ionized. The generated ions are then accelerated into

the field-free drift zone by the static electric field of the ion lenses, where they are mass analyzed. Their exact time-of-flight is determined by a detection unit triggered by a photodiode measuring the arriving laser pulses.

The transient photoelectron imaging (PEI) setup is similar to that of the ToF-MS until the molecular beam reaches the point of laser interaction. From then on, the PEI method has been designed to measure the kinetic energy of the ejected electrons created in the ionization process. The setup is shown in Figure 1.4. The electrons are ejected on a Newton sphere, whereas the respective three-dimensional distribution is depending on the direction of the transition moment. The sphere is projected along a specially shielded drift tube onto the imaging detector, which records a two-dimensional image. To be able to reconstruct the initial 3D distribution, the polarization of the pump and probe beam have to be parallel to the detector surface, as is indicated by the arrows representing the electric field vector of the laser pulses, to ensure cylindric symmetry. The kinetic energy and angular distribution  $P(E, \Theta)$  of the electrons gives information on the involved electronic states. By time-delaying the pump and probe pulses with respect to each other the population of the excited electronic states is monitored to shed light onto the non-radiative electronic dynamics.

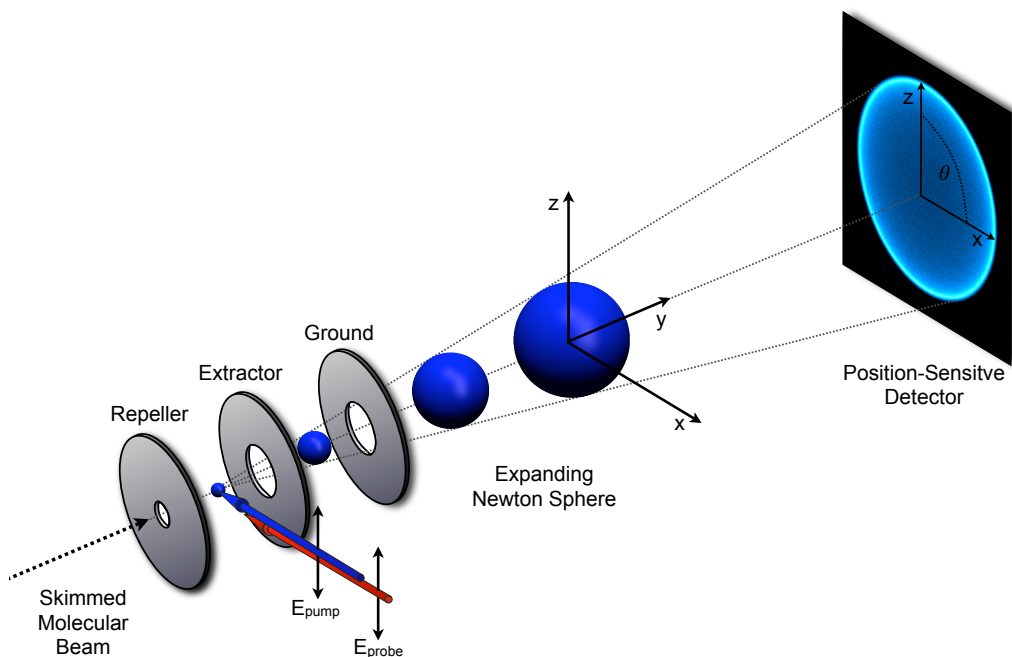


**Figure 1.4:** Schematic drawing of the photoelectron imaging setup.

The present thesis is organized in five chapters. This introduction is followed by an experimental chapter explaining the theory and technical realization of the newly constructed experimental setups for time-resolved ToF mass spectrometry and pho-

toelectron imaging. Continuing, Chapter “Results and Discussion” is divided into sections summarizing the current state of research for each molecule and presenting the measured results. Each section is closed by a discussion. The last chapter briefly summarizes the conclusions drawn for the respective molecules. Technical drawings, photographs, and the control, inversion and fitting programs are available in the appendix.

## 2 Experimental Chapter

This chapter describes the experimental setup which has been designed and built in the course of this work. It is divided into three parts, the time-of-flight mass spectrometer, the photoelectron imaging spectrometer, and the femtosecond pump-probe laser setup. Each part is subdivided into a theoretical and an experimental subsection.

### 2.1 Time-of-Flight Mass Spectrometry (ToF-MS)

The concept of a time-of-flight mass spectrometer (ToF-MS) was mentioned in literature for the first time in 1946 (see, for example [35, 36]). By now, ToF-MS has become a standard scientific and analytic method. Much of the technological development is owed to fast modern electronics and to the invention of the ion reflectron by Mamyrin in 1966 [37, 38]. Gentle ionization methods like plasma desorption (PD), field desorption (FD), laser desorption (LD), matrix assisted laser desorption (MALDI) and electrospray ionization (ESI) make ToF-MS applicable even to macromolecules, including proteins and polymers with masses up to and higher than  $10^6$  Da.

The application of fs lasers for resonance enhanced multiphoton ionization (REMPI) of the analyte molecules allows one to virtually eliminate the problem of fragmentation of the molecules and to study the dynamics of the excited electronic states.

#### 2.1.1 Basics of Time-of-Flight Mass Spectrometry

The simplest ToF-MS consists of an ion source, a field free drift zone, and an ion sensitive detector. After ionization of the molecules of interest, the generated ions are accelerated in an electric field  $\vec{E}$ . Each ion travels a field-free time-of-flight distance with a distinctive velocity, depending on the respective mass-to-charge ratio  $m/z$ , and therefore arrives at the detector after a defined flight-time. It must be taken into account that ions, which fragment after they have left the acceleration field, can arrive at the same time-of-flight as their parent ions. Thus, simple ToF-MS setups cannot distinguish this sort of fragmentation.

Every time-of-flight mass spectrometer consists at least of three components, as drawn schematically in Figure 2.1:

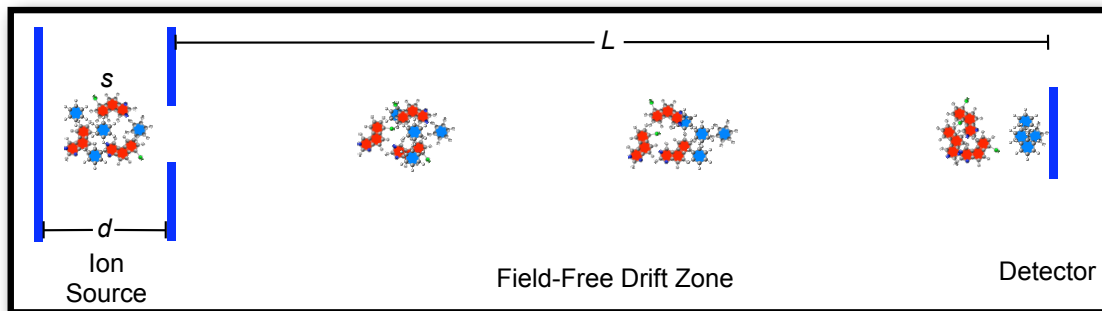


**Figure 2.1:** Sketch of a simple time-of-flight mass spectrometer. Shown are the point of ion formation  $s$ , the diameter  $d$  of the ion source, the length  $L$  of the field-free drift zone, and the detector.

1. The ion source is necessary to charge the molecules and to accelerate and focus the ions in the direction of the detector. The most simple setup consists of a one-step homogeneous electric field created by an acceleration potential  $\Delta U$  between two ion lenses (electrodes). The ions are generated in this electric field. The point of ion formation is the reference position for further calculations. The distance between the lenses determines the offset of the focal layer to the surface of the detector. More advanced ion sources consist of more than two electrodes. This allows for a focussing of the ions by adjusting different acceleration potentials (see Subsection 2.1.1.2).
2. Ions of different masses separate because of their differing velocities. This takes place in the field-free drift zone. Field-free operation can be guaranteed by grounding of the time-of-flight tube.
3. In most cases multi-channel plates (MCPs) are used to detect the incoming ions. At negative working voltage, the MCP causes an acceleration of the positive ions towards the detector. The higher impact velocity increases the sensitivity of the MCPs, which is beneficial for observing molecules with high masses.

From a measured intensity-time profile of the ions, the mass information can be calculated by the use of the following equations: The effect of the force  $\vec{F}$  in an electric field  $\vec{E}$  on a charged particle is given by

$$F = zeE = \frac{ze\Delta U}{d}, \quad (2.1)$$

where  $z$  is the charge number,  $e$  the elementary charge, and  $d$  the distance of the potential gradient  $\Delta U$ . The particles are thus accelerated by the force  $\vec{F}$  and leave the ion source with the kinetic energy.

$$E_{kin} = \frac{mv^2}{2} = ze\Delta U = E_{pot} \quad (2.2)$$

Equation 2.2 gives the mass-charge ratio as

$$\frac{m}{z} = \frac{2e\Delta U}{v^2} = \frac{2e\Delta U}{s^2} \cdot t^2, \quad (2.3)$$

Equation 2.3 shows that the mass per charge ratio ( $m/z$ ) is proportional to the time-of-flight  $t^2$ . Thus, particles with the same charge, but different masses, are separated by their different arrival times at the detector. The factor  $2e\Delta U/s^2$  depends only on the experimental settings and can be kept constant for all measurements.

### 2.1.1.1 Mass Resolution of a ToF-MS

Due to the counterpart of time and mass, the resolution of a ToF-MS can be defined as two times the time-of-flight difference  $\Delta t$  between two mass peaks divided by the time-of-flight  $t$  of the larger mass, *i.e.*,  $2\Delta t/t$ . Considering just one peak, the ratio between the full width at half maximum (FWHM) of this mass peak and its mass gives the maximal resolution  $\Delta m/m$ .

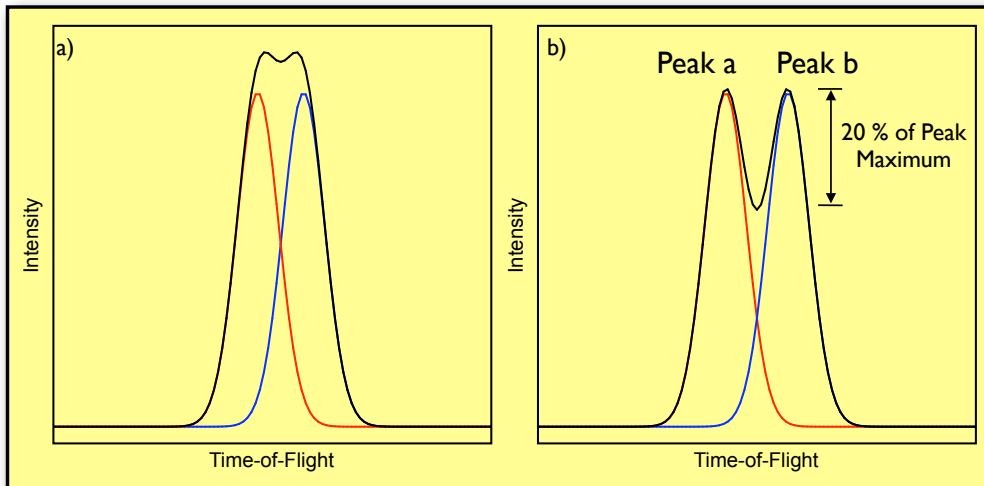


**Figure 2.2:** The mass resolution of a ToF-MS. a) If the resolution is too low, peaks cannot be resolved. b) The dip between two adjacent peaks should be at the least 20 % of their amplitudes in order to clearly resolve the peaks.

The resolution of a mass spectrometer depends basically on five points:

1. Because of the different velocities of ions of unequal masses in the field-free drift zone, the temporal separation can be increased by longer time-of-flight tubes

$$t_2^2 - t_1^2 = \frac{\Delta m_{(m_2-m_1)}}{2ze\Delta U} \cdot s^2 \quad (2.4)$$

Thus, the mass resolution is increasing with use of longer field-free drift zones.

2. To obtain a time-of-flight mass spectrum at all, the ion source has to be pulsed. The shorter the temporal width of the starting ion packet, the better is the resolution.
3. Aside from the temporal width, the spacial width has to be taken into account. Small discrepancies in the point of ion formation lead to a blurring of the resulting mass peaks. This can be avoided by space focussing (see Subsection 2.1.1.2).
4. The resulting mass peaks can be broadened by ion kinetic energy dispersion. To minimize this effect, energy focussing is needed (see Subsection 2.1.1.2).
5. The width of the mass peaks depends strongly on the rise time of the detector, which is limited by the quality of the MCP.

### 2.1.1.2 Space Defect and Space Focussing

Better mass resolution can be achieved by space focussing with a two-level ion lens, which consists of three electrodes. The ion lenses are called repeller, extractor and ground, as described by Wiley and McLaren in 1955 [39].

By choosing optimal potential gradients between repeller, extractor and ground plate, all molecules of the same mass can be detected simultaneously, independent from their place of formation.<sup>1</sup> The two-staged acceleration of the ions takes place between the three electrodes with the distances  $d_1$  and  $d_2$ . The potentials  $U_1$ ,  $U_2$  and  $U_3$  at the electrodes create the homogeneous electric fields  $E_1$  along  $d_1$  and  $E_2$  along  $d_2$ . The time-of-flight  $T_1$  of an ion formed at position  $s$  traveling to the extractor is calculated by the equation of motion

$$s = \frac{1}{2} \frac{z \cdot E_1}{m} T_1^2, \quad (2.5)$$

*i.e.*,

$$T_1 = \sqrt{\frac{2m \cdot s}{z \cdot E_1}}. \quad (2.6)$$

---

<sup>1</sup>As long as they have been generated between the repeller and extractor.



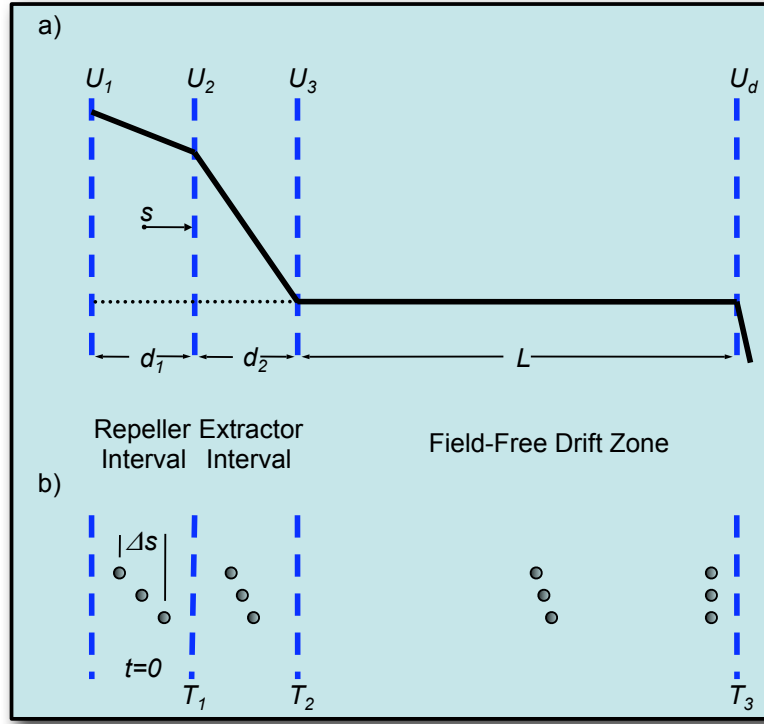


**Figure 2.3:** Two level *Wiley-McLaren* ion lens for space focussing. (a) Electrode position and potential gradient. (b) Space/time behavior of ions of the same mass but different points of formation.

The molecules reach the extractor with the velocity

$$v_1(s) = \frac{z \cdot E_1}{m} T_1. \quad (2.7)$$

After the second acceleration stage from the extractor to the mass plate, their velocity is given by

$$v_2 = v_1 + \frac{z \cdot E_2}{m} T_2. \quad (2.8)$$

The distance  $d_2$  can be calculated as

$$d_2 = v_1 T_2 + \frac{1}{2} \frac{z \cdot E_2}{m} T_2^2. \quad (2.9)$$

The time-of-flight through the field-free drift zone  $L$  is  $T_3 = L/v_2$ . The total time-of-flight  $T = T_1 + T_2 + T_3$  should be independent of the place of ion formation  $s$  to achieve space focussing. This can be realized by proper choice of the field strengths  $E_1$  and  $E_2$  for the given distance  $L$ , as is demonstrated in Figure 2.3. Here, the distance/time behavior for three ions of the same mass, but different formation points  $s$ ,  $s - \Delta s$  and  $s + \Delta s$  at  $t = 0$ , are shown. At time  $t = T_3$ , all ions are at the

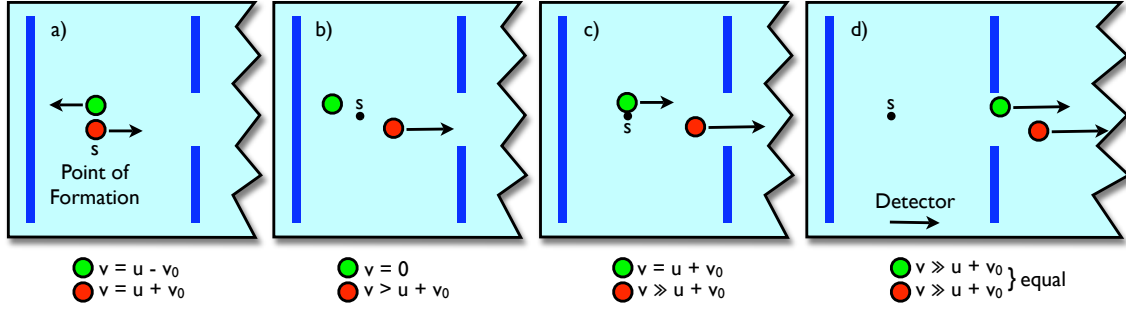


**Figure 2.4:** Kinetic energy dispersion. (a) The ions are generated at  $s$  within the potential gradient  $\Delta U$ . They have the same velocities in complementary directions. (b) First the green particle is slowed down to  $v = 0$  by  $\Delta U$ , and changes its flight direction, while the red one is accelerated further. (c) The green particle reaches the starting position of the red particle after the so called "turn-around time" ( $T_u$ ). (d) The delay in time between the particles, which now have the same velocity, is the  $2 \times T_u$ .

same position perpendicular to the detector and can be measured simultaneously. The independence of the total time-of-flight  $T$  from the spread of  $s$  is mathematically expressed by setting the derivative of  $dT/ds$  to zero. It follows that the drift length  $L$  is given by

$$L = d_1 \cdot k^{\frac{3}{2}} \left[ 1 - \frac{d_2}{d_1} \frac{1}{k + \sqrt{k}} \right] \quad (2.10)$$

with

$$k = 1 + 2 \frac{U_2}{U_1 - U_2}. \quad (2.11)$$

With Eq. 2.10, it is possible to predict the required voltage ratio  $U_1/U_2$  for a given drift length  $L$ .

### 2.1.1.3 Energy Defect and Energy Focussing

The described space focussing of the linear ToF-MS is limited by the finite energy focussing. Despite the supersonic expansion and the use of a skimmer, an energy discrepancy results from the spreading of the kinetic energy and the remaining angular distribution in the molecular beam. Furthermore, a part of the absorbed ionization energy can be released to the ions as recoil kinetic energy.

Ions of the same mass can have different orientations of velocity  $v_1$  and  $v_{-1}$  at  $s$ . Ions with  $v_{-1}$  initially travel opposite to the acceleration direction. Therefore, they

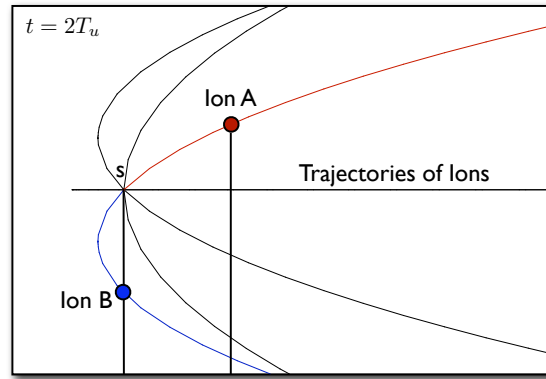


**Figure 2.5:** Ions with different kinetic energies, formed at point  $s$ , are accelerated by a homogeneous electric field in the direction of the detector. While ion A is gathering speed, ion B is first decelerated until it changes its flight direction. The time period to reach this point is called the turn-around time  $T_u$ . After the same time, thus at  $2T_u$ , ion B reaches the initial point of formation  $s$ . It has now the same velocity component towards the detector as ion A had in the beginning.

are slowed down and then accelerated towards the detector. The time, which the ions need to reach the initial starting point again, is called the turn-around time  $T_u$  (Figures 2.4 and 2.5). The ions need another  $T_u$  to catch up with those ions, which have started at  $s$  with  $v_1$ . The resolution limit of the ToF-MS is thus diminished, if  $2 \times T_u$  is greater than the  $\Delta t$ . Ions of high recoil energy have such a poor focussing that they may not hit the detector at all (see Figure 2.6).

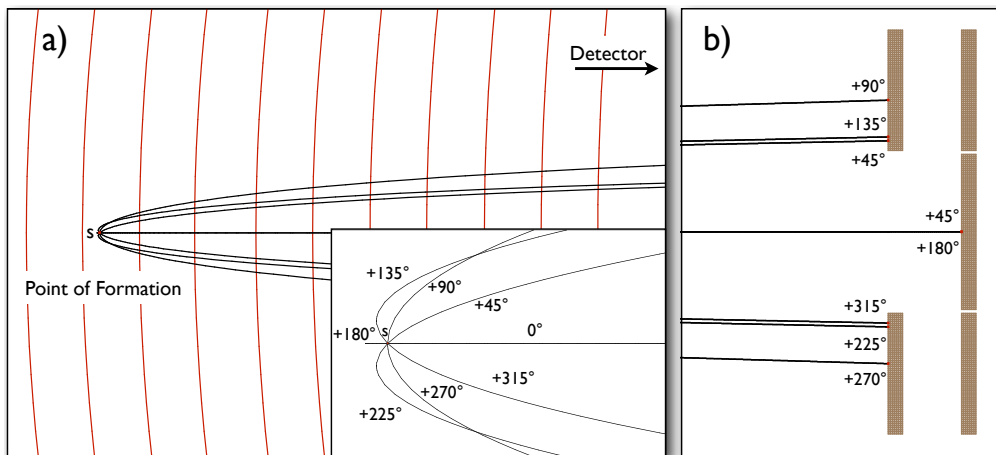


**Figure 2.6:** Ions of the same mass formed within a homogeneous acceleration field, but with velocities in different directions, are insufficiently focussed onto the detector.

## 2.1.2 Experimental Setup for Time-of-Flight Mass Spectroscopy

This Section briefly reports on the experimental setup of the newly constructed ToF mass spectrometer, which was used for investigating ultrafast electronic dynamics in the gas phase for the first time in our group. Additional to the technical details presented in this section, the Appendix contains to-scale technical drawings and photographs.

### 2.1.2.1 Vacuum Equipment

The ToF-MS experiment was performed in an electro-polished stainless steel chamber (see Figure 2.7) under ultrahigh vacuum (UHV) molecular beam conditions. The chamber was divided by a removable separating plate into two differentially pumped parts. Two water-cooled turbo molecular pumps (Pfeiffer, THM521 and THM261), which offer pumping speeds of 520 l/s and 210 l/s respectively, were used for evacuation.

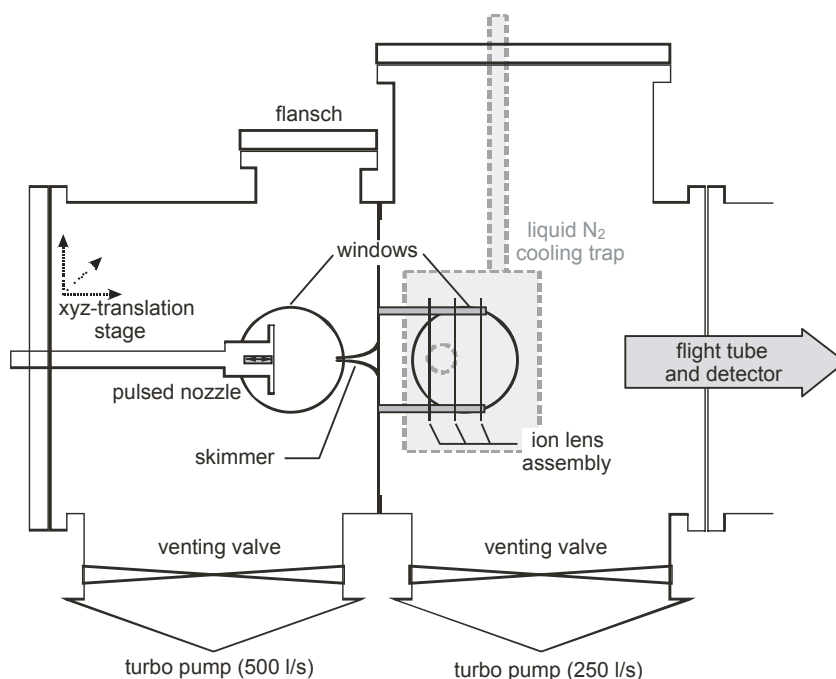


**Figure 2.7:** Sketch of the experimental setup of the ToF mass spectrometer. The entrance part of the vacuum chamber was composed of a pulsed nozzle, which formed the molecular beam, mounted on a xyz-translation stage and a conical skimmer. The ion lens assembly, the liquid nitrogen cooling trap, the flight tube and the detector were located in the detection part.

The connection between the turbo pumps and the vacuum chamber could be individually sealed by two venting valves (VAT, 100 CF and 200 CF). The necessary fore-vacuum was provided by two rotary vane pumps (Pfeiffer, DUO20M and DUO10M)

with a pumping capacity of 24 m<sup>3</sup>/h and 12 m<sup>3</sup>/h, respectively. To prevent oil exhalations in the chamber, molecular sieve (Leybold, Zeolith 13X) filled adsorption traps were inserted in between the fore and main pumps. Additionally, all devices were supplied by a power-guard, which turned off the electricity, if the pressure in the vacuum chamber exceeded 10<sup>-3</sup> mbar. The assembly provided a basic pressure of 1 · 10<sup>-7</sup> mbar in the entrance chamber and 3 · 10<sup>-8</sup> mbar in the detection chamber. At UHV level, the pressure was measured by cold cathode gauges (Pfeiffer, IKR251), and for lower pressures two Pirani gauges (Pfeiffer, TPR261) were available.

### 2.1.2.2 Sample Preparation

As described in Figure 2.8, a tube and valve system (“pick-up source” [40]) was used for the sample preparation. Helium carrier gas was passed through a reservoir, which contained the investigated sample. According to its vapor pressure, sample was carried along. The sample concentration in the molecular beam was controlled by adjusting the reservoir temperature. Because of a too long residence time in front of the pulsed nozzle the concentration of clusters in the molecular beam can be greatly increased. Therefore, the holding time was minimized by drawing the waste by an additionally rotary vane pump (Alcatel, LS71).

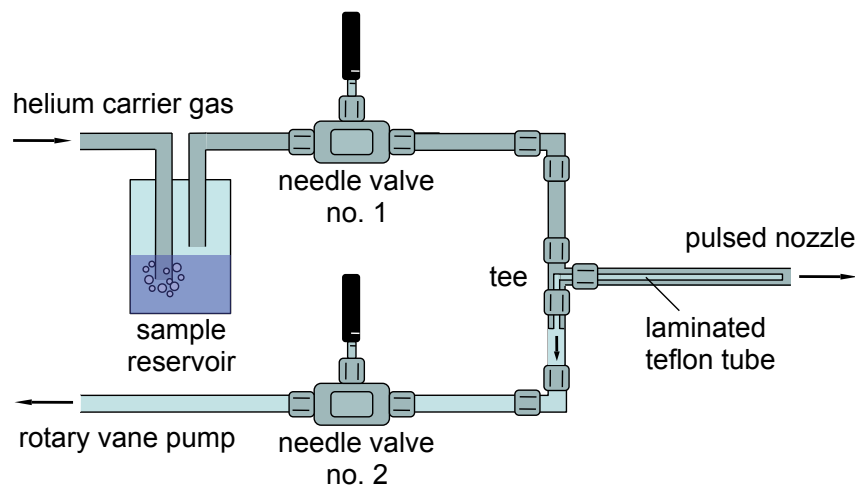


**Figure 2.8:** Plot of the sample preparation tube system. The He gas bubbled through the sample reservoir and carried along sample, according to its vapor pressure. Minimizing the residence time of the mixture in front of the pulsed valve gave a very low amount of clusters in the molecular beam. This was controlled by two needle valves and an extra rotary vane pump. The laminated teflon tube ensured that the mixture was drawn directly in front of the pulsed nozzle.

### 2.1.2.3 Pulsed Nozzle, Molecular Beam, and Flight Conditions

The gas mixture was expanded through the pulsed nozzle (General Valve, Series 9) into the entrance part of the vacuum chamber, forming a molecular beam. The concept of a pulsed molecular beam source was first established in 1977 by Gentry and Giese [41, 42]. The nozzle was positioned axially in front of the self-made skimmer by a xyz-translation stage to cut out the homogeneous inner part of the molecular beam. The diameter of the nozzle opening is 0.8 mm, that of the skimmer 1 mm, at a spacing between them of  $\approx 30 - 50$  mm. The opening time of the nozzle was tuned by a controller (General Valve, Iota One).

The skimmed molecular beam passed centrally through a hole in the first ion electrode (“repeller”) of the ion lens assembly. Thereby, the valve opening, the skimmer, and the repeller aperture formed a joint line. The distance between the back of the skimmer and the repeller plate was 25 mm. Entering through a quartz glass window ( $\varnothing = 25$  mm,  $d = 1$  mm, Suprasil I), the laser beams crossed the molecular beam in the middle between the repeller and the extractor plate (2nd ion electrode). The flight distance between the ground plate (last electrode) and the detector was 1270 mm. Field-free conditions were ensured by the ground plate and a metal shield in front of the detector, which were grounded jointly.

At a thermal equilibrium ( $T_1$ ), the one dimensional translational energy distribution is given by the Maxwell-Boltzmann Equation,

$$f(v_z) = \sqrt{m/2\pi kT_1} e^{-mv_z^2/kT_1}. \quad (2.12)$$

The adiabatic expansion through the small opening into the vacuum alters the translational, rotational, and vibrational energy distributions. As example, the translational energy distribution is shown in Figure 2.9 in thermal equilibrium, after the initial expansion, and in the skimmed molecular beam. After the adiabatic expansion ( $T_2$ ) into the vacuum, the distribution is shifted by the additional velocity  $u_z$ .

$$f(v_z - u_z) = \sqrt{m/2\pi kT_2} e^{-m(v_z - u_z)^2/kT_2} \quad (2.13)$$

In the skimmed molecular beam, the velocity distribution is very narrow, as illustrated in Figure 2.9 (f).

### 2.1.2.4 Ion Lens Assembly

The ion lens assembly consisted of three circular electro-polished stainless steel plates ( $\varnothing 70$  mm,  $d = 0.5$  mm), which were assembled at 15 mm distance on four threaded rods (M4, PVC). The repeller plate had a central hole of 2 mm diameter

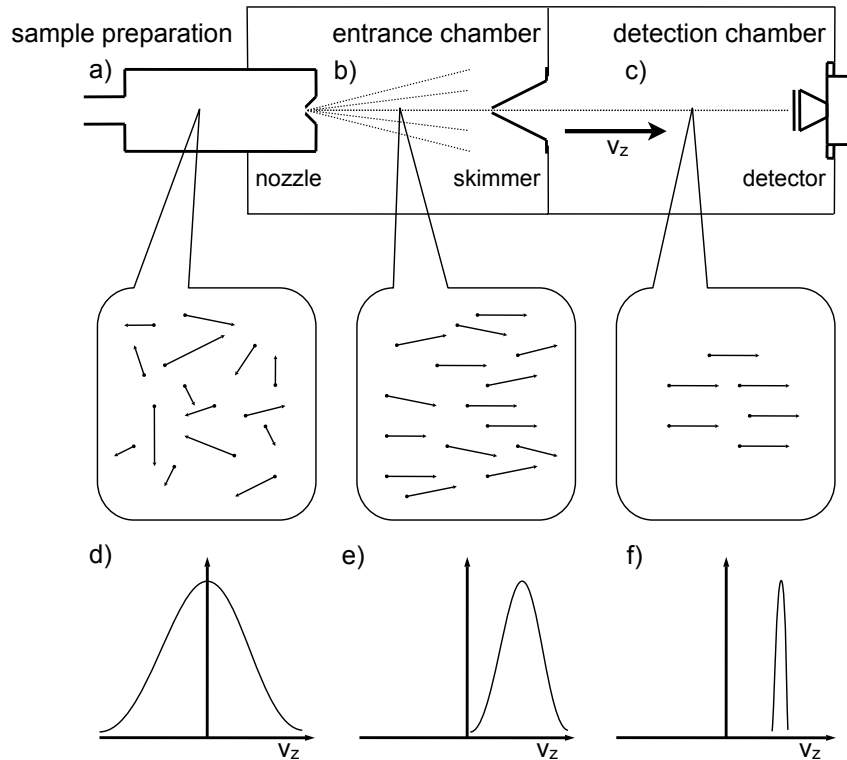


**Figure 2.9:** Molecules are in thermal equilibrium (a and d). After expansion a modified distribution is formed (b and e). The skimmer peels off all molecules with translational energy different then in  $z$  direction (c and f).

and the holes in the extractor and the ground plate were 20 mm. Mechanic rigidity was achieved by insulating ceramic spacers (Makor, 15 mm long) between the plates, which had groove and tongue joints (for details see Figure 2.10). Repeller and extractor were connected to two separate highly stable power supplies (FUG, HCE 35-6500), while the ground plate was conductively connected to the steel chamber. All silvery feed cables were isolated on their whole length by glass tubes.

To avoid background noise, a liquid nitrogen cooling trap surrounded the ion lens assembly. For the passing laser beam a clearance of 15 mm was worked in. The use of the trap improved the vacuum in the detection part by one order of magnitude.

### 2.1.2.5 Detector and Data Acquisition

The detector was home-built in our workshop and consisted of two multi-channel plates (MCP; Hamamatsu F4294-07,  $\varnothing = 32.8$  mm), which were consecutively assembled in chevron configuration. The pore size was  $10 \mu\text{m}$ , the channel bias was  $12^\circ$  to the perpendicular surface, and the distance between the channel centers was  $12 \mu\text{m}$ . The gain over both MCPs at 2 kV was  $0.289 \cdot 10^9$ . The MCPs were followed

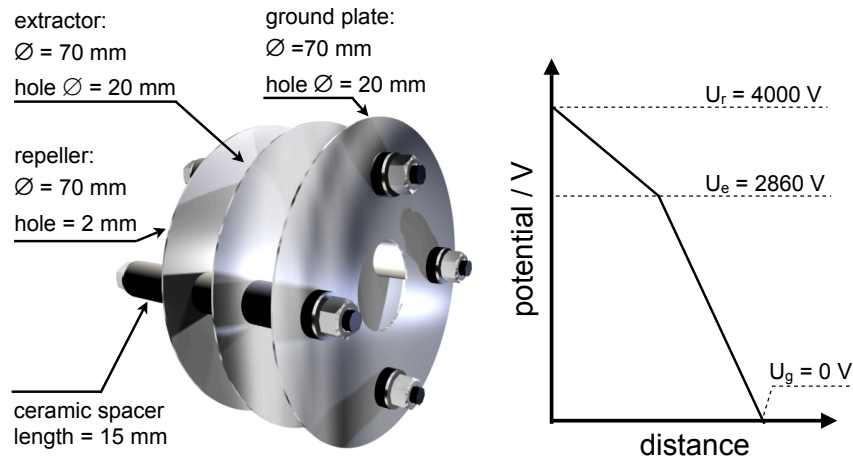


**Figure 2.10:** The ion lens assembly consisted of three electrodes, the repeller, the extractor, and the ground plate.

by a stainless steel hopper, which was connected directly to an oscilloscope (LeCroy, LT264). The assembly is shown in Figure 2.11. The MCPs and the steel hopper

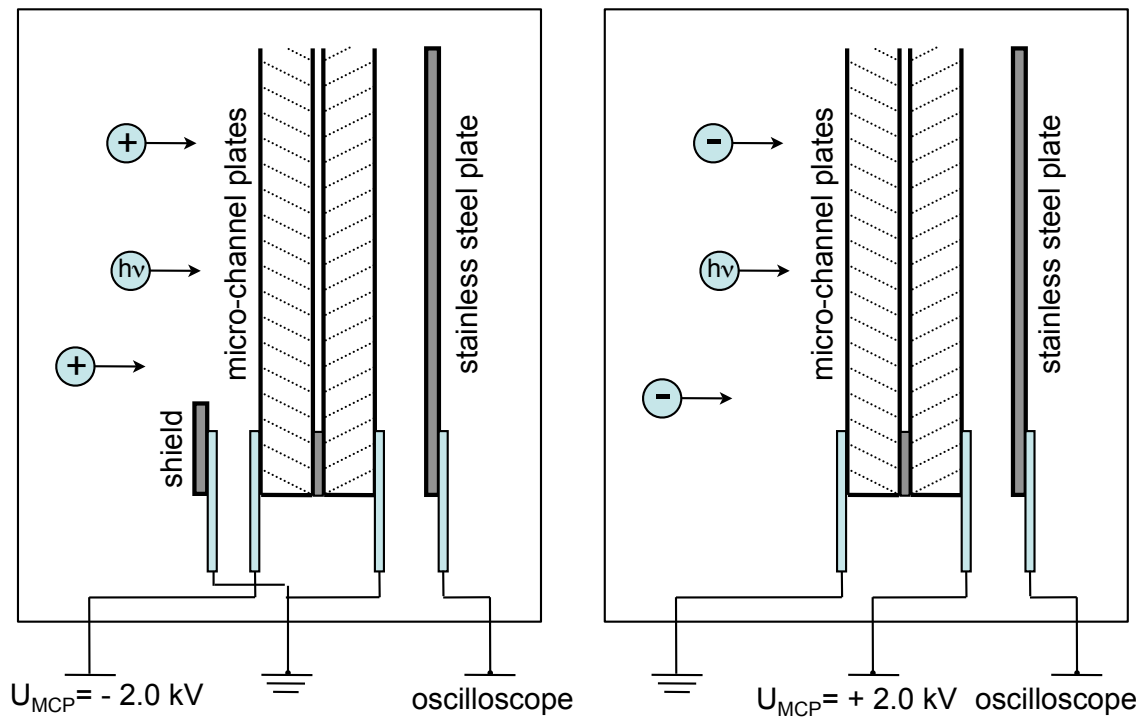


**Figure 2.11:** The detector consisted of two MCPs in a chevron followed by a stainless steel hopper. The assembly could be used for the detection of cations, and anions.

were built in a standard flange (NW 100 CF) and the detector was attached to the end of the flight tube. The bias was provided by a high voltage adapter (FUG, HCE



35-3500). The correct circuit depends on the detected particles and is described in Figure 2.11.

For readout, a digital oscilloscope (LeCroy, LT 264) was used. The oscilloscope had four channels with a bandwidth of 350 MHz at a digitizing speed of 1 GS/s (1 point  $\text{ns}^{-1}$ ). The mass peaks were summed up over 1250 laser shots using a special fast operating mode (sequence mode). A computer controlled the oscilloscope via a LabView (National Instruments, Version 8.2) program, which is explained in detail in the Appendix.

### 2.1.2.6 Achieved Mass Resolution

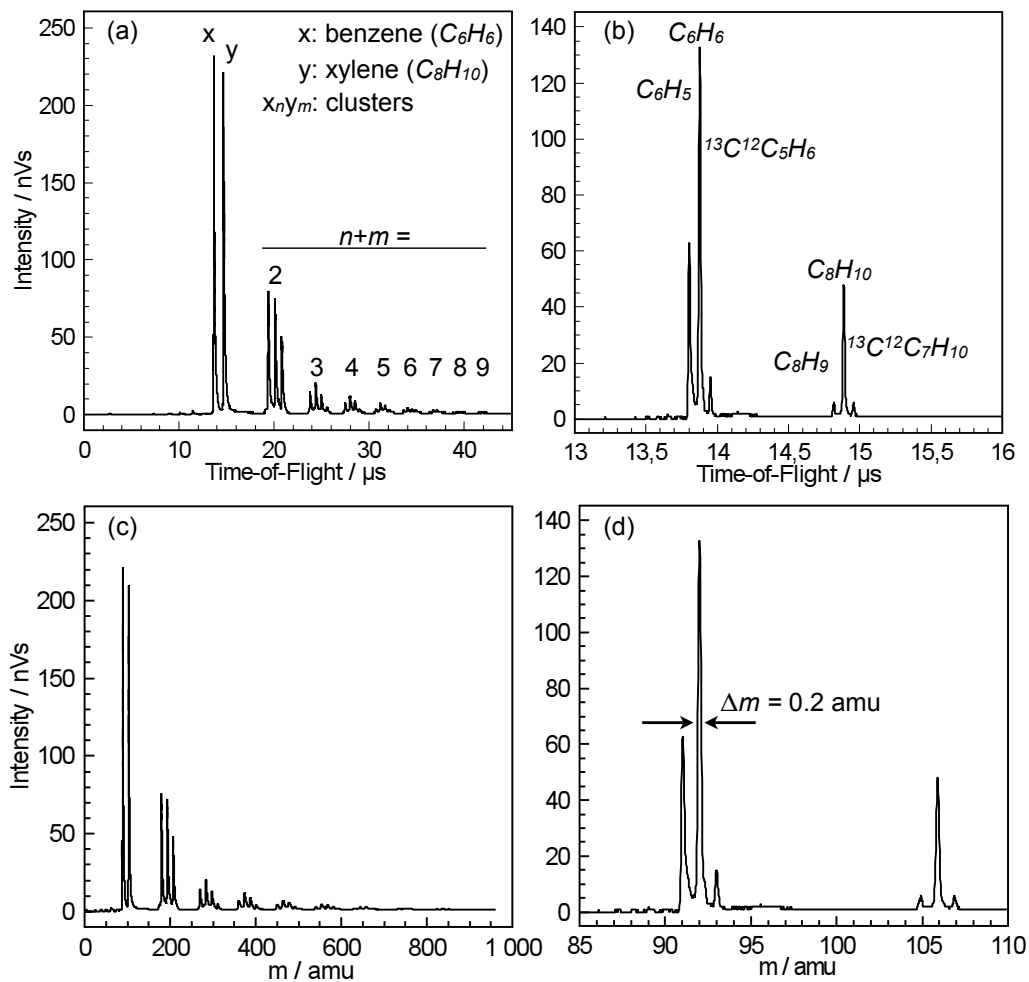


**Figure 2.12:** (a) Overview ToF spectrum showing peaks originating from benzene, xylene, and their clusters. (b) A zoomed-in view of (a) reveals that each peak in the spectrum corresponds to three peaks. (c) Overview mass spectrum calibrated on benzene and xylene parent peak positions. (d) The zoom of (c) reveals a peak width  $\Delta m = 0.2 \text{ amu}$  (FWHM).

The resolution of the ToF mass spectrometer was determined by a non-resonant multiphoton absorption at  $\lambda = 775$  nm, ionizing a sample mixture containing benzene and xylene with the ratio of 1:1. The top of Figure 2.12 shows the intensity/ToF profiles. The overview spectrum (a) exhibits several peaks at different time-of-flights that were assigned to benzene (x), xylene (y), and their clusters ( $x_n y_m$ ). Clusters corresponding to the agglomeration of up to  $n + m = 9$  monomers were detected. In the zoomed-in view (b) a splitting of each time-of-flight peak is observed. The satellites at slightly longer ToF correspond to molecules, containing a  $^{13}\text{C}$  carbon isotope. Additionally, satellites at shorter ToF were found, corresponding to molecules after dissociation of a H atom. Figure 2.12 (c) and (d) show the corresponding mass spectra. The mass calibration was performed using Equation 2.3 in Subsection 2.1.1. Thereby the parent peak positions of benzene and xylene were taken as reference. The width of the benzene parent mass peak at  $m = 96$  amu was determined to be  $\Delta m = 0.2$  amu, resulting in a mass resolution  $R = \Delta m/m = 2.1 \cdot 10^{-3}$  ( $1/R \approx 500$ ) of the spectrometer.

### 2.1.2.7 Timing of the Components

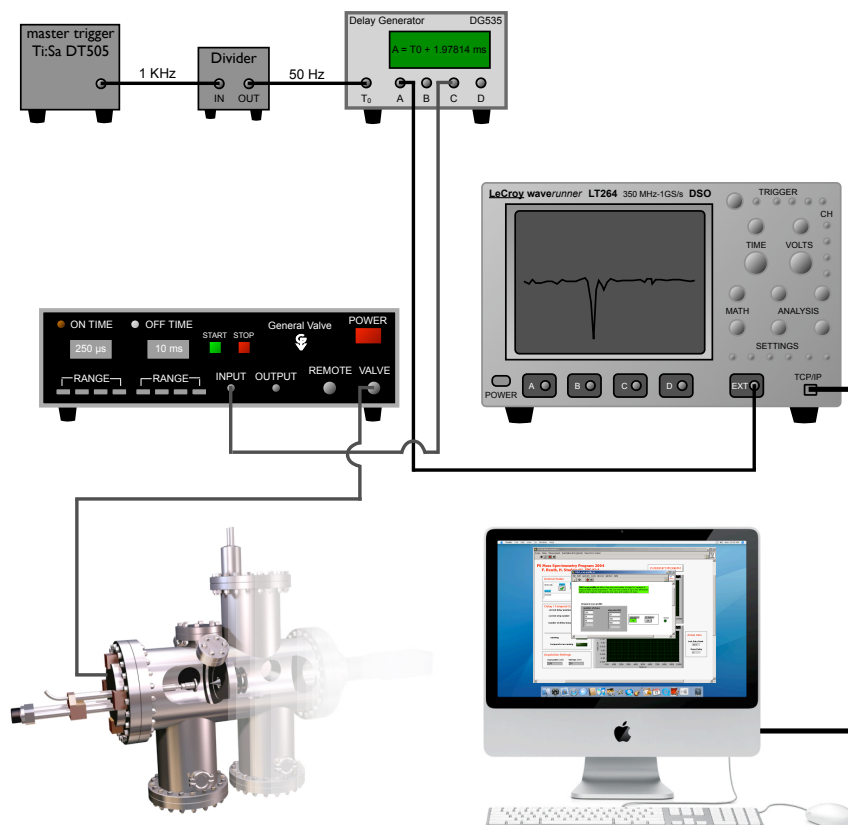


**Figure 2.13:** Control and timing of the experimental components by the delay generator.

A delay generator (Stanford Research, DG535) controlled the timing of the experimental setup. Figure 2.13 gives an view over all connections and triggered components. The delay generator was synchronized with the master trigger ( $T_0$ ), which was fixed in time by the Ti:Sa laser system. The repetition rate of 1 kHz of the master trigger was reduced to 50 Hz by an electronic divider (home-built) before entering the  $T_0$  input of the delay generator. The molecular beam needed  $\approx 1.5$  ms to arrive in the detection part of the vacuum chamber after the nozzle had opened. Therefore it was necessary to synchronize the measurements on the over-next laser shot (1 shot  $\text{ms}^{-1}$ ). This was achieved by delaying the nozzle opening by  $C = T_0 + 0.25$  ms. The oscilloscope was triggered recording the time-of-flight of the ions exactly when the third laser shot after the  $T_0$  trigger crossed the molecular beam. The timing was checked by a fast photodiode, which measured the arrival time of the laser pulse after it had passed experiment through a second glass window. The timing is shown schematically in Figure 2.14.

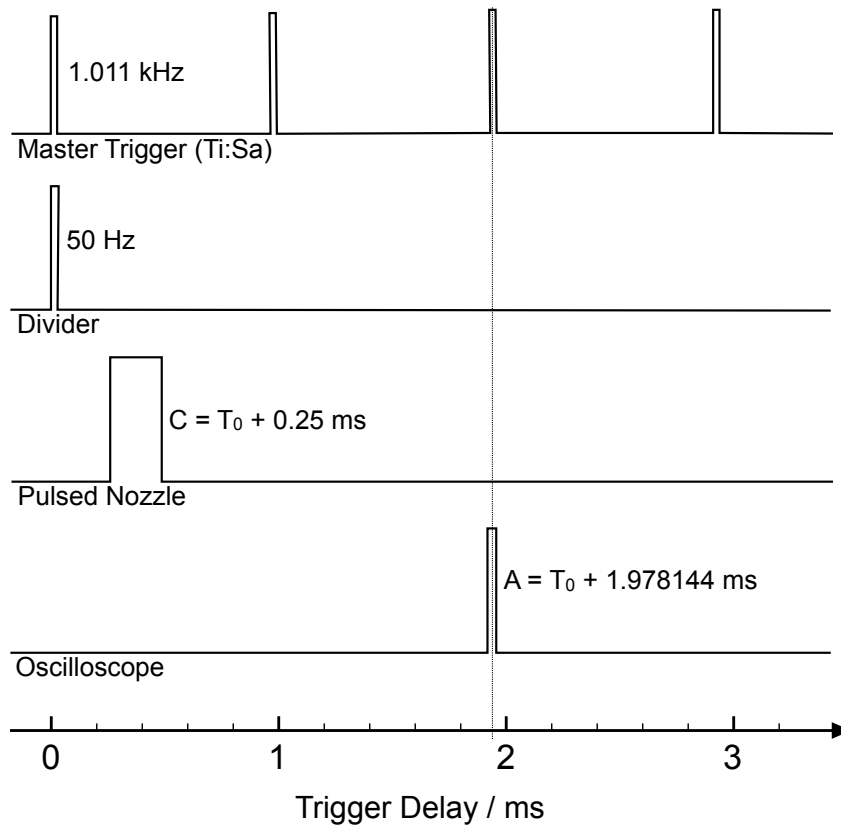


**Figure 2.14:** Schematic diagram illustrating the timing of the master trigger, the nozzle and the oscilloscope.

### 2.1.3 Data Analysis of Transient Mass Spectra

Since the measurement of physical properties is often a convolution of the real data with an instrument response function (IRF) of the experimental setup, the measured transient mass signals at a preselected  $m/z$  value (usually the molecular parent peak) are fitted with a sum of decaying exponential functions  $I(t)$  convoluted with the  $IRF(t, t_0)$ ,

$$y(t) = I(t) \otimes IRF(t, t_0), \quad (2.14)$$

and with

$$I(t) = \sum_i A_i \exp(-t/\tau_i), \quad (2.15)$$

and

$$IRF(t, t_0) = \frac{1}{\sigma\sqrt{2\pi}} \exp - \frac{(t - t_0)^2}{2\sigma^2} \quad (2.16)$$

$$y(t) = \sum_i A_i \exp(-t/\tau_i) \otimes \frac{1}{\sigma\sqrt{2\pi}} \exp - \frac{(t - t_0)^2}{2\sigma^2} \quad (2.17)$$

With the number of exponentials  $i$ ,  $A_i$  the amplitude,  $t$  the delay time, decay rate  $\tau_i$ , and the width  $\sigma$  for a Gaussian IRF. The reconstruction (deconvolution) gives the real parameters  $A_i$ ,  $\tau_i$ , and  $\sigma$  and is done by a Mathematica 6.0 fitting routine using the Levenberg-Marquardt algorithm [43]. The source code of the program is given in the Appendix.

## 2.2 Photoelectron Imaging

### 2.2.1 Introduction to Photoelectron Imaging

The time-resolved ion detection in the gas phase resolves only a part of the available information on the investigated molecular system. The detection of photoelectrons constitutes an important extension and refinement, revealing additional details on the electronic structure and energetics of the system. A combination with the femtosecond pump-probe technique allows one to follow the electronic dynamics of a photoexcited state [44]. Figure 2.15 shows schematically the time evolution of an excited molecular system and explains the principles of pump-probe photoelectron spectroscopy.

The system in Figure 2.15 is located initially in a well-defined vibrational level ( $E_{\nu=0}$ ) of the electronic ground state  $S_0$  (molecular beam conditions). The pump photon  $h\nu_{pump}$  excites the molecule into a coherent superposition of several excited vibrational levels. The width of this distribution is determined by the bandwidth of the laser pulse. After subsequent absorption of the probe photon  $h\nu_{probe}$ , the total energy of the system is given by  $E_{total} = h\nu_{pump} + h\nu_{probe}$ . If this energy exceeds the ionization energy (IE) and the system is probed without a delay, the molecule may be ionized. The internal energy distribution in the ionic state  $D_0$  depends on the Franck-Condon (FC) factors for the ionization process. An excess energy is converted

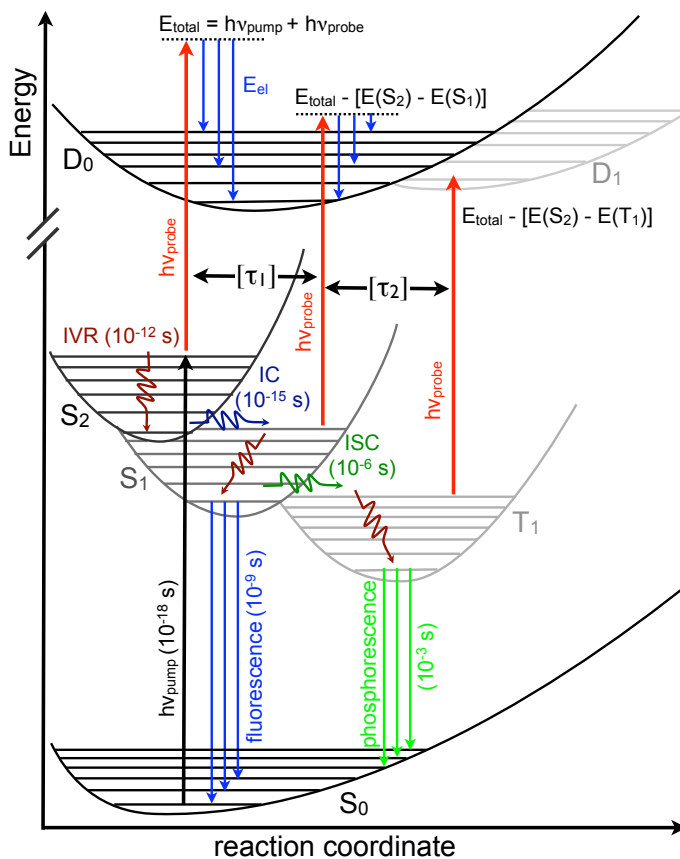


**Figure 2.15:** Schematic Jablonski diagram of the excited electronic state dynamics observed by pump-probe photoelectron spectroscopy.

to electron kinetic energy and carried away by the ejected electron. The full energy balance is written in Equation 3.1. This is the basis equation of photoelectron spectroscopy in isolated molecules.  $E_{\nu}^{Ion}$  is the vibrational energy in the system after ionization, which is measured by the electron energy  $E_{el}$ . The population of

the vibrational states in the ion depends on the FC overlap between the vibrational levels in the intermediate state and the ionic ground state.

$$h\nu_{pump} + h\nu_{probe} = E_{el} + IP + E_{\nu}^{Ion} \quad (2.18)$$

so that

$$E_{el} = h\nu_{pump} + h\nu_{probe} - IP - E_{\nu}^{Ion}. \quad (2.19)$$

An exception occurs when the potential energy surfaces for the excited and ionic states are very similar, so that also the FC factor are similar, leading to a propensity rule  $\Delta\nu = 0$ .

However, it is even possible to observe changes of the initially prepared intermediate state. Such changes can be due to internal vibrational energy redistribution (IVR), internal conversion involving electronic transitions (IC), intersystem crossing (ISC), dissociation, or other reactions. Pump-probe photoelectron spectroscopy can follow this dynamics as indicated in Figure 2.15 by delaying the probe pulse for a time  $\Delta t$  with respect to the pump pulse. In order to be able to interpret the results, one needs a more precise treatment, which is presented in the following subsection, and plausible models for the potential energy surfaces and the ensuing nuclear dynamics. These are preferably based on *ab initio* calculations.

In the last years many different experimental setups for femtosecond time-resolved photoelectron spectroscopy experiments have been reported in the literature. An early spectrometer with femtosecond time resolution was developed by Baumert *et al.* [45] in 1993 using the zero kinetic energy electron (ZEKE) detection, followed by the first recorded femtosecond photoelectron spectrum of 1,3,5-hexatriene in 1996 by Cyr and Hayden [46]. The experimental analysis of the kinetic energy is often done by a magnetic bottle combined with a time-of-flight spectrometer, which was published in literature by Kruit and Read in 1983 [47]. A recent example for such a state-of-the-art photoelectron spectrometer is described in [48, 49]. Latest developments involve time-resolved photoelectron imaging [50], and those principles are briefly discussed in this Section.

### 2.2.1.1 Energy Conservation in Isolated Molecules

The total energy deposited in an isolated molecule by the pump and probe pulses is conserved, unless the molecule fluoresces. Energy change or energy dissipation in the system refers to energy redistribution among the degrees of freedom, some of which are no longer accessible for ionization by the probe photon. The redistribution

processes are indicated in Figure 2.15, they may be due to the mentioned IVR, but also IC and ISC. Because different vibrational modes have different FC factors with the ionic ground state, the ionization of some molecules with excitation in these modes can be hampered. Since one does not excite a stable stationary state of the system, internal redistribution processes lead to time-dependent FC factors.

Aside from this, it is possible that the internal dynamics of the system allows access to a different ionic state of the system, as it is indicated for the ionization of the triplet state  $T_1$  in Figure 2.15. This situation could even be encountered when the molecule stays in the singlet state, because the energy dissipates into inaccessible degrees of freedom so that the delayed probe pulse is no longer sufficient to ionize the molecule, hence the photoelectron spectrum changes correspondingly. This is discussed more closely in terms of the Koopmans' picture in the next subsection.

For completeness, it is mentioned that a diffusion of an initially coherent wavepacket will lead to loss of electron signal as well as any changes in FC factors in the course of the wavepacket dynamics, even without any energy relaxation or redistribution in the system.

### 2.2.1.2 Koopmans' Theorem

The Koopmans' picture can be considered as special application of the Born-Oppenheimer approximation to the ionization of excited molecules by a single photon and states as follows: "An emission of an independent outer valence electron occurs without simultaneous electronic reorganization of the ion core". Therefore, this elementary correlation rule allows for the definition of the cation electronic state, which is formed upon single active electron ionization of a given molecular orbital [51].

Two correlation types of Koopmans' picture are distinguished. Figure 2.16 shows schematically the so called "type I" correlation, where an optically "bright" state  $\alpha$  is prepared by an ultrashort laser pulse. According to the Koopmans' picture, this state should ionize into the  $\alpha^+$  continuum, which corresponds to the electronic state of the cation obtained by removal of the outermost valence electron. The emitted photoelectrons form the band  $\varepsilon_1$ . If one considers a non-adiabatic coupling to an energetically lower lying and optically "dark" state  $\beta$ , it should ionize, again according to Koopmans' picture, into the  $\beta^+$  continuum, forming the photoelectron band  $\varepsilon_2$ . The type I correlation suggests that the electronic structure acts as a "template" for the disentangling of electronic from vibrational dynamics in the excited state, which can thus be observed via time-resolved photoelectron experiments as the development of the vibrational structure in the photoelectron band  $\varepsilon_1$  and  $\varepsilon_2$ . This has been shown by studying the non-adiabatic dynamics in a linear polyene [52].

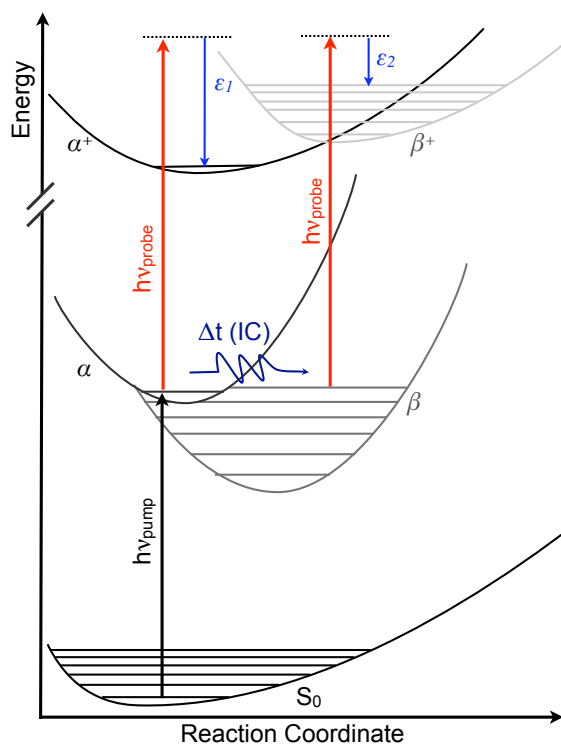


**Figure 2.16:** Schematic plot of the Koopmans' type I correlations.

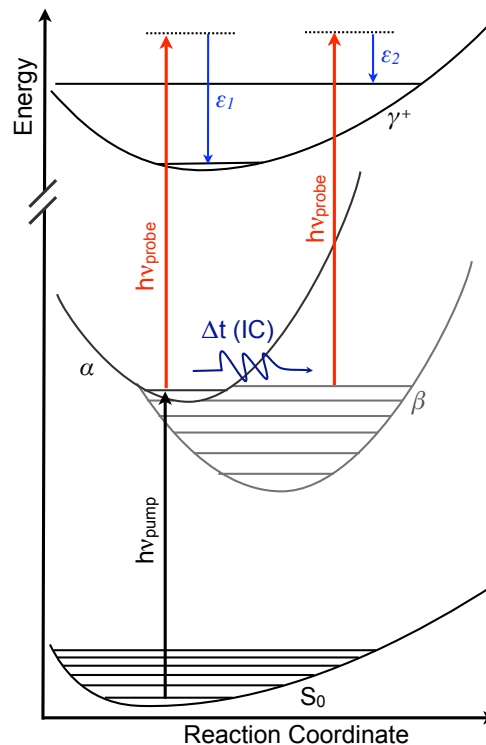


**Figure 2.17:** Schematic plot of the Koopmans' type II correlations.

The second correlation type is shown in Figure 2.17. The optically “bright” state  $\alpha$  as well as the “dark” state  $\beta$  are correlated with the same ionic state  $\gamma^+$ , producing the photoelectron bands  $\varepsilon_1$  and  $\varepsilon_2$ , respectively, upon ionization by a single laser photon. The states  $\alpha$ ,  $\beta$  and  $\gamma^+$  often possess significantly different geometries, which makes it impossible to conclude on the vibrational structures of  $\alpha$  and  $\beta$  by evaluation of the vibronic structure of the ionic state  $\gamma^+$ . Often the photoelectron bands  $\varepsilon_1$  and  $\varepsilon_2$  are strongly overlapped. Nevertheless, Koopmans' type II correlation is more easily accessible by quantum chemical calculations. Especially, the  $\beta^+$  state sets high requirements for theoretic considerations.

The other component of the molecular ionization process is the ejected electron. As discussed before, the kinetic energy of the emitted electron is directly correlated with the energy balance of the system. The next subsection describes, how the ejection angular distribution of the photoelectrons depend on the symmetry of the emitting electronic state.

### 2.2.1.3 Photoelectron Angular Distribution

The emitted electrons can be described as outgoing partial waves and their symmetries are likewise related to the symmetry of the electronic state undergoing ionization. In order to allow this transition, the requirement that the product of the symmetry species of the prepared excited state  $\Gamma_{ex}$  (readied by the pump), the dipole



operator  $\Gamma_\mu$ , the ion state  $\Gamma_{ion}$ , and the free electron wavefunctions  $\Gamma_{el}$  must contain the totally symmetric irreducible representation  $\Gamma_{TS}$  of the molecular symmetry group, as written in Equation 2.20.

$$\Gamma_{ex} \otimes \Gamma_\mu \otimes \Gamma_{ion} \otimes \Gamma_{el} \supseteq \Gamma_{TS} \quad (2.20)$$

If, because of a non-adiabatic process, the symmetry of the initial state  $\Gamma_{ex}$  changes, the symmetry species of the outgoing electron  $\Gamma_{el}$  must also change, such that the product remains (or contains) the totally symmetric species  $\Gamma_{TS}$ .

The symmetry species of the emitted electron wave correlates with the photoelectron angular distribution (PAD). The time-resolved measurement of PADs can be valuable, when the dynamical processes are not resolved by the photoelectron kinetic energy analysis alone [53, 54, 55].

If the excitation and ionization laser beams are both linearly polarized along the same axis  $z$ , and only one photon from each beam is absorbed, the photoelectron angular distribution can be described by

$$I(\theta) = \frac{1}{4\pi} [P_0 + \beta P_2(\cos(\theta)) + \gamma P_4(\cos(\theta)) + \delta P_6(\cos(\theta)) + \dots], \quad (2.21)$$

where  $\theta$  is the polar angle,  $I(\theta)$  the angle dependent intensity,  $\beta$ ,  $\gamma$ , and  $\delta$  are anisotropy parameters, and the  $P_n$  are the Legendre polynomials of the  $n$ -th order. The  $1/4\pi$  factor normalizes the equation, so that the Legendre polynomial of the zeroth-order  $P_0$ , which describes the total amount of detected electrons, becomes 1. All higher order polynomials do not change the total intensity, but change the distribution along the angle  $\theta$ . The symmetry species  $\Gamma_{el}$  of the outgoing electron partial waves are mirrored by the anisotropy parameters  $\beta$ ,  $\gamma$ , and  $\delta$ .

Spherical coordinates are used to describe the anisotropic shape of the emitted electrons, which span a spherical vector space as shown in Figure 2.18. If the laser

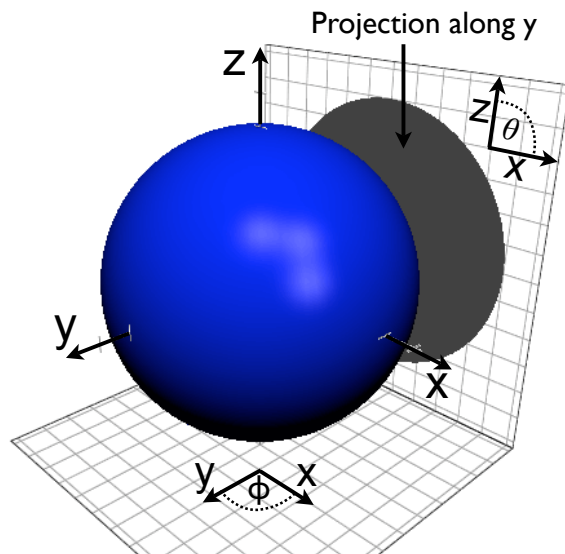


**Figure 2.18:** Schematic plot of a sphere in a cartesian coordinate system  $(x,y,z)$ . The polar angle  $\theta$  and the azimuth  $\phi$  are shown, too.

beams are polarized along the  $z$  axis and propagate along the  $x$  axis the photoelectron intensity distribution along the polar angle  $\theta$  is given by

$$\theta = \arctan \sqrt{\frac{x^2 + y^2}{z^2}}. \quad (2.22)$$

The azimuth angle  $\phi$  describes the distribution along the  $z$  axis, which is isotropic for constant values for  $\theta$ ,

$$\phi = \arctan \frac{y}{x}. \quad (2.23)$$

This means that the use of linear polarized light (along the  $z$  axis) reduces the spherical symmetry to cylindrical symmetry, which is important for the data analysis of the 2D projection (see Figure 2.18) of the 3D distribution. The data analysis is described in Section 2.2.3.

## 2.2.2 Technical Design

This section concerns the design of the newly constructed photoelectron imaging experiment (PEI), which is based on the ToF-MS setup introduced in Section 2.1.2. The vacuum equipment, the sample preparation, the molecular beam arrangement, and the ion lens assembly are equivalent to the ToF-MS spectrometer. Special provisions were made to insulate the flight tube, which has been shorted to 360 mm, from outer magnetic and electromagnetic stray fields to conserve the momentum of the ejected electrons. Furthermore, a position sensitive imaging detector assembly was installed to monitor, in addition to the time-of-flight of the electrons, also their velocities parallel to the detector surface ( $x,z$ -plane).

### 2.2.2.1 Shielding of Static and Dynamic Magnetic Fields

The ejected photoelectrons require, because of their small rest mass ( $m_e = 9.1093819 \times 10^{-31}$  kg), an effective shielding against static magnetic fields, such as the terrestrial magnetic field and dynamic magnetic fields, like those due to the 50 Hz commercial power frequency or of the solenoid driven molecular beam nozzles. Two different mechanisms are known that provide a very good shielding. First, static and alternating fields of frequencies  $\leq 50$  Hz are deflected by ferromagnetic metal alloys, like mu-metal (80 % Ni, 16 % Fe, and 4% Co), which because of their strong permeability ( $\mu_{mu} \approx 50\,000$  Vs/Am) guide the magnetic field around the vacuum. Second, dynamic fields of high frequencies  $\geq 50$  Hz are suppressed by an induced opposed field that derives from circling electrons in paramagnetic metals, like copper and aluminum. The electrons in those metals experience the so-called Lorentz force  $\vec{F}_L = e[\vec{v} \times \vec{B}]$  ( $e$  = charge,  $\vec{v}$  = velocity, and  $\vec{B}$  = magnetic field

strength), which forces the electrons to move in circles. The moving electrons create a magnetic field opposing to the outer magnetic field  $\vec{B}$ , compensating for it. In the case of superconductive conditions, the opposing fields annihilate themselves completely.

The protection against outer magnetic fields was accomplished by a tube with a diameter of 10 cm made from a 0.5 mm thick sheet of mu-metal (Goodfellow), which shielded the whole length of the flight tube from the ion lens assembly down to the detector. The shield tube held in position by the liquid  $N_2$  cooling trap and on the opposite side by a home-built aluminum holder. The shielding efficiency was good enough to allow for field-free propagation of the electrons.

### 2.2.2.2 Position Sensitive Detector

The 2D position sensitive imaging detector consisted of a chevron double multi-channel plate phosphorescence screen assembly (Photek Limited, 40 mm) shown in Figure 2.19 and a coupled-charged device (CCD) camera (PCO, 1600x1200 pixel, 12 bit). The pore size of the MCPs was  $10 \mu m$ , the channel bias was  $12^\circ$ , and the distance between the channel centers was  $12 \mu m$ . The gain over both MCPs at 1.6 kV was  $\approx 1 \cdot 10^8$ . The MCPs were followed by a phosphorescence screen. Its visible diameter of 36 mm was monitored from the back through a quartz glass window. A standard P43 phosphor was used, which has the following specifications: the emission ranged from 370 to 680 nm with a maximum at 545 nm at an luminescence period (intensity  $< 10 \%$ ) of  $\approx 1$  ms. The CCD camera imaged the light spots on the phosphorescence screen. The generated electron cascade exited the MCPs without a vertical spatial shift and hit the phosphorescence screen anode illuminating the phosphor.

The MCPs and the phosphorescence screen are assembled in a standard flange (NW100) and therefore the detector can be attached at the end of the flight tube. The power is supplied by two high voltage adapters (FUG, HCE 35-3500 and HCE 35-7000). To avoid detection of random electrons and stray photons, the power supply of the MCPs was gated by a fast transistor switch (Behlke, HTS 31;  $\tau_{min} = 30$  ns).

The CCD camera was connected via a spacer with the length 140 mm to the detector. The selected camera objective imaged the surface of the phosphorescence screen onto the CCD chip, which has 1600 x 1200 pixels at a dimension of  $7.4 \times 7.4 \mu m^2$ . The full frame rate is 30 fps. The quantum efficiency reaches 50 % at  $\lambda = 545$  nm. The camera was controlled via a firewire (1394) interface by a LabView program that additionally controlled the whole measurement. The program details are given in the appendix.

The total number of detected particles was kept  $< 50$  per image. This ensured that the spots were clearly separated from each others. The images were thresholded

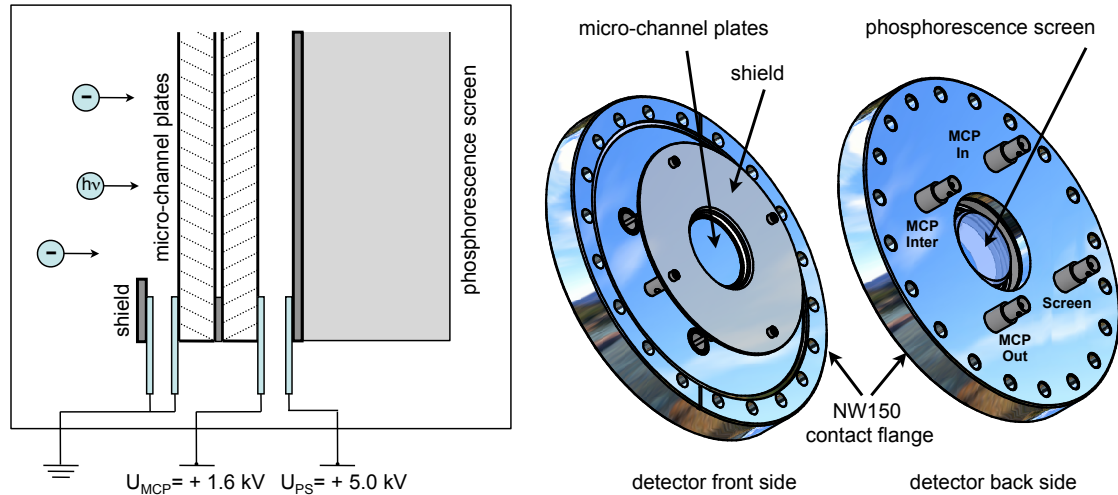


**Figure 2.19:** The detector assembly consists of two MCPs in chevron configuration followed by a phosphorescence screen. The assembly can be used for the position sensitive detection of electrons and ions.

and the positions of the light spots were determined by a peak search (center-of-mass) algorithm, which was implemented in the LabView control program. The peak positions  $(x, y)$  were stored in a list while the raw images were dropped. This image preprocessing drastically improved the recording speed and also enhanced the below discussed resolution limit enormously [56].

### 2.2.2.3 Reproduction Scale of the Camera System

Signals on the phosphorescence screen of the detector assembly were mapped by a lens system (Schneider-Kreuznach 1" c-mount objective, CNG F1, 8/16 mm) onto the CCD chip of the camera. The reproduction scale was determined by imaging a sheet of graph paper (1 mm squares), which was attached directly to the viewing window on the air side of the detector system. The paper was illuminated by a small photodiode. From Figure 2.20 follows for vertical and horizontal directions a common conversion factor for the camera of

$$1 \text{ pixel} = 52.91 \cdot 10^{-6} \text{ m},$$

or

$$1 \text{ mm} = 18.9 \text{ pixel}.$$

Additionally, the spatial resolution was determined by measuring the width of the detected electron peaks. The average peak width was 2.7 pixel ( $\hat{=}$  0.143 mm) at optimized conditions, as it is illustrated in Figure 2.20.

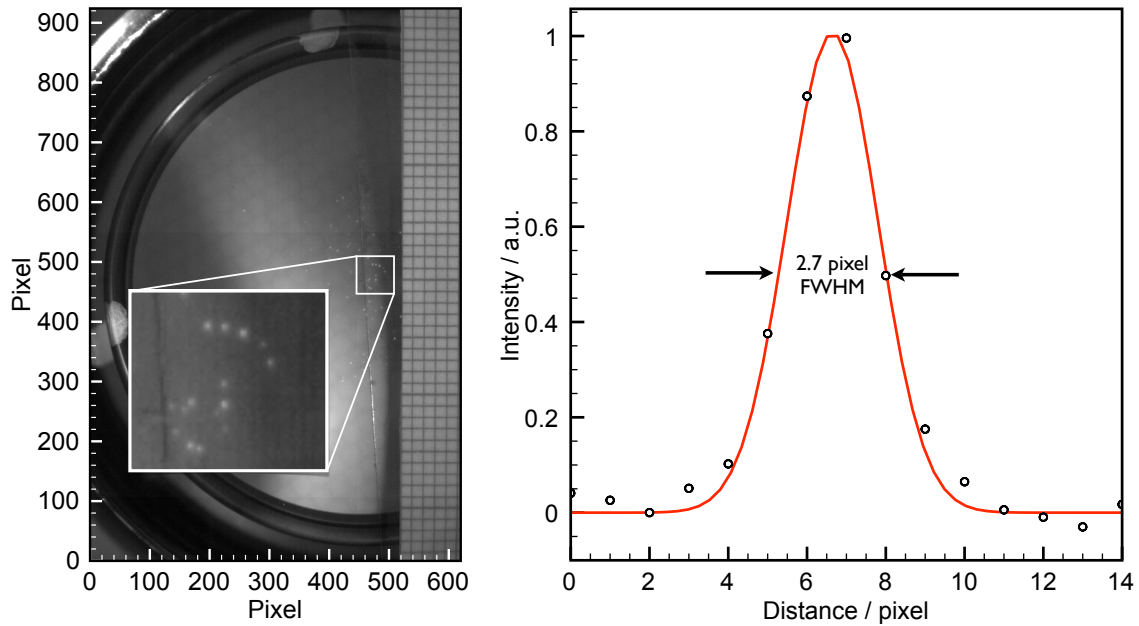


**Figure 2.20:** The reproduction scale was determined by mapping a graph paper. From the size of the light spots, which correspond to detected electrons, the spatial resolution of the detecting system was determined to 0.143 mm.

The temporal interaction of all experimental components, including the camera, is described in the next subsection.

#### 2.2.2.4 Temporal Sequence of the Experiment

As described in Subsection 2.1.2.7, the timing of the setup was achieved by a DG535 delay generator from Stanford Research. The controlled parts are shown schematically in Figure 2.21.

The delay generator was synchronized with the master trigger. For the imaging experiment, the 1.011 kHz repetition rate of the main trigger was reduced to 50 Hz. As shown in Figure 2.22, the MCPs were powered by the Behlke switch after a delay time of nearly 2 ms, because the molecular beam needs  $\approx 1.5$  ms to reach the point between repeller and extractor plate, where it interacts with the laser beams. After the main trigger the third laser pulse (pump/probe) was used for the experiment. The CCD camera recording started simultaneously with the trigger pulse for the Behlke switch (MCPs). The acquisition time was set to 100 ms to accumulate over 5 trigger events.

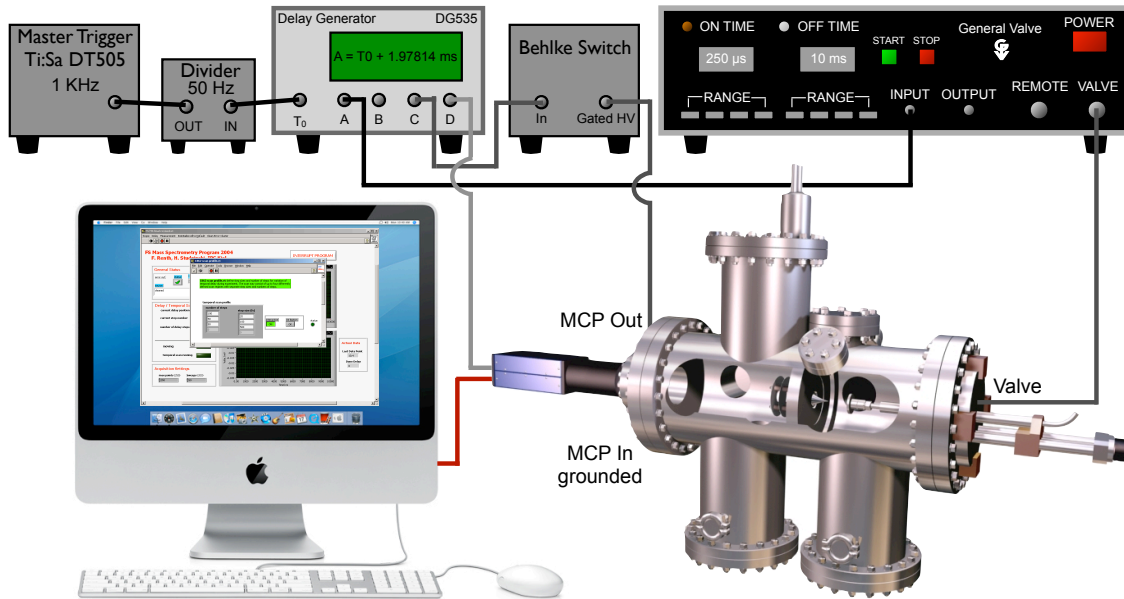


**Figure 2.21:** Control and timing of the photoelectron imaging experiment by a delay generator.

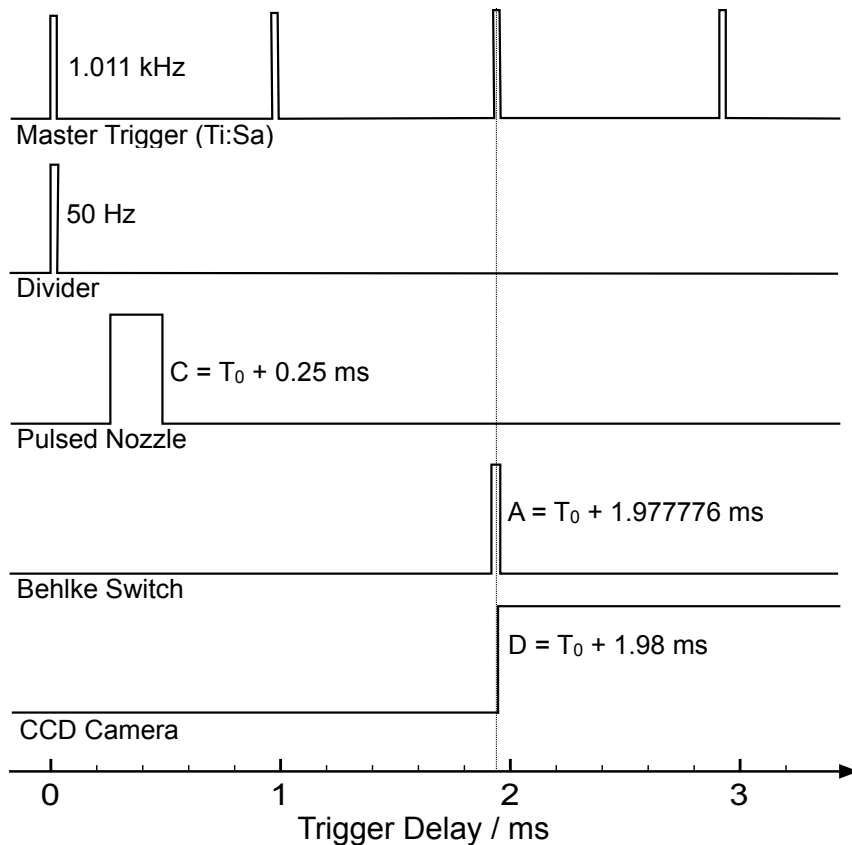


**Figure 2.22:** Schematic diagram illustrating the timing of the master trigger, the nozzle, the Behlke switch, and the CCD camera.

### 2.2.3 Projection and Reconstruction of the 3D Electron Distribution

After ionization of the molecules, the ejected three-dimensional (3D) photoelectron cloud  $(x, y, z)$ , the so-called “Newton Sphere”, in Figure 2.18 is projected by the ion lens assembly onto the two-dimensional (2D) imaging detector  $(x, z)$ . Owing to the use of polarized laser beams oriented parallel towards the detector surface and an ion lens assembly that is homogeneous and orthogonal to the flight direction of the electrons, the full anisotropy of the angular distribution is conserved upon projection onto the detector, because the polar angle  $\theta$  is in the  $x$ - $z$  projection plane. This provides the potential to reconstruct the 3D electron distributions from the recorded 2D velocity maps. The 2D projection  $P(x, z)$  of a 3D distribution  $I(x, y, z)$  along  $y$  is expressed by Equation 2.24,

$$P(x, z) = \int_{-\infty}^{\infty} I(x, y, z) dy. \quad (2.24)$$

The cylindrical symmetry of the electron cloud allows to transform Equation 2.24 in cylindrical coordinates, with

$$\begin{aligned} z &= z \\ r &= \sqrt{x^2 + y^2} \\ dy &= \frac{r}{\sqrt{r^2 - x^2}} dr, \end{aligned}$$

to

$$P(x, z) = 2 \int_0^{\infty} \frac{I(r, z)r}{\sqrt{r^2 - x^2}} dr. \quad (2.25)$$

The projection of a cylindrical function along the main axis (in this case  $y$ ) onto the  $x$ - $z$  plane, is known in the literature as Abel transformation [57]. For the reconstruction of the 3D distribution, different mathematical methods are applicable [27]. Two state-of-the-art methods, the Projected-Landweber (PL) method [58] and the pBASEX method [59], are introduced and compared to each other in the following.

#### 2.2.3.1 Introduction to the Inversion Methods

Since the beginning of photofragment imaging in the late 1980s [60], the technique has been applied to investigate fundamental dynamical processes like uni- and

bimolecular reactions, photodissociation, and photoionization [61]. All experiments have in common that an expanding sphere of charged particles, ions or electrons, are projected down a flight tube to create a 2D image. Thereby, both the angular and velocity information can be extracted, while maintaining full collection efficiency. However, to reconstruct the initially 3D distribution, the image has to be inverted, which has proven to be a major disadvantage compared to other charged particle analyzers.

This has been experimentally overcome by the use of the time-of-flight of the particles as third dimension [62]. In 1994, it was realized by laser sheet ionization, where the geometry of the laser pulse ionizes only a central slice of the expanding Newton sphere [63]. This method affords a disproportionately high experimental expense, because two laser are used, the first for photolysis and the second for sheet ionization. A slice imaging of photoelectrons is not possible with this method. A second approach is the direct current slice imaging [64], where the ion cloud is expanded in the direction of the detector by two additional ion lenses. This allows to time-select only the central slice for detection by gating the imaging detector itself or by the use of an extra gate electrode in front of the detector. This method is simpler, but still light particles like electrons cannot be sliced due to the limited resolution of the electronics. Thus, photoelectron imaging spectroscopy depends on an appropriate method for image inversion.

The simplest and fastest inversion methods are the onion-peeling [65] and backtracking algorithms [66]. However, the unpeeling method tends to oversubtract the contributions of fast particles, and, especially when dealing with noisy images, the statistical fluctuations in the outer regions of the detector cause a noise accumulation towards the center line of the images parallel to the electric vector of the light. This has been partially solved by fitting of Legendre functions to the layers prior to subtraction, to smooth the image and push the noise towards the center [67]. However, the method is still affected by cumulative error problems, as it remains an unpeeling algorithm. If the kinetic energy of the particles exceeds the initial energy by far, the backtracking algorithm can be applied. A more general algorithm developed by Winterhalter *et al.* [68] neglects this limitation. But it requires complicated laborious numerical solutions, if the electric field is not homogeneous, as is the case in velocity map imaging.

A commonly used analytical method is the inverse Abel transformation [69], which is fast and reliable for high quality images. As onion-peeling, it is based on the Fourier-Hankel algorithm to solve the inverse Abel integral and magnifies the noise of the image towards the center line. Other methods have been invented to overcome the noise problem [70, 71]. However, even the so-called “basis function



expansion" (BASEX) method still accumulates the noise towards the center line and renders useless the angular information in the images located in the critical areas around  $0^\circ$  and  $180^\circ$ .

In the following subsections, two recently developed methods are presented and compared with each other. The first method builds upon Dribinski's BASEX algorithm and is called polar basis function expansion (pBASEX) [59]. The main improvement arises from the use of polar coordinates instead of Cartesian, which are commonly used as in the original BASEX. The second method was invented in our group by Renth *et al.* [58]. It uses an iterative regularization and cross validation approach. Both methods have overcome the center-line noise challenge by different mathematical techniques.

### 2.2.3.2 Polar Basis Function Expansion (pBASEX)

The polar basis function expansion employs polar coordinates, which are the intuitive choice, since they correspond to the symmetry of photon-matter interaction in the gas phase. A better angular and energy resolution has been achieved, because the noise is accumulated towards the center-point of the image, which usually is not used for data evaluation anyway. The conversion of the Cartesian raw image into polar coordinates smoothes noise coming from the Cartesian grid of the detector system and makes the method less sensitive to this type of noise. The energy and angular distribution parameters are directly available without the need of additional fitting of Legendre polynomials. Furthermore, the chosen basis functions to solve the Abel integral allow for multiphoton processes and for the appearance of even and odd terms in the angular distributions of the photoelectrons. The latter are needed when dealing with molecules that are fixed in space [72, 73], aligned [74], or chiral and randomly oriented [75, 76].

pBASEX models the 3D energy distribution of the particles  $I(R, \theta)$  by an expansion of the Legendre polynomials in the form of a discrete number of Gaussian functions with a given width  $\sigma$ ,

$$I(R, \theta) = \sum_{k=0}^{k=k_{max}} \sum_{l=0}^{l=l_{max}} c_{kl} f_{kl}(R, \theta) \quad (2.26)$$

with

$$f_{kl}(R, \theta) = e^{-\frac{(R-R_k)^2}{\sigma}} P_l(\cos \theta). \quad (2.27)$$

$\theta$  is measured with respect to the polarization direction of the light,  $P_l$  is the Legendre polynomial of order  $l$  and  $R_n$  represents the center of the  $n$ th Gaussian. The

radius  $R$  of the particles in the image correspond to their ejection speed so that the kinetic energy distribution can be easily obtained from the radial counterpart. When the initial Newton sphere is projected onto a 2D detector and linear polarized light is used, the original distribution  $I(R, \theta)$  and the projected  $P(R', \theta')$  are related via the Abel integral [57]. This was described above (but not for polar coordinates) by

$$P(R', \theta') = 2 \int_{|x|}^{\infty} \frac{I(R, \theta)r}{\sqrt{r^2 - x^2}} dr \quad (2.28)$$

with

$$x = R' \sin \theta', \text{ and } r = R \sin \theta.$$

The basis functions are obtained by combining Equations 2.26, 2.27, and 2.28 to

$$g_{kl}(R', \theta') = 2 \int_{|x|}^{\infty} \frac{I(R, \theta)r f_{kl}}{\sqrt{r^2 - x^2}} dr. \quad (2.29)$$

Any 3D distribution that follows the mentioned restrictions can be expressed as 2D image using a linear expansion of the basis functions in Equation 2.29,

$$P(R', \theta') = \sum_{k=0} \sum_{l=0} c_{kl} g_{kl}(R', \theta'). \quad (2.30)$$

From this equation, the coefficients  $c_{kl}$  can be extracted and the original Newton sphere can be reconstructed by substitution into Equation 2.26.

The numerical reconstruction is performed by matrix inversion, applying the singular value decomposition (SVD) method [77]. The discrete matrix of Cartesian pixels obtained from the experimental measurements is therefore transformed to polar pixel coordinates by reverse transformation and bicubic interpolation [77] (polynomial and cubic spline interpolation methods).

The performance of pBASEX was tested by the inversion of two images. The first was constructed artificially and the second, a photoelectron image, was taken experimentally (see Subsection 3.4.4.3).

### 2.2.3.3 Projected-Landweber Method (PL)

The projected Landweber method combines and extends the successful concepts that were already applied in forward convolution and basis set expansion [70, 71,

59]. However, major changes are found in detail, as this method is an iterative method of direct constrained regularization [78, 79]. It is well known that, *e.g.*, the constrain of non-negativity dramatically improves the quality of 3D reconstructions of linear inverse problems [80, 81]. Another regularization parameter is the number of iterations. To avoid the need for a subjective choice, the image is partitioned into quarters and cross validation [82] is employed. Also, PL differs from other methods, because it takes into account the Poisson noise statistics by introduction of the noise term  $N(x, z)$ . The Cartesian projection  $P(x, z)$  is given by

$$P(x, z) = \sum_{k=1}^M a_k F_k(x, z) + N(x, z), \quad (2.31)$$

where  $M$  is the total number of basis functions,  $a_k$  are the expansion coefficients, and  $F_k(x, z)$  are the basis functions. The PL method is described in detail in [58].

#### 2.2.3.4 Comparison of pBASEX and PL

The performances of pBASEX and PL were tested on the simulated and the experimental images in Figure 2.23. For the simulated image, the Legendre

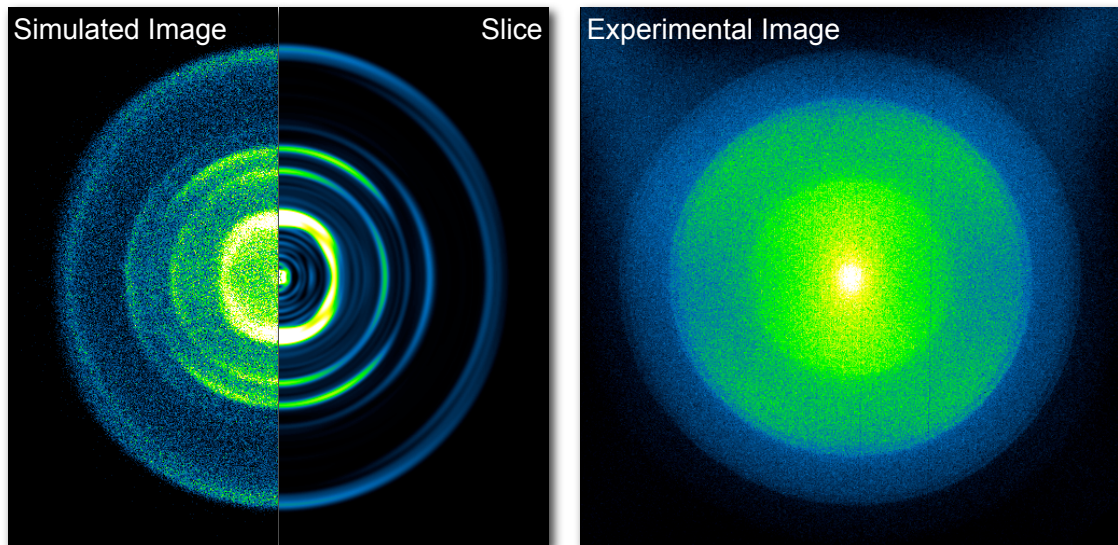


**Figure 2.23:** Left image: Simulated test image (left half) and meridional slice of the simulated image (right half). Right image: Experimental image. The intensities are displayed as a miscolored representation.

polynomial expansion of the angular distribution was restricted to even values of  $l$  and to a maximum value of  $l_{max} = 6$ . Eleven Gaussians “rings” were used, each characterized by an amplitude  $A_n$ , width  $\sigma_n$ , and center  $R_n$ . The anisotropy parameters  $\beta$ ,  $\gamma$ , and  $\delta$  correspond the 2nd, 4th, and 6th order of the Legendre polynomial angular distributions. The parameters of the simulated image are given

in Table 2.1. The features were chosen to represent “commonly” observed images in particle imaging. The broad rings 10 and 11 represent an unstructured background. The simulated image has a total intensity of  $\approx 0.6 \cdot 10^6$  counts and a size of 501 x 501 pixels, which corresponds to the size of the experimental image.

The experimental image was obtained by photoelectron imaging on an achiral molecule (hexafluorobenzene) using a (1+1’)-REMPI scheme. The details are presented in the results section.

The inversion of images by the pBASEX program has proven to be rather simple. After importing the image, the user can choose to center the image manually by a mouse click or use one of the two implemented algorithms (Auto-Center or Center-of-Mass), which worked fine for both test images. Further, one has to select the order, and between even or even and odd Legendre polynomials. For the test images, only even Legendre polynomial up to the 6th order for the simulated image and 4th order for the experimental one were used. A click on the bottom “Invert!” starts the process and the results are displayed ready for saving a second later. The program has built-in algorithms to symmetrize and transpose the image prior to reconstruction, both were not applied.

**Table 2.1:** Parameters for the simulation of the test image where chosen as in Reference [58].

Ring no.	$R_n$ pixel	$A_n$ a.u.	$\sigma_n$ pixel	Anisotropy P.		
				$\beta$	$\gamma$	$\delta$
1	0.0	21.0	8.0	0.0	0.0	0.0
2	51.8	10.0	4.2	0.0	0.2	0.8
3	59.2	6.8	4.2	1.8	-0.3	-0.4
4	98.6	3.6	3.3	0.0	0.9	0.0
5	119.3	3.2	3.3	2.0	0.0	-0.9
6	140.1	2.1	3.3	-1.0	0.25	0.0
7	195.9	1.4	4.2	-1.0	0.0	0.0
8	204.9	1.2	4.2	0.0	0.0	0.2
9	211.6	1.2	4.2	2.0	0.0	0.0
10	49.6	1.2	56.0	0.0	0.0	0.0
11	119.6	0.2	56.0	0.0	0.0	0.0

PL is as easy to use as pBasex, but the reconstruction via PL is more elaborate, since the raw images have to be centered manually by cutting or cropping of the image. Moreover, the fitting has to be repeated at least one or two times, because the number of iterations is a regularization parameter and can initially only be guessed.

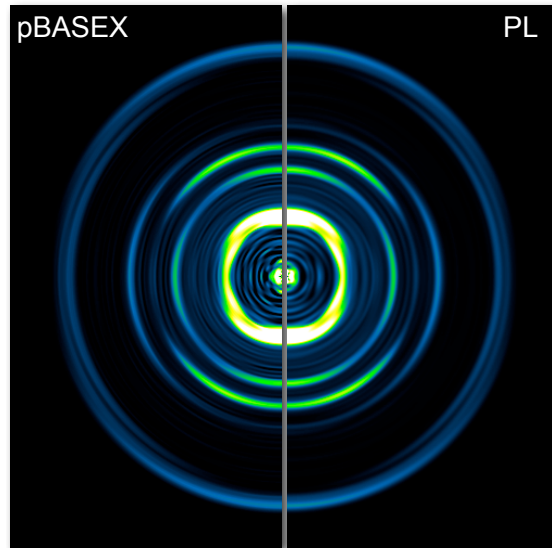


**Figure 2.24:** Meridional slice of the simulated test image. The left half shows the slice obtained by the pBASEX program while on the right half the PL result is shown.

The cross validation is a very good tool and allows for high quality reconstructions, but it can be also a major drawback. An image that shows strong inhomogeneities, like it can be experimentally found, is very sensitive on the quarter selection for the cross validation, such a case is discussed later on. No algorithms to symmetrize or transpose the image are implemented, and only even Legendre polynomials can be used for the reconstruction.

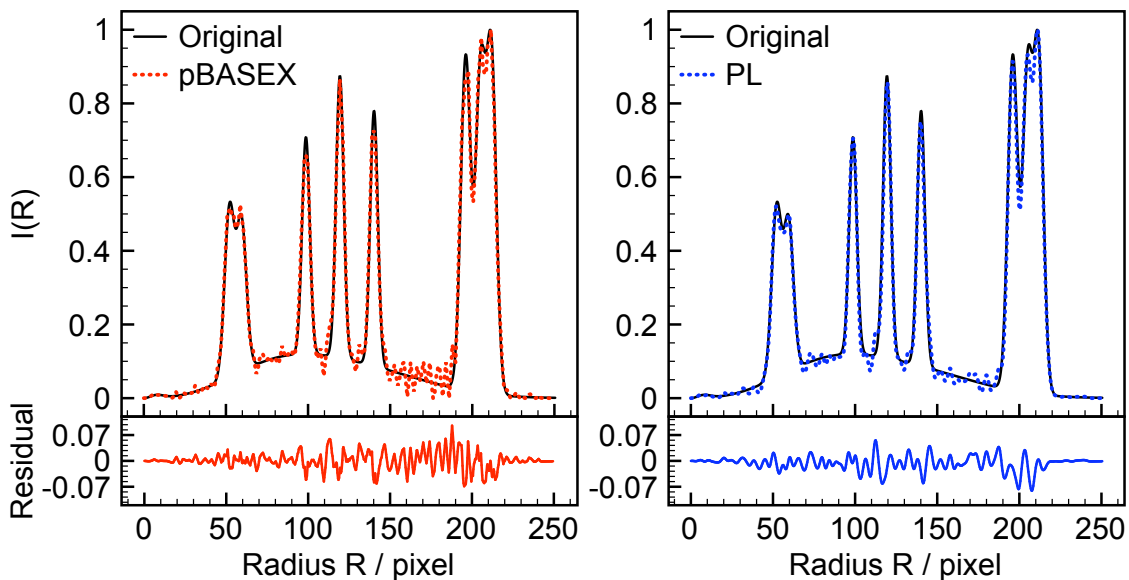


**Figure 2.25:** Normalized radial distributions  $I(R)$  of the simulated test image (solid lines) and the reconstruction via pBASEX (red dotted line, left) and via PL (blue dotted line, right) The residuals is given in the bottom of each plot.

Meridional slices of the reconstructed simulated test image are shown in Figure 2.24. The corresponding radial and angular distributions are presented in Figure 2.25 and 2.26 respectively. For the reconstruction, pBASEX uses 256 basis sets for each order of the Legendre polynomials. The amount is fixed and is automatically adjusted to the image size. The PL basis sets can be generated with user input. Here, 121 basis sets with a width of 2 pixels for each order of the Legendre polynomials were chosen for the reconstruction. The slice through the reconstructed simulated test image shows the results for pBASEX on the left half and for PL on the right. No differences are visible by the bare eye. Nevertheless, the corresponding radial distributions (Figure 2.25, pBASEX left, PL right) exhibit differences, which clearly show that pBASEX performs slightly poorer. Especially at higher radii, the pBASEX distributions are more noisy. The subjective impression is verified by the higher standard deviation of  $\sigma_R = 0.014$  for pBASEX compared to  $\sigma_R = 0.011$  for PL. The deviations have been calculated from the residuals obtained by subtraction of the reconstructed from the original distribution.

The angular distributions for  $\beta$ ,  $\gamma$ , and  $\delta$  are shown in Figure 2.26 in three separated plots. These were extracted from the reconstruction results. The performance of pBASEX and PL are both outstanding, but pBASEX performs slightly better as its angular terms are closer to the original values.

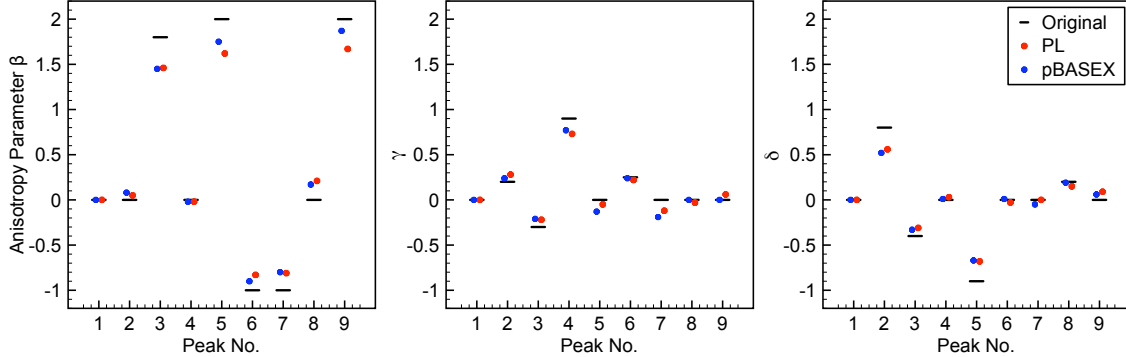


**Figure 2.26:** The anisotropy parameters  $\beta$  (left),  $\gamma$  (middle), and  $\delta$  (right) for the simulated test image calculated by pBASEX (blue dots) and PL (red dots) are compared with the original values for the simulation of the image (black sticks).

However, in the case of pBASEX, the extraction from the result file is problematic, because of too few points over the total radial distance, so that one has to average or extrapolate the exact value for the angular parameter at the corresponding peak position. The values for the angular parameters are summarized in Table 2.2 for comparison.

The experimental test image, on the right in Figure 2.23, was chosen because of its strong inhomogeneities visible in the upper part and because of the small splitting

**Table 2.2:** Values for the anisotropy parameters for the simulated test image reconstructed by pBASEX and PL. Peaks 10 and 11 were dropped, because they represent background noise.

Ring no.	pBASEX			PL		
	$\beta$	$\gamma$	$\delta$	$\beta$	$\gamma$	$\delta$
1	0.0	0.0	0.0	0.0	0.0	0.0
2	0.08	0.24	0.52	0.05	0.28	0.56
3	1.45	-0.21	-0.33	1.46	-0.22	-0.31
4	-0.02	0.77	0.01	-0.02	0.73	0.03
5	1.75	-0.13	-0.67	1.62	-0.05	-0.68
6	-0.9	0.24	0.01	-0.83	0.22	-0.03
7	-0.8	-0.19	-0.05	-0.81	-0.12	0.0
8	0.17	-0.08	0.19	0.21	-0.03	0.15
9	1.87	0.0	0.06	1.67	0.06	0.09

of the two outmost rings. The meridional slices through the reconstructed Newton sphere are shown in Figure 2.27 for pBASEX on the left and for PL on the right. A close look reveals small differences between the slices. pBASEX can distinguish the splitting of the third ring (small to big radii) better than PL, while PL highlights the outmost ring that is nearly not visible in the experimental test image.

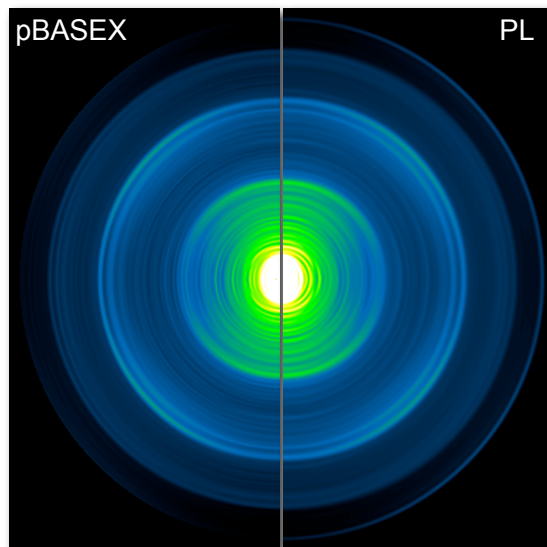


**Figure 2.27:** Meridional slice through the reconstructed experimental image. pBASEX left half, PL right half.

The radial distributions in Figure 2.28 (left plot) confirm the observations. The splitting of the peak around  $R = 200$  pixels is resolved much more clearly for pBASEX (red line) than by PL (blue dotted line). The outmost ring ( $R = 240$  pixels)

**Table 2.3:** Anisotropy of the reconstructed experimental test image.

Ring no.	Radius pixels	pBASEX		PL	
		$\beta$	$\gamma$	$\beta$	$\gamma$
1	90.6	0.38	-0.06	0.38	-0.04
2	157.8	0.02	-0.27	0.03	-0.27
3	165.6	0.19	-0.38	0.16	-0.26
4	200.0	-0.22	0.00	-0.10	-0.01
5	206.3	-0.21	-0.19	-0.10	-0.11
6	212.5	-0.21	-0.41	-0.17	-0.23
7	239.9	-0.60	-0.70	-0.10	-0.44

has a completely different amplitudes for pBASEX and PL. This is may be due to the fact that the PL basis sets with a width of 2 pixels have a maximal size of 242 pixels for the 501 x 501 pixels image so that the abrupt end produces an artificial ring. This can be suppressed by using basis sets with bigger radii.<sup>2</sup> The values of the angular parameters are summarized in Table 2.3.

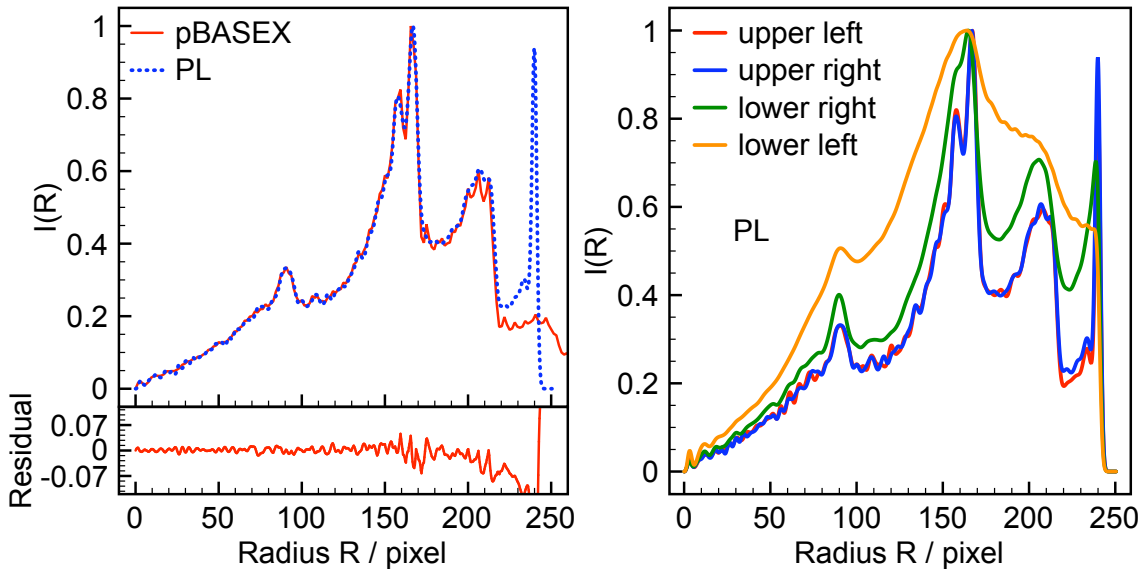


**Figure 2.28:** The radial distributions of the meridional slices obtained by pBASEX and PL for the reconstructed experimental image are shown in the left plot. The plot on the right shows the radial distribution for different cross validation quarter choices using the PL method.

The cross validation required by PL proved to be a disadvantage for the fitting of the experimental image. Depending on the chosen quarters, different reconstruction

<sup>2</sup>at even longer computing time



qualities were obtained. Figure 2.28 (right plot) shows the radial distributions for the four different quarters. When the upper left or right quarters were used for cross validation, the reconstruction quality was satisfying like already discussed above. However, if any of the lower quarters were taken, PL was not able to fit the features of the image. Consequently, for the reconstruction of inhomogeneous experimental images, one has to be very careful with the choice of quarters for cross validation.

**Table 2.4:** Time for the two inversion methods to reconstruct the simulated and experimental test images using a 2.0 GHz Intel Core Duo Processor with 2 GB of DDR2 memory. The factors in parenthesis indicated how often the fitting had to be repeated in order to obtain the optimal performance.

Test Image	pBASEX Time (s)	PL Time (s)
simulated	0.56 ( $\times 0$ )	953 ( $\times 1$ )
experimental	0.47 ( $\times 0$ )	377 ( $\times 1 + \times 3$ )

Although PL appears to give a slightly better performance in terms of energy for perfectly symmetric images, the pBASEX approach reconstructs inhomogeneous images with higher accuracy at less effort. Table 2.4 shows that photofragmentation images, simulated and experimental, are reconstructed much faster by pBASEX than with the iterative Cartesian PL method. After weighing all pro and contras, the conclusion was made to use pBASEX for the reconstruction of the experimentally obtained photoelectron images in this work.

## 2.3 Femtosecond Pump-Probe Laser System

This section focusses on the most important aspects of nonlinear ultrafast spectroscopy. It is divided into two parts. First, there will be a subsection on the operating principle of the Ti:Sa Laser used in this work and the general principles and processes of femtosecond spectroscopy. Then there will be a second subsection describing the setup of optical frequency conversion that was applied in this work to achieve ultrashort laser pulses of tunable wavelengths.

### 2.3.1 The Ti:Sa Laser System

The Ti:Sa laser used in this work (Clark-MXR CPA-2001) is Kerr-lense mode-locked and amplification is achieved by the principle of *chirped pulse amplification*.

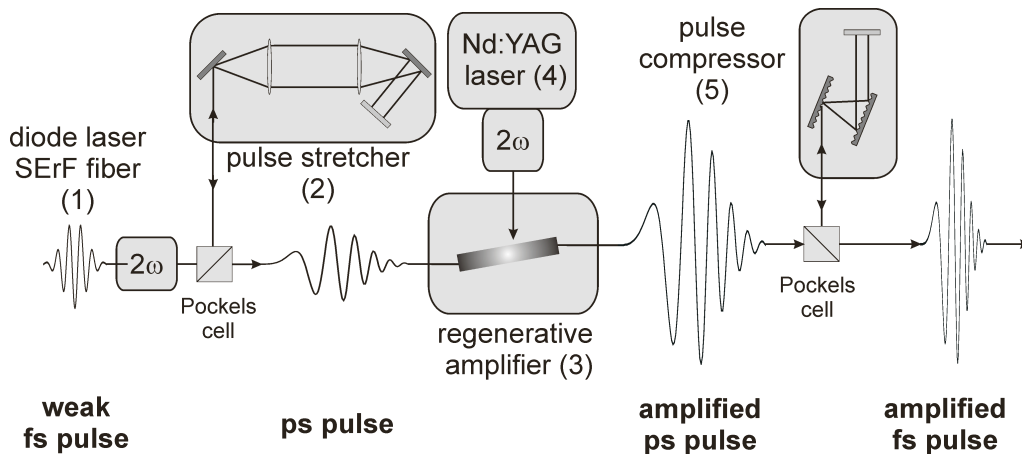


**Figure 2.29:** The Ti:Sa laser system uses the principle of chirped pulse amplification.

Initially generated weak femtosecond pulses are stretched in time, amplified and re-compressed. A scheme of the laser system is given in Fig 2.29.

The desired ultrashort laser pulses are generated by the Kerr lens effect (see 2.3.2.2) through *polarisation additive pulse-modelocking* (P-APM) inside an erbium fiber oscillator (SErF), which is pumped by a *cw*-photodiode ( $\lambda = 980$  nm, 184 mW, 309 mA). The fiber emits at  $\lambda = 1550$  nm with a repetition rate of 34.5 MHz. The pulses are compressed down to  $\approx 100$  fs pulse duration by a prism compressor. The fiber oscillator output is frequency doubled to  $\lambda = 775$  nm and temporarily stretched to  $\approx 200$  ps in a pulse stretcher. It acts subsequently as the seed pulse for the regenerative amplifier.

The core of the regenerative amplifier is a Ti:Sa crystal, pumped at  $\lambda = 532$  nm by a frequency doubled Nd:YAG laser. Its pump power is 7 W at 200 ns pulse duration

with a repetition rate of 1 kHz. The Nd:YAG laser creates a population inversion inside the Ti:Sa crystal, which is cleared by the  $\lambda = 775$  nm seed pulse. The seed pulse is injected into the amplifier cavity by a Pockel's cell. After several passes ( $\approx 10$ ) inside the cavity, the amplified seed is ejected through the same Pockel's cell mechanism. It is separated from the incoming weak seed pulse by a Faraday isolator and a polarised beam splitter. The amplified, but temporally stretched pulses are now re-compressed by a grating pair. Therefore, femtosecond pulses of 150 - 200 fs FWHM pulse duration, 775 nm output wavelength and  $\approx 900$  mW output power with a repetition rate of 1 kHz are obtained.

### 2.3.2 Nonlinear Optics and Optical Light Conversion Processes

For intense and strong electromagnetic fields, several nonlinear effects occur depending on the strength of the applied field. Typically, field powers of  $\geq 10^2$  to  $10^6$  W/cm<sup>2</sup> are needed. In this work, advantage was taken basically from three different nonlinear effects, which will be discussed in the following.

#### 2.3.2.1 Multi-Photon Absorption

The process of multi-photon absorption is quite simple. Two or more photons of the same energy produce an absorption transition equal to the sum of the frequencies of the constituent photons ( $\chi^3$  or  $\chi^n$  process, respectively, see 2.3.2.3). The interplay between the molecule and the applied electromagnetic field is very short ( $\leq 200$  fs) and therefore the very high field power does otherwise "damage" by the molecules. This process is exclusively used in the investigation of the molecules of interest (see Chapter 3).

#### 2.3.2.2 Optical Kerr-Effect and Group Velocity Dispersion

At very high electromagnetic fields, the refractive index depends on the irradiated light intensity,

$$n(I) = n_0 + n_2 \cdot I. \quad (2.32)$$

$n_0$  is the standard refractive index and  $n_2 \cdot I$  is the nonlinear, intensity-dependent part of the refractive index. The magnitude of  $n_2$  is  $\approx 10^{-16}$  cm<sup>2</sup>/W for solid state crystals. The intensity is highest along the laser beam axis and experiences a much higher refractive index, and therefore dispersion, than the outer parts of the beam. This is the so-called Kerr self-phase modulation. As a result, the weak pulse flanks are retarded, and, by a suitable aperture, the intensive peak center can be separated from the outer wings.

After passing the aperture, the pulse can be shortened in time by compensating for its group velocity dispersion (GVD). GVD is the frequency-dependent phase-shift that results, because different frequencies within a laser pulse travel at different speeds, leading to temporal dispersion. This is demonstrated by

$$\text{GVD} = \frac{\partial k}{\partial \omega^2} = \frac{\lambda^3}{2\pi c^2} \frac{\partial^2 n}{\partial \lambda^2}, \quad (2.33)$$

where  $k$  is the wave vector and  $\omega$  is the frequency. When the lower (higher) frequencies of an ultrashort laser pulse are traveling ahead, this is called a positive (negative) chirp. Ultrashort laser pulses have a high spectral bandwidth, so that the comprised frequencies spread along the pulse, when it propagates in time. GVD can be minimised through phase-correct reunion in a prism compressor, grating pair or via chirped mirrors. Self-focussing and self-phase modulation are  $\chi^3$  processes (see 2.3.2.3).

### 2.3.2.3 Frequency Conversion

A characteristic feature of nonlinear optics is the violation of the basic principle of frequency conservation of linear optics. The correlation between polarization  $\vec{\mathbf{P}}$  and electromagnetic field strength  $\vec{\mathbf{E}}$  is not linear, but terms of higher order emerge.  $\vec{\mathbf{P}}$  can be expressed in a series expansion. Normally, a consideration of terms up to  $\chi^3$  is fairly adequate, *e. g.*,

$$\vec{\mathbf{P}} = \epsilon_0[\chi^{(1)}\vec{\mathbf{E}} + \chi^{(2)}\vec{\mathbf{E}}^{(2)} + \chi^{(3)}\vec{\mathbf{E}}^{(3)} + \dots]. \quad (2.34)$$

$\chi$  is the susceptibility and a factor of proportionality between  $\vec{\mathbf{P}}$  and  $\vec{\mathbf{E}}$ . Its value depends on the nonlinear medium and its symmetry. For an electric wave

$$\vec{\mathbf{E}}(x, t) = \vec{\mathbf{E}}_0 \cos(\omega t + \vec{\mathbf{k}}(\omega)x), \quad (2.35)$$

where  $\vec{\mathbf{E}}_0$  is the amplitude,  $\omega$  the frequency, and  $\vec{\mathbf{k}}(\omega)x$  the wave vector, the following equation describes the macroscopic polarisation which can be observed, if intense fs laser beams of different frequency hit a nonlinear material that cause nonlinear contribution of the order of  $\chi^{(2)}$ :

$$\vec{\mathbf{P}} = \vec{\mathbf{P}}^{(1)} + \vec{\mathbf{P}}^{(2)} \quad (2.36)$$

with

$$\mathbf{P}^{(2)} = \epsilon_0 \chi^{(2)} [\vec{\mathbf{E}}_1 \cos(\omega_1 t) + \vec{\mathbf{E}}_2 \cos(\omega_2 t)]^2 \quad (2.37)$$

$$= \epsilon_0 \chi^{(2)} [\vec{\mathbf{E}}_1^2 \cos^2(\omega_1 t) + \vec{\mathbf{E}}_2^2 \cos^2(\omega_2 t) + 2\vec{\mathbf{E}}_1 \vec{\mathbf{E}}_2 \cos(\omega_1 t) \cos(\omega_2 t)] \quad (2.38)$$

$$= \epsilon_0 \chi^{(2)} \frac{1}{2} [(\vec{\mathbf{E}}_1^2 + \vec{\mathbf{E}}_2^2) + \vec{\mathbf{E}}_1^2 \cos^2(2\omega_1 t) + \vec{\mathbf{E}}_2^2 \cos^2(2\omega_2 t) + 2\vec{\mathbf{E}}_1 \vec{\mathbf{E}}_2 \cos[(\omega_1 + \omega_2)t] + 2\vec{\mathbf{E}}_1 \vec{\mathbf{E}}_2 \cos[(\omega_1 - \omega_2)t]] \quad (2.39)$$

Thus, the fundamental wave is converted to the second harmonic (SHG) and to frequency mixed terms of the sum frequency (SFG) and difference frequency (DFG). If  $\vec{\mathbf{E}}_1$  equals  $\vec{\mathbf{E}}_2$ , just SHG can be observed.

By applying very strong fields, higher harmonics like the third harmonic (THG) can be generated from the fundamental wave as well. However, it is more practicable to achieve this by SHG of the fundamental beam followed by an SFG step (SHG + fundamental).

For frequency conversion, the phase-matching condition must be fulfilled, in addition to energy conservation. This can be accomplished in anisotropic media that show birefringence. Under a certain angle of incidence with respect to the optical axis of a uniaxial crystal, like  $\beta$ -bariumborate (BBO), the refractive index of the ordinary and extraordinary beams become equal and phase-matching results. A detailed description can be found in [83, 84].

### 2.3.3 Schemes for Tunable Light Generation

Half of the fundamental laser output ( $\approx 400$  mW) was used to run the experiments described in the present thesis. This pulse was split equally into pump and probe beams, 200 mW each. The laser fundamental was used in all time-resolved ToF-MS experiments as the probe. The SHG and THG of the fundamental beams were used as probe in the PEI experiments. The required UV pump pulses were generated by different light conversion processes. In principle, different light conversion setups were designed that almost cover the whole spectral region from the UV up to 775 nm. An overview is given in Fig. 2.30. It is possible to generate light in the NIR as well, but a setup has not been implemented yet.

#### 2.3.3.1 Second Harmonic Generation

The setup for second harmonic generation consists just of a BBO crystal ( $\Theta = 30.2^\circ$ ,  $\varphi = 90^\circ$ , type I, 8x8x1 mm<sup>3</sup>, TOPAG), which is passed by the pump beam without

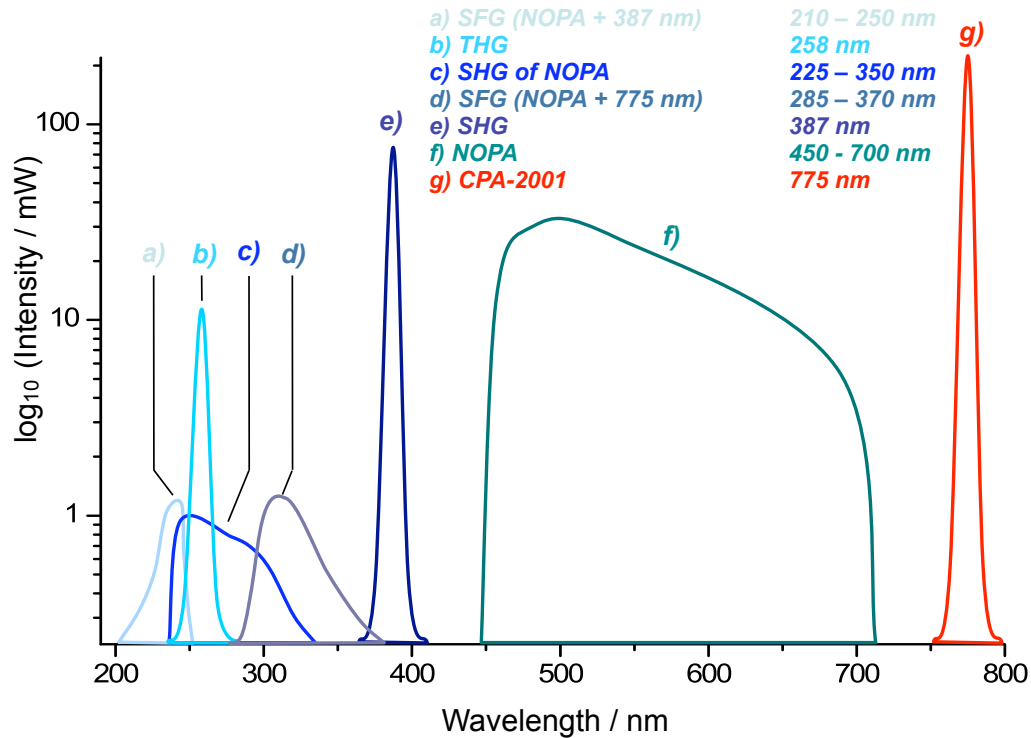


**Figure 2.30:** Overview of the applied light conversion processes. Virtually the whole spectral range from 210 nm to 775 nm can be generated, with a small gap of 75 nm below 450 nm.

any focussing. The conversion efficiency was up to 30 %. The SHG was separated from the residual fundamental by dielectric mirrors (HR 387 nm/45°, unpolarized, single stack, Laseroptik).

### 2.3.3.2 Third Harmonic Generation

In principle, the third harmonic generation setup shown in Figure 2.31 is an add-on of the SHG setup. The incoming pump beam is initially separated into two parts. The major part of 80% is used to generate the second harmonic as already described above. After passing a dielectric mirror (HR 387 nm/45°, unpolarized, single stack,  $d = 0.3$  mm, Laseroptik), it was focussed into a BBO crystal ( $\Theta = 46.3^\circ$ ,  $\varphi = 90^\circ$ , type I,  $8 \times 8 \times 0.25$  mm<sup>3</sup>, TOPAG) with a  $f = 200$  mm lens. The remaining 20 % of the fundamental beam are traveling through a  $\lambda/2$  plate and are collinearly focussed into the THG BBO crystal by the same  $f = 200$  mm lens through the back of the dielectric mirror HR 387nm. If SHG and fundamental beam are spatially and temporally properly overlapped inside the BBO crystal, THG can be observed. The conversion efficiency was 5 %. Dielectric mirrors (HR 243 nm/45°, unpolarized, single stack, Laseroptik) were used to separate the THG from the residuals.

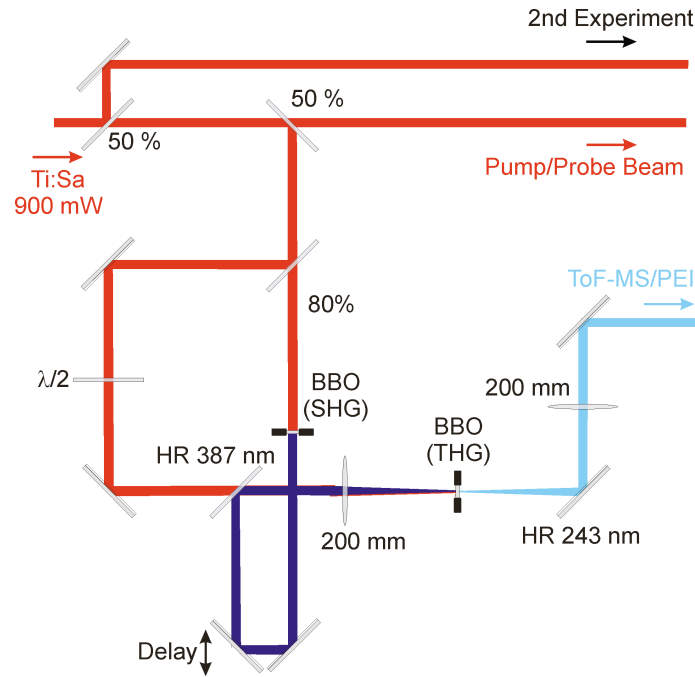


**Figure 2.31:** THG Setup. The SHG and the fundamental are mixed in a type I SFG process generating the THG.

### 2.3.3.3 Tunable Light Source: Non-Collinear Optical Parametric Amplification

Optical Parametric Amplification (OPA) was used to generate tunable pump wavelengths. A non-collinear OPA (NOPA) operating in the visible was built. The setup of the NOPA was already described elsewhere [83], however small changes in the alignment were made. The basic design is shown in Figure 2.32. 1 % of the fundamental 775 nm beam were split off by a quartz glass wedge, and focussed by a  $f = 50$  mm lens on a sapphire plate ( $d = 2.3$  mm, Newport) for white light generation. A suitable neutral density (ND) filter ( $d = 1$  mm, ITOS) was used to keep the power of this beam  $\leq 1 \mu\text{J}$ . The generated supercontinuum pulse contained wavelengths running from  $\approx 450$  nm to the NIR. A particular frequency was chosen and therefore acted as the seed for the subsequent amplifying process. A second lens with  $f = 35$  mm was used to collect and focus the seed into a BBO crystal ( $\Theta = 32^\circ$ ,  $\varphi = 90^\circ$ , type I,  $6 \times 6 \times 2$  mm<sup>3</sup>, TOPAG). The remaining 99 % of the fundamental were frequency doubled and focussed into the same BBO by a  $f = 300$  mm lens to serve as the pump pulse in the amplifying process. The pump was spatially and temporally overlapped with the seed after it passed a delay stage. By varying the delay time between pump and seed, different wavelengths within the white light supercontinuum pulse were amplified. A  $f = 150$  mm lens was used to collimate the NOPA output. A prism compressor (SQ, edge length = 20 mm,  $\approx 100$  cm distance, TOPAG) was used to compress the NOPA pulses down to 35 fs FWHM.

### 2.3.3.4 Frequency Doubling of a NOPA

Further frequency doubling of the NOPA output provided UV pump light between 235 and 340 nm.

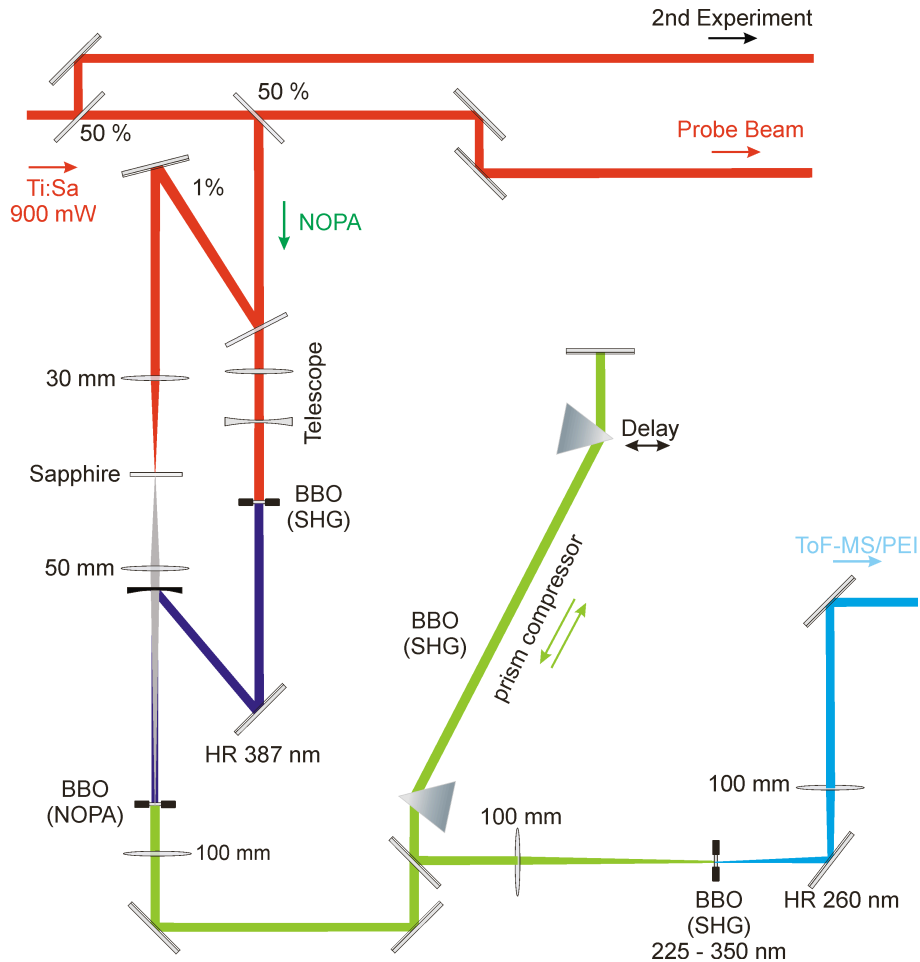


**Figure 2.32:** Setup for SHG of the NOPA Output.

A  $f = 100$  mm lens was used to focus the NOPA output into an BBO crystal. Different BBO crystals were used in the SHG processes for different NOPA output wavelengths. A second  $f = 100$  mm lens was used to collimate the frequency-doubled pulse of the NOPA. It was placed on a translation stage for better alignment. The conversion efficiencies varied between 5 % and 10 % depending on the wavelength.

### 2.3.3.5 Sum Frequency Generation of NOPA Output and Fundamental or SHG of the Fundamental

UV pump wavelengths at  $285 \text{ nm} \leq \lambda \leq 370 \text{ nm}$  were generated by sum frequency generation (SFG) between the visible NOPA output and the fundamental. The compressed NOPA output was focussed into a BBO crystal ( $\Theta = 33.2^\circ - 40.11^\circ$ ,



$\varphi = 90^\circ$ , type I,  $8 \times 8 \times 0.2 \text{ mm}^3$ , TOPAG) by a  $f = 200 \text{ mm}$  lens. In the BBO, it was spatially and temporally overlapped with the fundamental. The  $775 \text{ nm}$  are focussed into the BBO crystal by another  $f = 200 \text{ mm}$  lens in a non-collinear setup. The angle between the NOPA and the fundamental beam was  $\approx 10^\circ$ . For a detailed analysis of SFG in non-collinear configuration see [84].

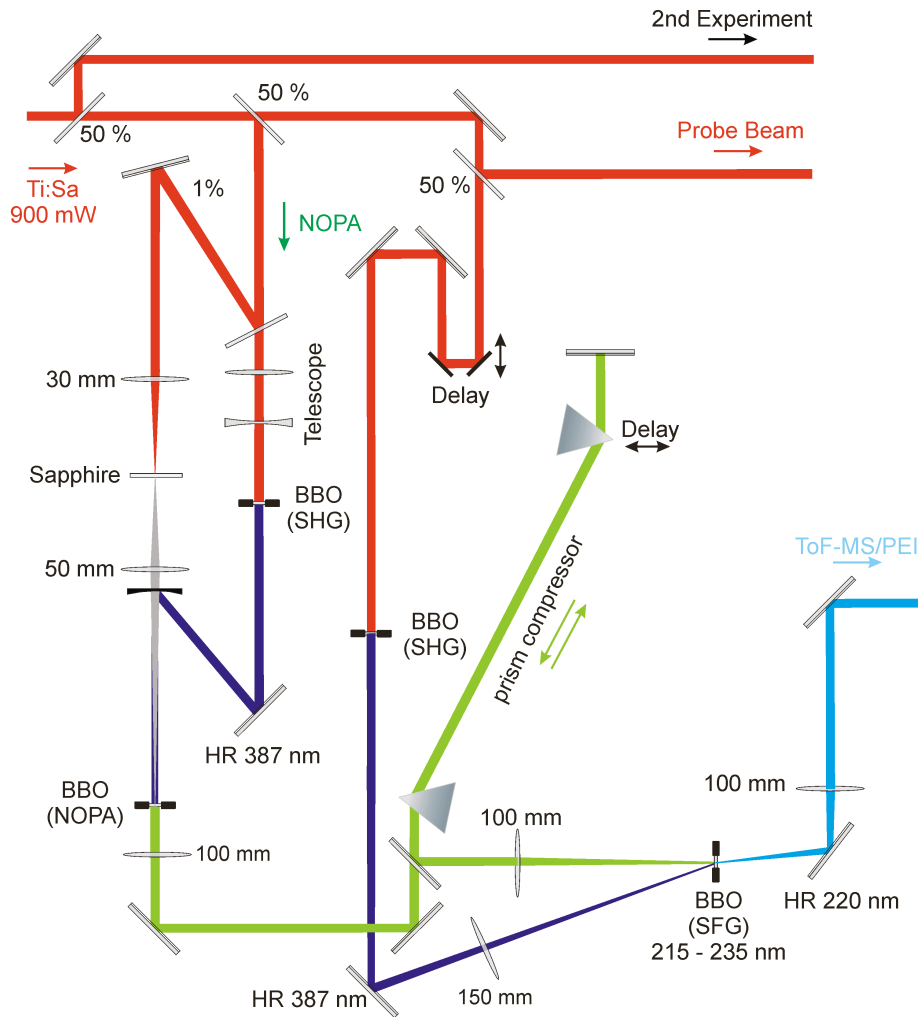


**Figure 2.33:** Setup for SFG of NOPA Output and SHG.

The SFG between NOPA output and the frequency-doubled fundamental ( $\lambda = 387 \text{ nm}$ ) produced UV pump wavelengths in a range from  $215 \text{ nm} \leq \lambda \leq 250 \text{ nm}$ . For the conversion processes different BBO crystals ( $\Theta = 52.6^\circ - 71.4^\circ$ ,  $\varphi = 90^\circ$ , type I,  $8 \times 8 \times 0.2 \text{ mm}^3$ , TOPAG) were used in the same non-collinear setup ( $10^\circ$ ) as described above.

The achieved conversion efficiencies for both schemes varied between 5 % and 10 %. Fig. 2.33 shows exemplarily a scheme of the setup for SFG between the NOPA output and the SHG of the fundamental.

## 3 Results and Discussion

Chapter 3 reports on the experimental results of the present work. It is divided into four sections.

Section 3.1 is concerned with fs time-resolved ToF-MS and PEI measurements on benzene, the prototypical aromatic molecule, and Section 3.2 is concerned with the methyl derivatives toluene, *o*-, *m*-, and *p*-xylene. Benzene, toluene, and the xylenes were studied mainly as test molecules to explore the potential of the experimental setup built in this work.

Section 3.3 reports the results for hexafluorobenzene (HFB;  $C_6F_6$ ) investigated over a wide range of excitation energies ( $265 \text{ nm} \geq \lambda \geq 217 \text{ nm}$ ). HFB showcases the elusive dynamics of a  $\pi\sigma^*$  electronic state which have recently been shown to be of great importance in heteroaromatic compounds, including pyrrole, phenol, [165] as well as the nucleic acid bases (*e.g.* adenine [85]).

Section 3.4 reports on the results of a series of fs ToF-MS and fs PEI measurements on pyrrole. Particular attention was directed to the deactivation dynamics of the molecule after excitation to the first  $\pi\pi^*$  state. Moreover, Section 3.5 presents the results for the substituted derivatives *N*-methylpyrrole, 2,4-dimethylpyrrole, and 2,5-dimethylpyrrole.

Each results section begins with an introduction, which lays out the motivation for our research work and summarizes previous results. This is followed by a brief experimental subsection that describes specific experimental details not covered by the general text in chapter 2. The main subsections then report the detailed experimental results and the analysis of the data, followed by discussions of the new results, with the aim to derive comprehensive pictures of the ensuing electronic dynamics.

## 3.1 Benzene

### 3.1.1 Introduction

Benzene is the prototype for all aromatic molecules. The determination of the chemical properties and structure of benzene posted a challenge to scientists for decades. In the mid-19th century, Kekulé postulated his famous planar hexagonal structure with alternating CC single and double bonds. From a spectroscopic point of view, however, it was not trivial to prove the planar hexagonal ground state structure ( $D_{6h}$ ) with bond delocalization over the aromatic ring [86].

The UV absorption spectrum of benzene in Figure 3.1 exhibits three characteristic peaks, all of which arise from  $\pi^* \leftarrow \pi$  transitions:

1. Band  $\alpha$  ( $S_1(^1B_{2u}) \leftarrow S_0(^1A_{1g})$ ): Absorption from 227 to 267 nm.
2. Band  $p$  ( $S_2(^1B_{1u}) \leftarrow S_0(^1A_{1g})$ ): Absorption from 185 to 205 nm.
3. Band  $\beta$  ( $S_3(^1E_{1u}) \leftarrow S_0(^1A_{1g})$ ): Absorption from 170 to 190 nm.

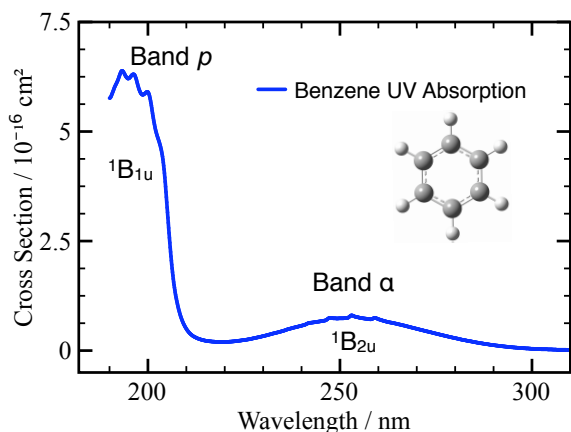


**Figure 3.1:** Gas phase UV absorption spectrum of benzene.

Bands  $\alpha$  and  $p$  stem from absorptions from the  $^1A_{1g}$  symmetry ground state to two optically dark states with the symmetry species  $^1B_{2u}$  and  $^1B_{1u}$ . Normally, these transitions are not allowed because of the unfulfilled electric dipole selection rule  $\Gamma''_e \otimes \Gamma'_e \supseteq \Gamma(T_{x,y,z})$ . However, a simultaneous excitation of normal modes with  $e_{2g}$  symmetry vibronically allow the transitions by the Herzberg-Teller mechanism. In the case of benzene, these modes are  $\nu_{6-9}$  (Wilson's notation, [87]). These are unsymmetric normal modes that are Jahn-Teller active in the cation [88, 89, 90, 91]. This feature is reflected in the UV absorption spectrum as vibronic progressions in bands  $\alpha$  and  $p$ . The progression in the  $\alpha$ -band consists of a combination of the normal modes  $\nu_6$  plus  $\nu_1$  or its higher harmonics.  $\nu_6$  is an unsymmetric in-plane ring deformation mode and  $\nu_1$  a symmetric ring breathing mode.

For nearly 40 years [92], the excited state lifetimes of benzene and benzene clusters have been experimentally and theoretically studied.

The electronic deactivations of the photo-excited  $S_1(^1B_{2u})$  and  $S_2(^1B_{1u})$  states were previously investigated by femtosecond pump-probe ToF-MS [93, 94]. The  $S_2$  state was also determined by time-resolved photoelectron spectroscopy (PES) [95]. Extensive quantum chemical computations have been performed by Sobolewski et al. [96], among others [97, 98, 99].

It was found, that for long excitation wavelengths and therefore low excess energies, the  $S_1$  lifetime depends on the symmetry of the respective excited vibrational state and ranges between 60 and 120 ns [100, 101]. The fluorescence quantum yield  $\phi_{fl}$  is  $\approx 0.2$  [102] and it was concluded that intersystem crossing (ISC) to the  $^3B_{1u}$  triplet state of benzene is responsible for the nonradiative deactivation.

For excess energies above  $3000\text{ cm}^{-1}$ , a step-like increase of the decay rates by up to three orders of magnitude occurs, which was first observed by Callomon et al. [86]. Consistent with the highly reduced excited state lifetime, they observed only diffuse vibronic bands in the measured spectra. Since they thought that none of the standard processes (IC, ISC or IVR) were responsible, this unknown phenomenon was named “channel three” [103, 104], and remained mysterious for a long time.

For  $S_2$  state excitation at  $\lambda = 200\text{ nm}$ , Radloff et al. found two exponential decay constants,  $\tau_1 = 0.05\text{ ps}$  and  $\tau_2 = 7.6\text{ ps}$  [93]. The decay rate  $\tau_1$  holds 99 % of the overall amplitude and the authors thus claimed that the  $S_2$  state is immediately deactivated through a two-step deactivation mechanism, including direct CI's to either the  $S_1$  state or the vibrationally hot ground state state. The second decay component (1 %) was attributed to ionization out of the hot  $S_1$  state which was ascribed a lifetime of  $\tau_2 = 7.6\text{ ps}$ . Additionally, they observed a vibronic progression in their PE spectra with an energy spacing of  $968\text{ cm}^{-1}$ , corresponding to the  $\nu_1$  vibrational mode.

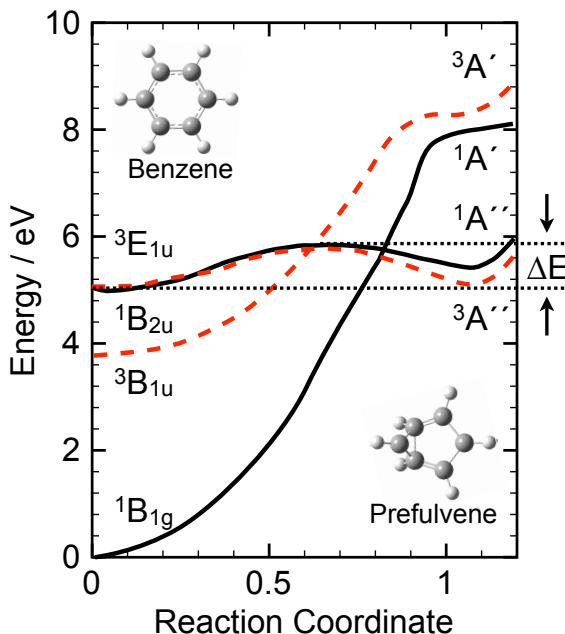


**Figure 3.2:** Potential energy curves of the lowest singlet (solid black lines) and triplet (dashed red lines) states of benzene along the reaction path to the prefulvene form, obtained at the CASSCF/DZ level by Domcke and coworkers [96].

*Ab initio* potential energy surfaces for the singlet and triplet states of benzene have been calculated by the group of Domcke [96] with CASSCF and MCRI methods including expensive basis sets. They succeeded to pinpoint CI's responsible for the electronic deactivation of benzene involving the benzene isomer prefulvene. The CI of interest is defined by the crossing of two potential curves. The first is formed along the adiabatic reaction path from a planar symmetric aromatic form of the  $S_1$  state to the  $S_0$  state of the biradical isomer prefulvene with  $^1A''$  symmetry. The second is connecting the ground state of benzene with the first excited singlet  $A'$  state of prefulvene. Figure 3.2 shows the respective potential curves and their crossing (reaction coordinate at 0.8), which acts as photochemical funnel (CI) for the deactivation of the excited benzene molecules. A small barrier of  $\Delta E = 3000 \text{ cm}^{-1}$  separates the  $S_1$  benzene state from the  $S_0$  state of prefulvene. The CI between the potential curves can only be accessed, when this barrier is overcome. Since the potential curve leading back to the benzene  $S_0$  state is by far steeper, it is the favored path.

Because of the reproducible and generally accepted chemical and quantum mechanical results on benzene, we decided to use benzene for calibrating our femtosecond pump-probe ToF-MS and also the femtosecond time-resolved PEI spectrometer.

### 3.1.2 Experimental

The ToF-MS and PEI experiments built in this work have been described in detail in Section 2.1 and 2.2.

A gas mixture containing  $\approx 1 \%$  of benzene in helium carrier gas was prepared by flowing the inert gas at 2 bar pressure through the liquid sample stored in a glass reservoir at  $-20 \text{ }^\circ\text{C}$ . The gases expanded into a differentially pumped electropolished steel vacuum chamber through a solenoid actuated pulsed valve (General Valve Series 9, Iota One) operated with a  $250 \mu\text{s}$  pulse opening time at 50 Hz repetition rate. A molecular beam entered the final vacuum chamber through a 1 mm diameter self-made conical skimmer. Based on previous experience under similar expansion conditions, the vibrational temperature of the benzene in the cold beam is expected to be in the range of  $T_{vib} \approx (50 \pm 10) \text{ K}$ . Benzene (puriss. p.a., standard for GC,  $\geq 99.9\%$ ) was purchased from Sigma-Aldrich and was used without further purification.

The optical setup used a regeneratively amplified Ti:Sa femtosecond laser system (Clark MXR CPA 2001) producing pulses of 200 fs duration (FWHM) at  $\lambda = 775 \text{ nm}$  with pulse energies of  $\approx 1 \text{ mJ}$  at 1 kHz repetition rate. Excitation pulses at

$\lambda = 258$  or  $387$  nm were generated in a home-built harmonic doubler/tripler, with durations of  $< 150$  fs (FWHM). Focussed pump pulses (at  $f = 300$  mm) of  $\approx 0.2$   $\mu\text{J}$  (258 nm) or  $0.75$   $\mu\text{J}$  (387 nm) intersected the molecular beam at right angle halfway between the repeller and extractor of the Wiley-McLaren electrostatic lens assembly. The excited molecules were ionized by  $\lambda = 775$  nm probe pulses taken from the Ti:Sa laser ( $\approx 20$   $\mu\text{J}$ ) copropagating with the pump laser beam. The polarization was set with the electric field vector perpendicular to the plane defined by the molecular beam and the laser beams using zero-order  $\lambda/2$  quartz wave plates.

The benzene cations were monitored by a self-made MCP detector. The data were recorded by integrating over the mass peaks for each delay time between the pump and probe/ionization pulses using a computer-controlled linear translation stage (Physik Instrumente M-126CG.). Every single step was accumulated over 1250 laser shots. In the PEI experiments the electrons were detected by a MCP phosphorescence screen detector (40 mm diameter, Photek). The back of the screen was imaged with a CCD camera ( $1600 \times 1200$  pixel, pco). The images were accumulated over 200k laser shots for each time-delay using a centroiding algorithm to improve the detection sensitivity and spatial resolution and to discriminate against noise. A mu-metal shield was installed in the flight tube to suppress outer static and dynamic magnetic fields of low frequency.

### 3.1.3 Results

#### 3.1.3.1 Time-Resolved ToF Mass Spectrometry

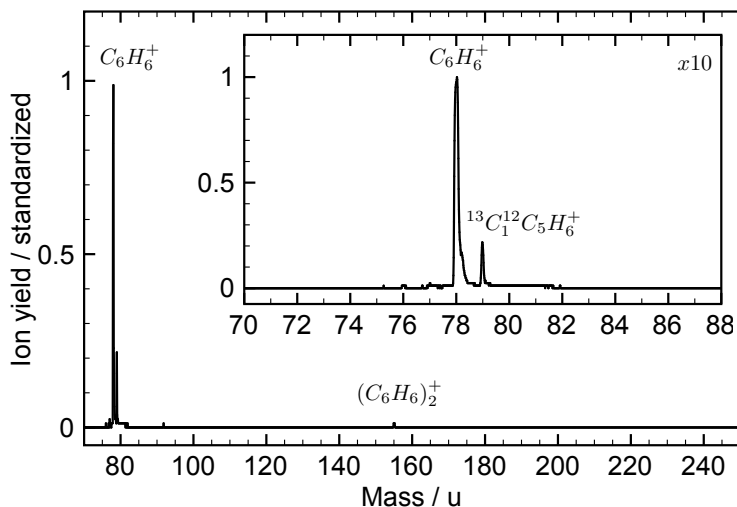


**Figure 3.3:** Typical mass spectrum of benzene and clusters, indicating only a very small fraction of clusters.

The presence of larger benzene clusters was carefully checked by ToF-MS measurements, because fragmentation of clusters can strongly influence the results of transient measurements. The cluster contribution depends on the backing pressure of the pulsed valve, the used carrier gas, the diameter and geometry of the valve orifice and the concentration of the sample in the molecular beam. Figure 3.3 shows that clusters were negligible, this was achieved by cooling of the benzene reservoir down to  $-20$  °C.

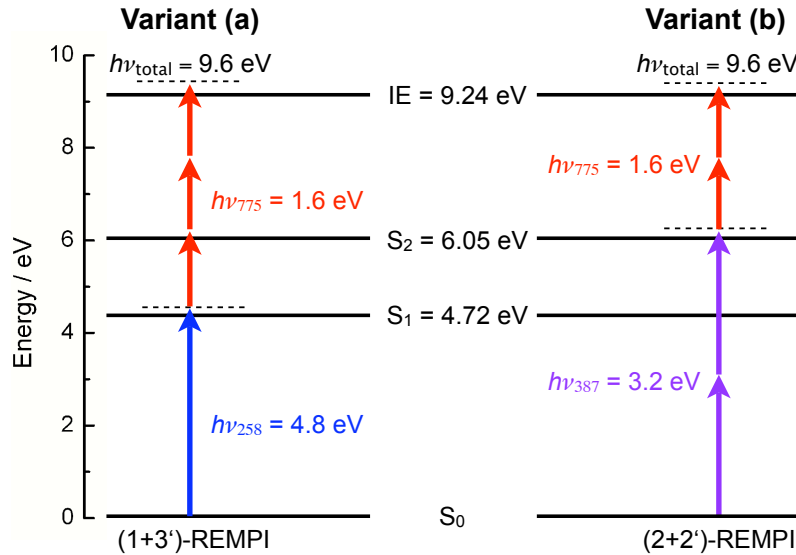


**Figure 3.4:** Pump-probe schemes realized for benzene: (a) (1+3')-REMPI probing the  $S_1$  state and (b) (2+2')-REMPI probing the  $S_2$  state.

Benzene molecules were pumped and probed following two resonance enhanced multiphoton ionization (REMPI) schemes as shown in Figure 3.4. In scheme a) the  $S_1$  state of benzene is excited by one photon absorption at  $\lambda = 258$  nm. As can be seen, the molecules are prepared with  $h\nu_{258} = 4.8$  eV just very slightly above the  $S_1$  origin ( $T_0(S_1) = 4.722$  eV; [86]). The excited  $S_1$  benzene molecules are then ionized by three-photon absorption at  $\lambda = 775$  nm ( $3 \times h\nu_{775} = 4.8$  eV), which results in an excess energy above the IE (9.246 eV [105]) of up to 0.354 eV.

The behavior of higher excited states of benzene was investigated by pumping the  $S_2$  state (6.05 eV; [95]) by two-photon absorption at  $\lambda = 387$  nm ( $2 \times h\nu_{387} = 6.4$  eV). The populated  $S_2$  state is probed/ionized time-resolved by two-photon absorption at  $\lambda = 775$  nm ( $2 \cdot h\nu_{775} = 3.6$  eV). Again, the ions contain an excess energy of 0.354 eV.

Figure 3.5 shows the measured time-resolved decay profiles of the  $C_6H_6$  peak in the mass spectra obtained for scheme (a) ( $\lambda_{pump} = 258$  nm) and scheme (b) ( $\lambda_{pump} = 387$  nm), exciting the  $S_1$  or  $S_2$  states, respectively. The decay profile in (a) consists



clearly of two components of similar amplitudes, but with decay rates of different magnitude. Likewise, (b) consists of two components, but just one is determining the transient mass spectrum. The decay profiles were fitted with the sum of two decaying exponentials convoluted with a Gaussian describing the IRF, using a non-linear least-squares routine based on the Levenberg-Marquardt algorithm.<sup>(1)</sup>

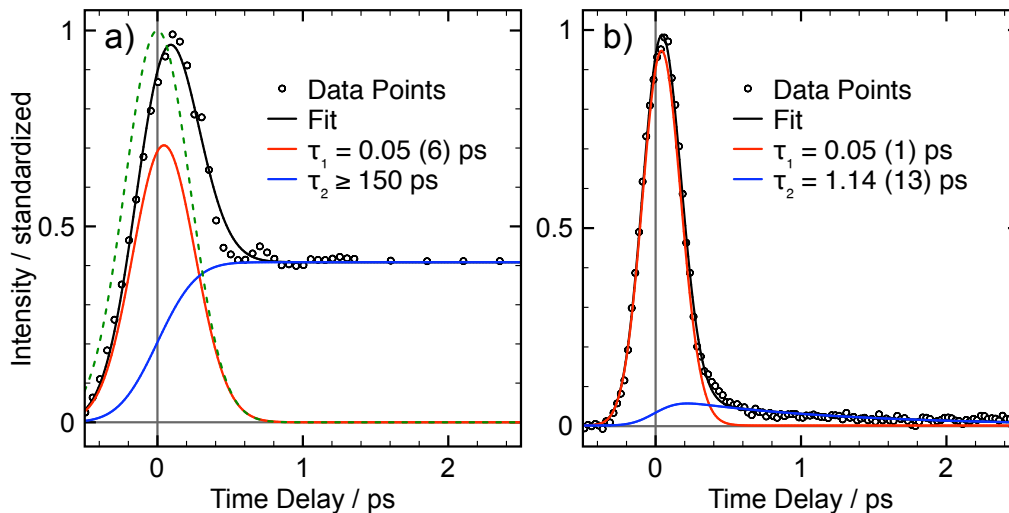


**Figure 3.5:** Ion signals of benzene ( $m/z = 78$ ) in the  $S_1$  (a) state and  $S_2$  (b) state as function of delay time  $\tau$  between the pump and probe pulses. The green dashed line in (a) shows the IRF. (a)  $\lambda_{pump} = 258$  nm,  $\lambda_{probe} = 3 \times 775$  nm. (b)  $\lambda_{pump} = 2 \times 387$  nm,  $\lambda_{probe} = 2 \times 775$  nm.

The observed time dependences are interpreted as follows. The measured transient decay curve of  $C_6H_6$  ( $S_1$ ) is fitted with a sum of two decaying exponentials convoluted with the IRF of the apparatus. At  $\lambda = 258$  nm, the jet-cooled benzene is excited into the  $S_1$  state with  $\approx 450$   $cm^{-1}$  excess energy. The non-linear fit results are  $\tau_1 = 0.05(6)$  ps and a  $\tau_2 \geq 150$  ps, where the values in parenthesis express the  $2\sigma$  standard deviation of the fit. According to the literature [94], no fast decaying component should be observable below the energy barrier of  $\Delta E = 3000$   $cm^{-1}$ . Therefore,  $\tau_1$  represent a coherent “artifact”, which shows up due to a cross correlation between the pump and probe laser beams. Cross correlated ion signals can be approved or ruled out by varying the pump and probe powers, because of their strong power dependences. Furthermore, the simultaneous interaction between the pump and probe pulses can lead to an excitation of higher states.

The second component with the decay rate  $\tau_2$  reflects the population of the  $^3B_{1u}$  triplet state of benzene. As the presented experimental setup allows us to perform

<sup>1</sup>Programmed in Mathematica 5.2 (Wolfram Research).

measurements on a time scale of up to  $\tau = 150$  ps, the lifetime of the population of the  ${}^3B_{1u}$  state is longer than this time scale and therefore  $\tau_2$  could not be assigned more accurately.

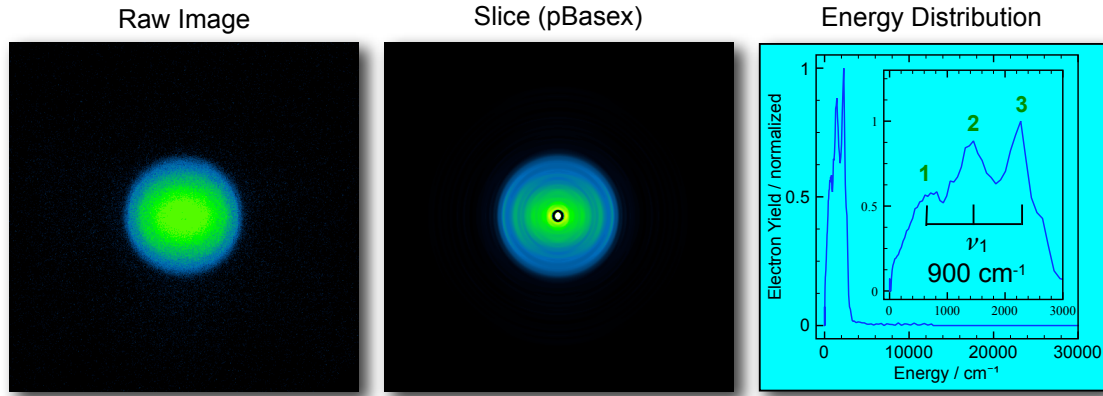
After excitation to the  $S_2$  state with 387 nm, a different biexponential decay behavior was found.  $\tau_1$  is still 0.05(1) ps and consistent with earlier results is interpreted as a very rapid internal conversion out of the  $S_2$  state into either the vibrational hot  $S_1$  state or the  $S_0$  state [93]. The  $S_1$  state is now populated above the  $3000\text{ cm}^{-1}$  threshold energy, the CI to the  $S_0$  state is accessible, and this reduces the  $S_1$  lifetime to  $\tau_2 = 1.14$  ps, as it was discussed above.

### 3.1.3.2 Transient Photoelectron Imaging

To achieve a good signal to noise ratio in pump-probe photoelectron imaging, it is necessary to avoid photoelectrons from absorption processes only by the pump or probe laser. Such one-color photoelectrons can be effectively suppressed by an off-resonant probe wavelength and by decreasing the pump and probe energies, until no photoelectrons are generated by the single pulses. Nevertheless, one-color photoelectron images are useful for energy calibration. Photoelectron background images measured by one-color (1+1) and (3+3)-REMPI schemes exciting at  $\lambda = 258$  and  $\lambda = 775$  nm with pulse energies of  $1\ \mu\text{J}$  and  $45\ \mu\text{J}$ , respectively, are shown in Figure 3.6. The raw images are displayed on the left and slices through the reconstructed 3D distributions are shown in the middle. In the right column, the corresponding electron kinetic energy distributions are given for  $\lambda = 258$  nm (in the first) and  $\lambda = 775$  nm (in the second row).

The  $S_1$  excited benzene photoelectron spectra for  $\lambda = 258$  nm (Figure 3.6, first row) reveals a vibrational progression on an enlarged scale, which can be assigned to the symmetric ring stretching mode  $\nu_1 = 900\text{ cm}^{-1}$  in the ionic state. A similar value has been found by Radloff et al. ( $965\text{ cm}^{-1}$ ; [95]), who excited the  $S_2$  state. The vibrational progression in the electron distribution does not represent the  $S_1$  state distribution, because excitation with  $\lambda = 258$  nm gives only an excess energy of  $\Delta E \approx 450\text{ cm}^{-1}$  in the prepared  $S_1$  state. This energy is insufficient to access the  $\nu_1$  vibration in the  $S_1$ . The photoelectron distribution shows vibrational states up to an energy of  $2850\text{ cm}^{-1}$ . The transition from the  $S_1$  state to the ionic state has to be associated with a significant change of the molecular geometry and only a broad Franck-Condon overlap can explain the activation of the vibrations. This has been reported for the  $S_2$  state, which suffers a significant distortion in its geometry by interaction with the neighboring higher electronic state of  $E_{1u}$  symmetry due to a pseudo Jahn-Teller effect [106]. The appearance of the vibrational progression in the  $S_1$  state is explained in Figure 3.7.

(1+1)-REMPI at  $\lambda = 258$  nm:



(3+3)-REMPI at  $\lambda = 775$  nm:

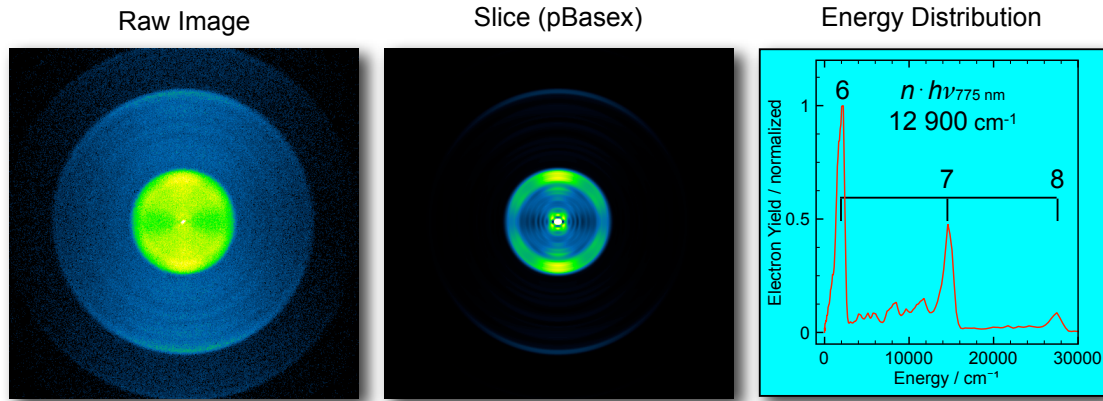


**Figure 3.6:** One-color single pulse PEI are normally unwanted and have to be negligible when performing time-resolved measurements, but they are useful for energy calibration and evaluation. The  $\lambda = 258$  nm PEI in the first row shows the  $\nu_1$  vibronic progression with an energy spacing of  $\Delta\tilde{\nu} \simeq 900$   $\text{cm}^{-1}$ . Too high laser power results in an over threshold ionization progression, which is shown in the lower row for  $\lambda = 775$  nm.

The kinetic energy of a photo-released electron is proportional to the photon energy and the corresponding internal energy of the related ion,

$$h\nu_{pump} + h\nu_{probe} = E_{int}^{ion} + E_{kin}^{el} - IP. \quad (3.1)$$

In the borderline case of ions with zero internal energies, and with respect to the mentioned REMPI excitation at  $\lambda = 258$  nm, Equation 3.1 can be simplified to the maximum photoelectron energy release  $E_{max}^{el}$  at  $\lambda = 258$  nm:

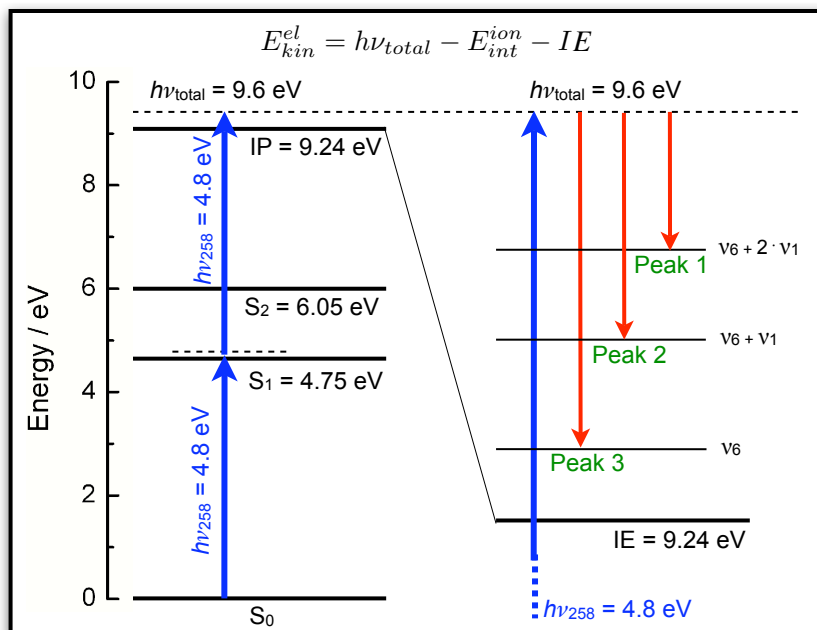


**Figure 3.7:** The diagram on the left explains the one-color pump probe scheme at  $\lambda = 258$  nm, which was used to receive the PEI in figure 3.6. The inset on the right shows a schematic diagram of the vibronic progression observed in the PEI. The size of the red arrows is equivalent to the photoelectron kinetic energies.

$$\begin{aligned}
 E_{max}^{el} &= h\nu_{pump} + h\nu_{probe} - IP & (3.2) \\
 &= 4.80 \text{ eV} + 4.80 \text{ eV} - 9.24 \text{ eV} \\
 &= 0.36 \text{ eV} \hat{=} \underline{2850 \text{ cm}^{-1}}
 \end{aligned}$$

The opposite extreme is zero electron kinetic energy (ZEKE), which corresponds to a maximum internal energy of the ion.

The observed anisotropy parameters (Table 3.1.3.2) of  $\beta = -0.27$  (Peak 1),  $-0.33$  (Peak 2),  $-0.35$  (Peak 3) and  $\gamma = 0$  (Peaks 1, 2, 3) suggest a vertical p-wave electron, which is consistent with an ionization from the vibrationally excited  $S_1$  state as explained above.

The second row in Figure 3.6 shows the result of a multi-photon “over-threshold ionization” [107] with  $\lambda = 775$  nm in two resonant steps involving eight photons. In the first step, three photons are absorbed and the benzene is transferred to the  $S_1$  state. This is followed by additional one-photon absorption into the  $S_2$  state. Ionization of the molecules can then happen by absorption of at least two more photons. Through further “over-threshold” absorption, two additional rings with

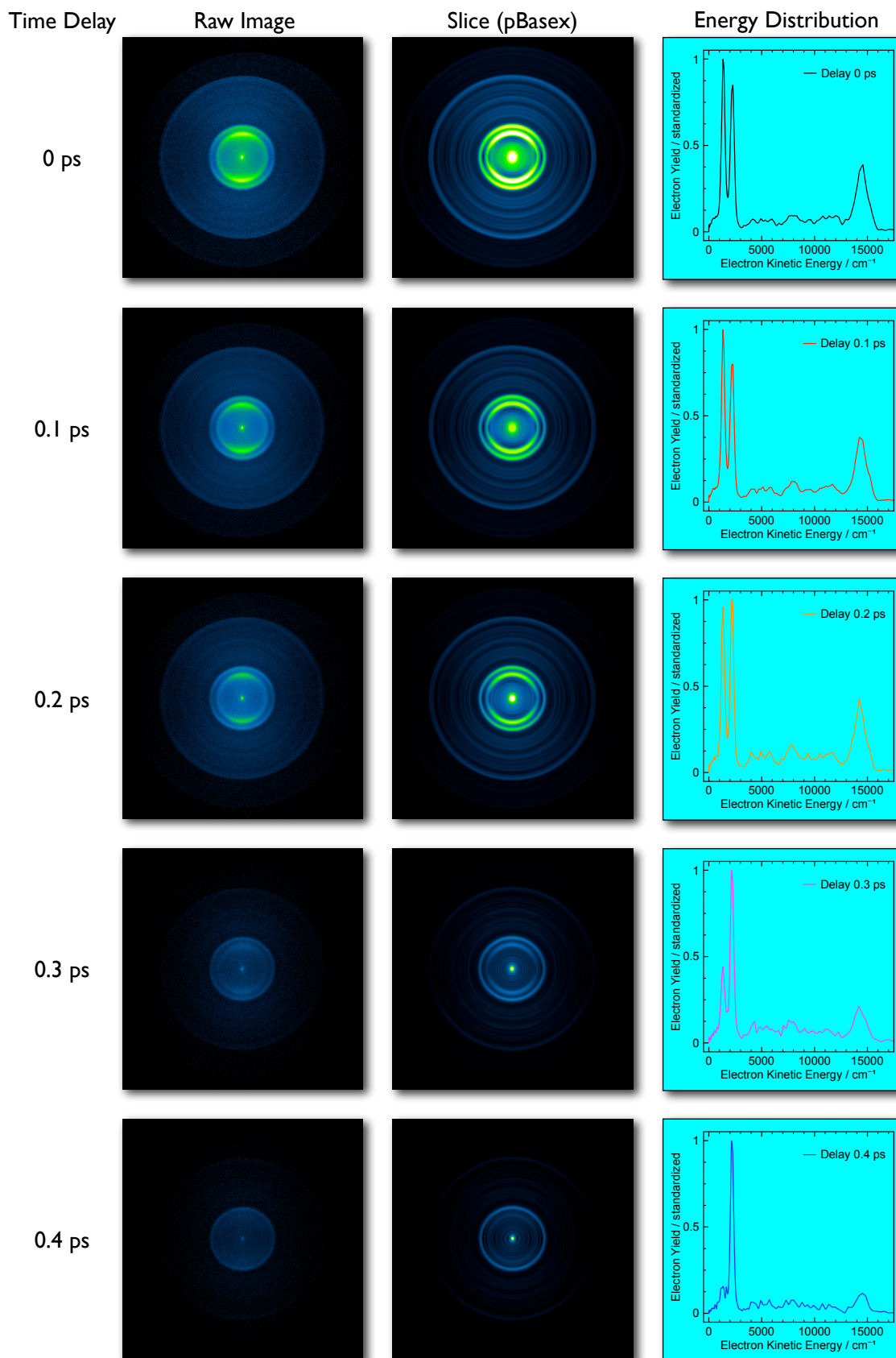


**Figure 3.8:** Summary of the time-resolved PEI results on benzene obtained by (2+2')-REMPI using  $\lambda_{pump} = 387$  nm and  $\lambda_{probe} = 775$  nm. Each time delay series contains the raw image, the pBasex fitted slice, and the corresponding normalized electron energy distributions.

**Table 3.1:** One-Color  $\lambda = 258$  nm PEI Results on Benzene

Peak Nr.	Energy $\text{cm}^{-1}$	Anisotropy Parameters	
		$\beta$	$\gamma$
1	570	-0.27	0
2	1 380	-0.33	0
3	2 270	-0.35	0

an energy spacing of the probe photon energy of  $h\nu_{775} = 12\,900 \text{ cm}^{-1}$  emerge. Over-threshold ionization is usually unwanted and an indicator for too high pulse powers, but it is very useful for calibration of the photoelectron images (Section 2.2).

The time-resolved PEIs of benzene shown in Figure 3.8 were obtained by exciting the  $S_2$  state at  $\lambda = 387$  nm and ionizing at  $\lambda = 775$  nm, following a (2+2')-REMPI scheme (scheme (b) in Figure 3.4), for time delays between the pump and probe pulse of 0 to 0.4 ps in 0.1 ps steps. The raw photoelectron images, the slices through the reconstructed 3D distributions, and the electron energy distributions calculated for the different delay times ( $\Delta t$ ) are shown in the rows of the figure. The intensities of the raw images and the 3D slices were radially scaled with the root of the radius to enhance the contrast and accent the high radius rings. The respective energy distributions are normalized to better visualize their temporal developments. Figure 3.9 shows the time-resolved photoelectron kinetic energy releases for every  $\Delta t$  unnormalized to emphasize their evolution.

**Table 3.2:** Time-Resolved PEI Results on Benzene.

Peak Nr.	Energy $\text{cm}^{-1}$	Anisotropy values at different time delays									
		$\Delta t = 0$ ps		$\Delta t = 0.1$ ps		$\Delta t = 0.2$ ps		$\Delta t = 0.3$ ps		$\Delta t = 0.4$ ps	
		$\beta$	$\gamma$	$\beta$	$\gamma$	$\beta$	$\gamma$	$\beta$	$\gamma$	$\beta$	$\gamma$
1	1 332	1.2	0.85	1.17	0.76	1.17	0.64	1.18	0.42	0.93	0.02
2	2 277	0.92	-0.11	0.99	-0.07	0.89	-0.1	0.64	-0.02	0.61	0.06
3	8 071										
4	14 236	not evaluable									
5	15 180										

The PEI overall intensities shown in Figure 3.8 are decreasing from a maximum at  $\Delta t = 0$  ps to less than 5 % at  $\Delta t = 0.4$  ps, which very well mirrors the time-resolved

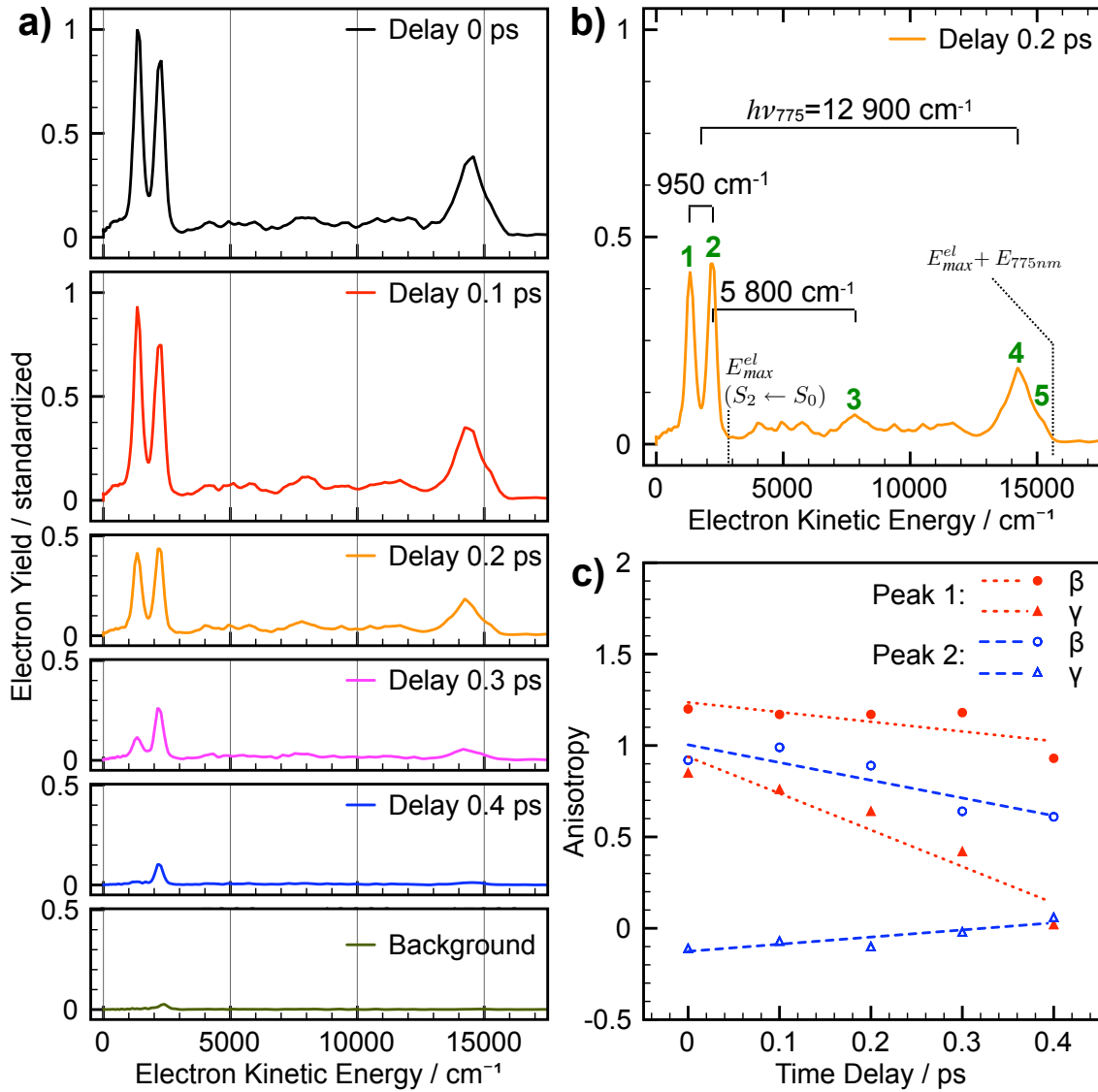


**Figure 3.9:** (a) Photoelectron kinetic energy releases for different values of  $\Delta t$ . (b) Assignment of peak positions: Peaks no. 1 and 2 are assigned to the vibronic progression  $\nu_6^1 + \nu_1^n$  ( $n = 1, 0$ ), peak 3 emerges from ions that are ionized after relaxation to the  $S_1$  state and peaks 4 and 5 arise due to “over-threshold” ionization by the absorption of one more probe photon. (c) Anisotropy parameters  $\beta$  and  $\gamma$  are shown for increasing  $\Delta t$ .

ToF-MS results of benzene after  $S_2$  excitation described above. The peaks referred to in Figure 3.9 b) are assigned as follows:

- **Peaks 1 and 2:** The maximum available photoelectron kinetic energy release  $E_{max}^{el} = 2850 \text{ cm}^{-1}$  for the (2+2')-REMPI has been assigned to the edge of peak 2. All other peaks with higher energies are produced differently as described below. The photoelectron peaks 1 and 2 at  $E_{kin(1)}^{el} = 1330 \text{ cm}^{-1}$  and  $E_{kin(2)}^{el} = 2280 \text{ cm}^{-1}$  have an energy difference of  $950 \text{ cm}^{-1}$ , which corresponds to the  $\nu_6^1\nu_1^n$  ( $n = 0, 1$ ) vibronic progression in the excited  $S_2$  state [108]. Radloff *et al.* published a similar energy spacing of  $965 \text{ cm}^{-1}$  [95]. With increasing  $\Delta t$ , peak 1 ( $\nu_6^1\nu_1^1$ ) vanishes significantly faster than peak 2 ( $\nu_6^1\nu_1^0$ ). Radloff *et al.* observed a collective decrease of the whole progression.

The peaks show a decreasing anisotropy with larger  $\Delta t$ . The  $\beta$  parameters of peaks 1 and 2 have comparable values with  $\beta = 1.2$  and  $0.9$ , respectively, at  $\Delta t = 0$ , and then decrease slowly until  $\Delta t = 0.4 \text{ ps}$  to values of  $\beta = 0.9$  and  $0.6$ . In contrast, the next higher anisotropy parameter  $\gamma$  is not comparable. For peak 1,  $\gamma = 0.9$  at  $\Delta t = 0 \text{ ps}$ , which decreases to  $\gamma = 0$  at  $\Delta t = 0.4 \text{ ps}$ . The  $\gamma$  parameter of peak 2 starts with a negative value of  $\gamma = -0.11$  at  $\Delta t = 0 \text{ ps}$  and ends with  $\gamma = 0$  at  $\Delta t = 0.4$ . Unfortunately, it is very challenging to interpret PEI anisotropies, when dealing with results gathered by mechanisms other than from a (1+1')-REMPI process.

- **Peak 3:** The ionization potential of a benzene dimer ( $8.65 \text{ eV}$ ; [109]) is  $0.59 \text{ eV}$  lower than ionization potential of a benzene monomer. Peak 3, which has an energy of  $\approx 8070 \text{ cm}^{-1}$ , corresponds to roughly the maximum kinetic energy of  $7620 \text{ cm}^{-1}$  after (2+2')-REMPI of benzene dimer. However, clusters were not observed in our ToF-MS measurements under the same experimental settings. Thus, it is concluded that peak 3 arises from ionization after redistribution from the  $S_2$  to the  $S_1$  state within the duration of the laser pulses.
- **Peak 4 and 5:** If one assumes that benzene monomers are the only ionized species, all photoelectron kinetic energies higher than  $2850 \text{ cm}^{-1}$  can only arise from over-threshold ionization. Peaks 4 and 5 show an energy spacing comparable to peaks 1 and 2 of exactly  $h\nu_{775} = 12900 \text{ cm}^{-1}$ . Because of the strong overlaps, the anisotropies of the peaks are not distinguishable.



### 3.1.4 Discussion

The photophysical and photochemical processes in benzene as the prototypical aromatic molecule were intensely investigated in the last decades experimentally for example by Schlag *et al.* [110] and theoretically by Domcke *et al.* [96]. Both the  $S_1$  state excited  $3000\text{ cm}^{-1}$  above the origin and the  $S_2$  state are deactivated to the  $S_0$  ground state on ultrafast time scales through conical intersections. This has been indirectly observed by the low fluorescence quantum yields [102] and was directly measured by means of femtosecond time-resolved ToF-MS in the group of Radloff [93]. For the  $S_2$  state, which has a lifetime of  $\approx 50$  fs, two deactivation pathways were observed. The direct population of the  $S_0$  state through a conical intersection, which was predicted by Domcke *et al.*, holds 99 % of the amplitude. The remaining 1 % are deactivated to the vibrational hot  $S_1$  state, which in turn deactivates to  $S_0$  with a decay time of  $\tau = 6.7$  ps. The investigations of excited benzene have shown that the lifetime of the  $S_1$  state depends strongly on the vibronic excess energy, regardless of whether the energy was obtained by direct or indirect excitation.

The measurements on  $S_1$  and  $S_2$  excited benzene presented in this work are fully consistent with the literature. The decay profile after exciting into the  $S_1$  state shows a biexponential character, with two decay rates,  $\tau_1 = 0.04$  ps and  $\tau_2 > 150$  ps.  $\tau_1$  is assigned to a coherent cross-correlation between the pump and probe beam and not a depopulation of the  $S_1$  state. The second lifetime ( $\tau_2$ ) is not determined very accurately. Nevertheless, the extrapolated state lifetime is  $\approx 0.7$  ns. The investigation of the  $S_2$  state of benzene revealed a radiationless biexponential deactivation with the decay times of  $\tau_1 = 0.02$  ps and  $\tau_2 = 1.12$  ps. Radloff's interpretation of the results can be directly adapted to the results after  $S_2$  excitation.

Time-resolved PEIs of benzene were obtained by exciting the  $S_2$  state. The first two peaks at photoelectron energies of  $E_1 = 1330\text{ cm}^{-1}$  and  $E_2 = 2280\text{ cm}^{-1}$  represent a vibronic progression of  $\nu_6$ , and  $\nu_1$ . The same modes are observed in the UV absorption bands  $\alpha$  and  $p$  (Figure 3.1). This progression was also observed by Radloff and coworkers in their PES experiments exciting benzene in the  $S_2$  state. They found an energy spacing of  $965\text{ cm}^{-1}$ , virtually identical with the spacing in this work ( $\Delta E = E_2 - E_1 = 950\text{ cm}^{-1}$ ). Quantum chemical calculations with the B3LYP//6-311<sup>++</sup>(3df,3pd) functional (DFT) performed in this work determined a frequency for the  $\nu_1$  vibrational normal mode of  $976\text{ cm}^{-1}$ , in good agreement.

With increasing delay time  $\Delta t$ , both peaks are decreasing, but peak 1, the energy of which corresponds to a higher internal energy in the  $S_2$  state, is decaying significantly faster than peak 2 (Figure 3.9). This is not astonishing, because with increasing energy the deactivation processes are becoming more efficient. Peaks 3, 4 and 5 derive from different (over-threshold) ionization schemes and have been

used for energy calibration.

### **3.1.5 Conclusion and Summary**

As shown, both the time-resolved ToF-MS and PEI results on benzene can be used to calibrate the experimental setups and the gathered results are comparable to literature values. All further measurements, in particular the PEI experiments, have been calibrated on benzene.

## 3.2 Toluene and *o*-, *m*-, *p*-Xylene

### 3.2.1 Introduction

In comparison to benzene, the methyl substitution in toluene yields an altered absorption behavior. The +I-effect of the methyl group lowers the electronic states, which is evident by a red-shift in the UV absorption spectrum. The reduced symmetry lifts the state degeneracy. And the higher density of vibrational states allows for a stronger non-adiabatic coupling between the electronic states.

The UV spectrum of toluene is shown in Figure 3.10. It consists of a weak, but structure-rich band around 260 nm, corresponding to the  ${}^1B_{2u} \leftarrow {}^1A_{1g}$  transition in benzene, and a stronger band with some vibrational structure near 200 nm, which represents the  ${}^1B_{1u} \leftarrow {}^1A_{1g}$  transition in benzene. A very strong and nearly continuous band near 185 nm is similar to the  ${}^1E_{1u} \leftarrow {}^1A_{1g}$  transition in benzene [111].

The fluorescence quantum yield and lifetime of the  $S_1$  state have been studied at nanosecond time resolution and in the gas phase at different excitation wavelengths using various methods. Fluorescence dispersion experiments provided a lifetime of  $\approx 90$  ns [112] after excitation to the  $S_1$  origin at  $37477\text{ cm}^{-1}$  [113, 114]. The fluorescence quantum yield has been estimated by single-photon counting experiments [115] to be  $\approx 1$ . For excess energies smaller than  $2200\text{ cm}^{-1}$ , monoexponential decay times between  $\tau_{fl} = 40 - 90$  ns have been measured. At  $E_{ex} > 2200\text{ cm}^{-1}$ , the fluorescence decays exhibit biexponential behavior with lifetimes of  $\tau_{fl1} < 35$  ns and  $\tau_{fl2} \leq 5$  ns. The fluorescence quantum yields are below 0.3. For excess energies  $> 3600\text{ cm}^{-1}$ , the longer-lived fluorescence component  $\tau_{fl1}$  cannot be detected anymore, and the fluorescence yield is  $< 0.02$ . The fast component  $\tau_{fl2}$  was still observable, but became faster than the instrumental resolution of 1 ns [115]. The results have been discussed in terms of those for benzene. With increasing excitation energy, more deactivation channels become available because of the increasing number of active vibrations. This results in a higher probability for IC to the ground state or ISC to the triplet state.

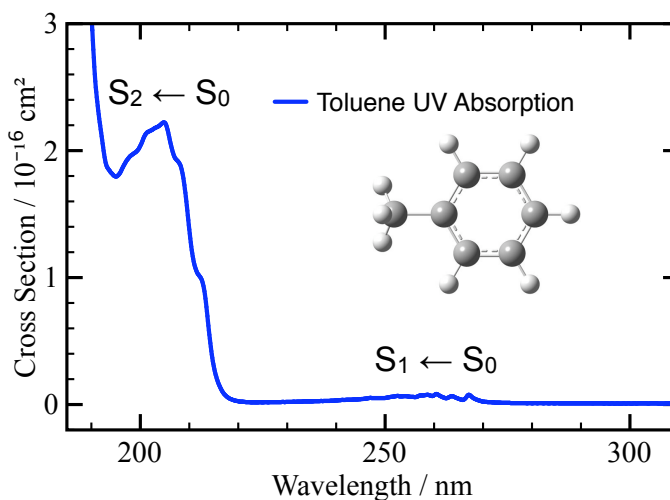


**Figure 3.10:** The gas phase UV absorption spectrum at  $p = 0.5$  mbar of toluene exhibits three bands similar to benzene.

Other groups investigated explicitly the methyl rotor in toluene [116, 117]. It is discussed, whether internal rotation of the methyl group alters the structure or, what seems more likely, whether it induces an electronic hyperconjugation that facilitates IC or ISC.

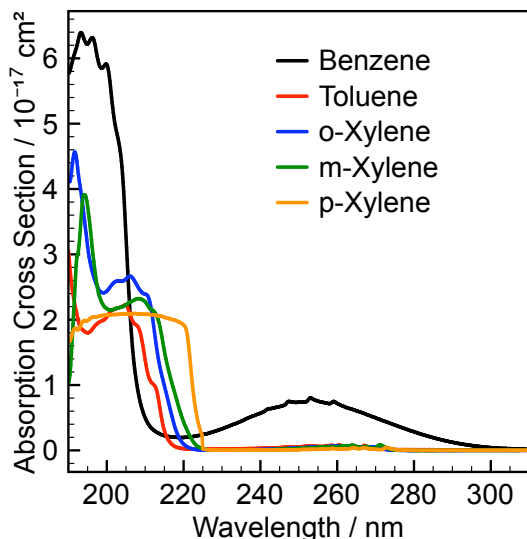


**Figure 3.11:** Comparison of the gas phase UV absorption spectra at  $p = 0.5$  mbar of benzene, toluene, and *o*-, *m*-, and *p*-xylene.

pump-probe delay times of  $\tau > 30$  ns. At this time, the  $S_1$  state population had decayed to virtually zero, except for the  $S_1$  vibrational ground state. The results of Whiteside and coworkers are controversial insofar as the observed radiationless redistribution lifetimes are faster than the measured overall fluorescence lifetimes obtained by other groups (see above). In principle, fluorescence lifetime should be a direct indicator for all other intra- and intermolecular deactivation processes [120, 30].

Transient femtosecond ToF-MS and PES investigations have been performed on the  $S_2$  state of toluene at ps resolution in the group of Hertel [121]. The molecules were excited close to the  $S_2$  origin. The results were interpreted similarly as the results obtained after  $S_2$  excitation of benzene. Accordingly,  $S_2$  toluene molecules deactivate within  $\tau < 50$  fs through two conical intersections to the  $S_1$  state and the  $S_0$  state. The populated  $S_1$  state deactivates with  $\tau = 4.3$  ps to the electronic ground state. The branching ratio between the deactivation path from  $S_2$  to  $S_1$  and directly to  $S_0$  is with 0.43 higher than that found for benzene (0.01).

Whiteside et al. [118, 119] investigated  $S_1$  toluene by nano- and picosecond time-resolved photoelectron spectroscopy. The excitation of different vibrational modes up to an excess energy of  $E_{ex} = 1200$   $\text{cm}^{-1}$  revealed non-radiative deactivation in several hundred ps to several ns from all of the prepared states. The rate of intramolecular vibrational energy redistribution (IVR) following excitation of the C-CH<sub>3</sub> stretching mode at 1193  $\text{cm}^{-1}$  was with  $\approx 10$  ps significantly faster than the IVR of other states. As mentioned above, this can be explained by a promoting activity of the methyl rotor. Furthermore, ISC to the triplet state was excluded. The rise of the triplet state was observed at

Xylene, or dimethylbenzene, has three isomers (*ortho*-, *meta*-, and *para*-xylene). The methyl groups raise the reactivity and the stability of substituted benzenes. The electronic stabilization, explained by a +I- and +R-effect, lowers the energy of the orbitals. The ground state profits less than the energetically higher excited states. As a result, the dimethylbenzenes have red-shifted absorption spectra, as is shown in Figure 3.11. The shift increases not only with the number of methyl groups, but also with the substitution pattern. The sequence  $\Delta E_{ortho} < \Delta E_{meta} < \Delta E_{para}$  can be calculated by the Hückel MO approximation [122]. The shifts are presented in Table 3.3.

**Table 3.3:** Band shifts by methyl substitution in *ortho*-, *meta*-, and *para*-position in toluene. The first row shows the toluene values, the next three rows the data for *o*-, *m*-, and *p*-xylene.  $S_1 \leftarrow S_0$  transition zero point energies have been taken from the literature [123]. The values for the  $S_2 \leftarrow S_0$  and  $S_3 \leftarrow S_0$  transitions are extrapolated from the absorption spectra in Figure 3.11

Molecule	$(S_1 \leftarrow S_0)$		$(S_2 \leftarrow S_0)$		$(S_3 \leftarrow S_0)$	
	E	$\Delta E$	E	$\Delta E$	E	$\Delta E$
	$\text{cm}^{-1}$					
Toluene	37 477	-	45 970	-	54 050	-
<i>o</i> -Xylene	37 308	169	45 330	640	52 360	1 690
<i>m</i> -Xylene	36 950	527	44 600	1 370	51 550	2 500
<i>p</i> -Xylene	36 727	750	44 424	1 545	-	-

In this work toluene, *o*-xylene, *m*-xylene and *p*-xylene have been investigated by means of femtosecond transient ToF-MS to elucidate the effects of single and multi-methylation on the electronic behavior of photoexcited benzenes. The results are presented in the following.

### 3.2.2 Experimental Setup

The same pump-probe schemes as for benzene were applied for toluene and the xylenes. The gas mixture composed of toluene ( $\approx 1\%$ ) and xylene ( $< 1\%$ ) was prepared by bubbling helium carrier gas through a glass reservoir containing the samples at  $-78\text{ }^\circ\text{C}$ .

### 3.2.3 Results

#### 3.2.3.1 Time-resolved ToF Mass Spectrometry

Figure 3.12 shows the energy excitation scheme used for toluene, with the ground state  $S_0$ , the excited states  $S_1$  and  $S_2$ , and the ionic state  $D_0$  (IE). Using (1+3')-REMPI (scheme a), toluene is excited to the  $S_1$  state (4.65 eV [124]) with an excess energy of 0.15 eV ( $\hat{=}$  1 230  $\text{cm}^{-1}$ ). The  $\lambda = 775$  nm probe pulse ionizes the excited species by three-photon absorption to a final excess energy in the ion (or rather the emitted electrons) of 0.74 eV ( $\hat{=}$  5 970  $\text{cm}^{-1}$ ) above the IE. Using (2+2')-REMPI (scheme b), the second excited state  $S_2$  is monitored. The  $S_2$  origin was estimated to be at  $E_{v_0}^{S_2} \approx 5.7$  eV from the UV absorption spectrum in Figure 3.10. Two photons at  $\lambda = 387$  nm prepare  $S_2$  excited toluene with a vibrational excess energy of 0.7 eV ( $\hat{=}$  5 650  $\text{cm}^{-1}$ ). After ionization at  $\lambda = 775$  nm, the total energy is the same as was realized in the (1+3')-REMPI experiment.

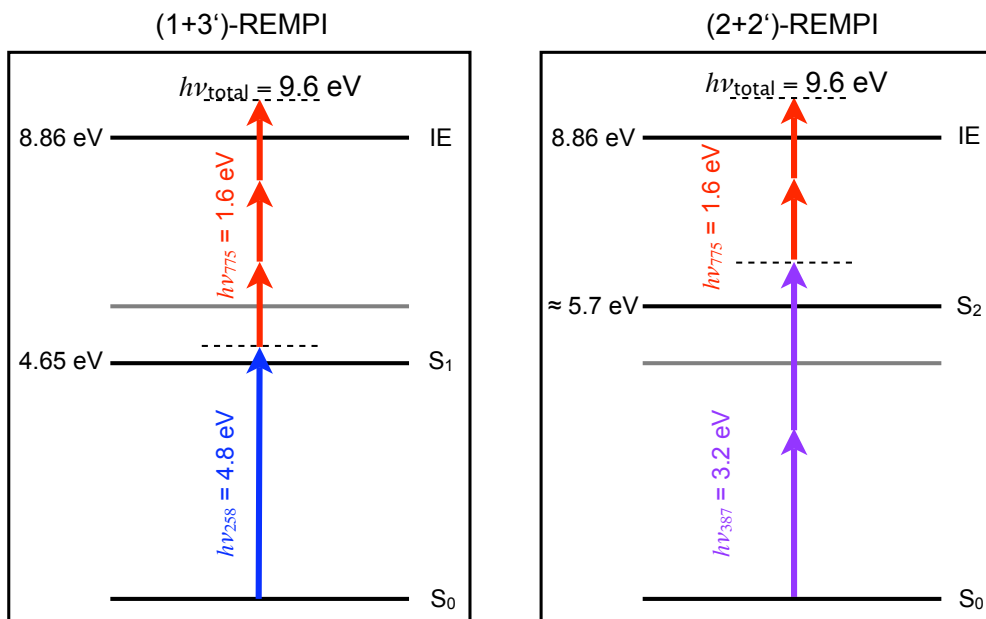


**Figure 3.12:** Excitation schemes for toluene. All involved electronic states are shown, as well as the ionization potential and the respective pump-probe laser energies for the two different REMPI schemes.

Figure 3.13 shows the time-resolved results for toluene obtained with both excitation schemes. The normalized ion yields are plotted versus the time delay in ps. They are interpreted as follows:

- (a) The fit results ( $\lambda_{pump} = 258$  nm) for  $S_1$  excited toluene revealed a decay time  $\tau_1 < 0.05$  ps, which is faster than the time resolution (0.1 ps) of the

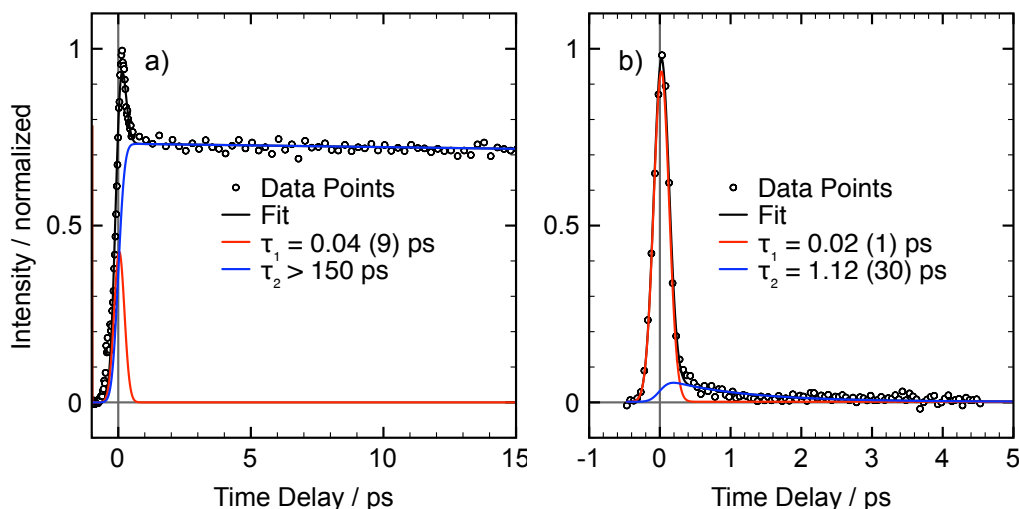


**Figure 3.13:** The results for toluene are displayed as follows: a) probing the  $S_1$  state by a (1+3')-REMPI ( $\lambda_{pump} = 258$  nm,  $\lambda_{probe} = 775$  nm), and b) probing the  $S_2$  state by a (2+2')-REMPI ( $\lambda_{pump} = 387$  nm,  $\lambda_{probe} = 775$  nm).

experiment. The second decay time  $\tau_2 > 150$  ps is long and cannot be accurately determined because it is far above the upper limit of the time delay stage (150 ps).

As discussed above, no fast decay component should be observable for threshold energies  $< 2200$   $\text{cm}^{-1}$ . The conclusion is that  $\tau_1$  represents either a coherent effect or an ultrafast internal conversion process to coupled vibrational modes within the  $S_1$  state. The latter has not been reported in the literature so far, but there are no data on extensive  $S_1$  lifetime studies with femtosecond time resolution available so far either.  $\tau_2$  reflects the population of the lower triplet state. The lifetime of the long-lived component can be estimated to  $\tau_2 \approx 0.7$  ns by extrapolation of the data.

- (b) Considering  $S_2$  excited toluene, reached with two 387 nm photons, a completely different decay behavior was found. The populated  $S_2$  state undergoes a very rapid internal conversion into vibrationally hot  $S_1$  and  $S_0$  states on a time scale of  $\tau_1 = 0.05$  ps. The molecules in the  $S_1$  state are populated with  $> 3000$   $\text{cm}^{-1}$  vibrational energy above the origin and can deactivate further through a CI to the  $S_0$  state. The decay rate for this process is  $\tau_2 = 1.14$  ps. Our results support the interpretations given by Radloff and coworkers [93].

The results for the double methylated benzene derivatives *o*-, *m*-, and *p*-xylene are shown in Figure 3.14. Plotted are the intensities and residues against the time delay for all xylenes. The molecules were pumped and probed using the (2+2')-REMPI scheme, as used for toluene and benzene, at  $\lambda_{pump} = 387$  nm and  $\lambda_{probe} = 775$  nm,

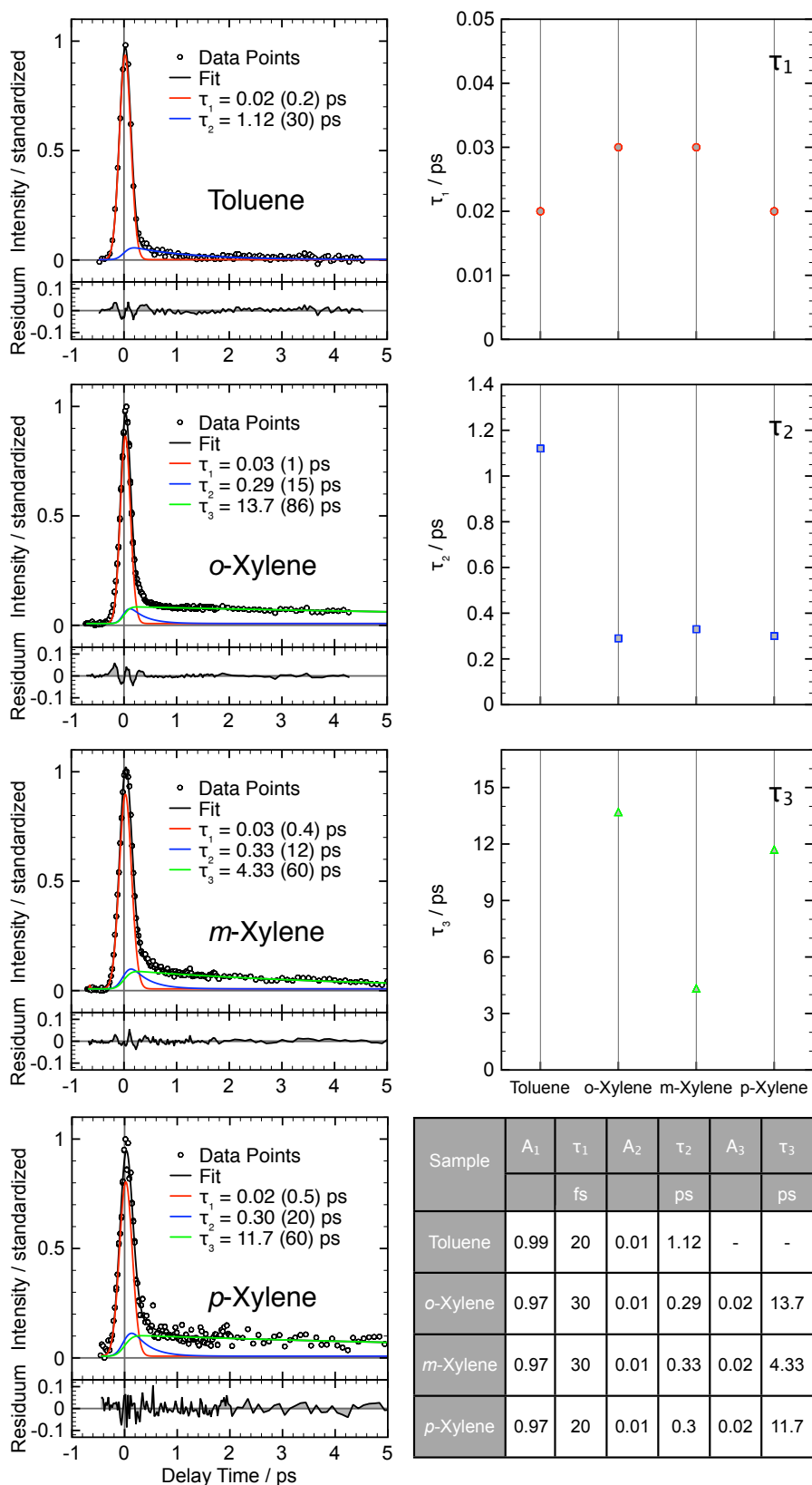


**Figure 3.14:** Transient decay profiles for *o*-, *m*- and *p*- xylene after excitation to the  $S_2$  state (left column). On the right are plotted the decay rates  $\tau_1$ ,  $\tau_2$  and  $\tau_3$ , which have been obtained by fitting with decaying exponentials. The results are summarized in the table.



respectively. The dimethylbenzenes show a similar radiationless deactivation behavior as observed for benzene and toluene, but three decay components  $\tau_1$ ,  $\tau_2$  and  $\tau_3$  are needed to describe the time profiles instead of two. The two-photon excitation energy of  $51\,700\text{ cm}^{-1}$  excites both the  $S_2$  state and the  $S_3$  state. The energies for the  $S_3$  origin are given in Table 3.3 and they show that the excitation may be not reaching the  $S_3$  origin of *o*-xylene. However, the values for the  $S_2$  and  $S_3$  energies estimated from the UV absorption spectra may not be precise enough. An excitation to the  $S_3$  state for *o*-xylene is likely.

- (a) For *o*-xylene, the sum of the  $S_2$  and  $S_3$  state profiles is shown in Figure 3.14. Three decay components are needed to describe the profile.  $\tau_1 = 0.02\text{ ps}$  and  $\tau_2 = 0.29\text{ ps}$  are attributed as for benzene and toluene. Within  $\tau_1$  the  $S_2$  state deactivates to both the  $S_1$  or  $S_0$  states. *o*-Xylene deactivated to  $S_1$  eventually reaches  $S_0$  within  $\tau_2$ . The third decay time  $\tau_3 = 13.7\text{ ps}$  may indicate the relaxation of  $S_3$  excited molecules. In comparison with toluene, the decay rates  $\tau_1$  and  $\tau_2$  are faster, which can be explained by the higher excess energy in the prepared  $S_2$  state.  $\tau_3$  has not been observed for toluene and benzene, since they were not excited to the  $S_3$  state.
- (b) The decay curve for *m*-xylene shows the same behavior with  $\tau_1 = 0.03\text{ ps}$  and  $\tau_2 = 0.33\text{ ps}$  as observed for *o*-xylene, but  $\tau_3 = 4.33\text{ ps}$  is smaller by a factor of  $\approx 3$ . The *meta*-position of the second methyl group could be the promoter.
- (c) The most symmetric isomer *p*-xylene has a time profile that virtually equals that of *o*-xylene. The decay times are  $\tau_1 = 0.02\text{ ps}$ ,  $\tau_2 = 0.3\text{ ps}$  and  $\tau_3 = 11.7\text{ ps}$ . All can be explained as in the case of *o*-xylene.

### 3.2.4 Discussion

The methyl- and dimethylbenzenes (toluene and xylenes) have been investigated not as intensely as benzene, but some literature is found concerning toluene [44, 92, 111, 112, 113, 114, 116, 117, 118, 119, 121, 123, 125, 126, 127, 128, 129, 130, 131, 132, 133, 134, 135, 136]. Work on the xylenes is very limited and spectroscopic investigations in the femtosecond time scale has so far been absent.

The femtosecond investigations on toluene in the group of Hertel have shown that the excited  $S_2$  state deactivates and behaves like the  $S_2$  state of benzene [137]. Two ultrafast redistribution pathways with decay rates of  $\tau_1 < 0.05$  ps and  $\tau_2 = 4.3$  ps were pinpointed and assigned as in benzene. The presented findings are consistent with the values of  $\tau_1 = 0.02$  ps and  $\tau_2 = 1.12$  ps, which have been observed after excitation to the  $S_2$  state in this work. The difference of the decay times can be explained by a higher excess energy and thus a higher vibronic state density.

The  $S_1$  state was previously only investigated in the ns and ps realms. Dispersed fluorescence experiments elucidated lifetimes ranging from  $< 1$  ns to 90 ns with mono- and biexponential character, depending on the excitation energy [115]. Below the threshold of  $2200\text{ cm}^{-1}$ , the fluorescence lifetimes are high (40 - 90 ns) and exhibit monoexponential decay. Above this threshold, biexponential behaviors were observed and the lifetimes drop drastically until they were not resolvable anymore at excitation energies higher than  $3600\text{ cm}^{-1}$ . At this point, the quantum yields are below 0.02. A similar behavior was found for benzene at threshold energies above  $3000\text{ cm}^{-1}$  ("Channel Three").

The  $S_1$  state behavior of toluene up to an excess energy of  $1300\text{ cm}^{-1}$  was investigated vibrationally resolved by Whiteside *et al.* with photoelectron spectroscopy using ps laser pulses [118, 119]. They observed a significant loss of vibronic structure within several ps to several ns, depending on the vibronic level. Because of different time scales, on which the loss ( $< \text{several ns}$ ) and the ISC ( $> 30\text{ ns}$ ) to the triplet state happen, ISC could be excluded and IVR was assumed to be responsible. After excitation of  $\nu_{13}$  at  $1193\text{ cm}^{-1}$ , the methyl stretching mode, IVR was completed after 10 ps, which is exceptionally fast. Investigations and calculations on the methyl rotor predict an acceleration of the IVR rate, resulting from an interaction of the orbitals in the methyl rotor with the orbitals in the ring (hyperconjugation).

Here, the  $S_1$  state was investigated by fs-ToF-MS, exciting at  $\lambda = 258\text{ nm}$ . The decay curve was fitted with two exponential decays,  $\tau_1 = 0.04\text{ ps}$  and  $\tau_2 > 150\text{ ps}$ . Both decay rates exceed the resolution limits,  $\tau_1$  is faster and  $\tau_2$  is slower

then the lower (0.1 ps) and the upper (150 ps) limit, respectively. Although no time dependent measurements on the femtosecond time scale are available for comparison,  $\tau_1$  has to be assigned to a cross-correlation between the pump and probe beam. The lifetime of the long-lived component exceeds the upper limit of the experiment, but can be extrapolated from the data to a decay time  $\tau_{(2,extp.)} \approx 0.7$  ns. Since the toluene  $S_1$  state was excited with an excess energy of  $\approx 1230$   $\text{cm}^{-1}$  to the  $\nu_{13}$  vibration, the results fit with the observations of Whiteside and coworkers, but are not consistent with the fluorescence measurements discussed above.

### 3.2.5 Conclusion and Summary

Femtosecond spectroscopic investigations on xylenes were not available in the literature. The present measurements show that the deactivation of the  $S_2$  states for all these xylenes are biexponential and can be explained following the interpretations for benzene and toluene. The decay times  $\tau_1 \approx 0.03$  ps and  $\tau_2 \approx 0.3$  ps agree for all three isomers. Furthermore, a third decay component, with  $\tau_3 = 13.7$  (*o*-xylene), 4.33 ps (*m*-xylene) and 11.7 ps (*p*-xylene) has been assigned to the deactivation of the  $S_3$  state reached within the excitation bandwidth.

### 3.3 Hexafluorobenzene

#### 3.3.1 Introduction

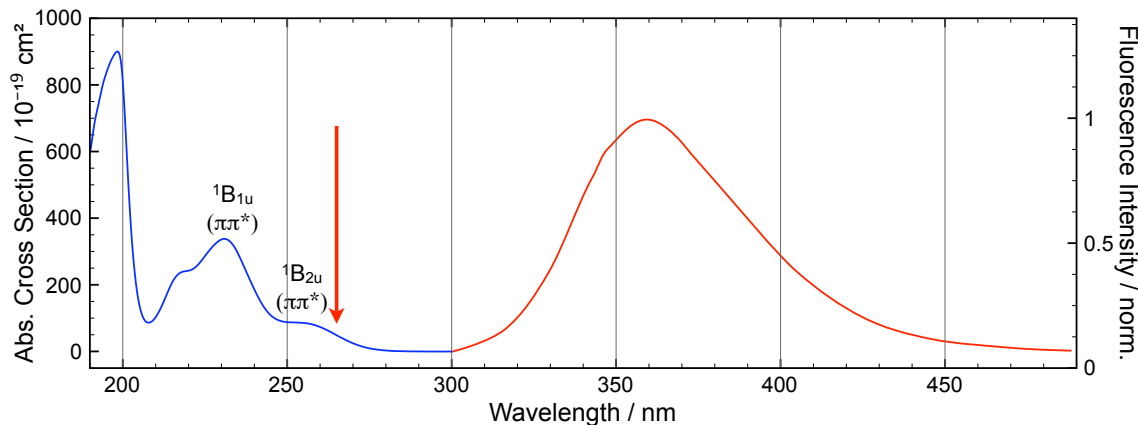


**Figure 3.15:** The gas phase UV absorption spectrum of hexafluorobenzene at  $p = 0.25$  mbar is shown in blue. The fluorescence emission shown in red after excitation at  $\lambda = 265$  nm (red arrow) has been adapted from Zgierski and coworkers. [138]

Figure 3.15 shows (in blue) the UV absorption spectrum of hexafluorobenzene (HFB) in the gas phase. The spectrum reveals four structureless broad bands. The first two bands have been assigned to the absorption from the ground state with  ${}^1A_{1g}$  symmetry to two different  $\pi\pi^*$  states with  ${}^1B_{2u}$  and  ${}^1B_{1u}$  symmetry, respectively.

Further ultraviolet absorption [28] and electron-impact spectra [139] of gaseous HFB revealed higher-energy features that are not present in benzene itself. Those features have been attributed to a transition from the ground state to the  $\pi\sigma^*$  singlet state, which is formed by promotion of an electron from the highest occupied molecular  $\pi$  orbital to the  $\sigma^*$  orbital localized on the  $C - F$  bond. The  $\pi\sigma^*$  state has a  ${}^1E_{1g}$  symmetry and is therefore dipole forbidden for a photoinduced transition directly from the  ${}^1A_{1g}$  ground state (not visible in Figure 3.15).

Evidence for an energetically low and optically “dark”  $\pi\sigma^*$  state has been obtained by dispersed fluorescence experiments [138]. After excitation at  $\lambda = 265$  nm to the  $\pi\pi^*$  state, structureless fluorescence (Figure 3.15, red curve) was detected with a maximum intensity at  $\lambda = 360$  nm, a fluorescence quantum yield of 0.05 and a spectral width of  $5500\text{ cm}^{-1}$ . The reasons for the conclusion that the lowest-energy  $\pi\pi^*$  state is not the state from which the fluorescence of HFB originates are the facts that the fluorescence band has no spectral overlap with the absorption spectra,

that the energy difference between the absorption and emission maxima is larger than  $11000\text{ cm}^{-1}$ , and that the full width at half maximum of the absorption is about  $3000\text{ cm}^{-1}$ , whereas that of the dispersed emission is about  $5500\text{ cm}^{-1}$ . All this suggests that the fluorescence appears from a state at lower energy than the excited  $\pi\pi^*$  state. TD-DFT calculations [138] predict a lowest-energy  $\pi\sigma^*$  state to be the emitting state of HFB (see results). Furthermore, the fluorescence band is structureless and the quantum yield is 0.05, which indicates that the population is deactivated mainly (95 %) by an ultrafast radiationless process.

Femtosecond experiments were done in solution [140] and on HFB on metal surfaces [141, 142]. Relevant for this work are only the transient absorption experiments in different solutions done by Kovalenko and coworkers [140]. That paper concentrates on measurements of pentafluorobenzene (PFB). The transient absorption spectrum of PFB was found to exhibit a coherent oscillation, which has been observed over the whole spectrum. Depending on the solvent, different oscillation frequencies were observed. It was found to be  $\hat{\nu}_{Osc} = 94\text{ cm}^{-1}$  in the polar solvent acetonitrile, while in the apolar solvent hexane, the frequency was measured to be  $\hat{\nu}_{Osc} = 86\text{ cm}^{-1}$ . For HFB, the same frequencies for both solvents were found ( $\hat{\nu}_{Osc} = 104\text{ cm}^{-1}$  in acetonitrile and  $\hat{\nu}_{Osc} = 103\text{ cm}^{-1}$  in hexane). Kovalenko *et al.* attributed this oscillations to an electronic coherence between the optically excited ( $\lambda = 265\text{ nm}$ , OE) state and an electron transfer (ET) state.

### 3.3.2 Experimental Setup

A gas mixture containing 1.5 % of HFB (calculated from the vapor pressure; [143]) in helium carrier gas was prepared by flowing the inert gas at 2 bar pressure through the liquid sample stored in a glass reservoir at  $0\text{ }^\circ\text{C}$ . The gases expanded into a differentially pumped electropolished stainless steel vacuum chamber through a solenoid actuated pulsed valve (General Valve Series 9, Iota One) operated with a  $250\text{ }\mu\text{s pulse}^{-1}$  opening time at 50 Hz repetition rate. A molecular beam entered the high vacuum chamber through a 1 mm diameter conical skimmer. Based on previous experiments under similar expansion conditions, the vibrational temperature of the benzene in the cold beam was expected to be in the range of  $T_{vib} \approx (50 \pm 10)\text{K}$ . Hexafluorobenzene (puriss.,  $\geq 99.0\%$  (GC)) was purchased from Sigma-Aldrich and used without further purification.

The optical setup used a regenerative amplified Ti:Sa femtosecond laser system (Clark MXR CPA 2001) producing pulses of 200 fs duration (FWHM) at  $\lambda = 775\text{ nm}$  with pulse energies of  $\approx 1\text{ mJ}$  at 1 kHz repetition rate. Excitation pulses in the range  $215\text{ nm} < \lambda < 235\text{ nm}$  were prepared by sum frequency mixing (SFG) of the compressed ( $< 50\text{ fs FWHM}$ ) output of a home-built non-collinear optical

parametric amplifier (NOPA) with the second harmonic of the Ti:Sa fundamental. Excitation pulses at  $\lambda > 235$  nm were generated by frequency doubling of the NOPA output. Focused pump pulses ( $f = 300$  mm) of  $< 0.2 \mu\text{J pulse}^{-1}$  intersected the molecular beam at right angle halfway between the repeller and extractor of a Wiley-McLaren electrostatic lens assembly. The excited molecules were ionized by a  $\lambda = 775$  nm probe pulse taken from the Ti:Sa laser ( $\approx 25 \mu\text{J}$ ) co-propagating with the pump laser beam. The polarization was set with the electric field vector perpendicular to the plane defined by the molecular beam and the laser beams using zero-order  $\lambda/2$  quartz wave plates.

The  $C_6F_6^+$  cations were detected with a self-made MCP detector. The data were recorded by integrating over the mass peaks for each delay time between the pump and probe/ionization pulses using a computer-controlled linear translation stage (Physik Instrumente M-126CG.). Data at every single step were accumulated over 1250 laser shots.

### 3.3.3 Computational Methods

Time-dependent density functional theory (TD-DFT) calculations were performed with the GAUSSIAN 03 [144] program suite to estimate vertical excitation energies of HFB ( $C_6F_6$ ). Optimizations of the excited states were done with TURBOMOLE [145].

### 3.3.4 Results

#### 3.3.4.1 DFT and TDDFT Calculations

Density functional theory (DFT) and time-dependent density functional theory (TD-DFT) calculations were performed with different functionals (B3LYP, HCTH) and different basis-sets (TZVP, 6-311<sup>++</sup>G<sup>\*\*</sup>) to derive transition energies, structures, electron density distributions, and the characters of the molecular orbitals in both the ground and excited states of HFB.

Figure 3.16 shows the electron density distributions of HFB and benzene calculated for their ground states. While the highest electron density in the case of benzene is found centered around the carbon atoms, the maximum for HFB is shifted to the rim by the strong electronegativity of the fluorine atoms. This so-called “perfluorine effect” energetically stabilizes all orbitals, but has an unequally strong influence on  $\pi$  and  $\sigma$  molecular orbitals. The  $\sigma$  molecular orbitals of interest consist partly of fluorine orbitals, which causes a more efficient stabilization compared to orbitals, which do not consist of fluorine orbitals.

The vertical excitation energies of the  $\pi\pi^*$  states is nearly the same as in benzene, while those for the  $\pi\sigma^*$  states is significantly lower. The calculations in Figure 3.17 show that, because of this shift, the characters of the  $S_1$  states of benzene ( $\pi\pi^*$ ) and HFB ( $\pi\sigma^*$ ) are different. In the figure, the energy of the highest occupied molecular orbital (HOMO) of benzene has been set to zero and all other orbitals are shown with respect to this. To be able to compare benzene and HFB, the difference of the ionization potentials ( $IE_{HFB} - IE_{Benzene} = 0.656$  eV) has been subtracted from the orbitals of HFB. The HOMO for both molecules is a  $\pi$  orbital, whereas the lowest unoccupied molecular orbital (LUMO) in the case of benzene is a  $\pi^*$  orbital and in the case of HFB a  $\sigma^*$  orbital. The calculated vertical excitation energy for the LUMO  $\leftarrow$  HOMO ( $\pi\sigma^*(^1E_{1g}) \leftarrow \pi\pi^*(^1B_{2u})$ ) transition for HFB is 4.6019 eV (269.4 nm). The vertical and adiabatic transition energies for the excited states were calculated by the use of different functionals and are given in Table 3.4.

The results of the geometry optimization for the ground and the excited states of HFB are shown in Figure 3.19. The  $S_0$  state has a highly symmetric (planar) structure of  $D_{6h}$  symmetry, but the  $S_1$  state geometry is strongly distorted ( $C_s$  sym-

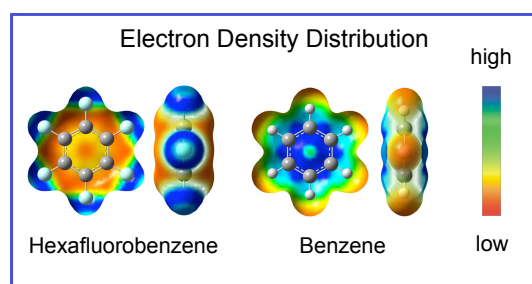


**Figure 3.16:** The electron density distribution of hexafluorobenzene and benzene in comparison. For benzene the highest density is centered around the carbon atoms. The strong electronegativity of the fluorine atoms pulls the electrons towards the rim.

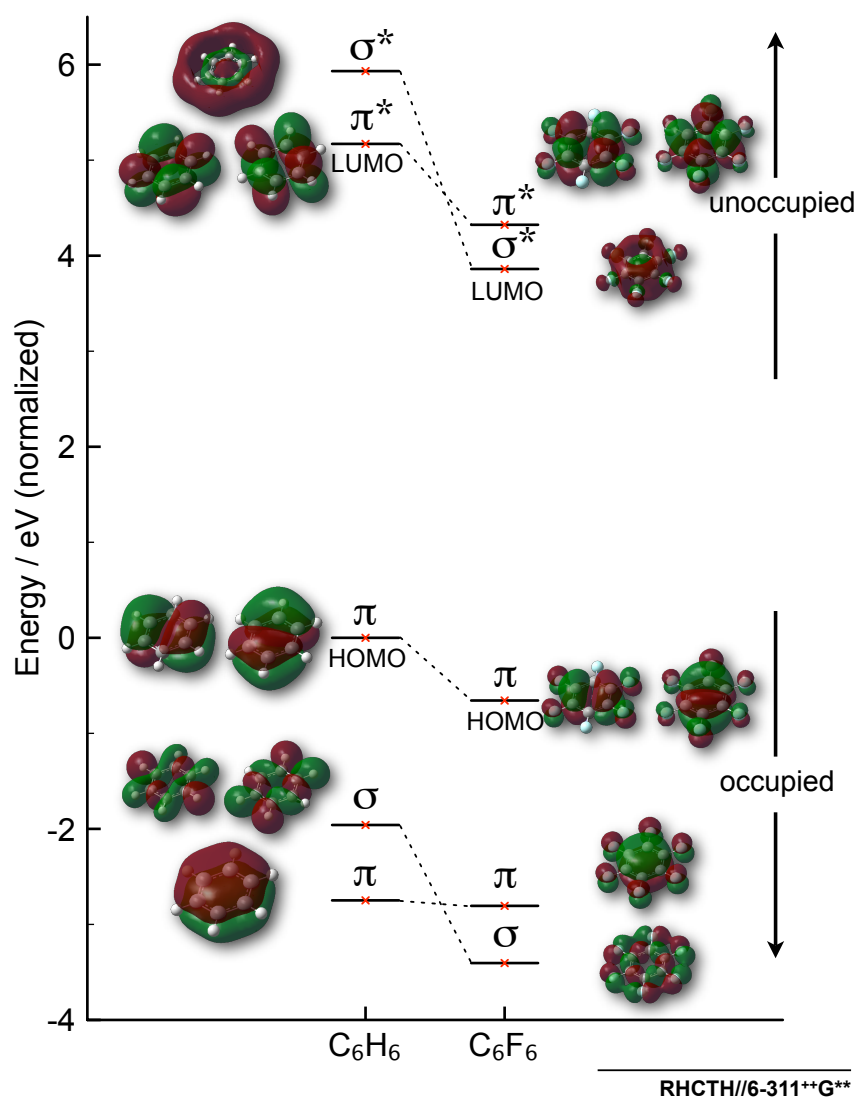


**Figure 3.17:** The vertical excitation energies of the electronic states and corresponding molecular orbitals calculated for benzene ( $C_6H_6$ , left) and HFB ( $C_6F_6$ , right) are shown in comparison. All molecular orbitals of HFB are energetically lower than the corresponding benzene orbitals. Furthermore, orbitals that involve fluorine atomic orbitals ( $\sigma$  and  $\sigma^*$ ) are stabilized even more efficiently.

metry). The  $S_2$  state optimization did not converge, but information was gathered from the optimization steps. The geometry changed with proceeding optimization from a planar structure ( $D_{6h}$ , like the  $S_0$ ) to a structure that is comparable to that of the optimized  $S_1$  state ( $\pi\sigma^*$ ,  $C_s$ ). Four selected optimization steps for the  $S_2$  state are shown in Figure 3.19. With each step the  $S_2$  state becomes more and more like the structure and energy found for the optimized  $S_1$  state. This motion towards the  $S_1$  equilibrium structure is a clear sign for a CI between the  $S_2$  and  $S_1$  state potential surfaces.



**Table 3.4:** Vertical excitation energies ( $\Delta E_{vert.}$ ), energies of the adiabatic vibronic ground states ( $\Delta E_{adiab.}$ ). The oscillator strength  $f$  for the excited states ( $S_1 - S_3$ ) had the same value for all different functionals ( $f = 0$ ).

State	Symm.	$\Delta E_{vert.}^a / \text{eV}$				$\Delta E_{adiab.}^b / \text{eV}$
		PBE1PBE	B3LYP	HCTH	BP86	B3LYP
$S_1 (\pi\sigma^*)$	${}^1E_{1g}$	5.234	5.109	4.602	4.641	4.515
$S_2 (\pi\pi^*)$	${}^1B_{2u}$	5.443	5.335	5.059	5.025	not conv.
$S_3 (\pi\pi^*)$	${}^1B_{1u}$	6.207	6.093	5.896	5.853	5.252

<sup>a</sup>Performed with TD-DFT (GAUSSIAN 03 SUITE).

<sup>b</sup>Optimized with TD-DFT (TURBOMOLE).

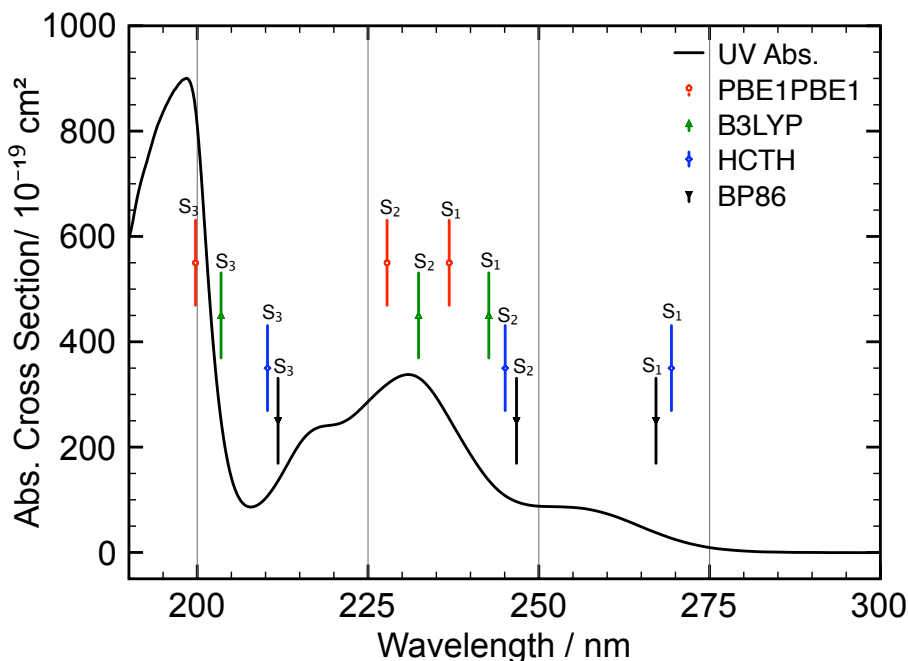


**Figure 3.18:** Vertical excitation energies of the  $S_1$ ,  $S_2$  and  $S_3$  states of HFB. The energies, calculated with different functionals, are compared with the UV absorption spectrum.

When switching from one potential surface to another through a CI, the symmetry of the molecule in the starting state has to be preserved on its way to and through the CI reaching the final state. When the electronic states have different symmetries this can be achieved by a vibronic coupling with an appropriate mode. In this special case of a CI from the  $S_2({}^1B_{2u})$  to  $S_1({}^1E_{1g})$ , an  $E_{2u}$  vibrational mode is needed for the coupling. This is expressed using the irreducible representations below as

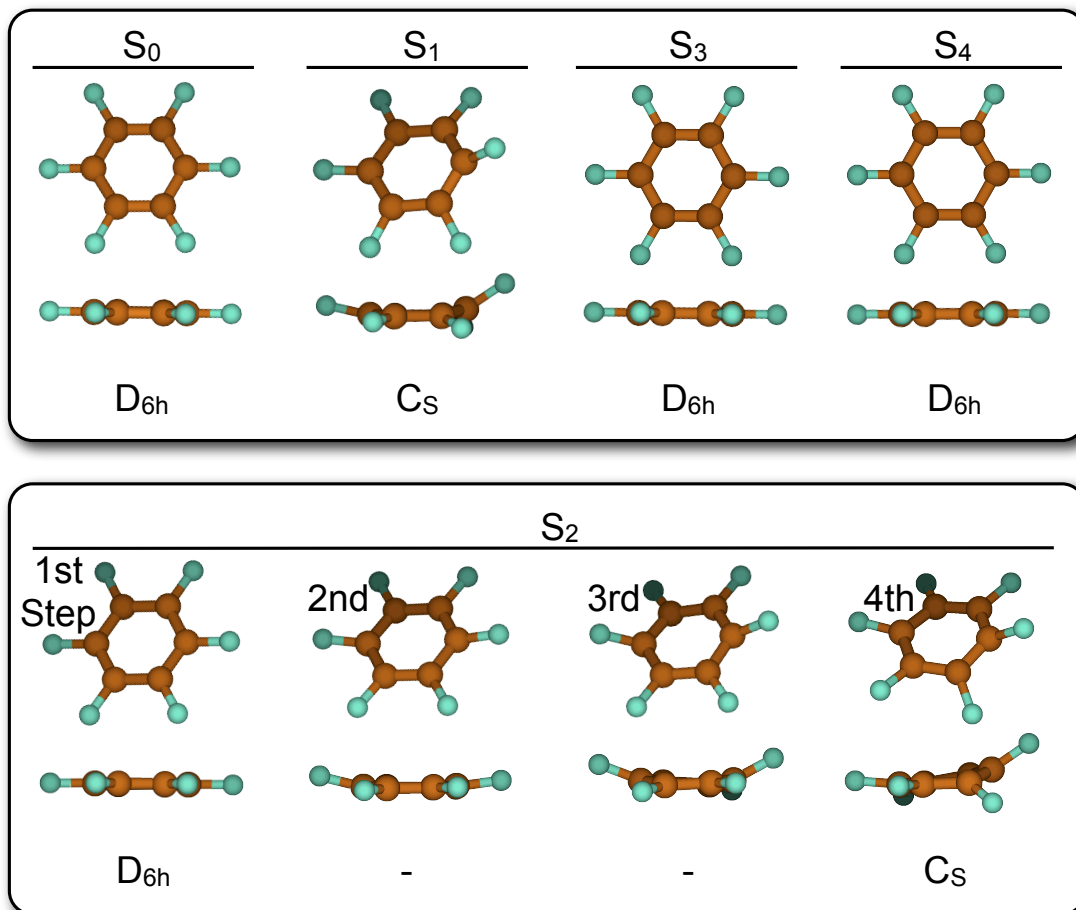


**Figure 3.19:** Geometries for the  $S_1$ ,  $S_2$ ,  $S_3$  and  $S_4$  states. The geometry optimization did not converge for the  $S_2$  state, hence the optimization path is shown step by step (1st - 4th). As can be seen the optimization leads to a geometry that is very similar to the  $S_1$  state geometry. The excited state optimization was done by TD-B3LYP//TZVP calculations with Turbomole program package.

$$\Gamma_{1B_{2u}} = \Gamma_{1E_{1g}} \otimes \Gamma_{\text{coupling}} \quad (3.3)$$

with

$$\Gamma_{\text{coupling}} = \Gamma_{E_{2u}}. \quad (3.4)$$

A normal mode analysis showed that HFB has four  $E_{2u}$  vibrations, which all are “out-of-plane” deformation modes. Using to the notation for benzene [87], these modes are  $\nu_{16a}$ ,  $\nu_{16b}$ ,  $\nu_{17a}$  and  $\nu_{17b}$ . The frequencies of those modes were calculated for the  $S_0$  and  $S_1$  states and are given in Table 3.5. The vibrations are illustrated in Figure 3.20 for the planar ground state, but their motions are similar in the  $S_1$  state.

**Table 3.5:**  $S_2/S_1$  coupling frequencies of the  $E_{2u}$  vibrations calculated for the geometry optimized ground ( $S_0$ ) and first excited ( $S_1$ ) state of HFB.

State	Mode <sup>a</sup>			
	$\nu_{16a}$ cm <sup>-1</sup>	$\nu_{16b}$	$\nu_{17a}$	$\nu_{17b}$
$S_0$	132.48	132.47	635.98	635.95
$S_1$ ( $\pi\sigma^*$ )	90.67	189.93	615.98	607.21

<sup>a</sup>Performed in TURBOMOLE with TD-B3LYP//TZVP accuracy.

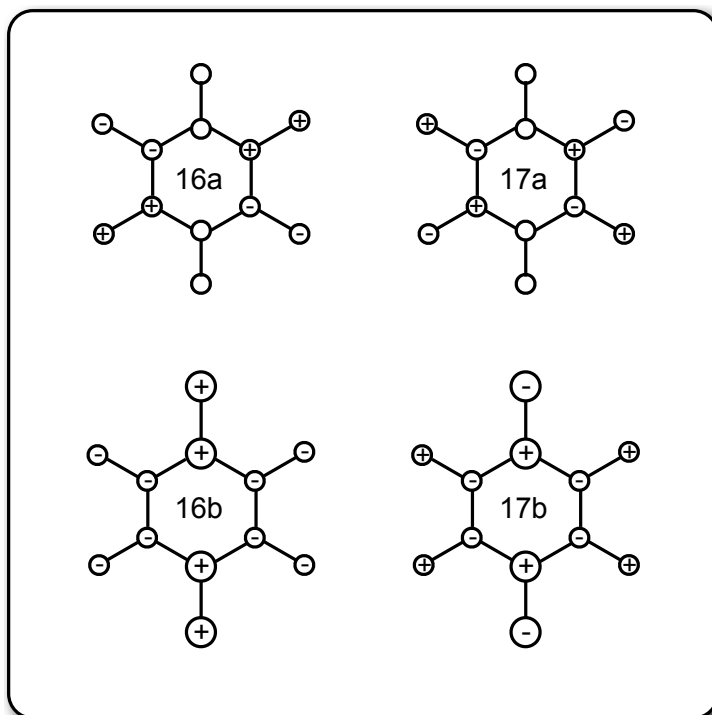


**Figure 3.20:** The normal vibrational modes of HFB with  $E_{2u}$  symmetry.

### 3.3.4.2 Time-Resolved ToF Mass Spectrometry

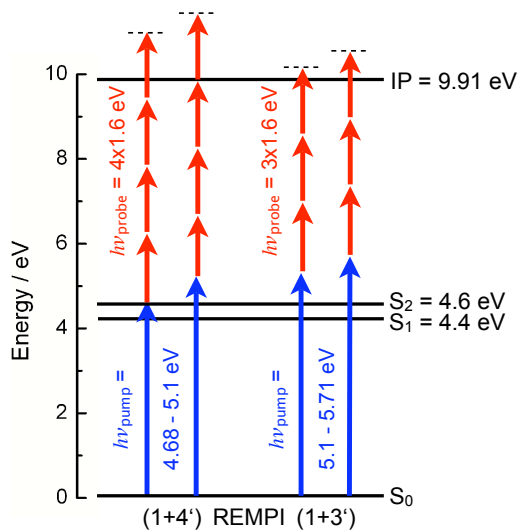


**Figure 3.21:** HFB was excited at wavelengths between  $265 \text{ nm} \geq \lambda \geq 217 \text{ nm}$ . Excited state energies have been estimated from the UV absorption spectrum in Figure 3.15.

Femtosecond pump-probe “time-of-flight” mass spectrometry on HFB was performed over a wide range of excitation energies ( $265 \text{ nm} \geq \lambda_{ex} \geq > 217 \text{ nm}$ ) to elucidate the excited state lifetimes and to unravel the involved deactivation mechanisms. The pump-probe schemes are illustrated in Figure 3.21. The photo-excited HFB molecules were ionized by the fundamental and mass selectively detected as function of the time delay between pump and probe. All measurements are shown in Figure 3.22. In addition, all results are collected in an overview plot (bottom, right). As can be seen, the time profiles exhibit a biexponential behavior. Superimposed on the decay is a coherent oscillation.

**Table 3.6:** Fit Results for the Transient Mass Decay Data of HFB.

$\lambda$ nm	IRF FWHM <sup>a</sup>	$A_1$ norm.	$\tau_1$ ps	$A_2$ norm.	$\tau_2$ ps	$A_D$ norm.	$\tau_D$ ps	$\tilde{\nu}_{osc}$ $\text{cm}^{-1}$	$\phi_{osc}$ $^\circ$
265	0.18	0.17	0.46	0.40	493	0.43	0.69	97	6
260	0.14	0.31	0.54	0.40	403	0.29	1.18	97	-62
255	0.23	0.30	0.23	0.46	132	0.24	1.17	94	5
250	0.20	0.34	0.38	0.34	70.7	0.32	0.96	98	-62
245	0.16	0.46	0.20	0.23	17.5	0.31	0.78	97	-57
240	0.18	0.46	0.21	0.21	16.9	0.34	0.53	97	-63
235	0.20	0.44	0.15	0.19	15.5	0.37	0.52	97	-34
230	0.16	0.34	0.37	0.28	6.76	0.38	0.50	103	-99
226	0.25	0.50	0.14	0.17	6.41	0.33	0.69	103	-78
223	0.25	0.36	0.10	0.08	5.84	0.38	0.36	102	-78
217	0.27	0.16	0.16	0.07	4.67	0.77	0.43	107	-77

<sup>a</sup>Assuming a Gaussian laser profile.

A non-linear fit with two exponentials and a damped oscillation convoluted with the instrument response function revealed a fast decay component,  $\tau_1 = 0.1 - 0.6 \text{ ps}$ , a long-lived  $\tau_2 = 4.5 - 500 \text{ ps}$ , and a damping of the oscillation with  $\tau_D = 0.4 - 1.1$

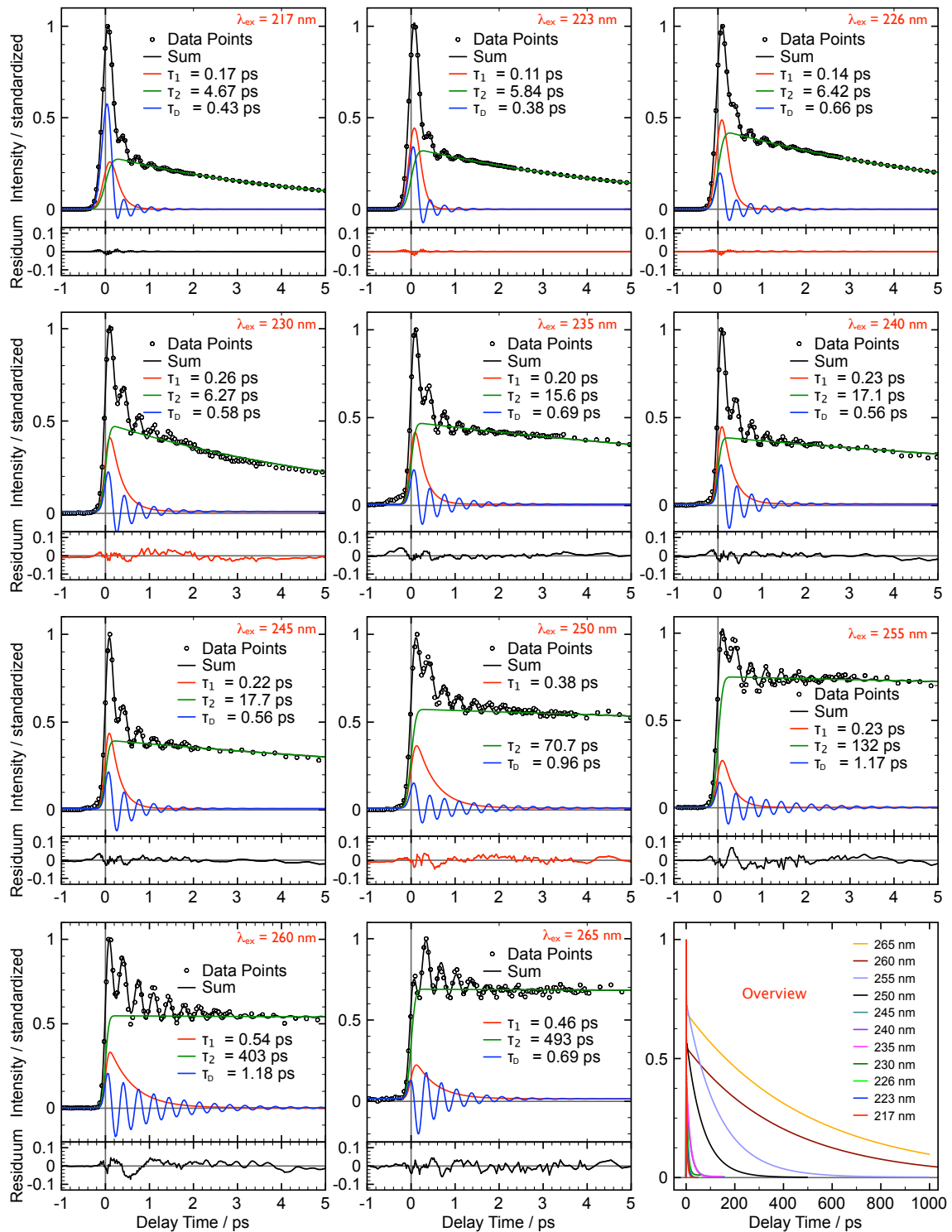


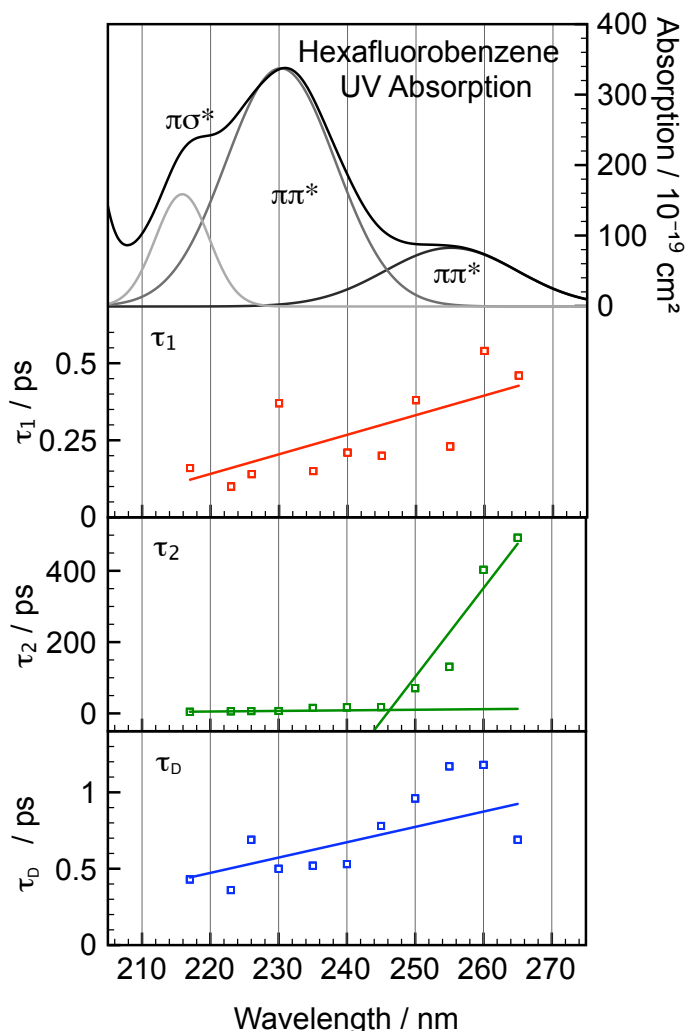
**Figure 3.22:** Time-resolved ToF-MS results probing hexafluorobenzene over a wide range of excitation wavelengths ( $265 \text{ nm} \geq \lambda_{ex} \geq 217 \text{ nm}$ ). The transient profiles are clearly faster with increasing excitation energy. The fit residues are given at the bottom of each panel. An overview over all measurements is shown on the right in the last row.

ps. The oscillation has a frequency corresponding to a period of  $T = 0.31 - 0.34$  ps (equivalent to  $\hat{\nu} = 107 - 97 \text{ cm}^{-1}$ ). Furthermore, the phase angles were practically constant at  $\phi = -2.5 - 0.1^\circ$ . The precise results depend on the excitation wavelength and are collected in Table 3.6.

### 3.3.5 Discussion

The time constants  $\tau_1$ ,  $\tau_2$  and  $\tau_D$  are dependent on the excitation wavelengths. They decrease with increasing excess energy.

While  $\tau_1$  and  $\tau_D$  are decreasing by a factor of two for  $\lambda_{ex} = 265$  to 217 nm,  $\tau_2$  is decreasing dramatically from 500 ps at  $\lambda_{ex} = 265$  nm to 17 ps at  $\lambda_{ex} = 245$  nm. From then on,  $\tau_2$  decreases with approximately the same rate as  $\tau_1$  and  $\tau_D$ . These results are summarized in Figure 3.23 and are compared with the UV absorption spectrum of HFB (bands fitted with Gaussians). As can be seen, the changes in the behavior of  $\tau_2$  are connected with the excited absorption band. This gives evidence for different deactivation pathways depending on the excited electronic state.



In Figure 3.24 shows the potential energy surfaces (PES) of HFB for the ground state ( $^1A_{1g}$ ), the excited states ( $^1E_{1g}$ ,  $^1B_{2u}$ , and  $^1B_{1u}$ ), and the ionic state  $D_0$ . The surfaces are estimated from the

calculated and optimized structures, which were introduced in the previous section. On the basis of the calculations, the structures were determined to be planar for the ground state, both  $\pi\pi^*$  states and the ionic state, they belong to the  $D_{6h}$  point group. In contrast, the  $\pi\sigma^*$  state is highly non-planar and belongs to the  $C_s$  point group. Therefore, the PES of the states with planar structures are nearly vertically

**Figure 3.23:** The decay components  $\tau_1$ ,  $\tau_2$ , and  $\tau_D$  are plotted against the excitation wavelength and compared with the UV absorption spectrum ( $p = 0.5$  mbar). The absorption bands are fitted with Gaussian curves.

on top of each other, while that for the  $\pi\sigma^*$  state is shifted sideways. The curves have to be treated with care insofar as they are not calculated and could differ in detail. Nevertheless, at the present state of research, they are adequate and can explain the observed decay behaviors of the excited HFB molecules.

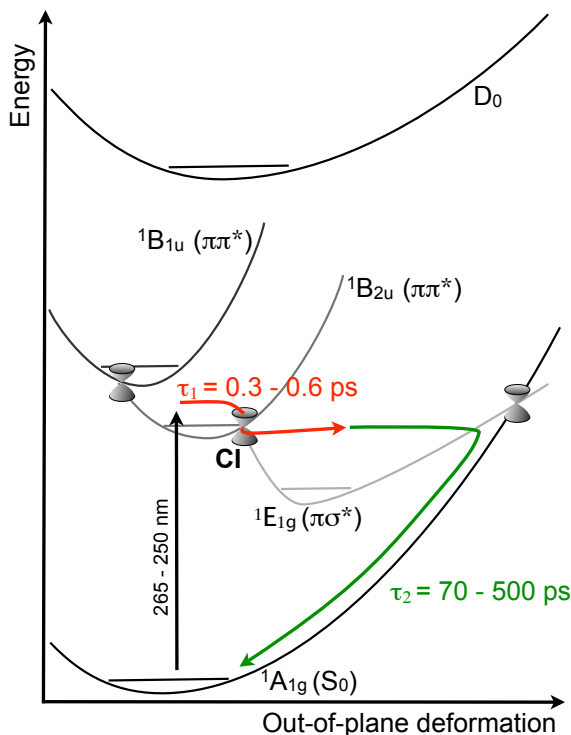


**Figure 3.24: Exciting the  ${}^1B_{2u}$   $\pi\pi^*$  state.**

Excitation pulses at  $\lambda = 265 - 245$  nm initially populate the first  $\pi\pi^*$  state ( ${}^1B_{2u}$ , black arrow), which deactivates within  $\tau_1$  to the energetically lower  $\pi\sigma^*$  state through a non-adiabatic crossing (red arrow). The energy in the  $\pi\sigma^*$  is below a second CI which leads to the ground state, but through tunneling the population leaks down to the ground state in  $\tau_2$  (green arrow).

black, red, and green arrows. The black arrow represents the excitation with low excess energy to the first  $\pi\pi^*$  state. The red arrow indicates the path on the  $\pi\pi^*$  surface to and through the intersection with the energetically lower  $\pi\sigma^*$  surface. The green arrow represents the population, which tunnels down to the ground state.

At higher excitation energies ( $\lambda_{pump} < 245$  nm) the second excited  $\pi\pi^*$  state is reached. The deactivation of this  ${}^1B_{1u}$  state can be described by a two-step

The potential curves in this model have three non-adiabatic crossings (CIs, as indicated by the double cones). These are positioned between both  $\pi\pi^*$  states ( ${}^1B_{1u}$  and  ${}^1B_{2u}$ ), the lower  $\pi\pi^*$  ( ${}^1B_{2u}$ ) and the  $\pi\sigma^*$  ( ${}^1E_{1g}$ ) state, and between the  $\pi\sigma^*$  ( ${}^1E_{1g}$ ) and the ground state ( ${}^1A_{1g}$ ). A wavepacket could travel through all these CIs switching from one potential surface to another, if its energy is high enough.

With excitation wavelengths of  $\lambda = 265 - 250$  nm, the first  $\pi\pi^*$  state is populated and the deactivation process can be explained with the model in Figure 3.24. The  ${}^1B_{2u}$  excited molecules deactivate through the CI between the  $\pi\pi^*$  state and the  $\pi\sigma^*$  state on a time scale of  $\tau_1 = 0.3 - 0.6$  ps. Now on the  $\pi\sigma^*$  state, the energy is insufficient to pass the CI to the ground state, but population tunnels through the potential barrier on the way to the CI and leaks down to the ground state in  $\tau_2 = 36 - 500$  ps. This is explained schematically in Figure 3.24 by the



mechanism, which is shown in Figure 3.25, or by a mechanism with three steps. In the two-step mechanism the excited HFB deactivates first to the  ${}^1E_{1g}$  state in  $\tau_1 = 0.1 - 0.3$  ps (red arrow), followed by the relaxation to the  ${}^1A_{1g}$  ground state in  $\tau_2 = 4.5 - 17$  ps (green arrow). In the three-step mechanism the molecule first relaxes to the lower  $\pi\pi^*$  state of  ${}^1B_{2u}$  symmetry and in the second step to the  ${}^1E_{1g}$  state. Both steps would then be described with one exponential decay, because the underlying processes are too rapid to keep them apart. The third step is the same as in the two-step mechanism. The two-step mechanism involves the same vibrational coupling modes of  $e_{2u}$  symmetry for the CI between the  ${}^1B_{1u}$  and  ${}^1E_{1g}$  states, whereas the CIs in the three-step mechanism involve modes of different symmetries.

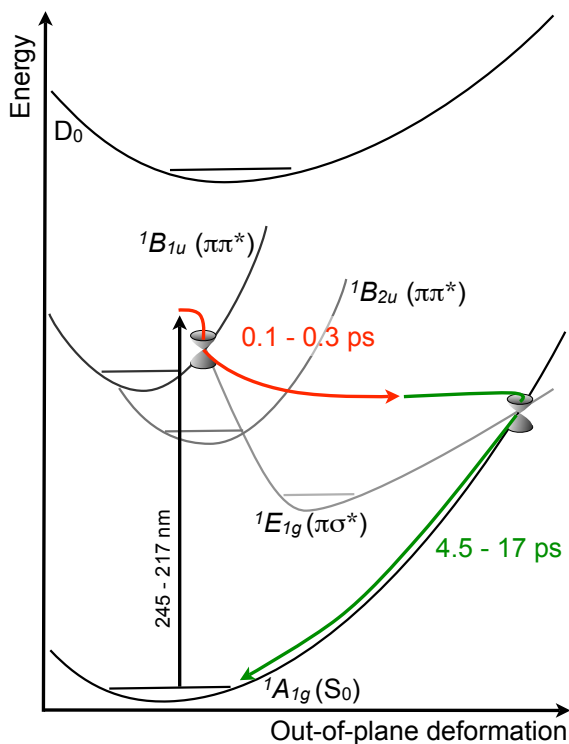


**Figure 3.25: Exciting the  ${}^1B_{1u} \pi\pi^*$  state.** The principles are the same. After excitation of the second  $\pi\pi^*$  state is the population transferred to the  $\pi\sigma^*$  with a much higher excess energy. The energy equals now the energy that is needed to pass directly through the CI and the ground state is reached much faster within  $\tau_2 < 17$  ps.

also conceivable for HFB after excitation to the 2nd  $\pi\pi^*$  state ( ${}^1B_{1u}$ ). The results of the measurements give no hint for such an ultrafast process. Nevertheless, one

$\tau_1$  is two times faster than the corresponding value for  ${}^1B_{2u} \pi\pi^*$  state excitation at lower energy. This can be explained by the fact that, with increasing energy, the amount of accessible active coupling modes is increasing dramatically. The deactivation of the  $\pi\sigma^*$  state to the ground state is significantly more effective, because the energy which has been deposited into the  $\pi\sigma^*$  state is higher than what is needed to pass the CI to  $S_0$ .

From  $S_2(\pi\pi^*)$  excited benzene, it is known that the molecules undergo an ultrafast deactivation directly back to the ground state via a CI between these two states in 0.05 ps. The determination of the time scale for this process has been done in this work and the results were described in Section 3.1. Such an alternative deactivation path is

also conceivable for HFB after excitation to the 2nd  $\pi\pi^*$  state ( ${}^1B_{1u}$ ). The results of the measurements give no hint for such an ultrafast process. Nevertheless, one

should not forget such possibility. It would outspeed the time resolution (0.2 ps Gaussian FWHM).

All measurements show a superimposed oscillation with a frequency that corresponds to  $\hat{\nu} = 97 - 107 \text{ cm}^{-1}$ . There are several explanations for their appearance in femtosecond experiments, and these are listed and stated in the following.

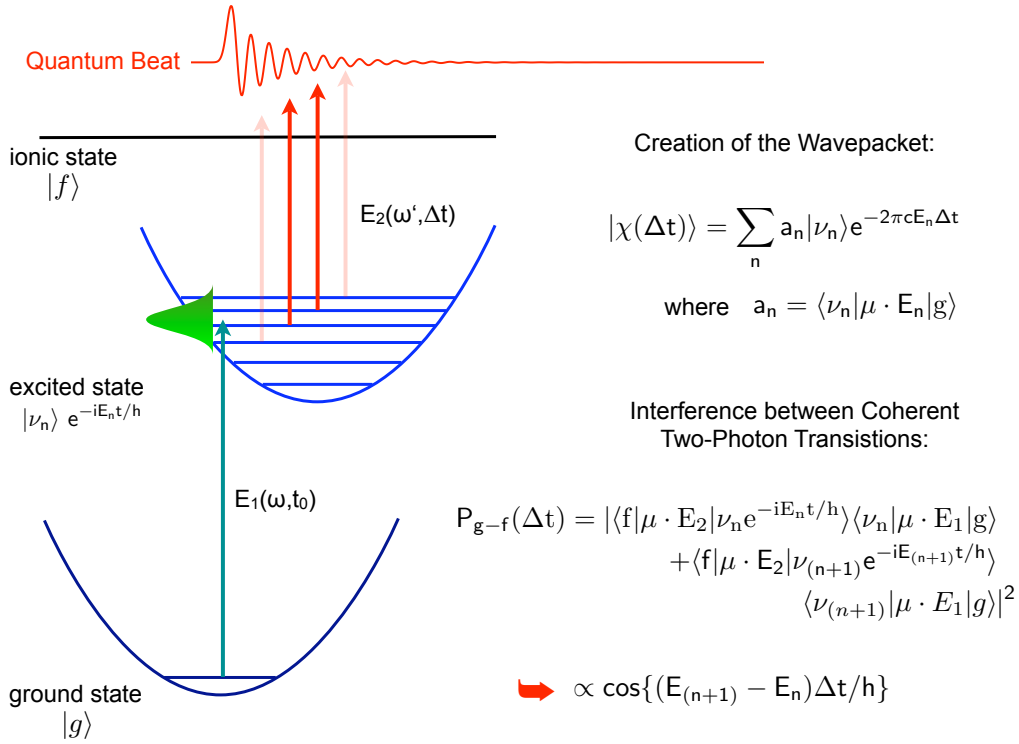


**Figure 3.26:** A coherent oscillation occurs, if the pump pulse  $E_1$  excites more than one vibrational mode simultaneously. The in the electronic state placed wavepackets interfere with each other and a time-dependent pattern is formed, like it is known from light scattering at a number of slits. As a result the excited state dynamics are superimposed by the coherent vibronic oscillation. The phenomenon is named “Quantum Beat”.

1. The coherent excitation of a vibronic two-level system leads to a destructive and constructive interference of the excited state wavepackets [146, 9] (so-called “quantum beat”). This can be observed experimentally as an oscillating pump-probe signal, only if the vibrational modes are excited with a spectrally broad pump pulse simultaneously, and if the time-resolution of the experiment is significantly faster than the time period of the superimposed oscillation (Figure 3.26). The frequency corresponds to the energy gap between the

vibrational modes and is given by  $\omega = (E_2 - E_1)\Delta t/h$  (Figure 3.26).

The frequency of such a quantum beat depends on the energy difference of the coherently excited vibronic states. With increasing excitation energy, the beat frequencies should become lower because of the anharmonicity. The observed oscillations after excitation of HFB show little dependence on the excitation wavelengths. This leads to the conclusion that the oscillations do not represent quantum beats in the initially excited state.

2. A coherent oscillation can also occur because of excitation of anharmonically coupled vibrational modes. This has been reported in the literature for many molecules. However, the oscillations should disappear rapidly with increasing the excitation energy because of the increasing density of states.

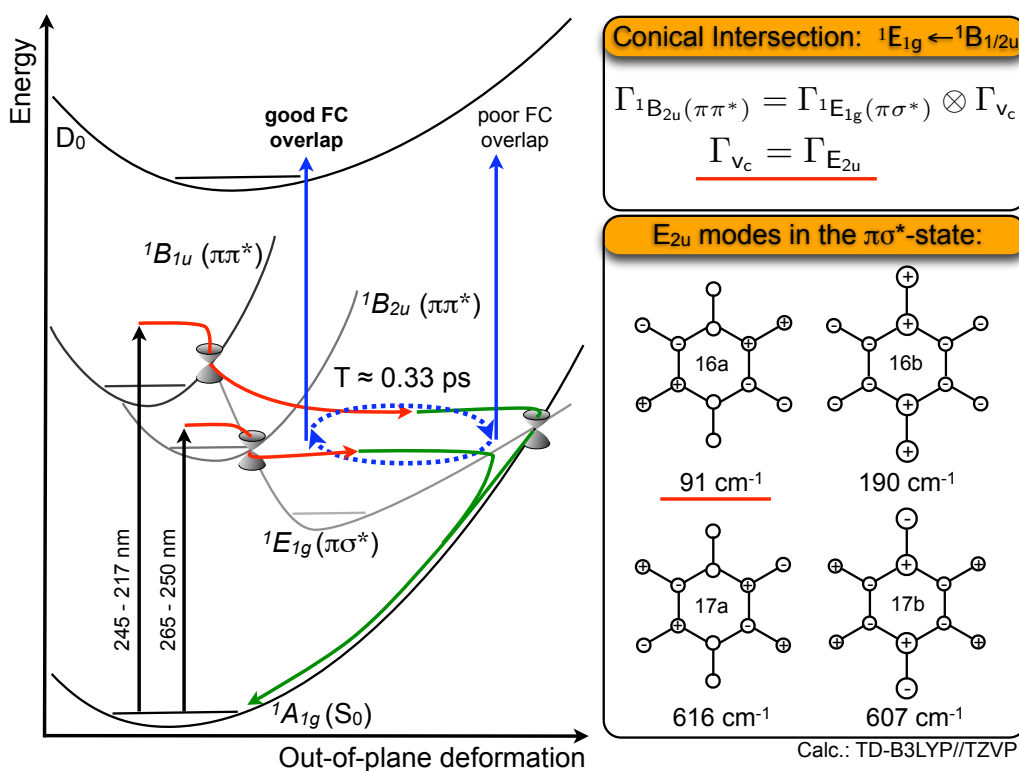


**Figure 3.27:** A coherent oscillation superimposes the decay profiles over the whole range of excitation wavelengths ( $265 \text{ nm} \geq \lambda_{ex} \geq 217 \text{ nm}$ ). The coupling mode  $\hat{\nu}_c = 97 - 107 \text{ cm}^{-1}$ , which is activated when passing through the CI, has different Frank-Condon overlap integrals while swinging from maximum to minimum displacement. The altered Frank-Condon factors can be observed directly in the transient mass spectra as oscillating ion yields.

- Vibrational coherence persists throughout the course of time of a photochemical reaction and is observed in the product. This case is the most interesting because it elucidates the role of nonstationary states in the ultrafast reaction dynamics.

In the case of HFB, after excitation of the  $\pi\pi^*$  state, the molecules deactivate through the CI to the energetically lower  $\pi\sigma^*$  state. To allow the switch from one potential surface to the other, the symmetry of the wave function has to be conserved. For the  ${}^1B_{2u}$   $\pi\pi^*$  and the  ${}^1B_{1u}$   $\pi\pi^*$  states a coupling mode of  $e_{2u}$  symmetry is needed for a CI with the  ${}^1E_{1g}$   $\pi\sigma^*$  state. As described in Section 3.3.3, these modes are antisymmetric out-of-plane modes so that the condition for an observation in the product state is fulfilled. The calculated frequencies are 91, 190, 616, and 607  $\text{cm}^{-1}$  for modes 16a, 16b, 17a and, 17b, respectively. The 16a mode (91  $\text{cm}^{-1}$ ) is the only mode for which the energy matches the observed oscillation in HFB ( $\approx 100 \text{ cm}^{-1}$ ). Similar conclusions were drawn by Okuyama et al. [147] for the coupling between the  $\pi\pi^*$  and the  $\pi\sigma^*$  states in 1,2,4,5-tetrafluorobenzene (TFB).

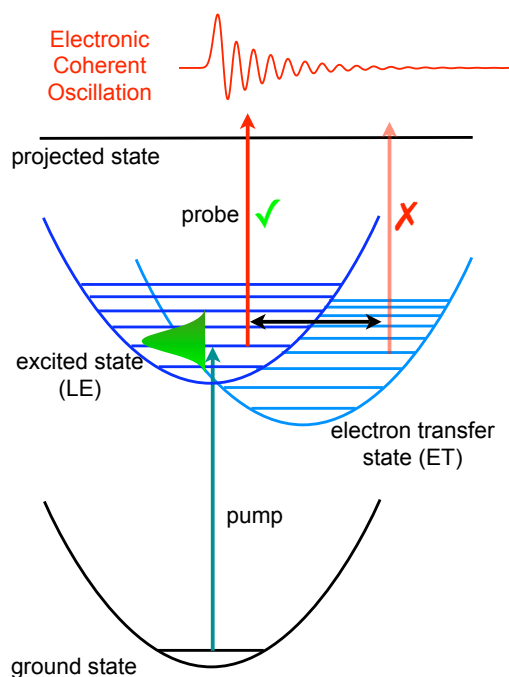


**Figure 3.28:** The pump pulse coherently excites the LE state and the ET state, which are nearly degenerated in energy. Because of the different properties of the states it is possible to detect the oscillation. In the case of mass spectrometry this would be the different Franck-Condon overlaps for the ionization.

- If the system consists of two or more energetically close-by electronic states, which could be excited with a spectral broad laser pulse, the population

will oscillate coherently between the neighboring electronic states (electronic quantum beat). Kovalenko and coworkers [140] observed coherent oscillations investigating TFB, PFB, and HFB with transient absorption. The molecules were excited in acetonitrile or hexane at  $\lambda_{pump} = 265$  nm and were probed time-delayed by a supercontinuum pulse (334 - 1072 nm). The main feature was a strong oscillatory behavior of the signal over the full probe spectral range. In the case of TFB ( $\hat{\nu}_{hex} = 80$  cm<sup>-1</sup>,  $\hat{\nu}_{ACN} = 87$  cm<sup>-1</sup>) and PFB ( $\hat{\nu}_{hex} = 86$  cm<sup>-1</sup>,  $\hat{\nu}_{ACN} = 94$  cm<sup>-1</sup>) the oscillation frequency was depending on the solvent, but for HFB ( $\hat{\nu}_{hex} = 103$  cm<sup>-1</sup>,  $\hat{\nu}_{ACN} = 104$  cm<sup>-1</sup>) it was not. They concluded that the oscillations derive from a coherent electron transfer (ET) process from the local excited (LE) state to the ET state, which is shown in Figure 3.28. The LE and ET states have been considered to be nearly degenerate. Their quantum chemical calculations showed that the vibrational frequency of the reaction mode, which is associated with the ET state, is below 100 cm<sup>-1</sup> and represents the oscillatory feature in their results.

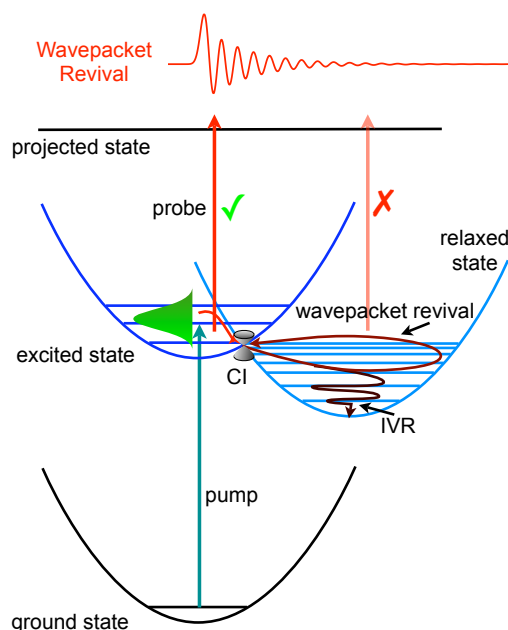


**Figure 3.29:** The pump pulse creates a wavepacket on the excited state. The wavepacket relaxes through the CI to the energetically lower state. When the motion of the wavepacket are conserved, it can travel back up to the starting state through the same CI. But an effective coupling to low-frequency modes (IVR) is decreasing the probability for a revival to almost zero. An oscillation occurs, when the electronic states have different ionization transition moments.

In this thesis, however, no dependence of the oscillation frequency for different excitation energies was observed. On the basis of Figure 3.28, it is noticeable that there should be a shift in frequency, if the excitation energy rises or

declines, because of the different energy spacings of the involved vibrations in the two electronic states. Therefore, a shift of frequency is anticipated, but was not observed. Furthermore, the excited state lifetimes of the  $\pi\pi^*$  states are two times shorter than the damping  $\tau_D$  of the oscillation, therefore those states cannot be involved in the oscillation.

5. Eventually, it is well known that, if only a few coupled vibrational modes are taken into account, a wavepacket placed on the excited PES returns to its starting state, even if it has relaxed to a slightly energetically lower state through a conical intersection. This happens in distinctive time periods and would be observed in the experiment as an oscillating signal, if the two states have different ionization probabilities. But in a system like HFB, revival of the wavepacket is unlikely, because after relaxation to the  $\pi\sigma^*$  state a large number of coupled vibrations become active, which dissipate the energy very efficiently through IVR (see Figure 3.29).

### 3.3.6 Conclusion and Summary

Measurements over a broad excitation range from  $\lambda_{ex} = 265$  to 217 nm have been performed on HFB. These showed that the electronic dynamics in the first and second excited states can be described by two exponential decays and a superimposed oscillation. The fast decay component  $\tau_1$  mirrors the relaxation from the initially excited  $\pi\pi^*$  state to the energetically lower  $\pi\sigma^*$  state. Furthermore,  $\tau_1$  declined linearly with rising excitation energy. The second component  $\tau_2$  characterizes the decay of the  $\pi\sigma^*$  state back to the ground state. However, in contrast to  $\tau_1$ ,  $\tau_2$  exhibits a different behavior over the excitation range. At low excitation energies,  $\tau_2$  is slow (500 ps), but at  $\lambda_{ex} < 245$  nm a dramatic decrease of  $\tau_2$  has been observed. This is because the CI from the  $\pi\sigma^*$  state to the ground state can now be overcome.

The origin of the superimposed oscillation has been discussed in Subsection 3.3.4. First, the oscillation frequency of  $\hat{\nu} = 100 \pm 5 \text{ cm}^{-1}$  does not depend significantly on the excitation wavelength. This seems to exclude the option of coherently excited electronic oscillations. Second, the damping of the oscillation  $\tau_D = 0.4 - 1.2 \text{ ps}$  is at least two times slower than the deactivation of the excited  $\pi\pi^*$  states and therefore those states cannot be involved in the oscillation. Last, the calculated frequency of the CI reaction mode  $\hat{\nu}_{16a} = 91 \text{ cm}^{-1}$  is very similar to the observed frequencies of the oscillations. Careful balancing of these arguments leads to the conclusion that the coherent vibrational oscillation in the product state provides the correct explanation.

## 3.4 Pyrrole

### 3.4.1 Introduction

The UV absorption spectrum of pyrrole shown in Figure 3.30 is determined by a strong double-peaked and otherwise unstructured band [148, 149, 150], with intensity maxima at  $\lambda = 210$  and  $\lambda = 205$  nm. Another strong band is located around  $\lambda = 165$  nm, which is not shown. The peak centered at  $\lambda = 210$  nm is broadened by a shoulder at  $\lambda = 217$  nm. The assignment of the band was challenging, but by means of electron energy-loss [151], photoelectron spectroscopy [152] and REMPI experiments [153] some expertise could be acquired. Accompanying theoretical calculations [151, 154, 155] determined the electronic structure and it was possible to assign the band at  $\lambda = 210$  nm to an electronic state with  $1^1B_2$  symmetry [156]. Additionally, the second electronic state with  $2^1A_1$  symmetry was found nearby ( $\lambda = 205$  nm), superimposing the former in the UV spectrum. The two states have different oscillator strengths, with a ratio of  $\approx 11 : 2$ .

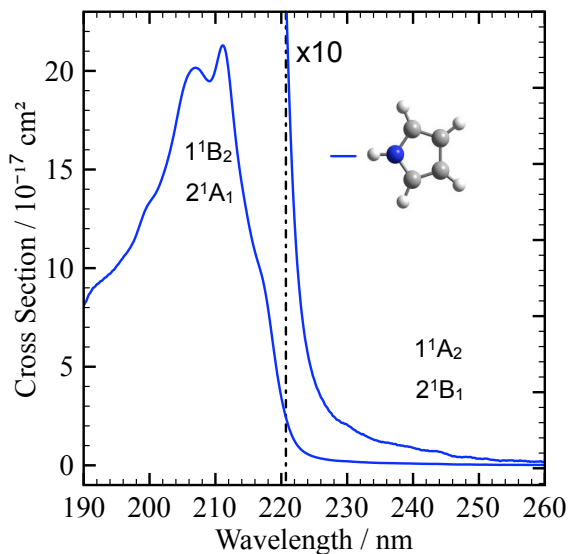


**Figure 3.30:** Gas phase UV absorption spectrum of pyrrole at  $p = 0.5$  mbar.

Another weak band in the UV spectrum, only visible after magnification by a factor of 10, has its origin around  $\lambda = 260$  nm. It is controversially discussed, whether it originates from an excited valence bond state with  $2^1A_1$  symmetry or a combination of two Rydberg like states ( $1^1A_2$  and  $2^1B_1$ ); a final assignment is still missing. Its very low oscillator strength hints at the electric dipole forbidden Rydberg states, which obtain intensity through vibronic coupling from the  $1^1B_2$  (or  $1^1A_1$ ) state. A  $b_1$  ( $a_2$ ) symmetry mode has been suggested as vibronic coupling mode [155, 156]. Both correspond to “out-of-plane” bending modes. Another hint was given by the calculated electron density distribution, shown in Figure 3.31, which despite of its valence character is very diffuse in the shown  $\pi\sigma^*$  states, which is an attribute of Rydberg states.

Early calculations performed by Domcke and Sobolewski [25, 24] showed that a stretching of the  $N-H$  bond results in a non-binding character of the  $\pi\sigma^*$  states. They predicted CIs with the energetically higher  $\pi\pi^*$  states, as well as with the ground state. The results of their calculations are given in Figure 3.32, where a cut

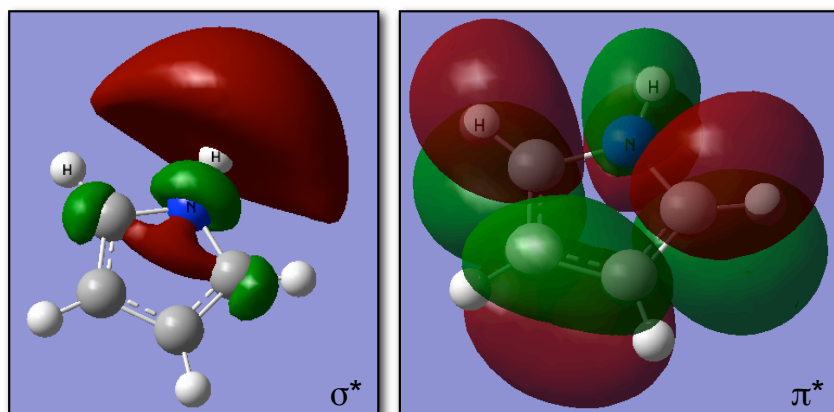


**Figure 3.31:** Electron density distribution of the first  $\sigma^*$  and  $\pi^*$  orbitals in pyrrole. The diffuse distribution of the  $\sigma^*$  orbital and the high density outside of the ring are typically for a Rydberg-like state.

through the calculated PES along the  $N-H$  stretching coordinate is shown. The funnels between the  $\pi\pi^*$  states and the  $\pi\sigma^*$  states are not shown, because the  $N-H$  stretching mode is not involved in that coupling. The intersections with the ground state are found at an  $N-H$  distance of  $\approx 1.85$  and  $\approx 1.95$  Å.  $\pi\sigma^*$  excited pyrrole can deactivate through the CIs with the ground state, or the repulsive gradient along the  $N-H$  stretching coordinate leads to a dissociation of the  $N-H$  group. Because of the steep potential of the  $\pi\sigma^*$  state, these processes take place on an ultrafast timescale and therefore the relaxation is very efficient and competing processes are suppressed.

By absorption at  $\lambda = 217$  nm, pyrrole is excited to the  $\pi\pi^*$  state with  $1^1B_2$  symmetry. In the literature, two competing deactivation channels for the  $\pi\pi^*$  states can be found. First, a direct excited state deactivation down to the ground state can occur, which involves out-of-plane ring distortion motions [157]. Second, there is a two-step mechanism, where the  $\pi\pi^*$  states relax to one of the energetically lower  $\pi\sigma^*$  states, which then, as discussed above, relax further to either the ground state or the molecule dissociates [158, 159].

Analogous mechanisms were postulated to be responsible for the electronic relaxation of biologically important molecules like amino acids [32, 33] and the DNA bases [160, 161]. Excited state intramolecular H-atom transfer (ESIHT) [162, 163] as well as intermolecular H atom exchange in H-bond-bridged systems are other mechanisms, which are discussed for ultrafast relaxation in these systems [33, 164, 165, 166, 167].

It was not clear for some time, whether the repulsive character of the  $\pi\sigma^*$  state only could be confirmed indirectly or whether the resulting H-atom elimination could



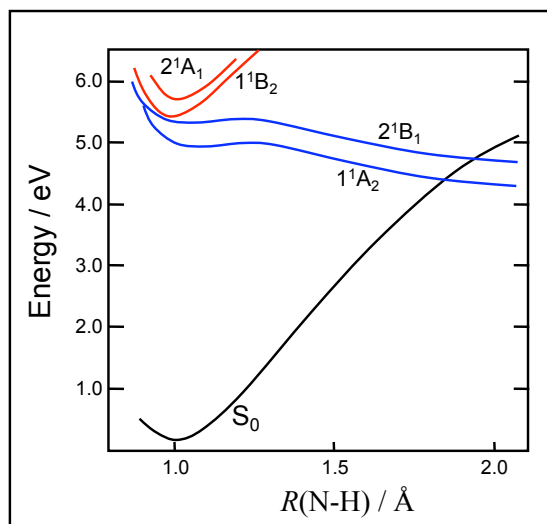


**Figure 3.32:** Schematic Plot of the for the relaxation responsible potential curves. The potential energies for the  $\pi\sigma^*$  ( $1^1A_2$  and  $2^1B_1$ ) and  $\pi\pi^*$  ( $1^1B_2$  and  $2^1A_1$ ) of pyrrole along the  $N-H$  bond stretching were calculated by Domcke and Sobolewski [25].

also be observed directly. Experiments performed in our group have demonstrated H-atom detachment from pyrrole in the excited  $\pi\sigma^*$  state and the  $\pi\pi^*$  state by using photofragment velocity map imaging [26] for the first time. One-color experiments at  $\lambda = 243.1$  nm produced a dominant H-atom contribution (76 %) with a narrow kinetic energy distribution, which was assigned to a rapid, direct  $N-H$  bond dissociation, in agreement with the repulsive character of the  $\pi\sigma^*$  state. A second broad kinetic energy distribution with a maximum at smaller velocities was found. These slower H-atoms were attributed to fragmentation of molecules in the ground state  $S_0$  after internal conversion through the predicted CI. Methyl substitution of the H-atom in the  $N-H$  group leads to the disappearance of the fast component; this confirmed that the fast component is, in fact, due to the direct dissociation of pyrrole in the  $\pi\sigma^*$  state along the  $N-H$  bond. Similar conclusions were drawn from earlier photofragment translational spectroscopy [168] experiments and, later, from Rydberg-imaging translational spectroscopy of the H atom in the group of Ashfold [169], who were able to prove that upon excitation, the  $1^1A_2$  state borrows intensity by vibronic coupling through  $\nu_{10}(a_2)$ ,  $\nu_{15}(b_2)$ ,  $\nu_{22}(b_1)$ , and  $\nu_{23}(b_1)$  from nearby states of  $A_1$ ,  $B_1$ , and  $B_2$  symmetry.

Lippert *et al.* performed two-color pump-probe mass spectrometry experiments with femtosecond laser pulses probing H-atoms after photoinduced dissociation. Two channels with the time constants  $\tau_1 \approx 0.1$  ps and  $\tau_2 \approx 1.1$  ps of subsequent H-atom formation channels were found and assigned to the direct  $N-H$  dissociation along

the  $N-H$  coordinate in the  $\pi\sigma^*$  state and, after passing through the CI, indirect  $N-H$  dissociation of the vibrational hot  $S_0$  ground state. The transient parent ion (pyrrole<sup>+</sup>) signal was decreasing faster than the time resolution of the experiment and a decay rate was not determined. The corresponding pyrrolyl radical mass channel was completely absent and it was concluded that the detection efficiency was too low due to a rather high ionization potential and a poor Franck-Condon overlap.

In this thesis, further femtosecond spectroscopy has been performed on pyrrole to investigate the excited state relaxation mechanisms in more detail. Especially, the PEI experiments shed more light on the involved electronic and vibrational states after excitation of the  $\pi\pi^*$  states.

### 3.4.2 Experimental Setup

A gas mixture containing  $\approx 1\%$  pyrrole in helium carrier gas was prepared by flowing the inert gas at 2 bar pressure through the liquid sample stored in a glass reservoir at 0 °C. The gases expanded into a differentially pumped electropolished stainless steel vacuum chamber through a solenoid actuated pulsed valve (General Valve Series 9, Iota One) operated with a 250  $\mu\text{s}$  pulse<sup>-1</sup> opening time at 50 Hz repetition rate. The molecular beam then entered the high vacuum chamber through a 1 mm diameter self-made conical skimmer. Based on previous experience under similar expansion conditions, the vibrational temperature of the pyrrole in the cold beam is expected to be in the range of  $T_{vib} \approx (50 \pm 10)\text{K}$ . Pyrrole (prium,  $\geq 97.0\%$  (GC)) from Sigma-Aldrich was distilled to remove aggregates due to self polymerization before it was used.

The optical setup employed a regenerative amplified Ti:Sa femtosecond laser system (Clark MXR CPA 2001) producing pulses of 200 fs duration (FWHM) at  $\lambda = 775$  nm with pulse energies of  $\approx 1$  mJ at 1 kHz repetition rate. The excitation pulses in the range of  $215\text{ nm} < \lambda < 235\text{ nm}$  were prepared by sum frequency mixing (SFG) of the compressed ( $< 50$  fs FWHM) output of a home-built non-collinear optical parametric amplifier (NOPA) with the second harmonic of the Ti:Sa fundamental. Focussed pump pulses (lens,  $f = 300$  mm) of  $< 0.2\ \mu\text{J}$  pulse<sup>-1</sup> intersected the molecular beam at right angle halfway between the repeller and extractor of a Wiley-McLaren electrostatic assembly. The excited molecules were ionized by a  $\lambda = 775$  nm probe pulse taken from the Ti:Sa laser ( $\approx 25\ \mu\text{J}$ ) propagating with the pump laser beam. The polarization was set with the electric field vector perpendicular to the plane defined by the molecular beam and the laser beams using zero-order  $\lambda/2$  quartz wave plates.

The  $C_4N_1H_5^+$  cations were detected with a home-built MCP detector. The data were recorded by integrating over the mass peaks for each delay time between the pump and probe/ionization pulses using a computer-controlled linear translation stage (Physik Instrumente M-126CG.). At every single step, the signal was accumulated over 1250 pulses. In the PEI experiments, the electrons were detected by a MCP phosphorescence screen detector (40 mm diameter, Photek). The back of the screen was imaged with a CCD camera (1600 × 1200 pixel, pco). The images were accumulated over 200k laser shots for each time-delay. A centroiding algorithm was used to improve the detection sensitivity, spatial resolution, and to discriminate against noise. A mu-metal shield was installed in the flight tube to suppress outer static and dynamic magnetic fields of low frequency.

### 3.4.3 Computational Methods

Density functional theory (DFT) calculations were performed with the GAUSSIAN 03 [144] suite of programs to estimate the vibrational frequencies and vertical excitation energies of pyrrole in the ground state and ionic state.

### 3.4.4 Results

This section reports the results on pyrrole, which were obtained by quantum chemical calculations, time-dependent ToF-MS, and PEI.

#### 3.4.4.1 DFT Calculations

The calculations introduced in this subsection focus on pyrrole and on single positively charged pyrrole ions. Especially for the interpretation of the measured PE distributions, it is necessary to know the symmetries of the involved states, their structures, and their vibrational frequencies. Therefore, the ground and ionic state structures were optimized and vibrational frequencies were calculated. Furthermore, the excited state vertical transition energies were calculated for the neutral and the ion. The calculations were performed with the Gaussian Program Suite [144] using density functional theory and RHCTH and PBE1PBE functionals, respectively.

The calculations show that the ground states of neutral pyrrole and the single positively charged pyrrole ion are both planar and belong to the  $C_{2v}$  point group. This was proved experimentally for the ground state by microwave spectroscopy [170].

**Table 3.7:** Harmonic vibrational frequencies of the ground state of neutral and ionic pyrrole obtained by the HCTH//6-311<sup>++</sup>g(3df,3pd) method.

Mode	Symmetry	$\omega$ in $\text{cm}^{-1}$		Intensity in a. u.	
		Neutral	Ion	Neutral	Ion
$\nu_1$	$a_1$	3618.1	3599.7	46.95	199.81
$\nu_2$	$a_1$	3217.8	3253.8	0.03	17.18
$\nu_3$	$a_1$	3196.1	3231.8	8.09	9.12
$\nu_4$	$a_1$	1454.4	1531.5	9.92	3.55
$\nu_5$	$a_1$	1367.5	1457.2	2.96	31.67
$\nu_6$	$a_1$	1131.3	1167.5	1.00	2.52
$\nu_7$	$a_1$	1065.9	1086.5	5.58	0.13
$\nu_8$	$a_1$	1007.4	1067.3	31.12	35.32
$\nu_9$	$a_1$	875.1	879.1	0.18	1.00
$\nu_{10}$	$a_2$	848.9	949.0	0.00	0.00
$\nu_{11}$	$a_2$	653.7	830.1	0.00	0.00
$\nu_{12}$	$a_2$	606.5	494.6	0.00	0.00
$\nu_{13}$	$b_2$	3212.6	3241.2	7.86	25.59
$\nu_{14}$	$b_2$	3184.4	3226.7	3.67	11.05
$\nu_{15}$	$b_2$	1525.5	1474.8	0.76	106.07
$\nu_{16}$	$b_2$	1396.4	1306.7	6.43	11.84
$\nu_{17}$	$b_2$	1280.0	1265.9	0.49	5.92
$\nu_{18}$	$b_2$	1133.1	1038.6	1.01	14.53
$\nu_{19}$	$b_2$	1039.0	992.2	24.00	1.51
$\nu_{20}$	$b_2$	851.4	746.0	1.24	23.12
$\nu_{21}$	$b_1$	801.1	877.6	3.37	6.10
$\nu_{22}$	$b_1$	706.1	727.3	158.44	76.07
$\nu_{23}$	$b_1$	619.4	472.1	0.25	37.90
$\nu_{24}$	$b_1$	443.9	658.8	58.68	57.39

In our studies, we were mainly interested in the coupling mechanisms between the mentioned  $\pi\pi^*$  states and the  $\pi\sigma^*$  states. As written in the introduction, CIs between these states have been suggested. For such mechanisms, the symmetry of the molecule in the initially populated state has to be conserved through out the deactivation into the final state. Vibrational modes of  $a_2$  or  $b_1$  symmetry have been suggested as coupling modes [158, 159]. The symmetries of the coupling modes for the four possible combinations are given in Table 3.8.

The harmonic vibrational frequencies (in  $\text{cm}^{-1}$ ) of the three  $a_2$  symmetry and four  $b_1$  symmetry coupling modes are summarized in Table 3.7 and shown in Figure 3.33. The frequencies were calculated for pyrrole in the neutral ground state and in

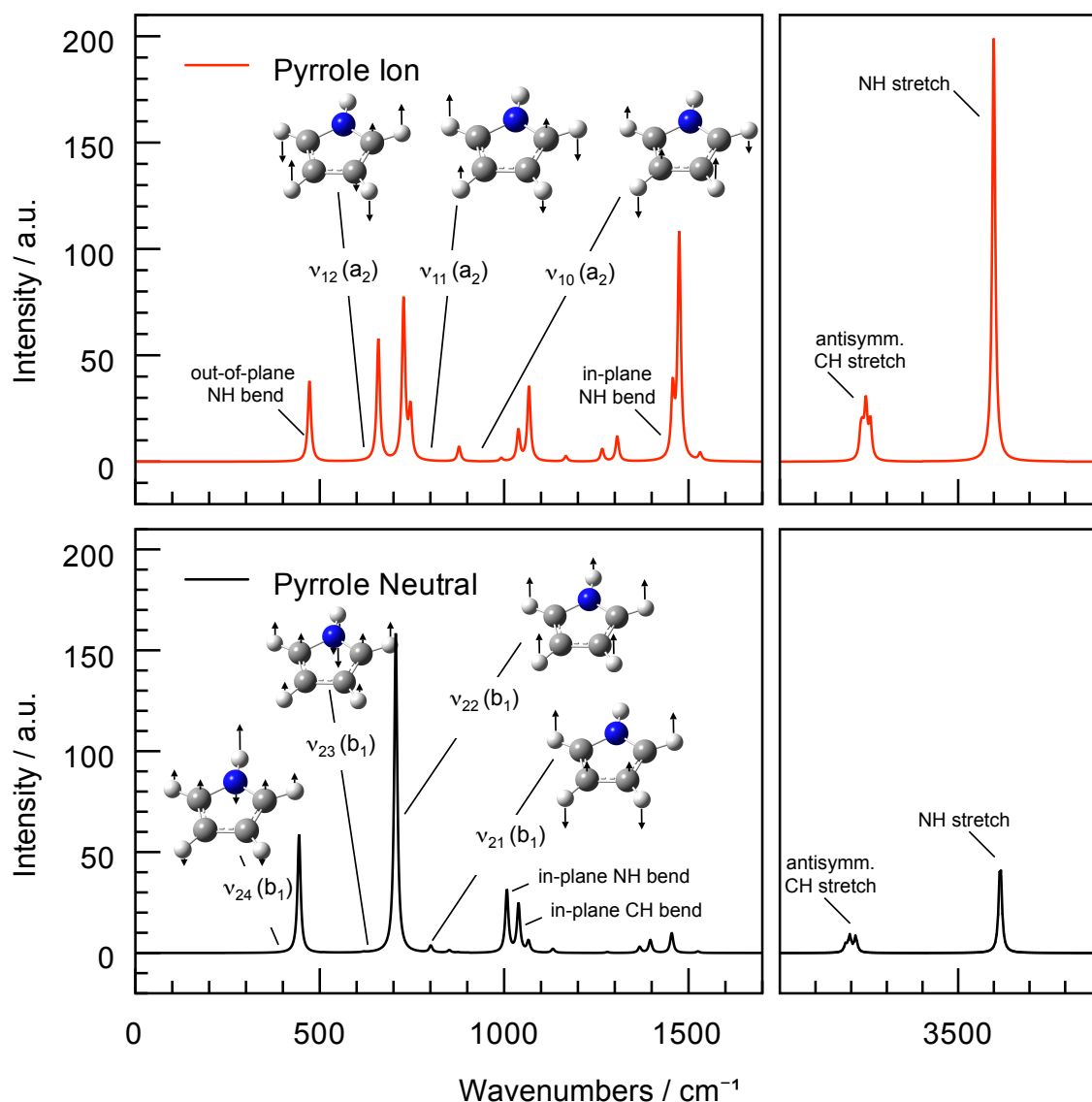


**Figure 3.33:** Calculated vibrational frequencies of pyrrole in its electronic ground state and in the ionic ground state.

the positively charged ionic ground state. In particular, the vibrational energies of pyrrole in the ionic ground state are of interest, as the photoelectron distributions mirror the energies of the vibrations in the ionic state.

The assignment of the UV absorption bands of pyrrole has been highly controversial and discussed in the literature for a long time [171, 172, 173]. A serious problem is the calculation of the  ${}^1B_2$   $\pi\pi^*$  transition, because of its strong valence/Rydberg mixing. CASPT2 results, which are very accurate, predict the energy of this transition to be within the range of 5.8 - 6.0 eV [154, 156, 171]. Table 3.9 shows the results for calculations performed with the CASPT2 method [173],

**Table 3.8:** Symmetries of the vibrational coupling modes for conical intersections between the  $\pi\pi^*$  states and the  $\pi\sigma^*$  states.

CI between	${}^1B_2(\pi\pi^*)$	${}^1A_1(\pi\pi^*)$
${}^1A_2(\pi\sigma^*)$	$b_1$	$a_2$
${}^1B_1(\pi\sigma^*)$	$a_2$	$b_1$

the vertical transition energies of our own TD-DFT calculations performed with the PBE1PBE//6-311<sup>++</sup>g(3df,3pd) functional, and, for comparison, experimental values taken from the literature [154]. As can be seen, the TD-DFT values are too high, except for the too low  $\pi\sigma^*$  states.

**Table 3.9:** Calculated vertical transition energies compared with experimental values (energies in eV with oscillator strengths in parenthesis).

Transition	PBE1PBE <sup>a</sup>	CASPT2 <sup>b</sup>	Experiment <sup>b</sup>
${}^1A_2(\pi\sigma^*)$	5.04 (f)	5.08 (f)	5.22
${}^1B_1(\pi\sigma^*)$	5.78 (0.023)	5.97 (0.001)	-
${}^1A_2(3p)$	5.80 (f)	5.83 (f)	-
${}^1B_1(3p)$	5.92 (0.002)	5.85 (0.024)	5.88
${}^1B_2(3p)$	6.13 (0.186)	5.78 (0.004)	5.86
${}^1A_1(\pi\pi^*)$	6.44 (0.001)	5.92 (0.020)	-
${}^1A_2(3d)$	6.38 (f)	6.42 (f)	-
${}^1B_2(\pi\pi^*)$	6.65 (0.023)	6.00 (0.125)	5.98
${}^1B_1(3d)$	6.44 (0.005)	6.40 (0.012)	6.43
${}^1A_2(3d)$	6.74 (f)	6.51 (f)	-
${}^1B_2(3d)$	7.01 (0.008)	6.53 (0.001)	6.50

<sup>a</sup> PBE1PBE//6-311<sup>++</sup>g(3df,3pd)

<sup>b</sup> Reference [154] and references within.

### 3.4.4.2 Time-Resolved ToF Mass Spectrometry

Femtosecond pump-probe ToF mass spectrometry on pyrrole was performed with two different excitation/ionization schemes, which are illustrated in Figure 3.34.

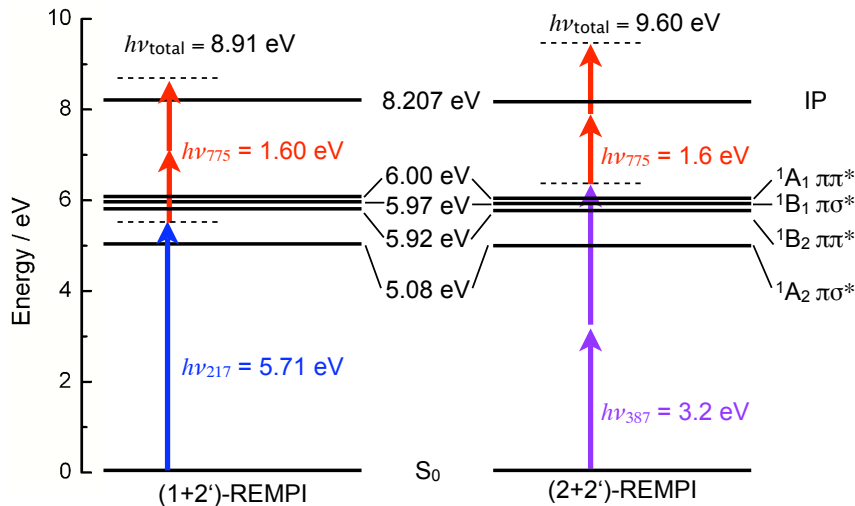


**Figure 3.34:** Pyrrole was excited following two different REMPI schemes. With (1+2')-REMPI, using  $\lambda_{pump} = 217$  nm and  $2 \times \lambda_{probe} = 775$  nm, the  ${}^1B_2 \pi\pi^*$  state is mainly excited. The second scheme excites the  ${}^1A_1 \pi\pi^*$  state by two-photon absorption at  $2 \times \lambda_{pump} = 387$  nm and  $2 \times \lambda_{probe} = 775$  nm [(2+2')-REMPI]. The vertical excitation energies have been adapted from references [154, 171].

The measurement done by the (1+2')-REMPI scheme with the pump wavelength at  $\lambda_{ex} = 217$  nm excited pyrrole close to the origin of the  ${}^1B_2 \pi\pi^*$  state. The excited molecules were ionized by two-photon absorption at  $\lambda = 775$  nm ( $2 \times h\nu_{775} = 3.2$  eV), which results in an excess energy of up to 0.707 eV above the IE (8.207 eV [153]).

Following the second (2+2')-REMPI scheme, an investigation of higher excited states of pyrrole by pumping the  ${}^1A_1 \pi\pi^*$  state with pulses at  $\lambda = 387$  nm ( $2 \times h\nu_{387} = 6.4$  eV), is possible. The probe pulse ionized the excited molecule at  $\lambda = 775$  nm ( $2 \times h\nu_{775} = 3.2$  eV). This created an excess energy of up to 1.393 eV.

The measured time-resolved decay profiles of the pyrrole peak in the mass spectra, which have been obtained for both REMPI schemes are shown in Figure 3.35. The transient mass spectra were fitted with a sum of two decaying exponentials convoluted with a Gaussian function for the IRF. The upper profile shows the results after excitation at  $\lambda = 217$  nm into the energetically lower lying  ${}^1B_2 \pi\pi^*$  state and ionization with  $\lambda = 775$  nm. The intensity is plotted in arbitrary units against the decay time in ps. The data are drawn as open circles, the non-linear fit is shown as a red line for  $\tau_1 = 0.38(1)$  ps, and as a blue line for the second

component  $\tau_2 \geq 150$  ps. The fit residuum is given in the bottom of the plot. The components exhibit very different amplitudes and decay rates. The fast component  $\tau_1$  holds 99 % of the amplitude and decays within 0.38 ps, while  $\tau_2$  possesses 1 % of the amplitude and decays on a time scale ( $\geq 150$  ps) that cannot be determined precisely enough with the translation stage used.

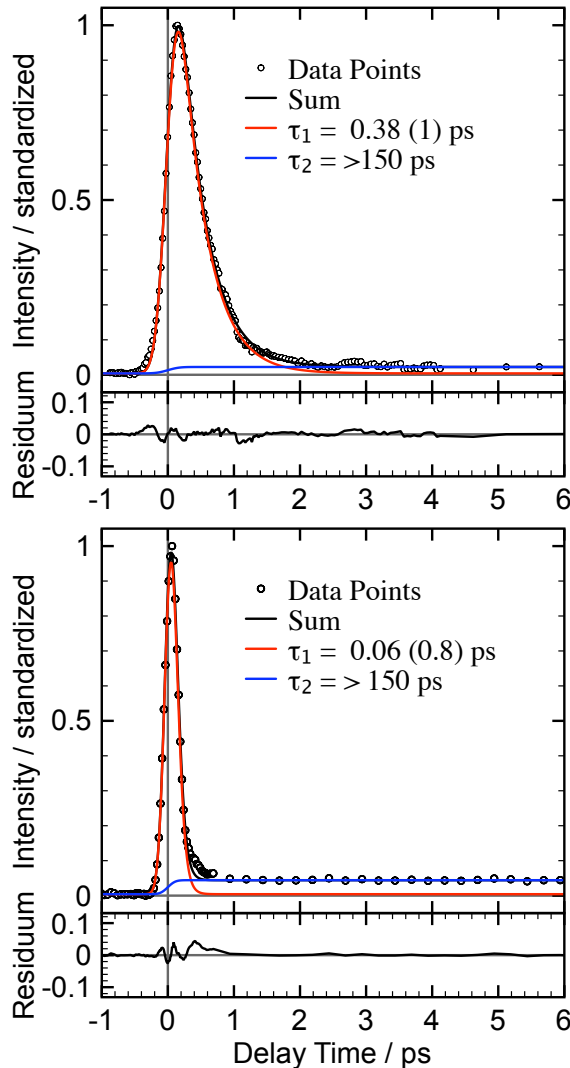


**Figure 3.35:** Top: Time-resolved ToF-MS result on pyrrole applying the (1+2')-REMPI scheme. Two decay rates,  $\tau_1 = 0.38(1)$  ps and  $\tau_2 \geq 150$  ps contribute to the spectrum. Bottom: Results of the (2+2')-REMPI on pyrrole with  $\tau_1 = 0.06(1)$  ps and  $\tau_2 \geq 150$  ps.

It was found that the contribution of  $\tau_2$  to the overall signal amplitude depends on the amount of pyrrole clusters in the molecular beam. By decreasing the vapor pressure of pyrrole by cooling the reservoir down to 273 K, it was possible to reduce the contribution of clusters strongly so that it became negligible.

The profile in the bottom of Figure 3.35 shows the result of the measurement after applying the (2+2')-REMPI scheme. Pyrrole is excited to the  ${}^1A_1 \pi\pi^*$  state by two-photon absorption at  $\lambda = 387$  nm and is ionized by a time delayed pulse at  $\lambda = 775$  nm. The open circles represent the data and the red and blue lines are the result of the fitting procedure. The fast decay rate  $\tau_1 = 0.06(1)$  ps is faster than the time resolution of the experiment (IRF = 0.098 ps ( $\sigma$ ) or 0.23 ps (FWHM)) and holds 95 % of the overall amplitude. The second decay rate  $\tau_2 \geq 150$  ps contributes with 5 % and represents the cluster formation, which will be ignored in the discussion. The fitting parameters, namely the instrument response function, the amplitudes, and the decay times, are summarized in Table 3.10 for both REMPI schemes applied.



**Table 3.10:** Results of the data fitting routine for the time-resolved measurements on pyrrole following the two different REMPI schemes.

REMPI	$\lambda_{pump}$	$\lambda_{probe}$	IRF <sup>a</sup>	$A_1$	$\tau_1$	$A_2$	$\tau_2$
scheme	nm	nm	ps	norm.	ps	norm.	ps
1+2'	217	775	0.31	0.99	0.38(1)	0.01	$\geq 150$
2+2'	387	775	0.23	0.95	0.06(1)	0.05	$\geq 150$

<sup>a</sup>FWHM (Gaussian)

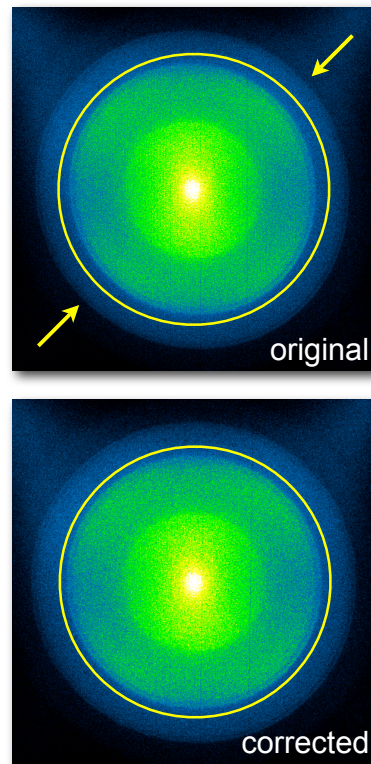
### 3.4.4.3 Transient Photoelectron Imaging

Time-resolved PEIs of pyrrole were measured with the (1+1')-REMPI scheme using  $\lambda_{pump} = 219$  ( $h\nu_{219} = 5.66$  eV) and  $\lambda_{probe} = 258$  nm ( $h\nu_{258} = 4.80$  eV), probing the  $1^1B_2 \pi\pi^*$  state as described in the previous subsection. Four different time delays between the pump and probe pulses (-0.1, 0, 0.2, and 0.35 ps) were monitored.

The raw images were not completely circular due to an electric force field distortion. This was corrected by an algorithm<sup>2</sup> that stretched the image along a selected coordinate. The effects are demonstrated in Figure 3.36. The correction increased the resolution of the energy distributions enormously. All images were treated like this unless stated otherwise.

The maximum kinetic energy release (MKER) for this scheme is  $18\,150\text{ cm}^{-1}$  given by the equation below.

$$\begin{aligned}
 E_{el}^{max} &= h\nu_{pump} + h\nu_{probe} - IE & (3.5) \\
 &= 5.66\text{ eV} + 4.80\text{ eV} - 8.21\text{ eV} \\
 &= 2.25\text{ eV} \hat{=} \underline{18\,150\text{ cm}^{-1}}
 \end{aligned}$$

**Figure 3.36:** Top: Distorted raw image. Bottom: Corrected photoelectron image. A symmetric yellow ring included for comparison.

The corrected raw photoelectron images, slices through the reconstructed 3D distribution (pBASEX), and the respective electron energy distributions calculated for the different delay times ( $\Delta t$ ) are shown in Figure 3.37. The intensities of the raw and sliced images are plotted proportional to their respective total electron

<sup>2</sup>Programmed for ImageJ (freeware, <http://rsb.info.nih.gov/ij/>) and implemented as a macro.

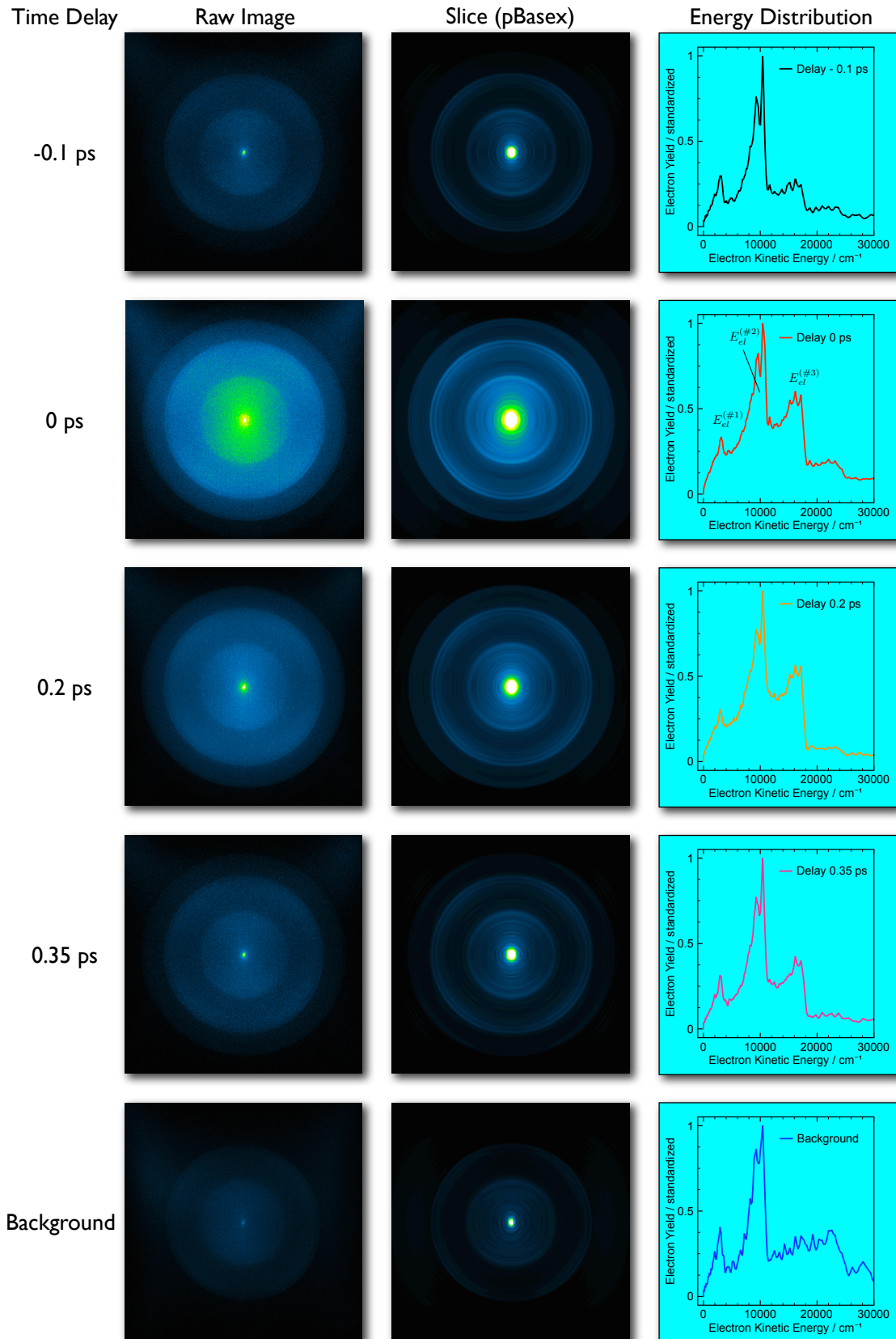


**Figure 3.37:** Summary of the transient PEI results on pyrrole obtained by (1+1')-REMPI using  $\lambda_{pump} = 219$  nm and  $\lambda_{probe} = 258$  nm. Each row contains the raw image, the pBasex fitted slice, and the corresponding normalized electron energy distribution.

yields, whereas the energy distributions are normalized so that the greatest peak equals 1. Each two-color image has peaks at electron energies of  $E_{el}^{(\#1)} = 3100$ ,  $E_{el}^{(\#2)} = 10425$ , and  $E_{el}^{(\#3)} = 17150 \text{ cm}^{-1}$  (for assignment see Figure 3.37). Peaks 2 and 3 are split by vibrational progressions. The peaks rise to a maximum at  $\Delta t = 0 \text{ ps}$ , followed by a decay to an intensity that is comparable to that of the background image at  $\Delta t \approx 1 \text{ ps}$ . The decay matches the decay time  $\tau_1 = 0.38 \text{ ps}$  that was observed by the time-resolved ToF-MS measurements at  $\lambda_{pump} = 217 \text{ nm}$ , introduced in the previous subsection.

Unfortunately, all images have strong contributions due to one-color backgrounds that arise by two-photon absorption at wavelengths of  $\lambda_{pump} = 219 \text{ nm}$  and  $\lambda_{probe} = 258 \text{ nm}$ , respectively. Each background was measured separately and their sum is shown in Figure 3.37 at the bottom. The background peaks at an electron kinetic energy of  $3100 \text{ cm}^{-1}$  and  $10425 \text{ cm}^{-1}$  can be assigned to the two-photon absorption at  $\lambda = 258 \text{ nm}$ , which is equivalent to a resonant (1+1)-REMPI excitation into the energetically lower  $^1A_2(\pi\sigma^*)$  state. The MKER of the ejected electrons is  $11250 \text{ cm}^{-1}$  after ionization through absorption of the second photon. The broad noisy band centered around  $23000 \text{ cm}^{-1}$  arises from two-photon absorption at the pump wavelength of  $\lambda = 219 \text{ nm}$ . Using this (1+1)-REMPI scheme, the MKER is  $25130 \text{ cm}^{-1}$ .

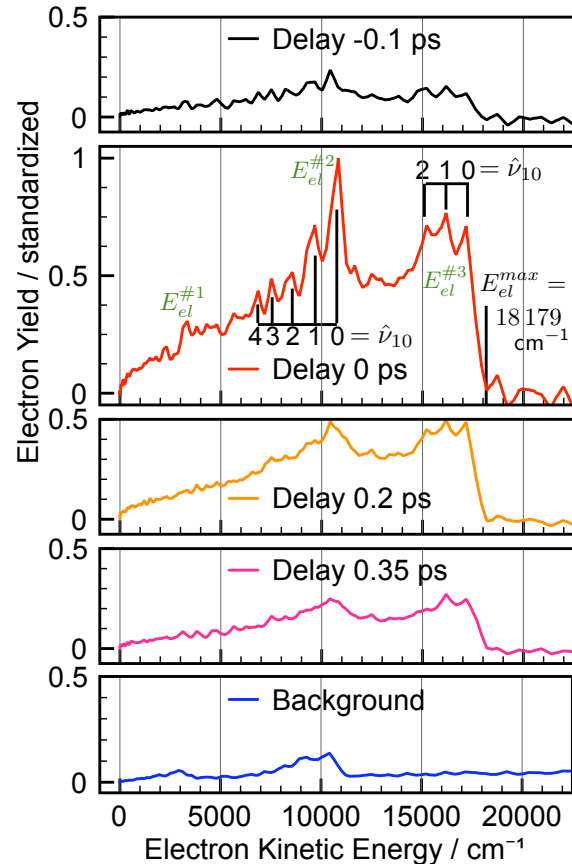


**Figure 3.38:** Photoelectron kinetic energy releases for different values of  $\Delta t$ . The intensities are shown relative to the normalized  $\Delta t = 0 \text{ ps}$  distribution.

For a better analysis, the electron energy distributions in Figure 3.38 were background corrected and the electron yields are shown relative to the normalized distribution at  $\Delta t = 0 \text{ ps}$ . Two peaks persist at energies of  $E_{el}^{(\#2)} = 10425 \text{ cm}^{-1}$  and  $E_{el}^{(\#3)} = 17150 \text{ cm}^{-1}$ , while the third one at  $E_{el}^{(\#1)} = 3100 \text{ cm}^{-1}$  vanishes completely after background subtraction. The remaining peaks show a vibrational progressions, which is most prominent at  $\Delta t = 0 \text{ ps}$ , with an energy spacing of  $\Delta E \approx 1000 \text{ cm}^{-1}$ . The  $\approx 150 \text{ cm}^{-1}$  energy uncertainty of the experiment allows

a tentative assignment of the observed progressions.  $\hat{\nu}_8 = 1070 \text{ cm}^{-1}$ ,  $\hat{\nu}_{10} = 950 \text{ cm}^{-1}$ ,  $\hat{\nu}_{18} = 1040 \text{ cm}^{-1}$ , and  $\hat{\nu}_{19} = 990 \text{ cm}^{-1}$  are possible modes, but  $\hat{\nu}_{10}$ , which has  $a_2$  symmetry, is the only mode that vibronically couples the excited  ${}^1B_2(\pi\pi^*)$  state to one of the  $\pi\sigma^*$  states ( ${}^1B_1$ ). Detailed information about the coupling mechanisms and involved vibronic modes are given in Subsection 3.4.4.1. The anisotropy parameters  $\beta$  and  $\gamma$  of each peak are summarized in Table 3.11.

**Table 3.11:** Anisotropy parameters for the photoelectron distributions of pyrrole.

$\Delta t$	$E_{el}^2 = 10\,425 \text{ cm}^{-1}$		$E_{el}^3 = 17\,160 \text{ cm}^{-1}$	
ps	$\beta$	$\gamma$	$\beta$	$\gamma$
-0.1	-0.01	-0.54	-0.29	-0.53
0	0.19	-0.38	-0.21	-0.41
0.2	0.08	-0.40	-0.04	-0.50
0.35	0.06	-0.49	0.04	-0.46

### 3.4.5 Discussion

One-photon absorption at a pump wavelength of  $\lambda_{pump} = 219$  nm excites pyrrole to the energetically lower  $\pi\pi^*$  state of  $B_2$  symmetry. The time-resolved ToF-MS measurement revealed an electronic relaxation with a decay rate  $\tau_1 = 0.38$  ps (Figure 3.34, (1+2')-REMPI). An explanation is provided by the calculated potential energy surfaces done by Domcke and coworkers, which are shown schematically in Figure 3.39.

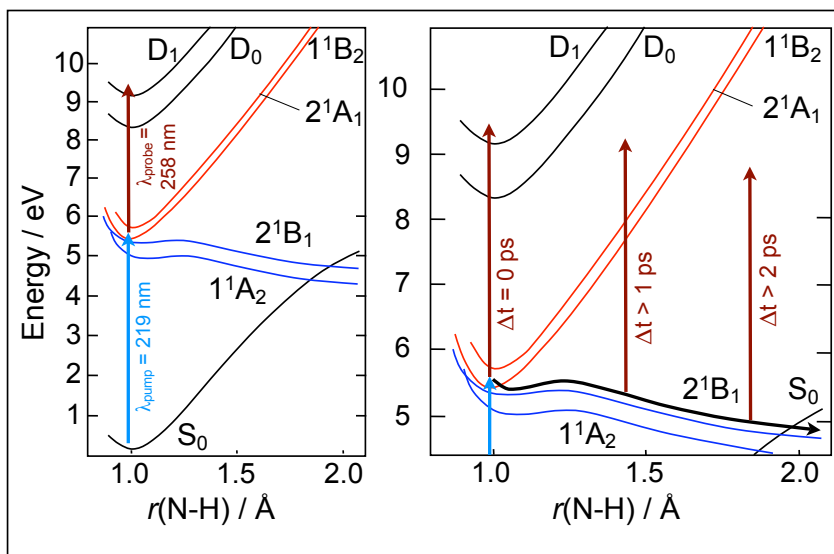


**Figure 3.39:** Pyrrole was investigated with a (1+2')-REMPI scheme, where the  $1^1B_2$   $\pi\pi^*$  state is pumped at  $\lambda = 219$  nm and probed time-delayed at  $\lambda = 775$  nm. After relaxation to the  $2^1B_1$   $\pi\sigma^*$  state through a conical intersection ( $a_2$  vibrational coupling mode), the molecule deactivates further following the  $N-H$  stretching coordinate. Along the  $N-H$  coordinate two channels open up: First, deactivation into the vibrational hot ground state can occur through a CI ( $b_1$  vibrational coupling mode) and second, a direct dissociation along the  $N-H$  coordinate, as is discussed in the introduction, must be taken into account.

The excited molecules deactivate from the  $1^1B_2$  state to the  $2^1B_1$  state or to the  $1^1A_2$  state through funnels that are spanned by an  $a_2$  or a  $b_1$  symmetry vibrational coupling mode, respectively, as it was described in Subsection 3.4.4.1. Both  $\pi\sigma^*$  states have a steep repulsive potential surface along the  $N-H$  coordinate, which leads to a homolytic dissociation to the pyrrolyl radical and an H radical (atom). A second competing channel, relaxation through a CI connecting the  $2^1B_1$  state and the vibrational hot ground state of  $A_1$  symmetry, opens up at an  $N-H$  distance of  $1.95$  Å ( $1.85$  Å for the  $1^1A_2$  state). However, the consecutive deactivation steps cannot be monitored by the ToF-MS experiment as explained

by Figure 3.39. For a  $N-H$  distance  $> 1.0 \text{ \AA}$  the ionic state is raised in energy so much that excited pyrrole molecules following this deactivation coordinate ( $N-H$  bond elongation) cannot be ionized by the probe pulse anymore. The ToF-MS measurement showed that, to delay times of  $\Delta t > 2 \text{ ps}$ , virtually all excited molecules have left the region where the ionization pulse is able to probe them.

Applying the (2+2')-REMPI scheme at  $\lambda_{pump} = 387 \text{ nm}$  and  $\lambda_{probe} = 775 \text{ nm}$ , the time-resolved ToF-MS results are similar. The decay rate  $\tau_1 = 0.06 \text{ ps}$  is faster by a factor of  $\approx 5$ , as it was expected because of the much higher excess energy that is released into the  $\pi\pi^*$  state(s). The results do not give new insights drawn for the (1+2')-REMPI scheme.

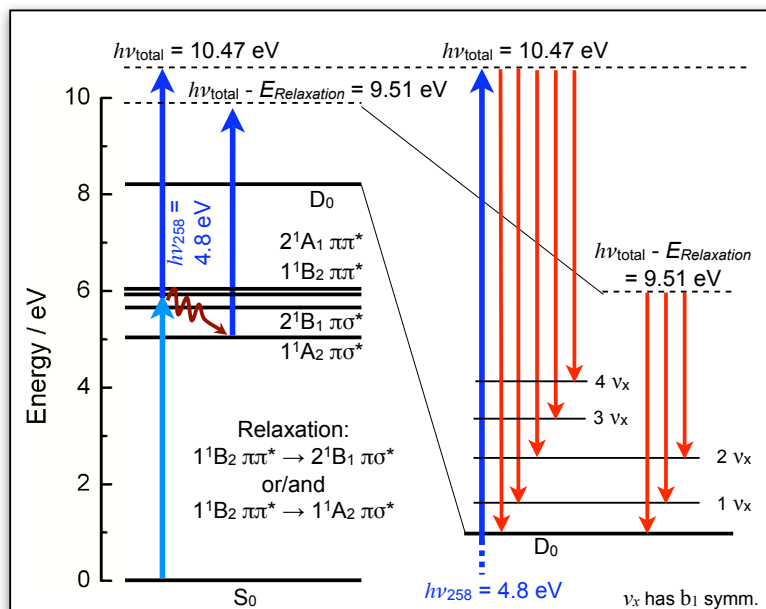


**Figure 3.40:** Pyrrole excited to the  $1^1B_2 \pi\pi^*$  state relaxes to the  $2^1B_2 \pi\sigma^*$  state and/or to the  $1^1A_2 \pi\sigma^*$  state. The time-delayed probe pulse ionized the molecules and, depending on the accessible energy, different photoelectron bands are observed ( $h\nu_{total} = 10.47 \text{ eV}$  and  $h\nu_{total} - E_{Relaxation} = 9.51 \text{ eV}$ ). This explains the two peaks in the observed electron distributions of the respective PE images. Furthermore, each peak shows a vibrational progression, which is assigned to the  $\nu_{10}$  vibrational mode.

The PEI data, taken with (1+1')-REMPI ( $\lambda_{pump} = 219 \text{ nm}$ ;  $\lambda_{probe} = 258 \text{ nm}$ ) exhibited new features. At a delay time of  $\Delta t = 0 \text{ ps}$ , the background subtracted images contain two peaks at an electron kinetic energy of  $E_{el}^{(\#2)} = 10425 \text{ cm}^{-1}$  and  $E_{el}^{(\#3)} = 17150 \text{ cm}^{-1}$ , giving a difference of  $\Delta E_{el}^{(\#3-\#2)} = 6725 \text{ cm}^{-1}$ . Both peaks show a vibrational progression with similar energy spacings ( $\Delta E_{vib}^{(\#2)} \approx 1200$

$\text{cm}^{-1}$ ,  $\Delta E_{vib}^{(3\#)} \approx 1000 \text{ cm}^{-1}$ ). All images at other delay times show the same peaks however with less intensity. The decay of the overall electron yield reflects the decay rate  $\tau_1 = 0.38 \text{ ps}$ , found for the (1+2')-REMPI time-resolved ToF-MS measurement.

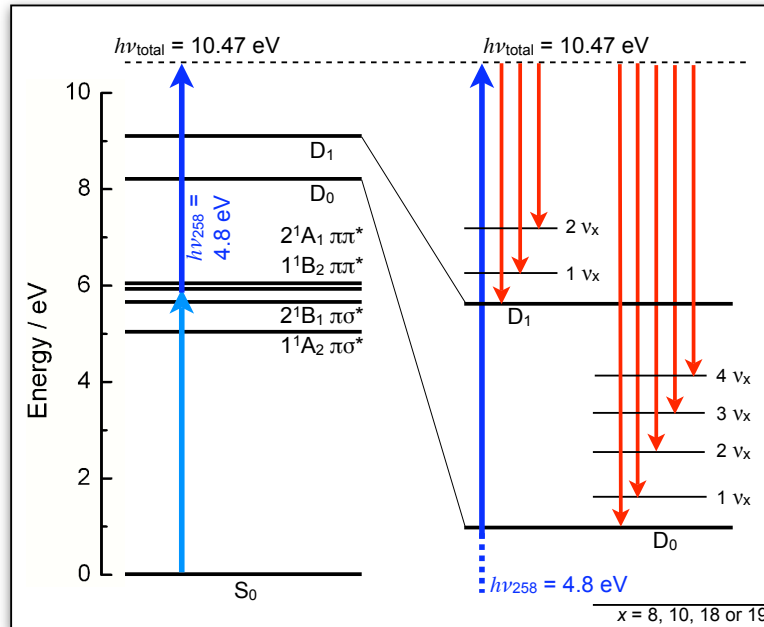


**Figure 3.41:** Pyrrole excited to the  $1^1B_2 \pi\pi^*$  state is ionized by the probe pulse, resulting in a total photon energy of  $h\nu_{total} = 10.47 \text{ eV}$ . This is enough energy to transfer pyrrole to the ionic ground state ( $D_0$ ) or to the ionic first excited state ( $D_1$ ), where the peak at higher KER corresponds to the  $D_0$  state and the peak at lower KER to the  $D_1$  state. Each peak shows a vibrational progression, which could be assigned to either  $\nu_8 = 1070 \text{ cm}^{-1}$ ,  $\nu_{10} = 950 \text{ cm}^{-1}$ ,  $\nu_{18} = 1040 \text{ cm}^{-1}$ , or  $\nu_{19} = 990 \text{ cm}^{-1}$ .

The photoelectron peak assignments are not straightforward, but two models were employed. In the first model (see Figure 3.40), the excited  $1^1B_2 \pi\pi^*$  state relaxes to one of the energetically lower  $\pi\sigma^*$  states and the time-delayed probe pulse ionizes both states, resulting in two energy distributions which should have an energy spacing corresponding to the difference in the vertical excitation energies of the involved states ( $1^1B_2 \pi\pi^* \rightarrow 2^1B_1 \pi\sigma^*$  or  $1^1A_2 \pi\sigma^*$ ). The peaks are separated by  $\Delta E_{el}^{(\#3-\#2)} = 6725 \text{ cm}^{-1} \hat{=} 0.84 \text{ eV}$ . This corresponds roughly to the vertical energy spacing between the  $1^1B_2 \pi\pi^*$  state (5.98 eV)<sup>3</sup> and the  $1^1A_2 \pi\sigma^*$  state (5.08 eV). A CI between those two states involves one of the four  $b_1$  coupling modes (see Table 3.7), which should be excited in the state relaxed to. For peak 2 ( $E_{el}^{(\#2)} = 10425 \text{ cm}^{-1}$ ), a progression with  $\approx 1200 \text{ cm}^{-1}$  was observed, which cannot be assigned to

<sup>3</sup>CASPT2 calculations in Table 3.9

an isolated  $b_1$  mode. Several combination modes (total symmetry corresponds to  $b_1$ ) are valid:  $b_1 \otimes a_1$ , and  $b_2 \otimes a_2$ . But as there are too many possible combinations, no exact assignment can be carried out. Figure 3.40 schematically shows the electronic excitation, relaxation, and ionization forming photoelectrons with different kinetic energies.

The second model is shown in Figure 3.41. The  $1^1B_2 \pi\pi^*$  excited pyrrole is transferred by the probe pulse to the ionic ground state  $D_0$  and to the ionic first excited state  $D_1$ . The peaks at  $E_{el}^3 = 17150 \text{ cm}^{-1}$  and  $E_{el}^2 = 10425 \text{ cm}^{-1}$  correspond to  $D_0$  and  $D_1$ , respectively. Both peaks show vibrational progressions, these cannot be assigned for sure to one of the normal modes, because of an energy uncertainty of  $\approx 150 \text{ cm}^{-1}$  of the experiment. Possible modes are  $\nu_8 = 1070 \text{ cm}^{-1}$ ,  $\nu_{10} = 950 \text{ cm}^{-1}$ ,  $\nu_{18} = 1040 \text{ cm}^{-1}$ , and  $\nu_{19} = 990 \text{ cm}^{-1}$ . The slightly different energies of the progressions are explained by the different vibrational energies found for the ionic ground state and the ionic first excited state. Furthermore, this model assumes that the probe beam is not able to ionize the molecules after the initially excited state has relaxed.

Ashfold and coworkers [169] investigated the relaxation pathways of pyrrole after exciting the  $1^1B_2 \pi\pi^*$  state and the  $1^1A_2 \pi\sigma^*$  state by measuring the kinetic energy of dissociated H atoms. Their analysis showed that the  $\nu_{10}(a_2)$ ,  $\nu_{15}(b_2)$ ,  $\nu_{16}(b_2)$ , and  $\nu_{23}(b_1)$  modes were most prominent and all lend vibronic transition probability to the  $1^1A_2 \leftarrow X^1A_1$  transition by intensity borrowing from nearby states. Only the  $a_2$  symmetry mode  $\nu_{10}$  corresponds in magnitude to the above described progressions in the PE images.

### 3.4.6 Conclusion and Summary

The time-resolved ToF-MS measurements in combination with the transient PEI results showed that the electronic dynamics of pyrrole excited to the energetically lowest  $\pi\pi^*$  state exhibits an ultrafast monoexponential decay with  $\tau_1 = 0.38 \text{ ps}$ . The photoelectron energy distributions define a deactivation pathway that involves the repulsive  $\pi\sigma^*$  states. They can be accessed from the  $\pi\pi^*$  state by funnels (CIs) between their potential surfaces. To allow for the crossings, an  $a_2$  or  $b_1$  vibrational coupling mode has to be involved for symmetry reasons. The observed vibrational progressions can be assigned with some uncertainty to the  $a_2$  mode  $\nu_{10} = 950 \text{ cm}^{-1}$ . Therefore,  $\pi\pi^* (B_2)$  deactivation proceeds by the second  $\pi\sigma^* (B_1)$  state.



### 3.5 *N*-Methylpyrrole, and 2,4-, and 2,5-Dimethylpyrrole

#### 3.5.1 Introduction

The UV absorption spectra of the pyrrole derivatives *N*-methylpyrrole (NMP), 2,4-(2,4-DMP), and 2,5-dimethylpyrrole (2,5-DMP) are shown in Figure 3.42.

All mentioned methyl substituted pyrrole derivatives show red shifted bands. The NMP spectrum exhibits three bands. The first broad and unstructured band from 250 to 230 nm is assigned to the  $3s \leftarrow a_2(\pi)$  transition that is one-photon symmetry forbidden but two-photon allowed [153, 174]. The origin of the  $S_1$  transition at  $41\,195\text{ cm}^{-1}$  ( $\lambda_{S_1} = 241.43\text{ nm}$ ) has been determined by Cooper et al. amongst others using (2+2)-REMPI spectroscopy [153, 175, 176, 177]. However, the one-photon transition gains intensity by an electronic motion-internal rotation coupling mechanism involving the methyl-rotor [178] and therefore it is visible in the UV absorption spectrum as very weak band. The second and third electronic ground state transitions have their origins at  $43\,650\text{ cm}^{-1}$  ( $\lambda_{S_2} = 229.08\text{ nm}$ ) and  $46\,125\text{ cm}^{-1}$  ( $\lambda_{S_3} = 216.80\text{ nm}$ ), respectively. The corresponding bands are superimposed in the UV absorption spectrum at 242 to 200 nm. McDiarmid and coworkers assigned them to the  $3p \leftarrow a_2(\pi)$  and  $3p' \leftarrow a_2(\pi)$  transitions.

No REMPI measurements or quantum chemical calculations are available in the literature at the present time, but similar conclusions can be drawn for 2,4-, and 2,5-dimethylpyrrole.

The electronic dynamics of *N*-methylpyrrole were investigated in our group [26] by photofragment velocity imaging experiments focussing on the H atom detachment after excitation at  $\lambda = 243.1$  and 217 nm by nanosecond laser pulses. The measurements revealed only slow H photodissociation channels. This confirmed that the fast and narrow H atom channel, which was observed under similar conditions for pyrrole, is in fact due to the direct *N-H* predissociation predicted by Domcke *et al.* [25].

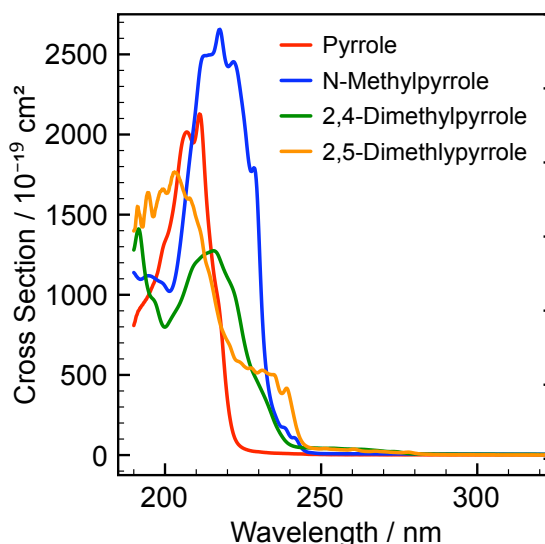


**Figure 3.42:** The gas phase UV absorption spectrum of pyrrole ( $p = 0.5\text{ mbar}$ ), *N*-methylpyrrole ( $p=0.5\text{ mbar}$ ), 2,4-, and 2,5-dimethylpyrrole ( $p=1.6\text{ mbar}$ ).

Not much is known about the electronic dynamics of the mentioned pyrrole derivatives after UV excitation at  $217 \text{ nm} \leq \lambda_{\text{pump}} \leq 230 \text{ nm}$ . The molecules were thus investigated by femtosecond time-resolved ToF mass spectrometry in the gas phase in this thesis for the first time.

### 3.5.2 Experimental Setup

The same pump-probe schemes as for pyrrole were applied for *N*-methylpyrrole, *2,4*- and *2,5*-dimethylpyrrole. The gas mixtures composed of *N*-methylpyrrole ( $\approx 1 \%$ ), *2,4*- or *2,5*-dimethylpyrrole ( $< 1 \%$ ) were prepared by bubbling helium carrier gas through a glass reservoir containing the samples at  $-35 \text{ }^\circ\text{C}$ .

### 3.5.3 Results for *N*-Methylpyrrole

#### 3.5.3.1 Time-Resolved ToF Mass Spectrometry

*N*-methylpyrrole was investigated by time-resolved TOF mass spectrometry pumping the first UV absorption band at  $217 \text{ nm} \leq \lambda_{\text{pump}} \leq 230 \text{ nm}$  and probing at  $\lambda_{\text{probe}} = 775 \text{ nm}$ . The results obtained by the (1+3')-REMPI scheme are shown in Figure 3.43. The transient mass spectra were fitted with a sum of two decaying exponential functions convoluted with a Gaussian IRF.

The upper profile shows the data (open circles) after excitation at  $\lambda = 217 \text{ nm}$ . Plotted is the intensity in arbitrary units against the decay time in ps. The non-linear fit result is shown as red line ( $\tau_1 = 0.22(2) \text{ ps}$ ) and blue line ( $\tau_2 = 0.55(20) \text{ ps}$ ). The components  $\tau_1$  and  $\tau_2$  have relative amplitudes of 0.89 and 0.11, respectively.

The profile in the middle shows the results after excitation at  $\lambda_{\text{pump}} = 222 \text{ nm}$ . The open circles represent the data and the red and blue lines are the fit results ( $\tau_1 = 0.36(2) \text{ ps}$  and  $\tau_2 = 1.2(70) \text{ ps}$ , respectively). The amplitudes have similar proportions as for the excitation at  $\lambda_{\text{pump}} = 217 \text{ nm}$  ( $A_1 = 0.95$  and  $A_2 = 0.05$ ).

The bottom panel of Figure 3.43 shows the transient mass signal (open circles) for a pump wavelength of  $\lambda_{\text{pump}} = 229 \text{ nm}$ . The fit is given as red line for the decay time  $\tau_1 = 0.13(1) \text{ ps}$  and as blue line for the second component  $\tau_2 = 1.00(6) \text{ ps}$ . The amplitude ratio of  $A_1 = 0.76$  and  $A_2 = 0.24$  strongly varies at this excitation wavelength compared the measurements at higher pump energy. The fit residua are given in each plot in the lower panel. The results are summarized in Table 3.12.

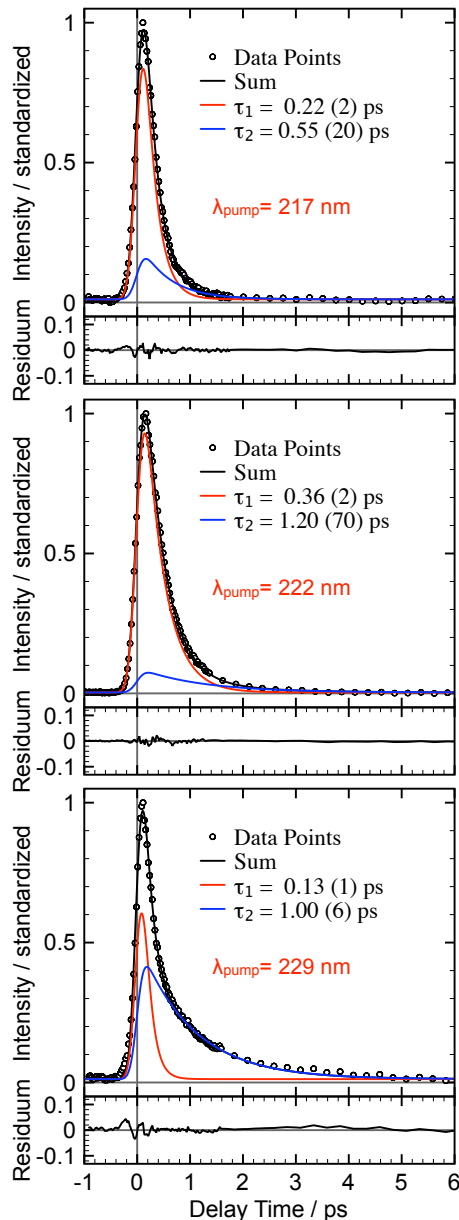


**Figure 3.43:** Time-resolved ToF-MS results on *N*-methylpyrrole for 217, 222, and 229 nm excitation wavelengths.

**Table 3.12:** Summary of the transient ToF-MS fit results for *N*-methylpyrrole.

$\lambda_{pump}$	IRF ( $\sigma$ )	$\tau_1$	$A_1$	$\tau_2$	$A_2$
nm	ps	ps	norm.	ps	norm.
217	0.11(1)	0.22(2)	0.89	0.55(20)	0.11
222	0.12(1)	0.36(2)	0.95	1.20(70)	0.05
230	0.10(1)	0.13(1)	0.76	1.00(6)	0.24

No other investigated derivative nor pyrrole itself exhibits such a strong affinity to cluster formation as *N*-methylpyrrole. To diminish clusters, the liquid sample in the reservoir was cooled down to  $-35$  °C to decrease the concentration of gaseous *N*-methylpyrrole in the molecular beam. Furthermore, the carrier gas pressure was decreased to 1 atm and the dwell time in front of the nozzle was minimized as described in Subsection 2.1.2.2. The experience showed that, under such expansion conditions, it was possible to achieve virtually cluster-free experimental conditions.

### 3.5.3.2 Transient Photoelectron Imaging

PEIs were recorded after exciting *N*-methylpyrrole at  $\lambda_{pump} = 217$  nm ( $h\nu = 5.71$  eV) and ionizing at  $\lambda_{probe} = 258$  nm ( $h\nu = 4.81$  eV). Measured images are shown in Figure 3.44.

The maximum kinetic energy release (MKER) for this scheme is calculated by the following equation.

$$\begin{aligned}
 E_{kin,max}^{el} &= h\nu_{pump} + h\nu_{probe} - IP & (3.6) \\
 &= 5.71 \text{ eV} + 4.81 \text{ eV} - 7.99 \text{ eV} \\
 &= 2.57 \text{ eV} \hat{=} \underline{20\,350 \text{ cm}^{-1}}
 \end{aligned}$$

The raw photoelectron images, the slices through the reconstructed 3D distributions (pBASEX), and the electron energy distributions for the measured delay times ( $\Delta t$ ) are shown in Figure 3.44 without correction for the one-color background. The intensities of the raw images and slices are plotted proportional to their respective total electron yields and the energy distributions are shown normalized (highest peak = 1). The images have two peaks at electron energies of  $E_{el}^1 = 14\,250 \text{ cm}^{-1}$  and  $E_{el}^2 = 19\,250 \text{ cm}^{-1}$ . The peaks show no splittings or vibrational progressions. The decay of the total electron yield ( $\Delta t = -0.2 - 0.4$  ps) mirrors the time-resolved ToF-MS results ( $\tau_1 = 0.22$  ps) presented in the former subsection.

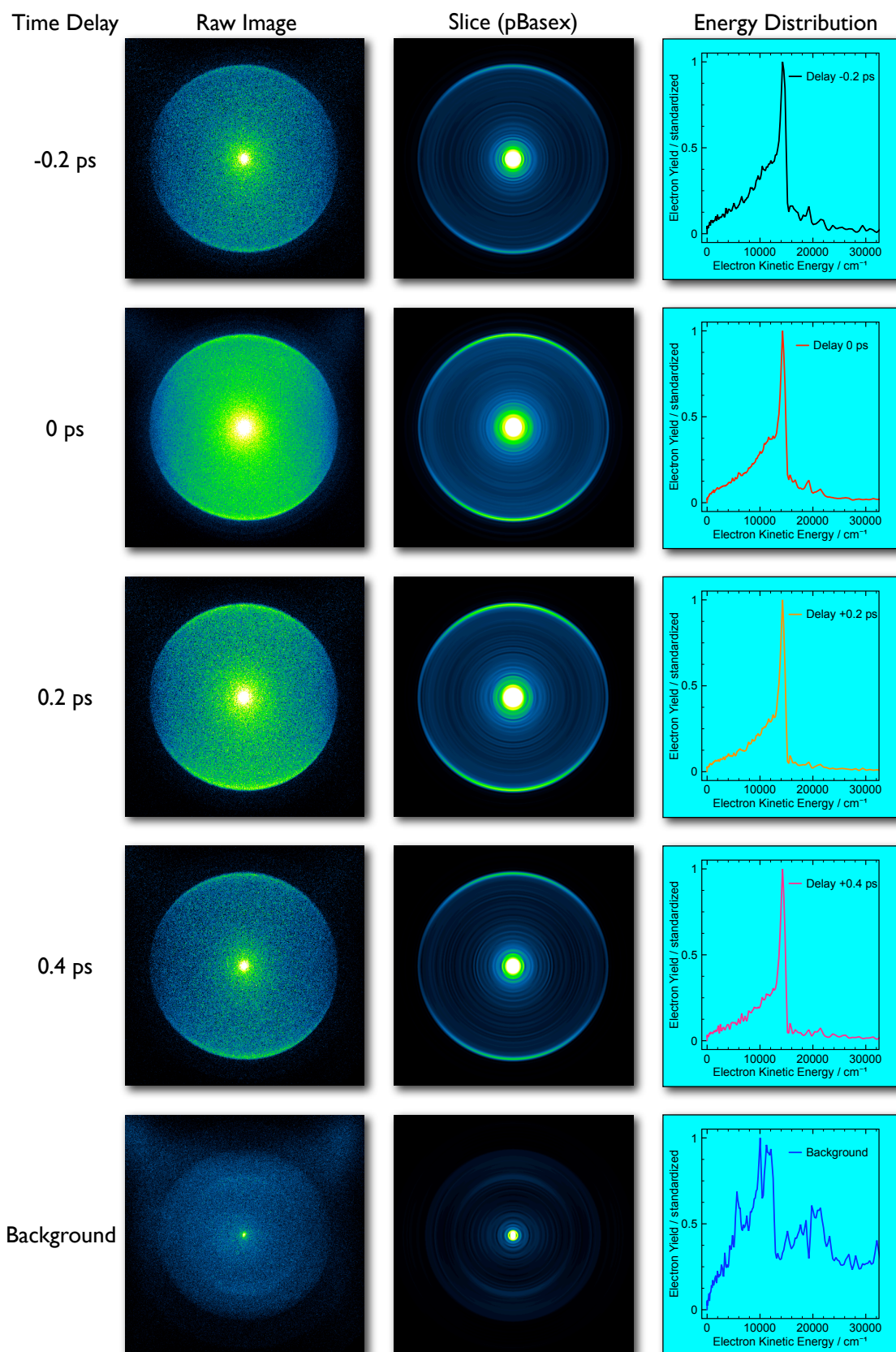


**Figure 3.44:** Summary of the transient PEI results on *N*-methylpyrrole obtained by (1+1')-REMPI using  $\lambda_{pump} = 217$  nm and  $\lambda_{probe} = 258$  nm. Each time delay series contains the raw image, the pBASEX fitted slice, and the corresponding normalized electron energy distribution.

The photoelectron energy distributions in Figure 3.45 have been background corrected to highlight the significant two-color features. In this plot, the relative electron yields of the distributions are shown. The background subtraction has no impact on the peak positions, but, at all delay times, the peak at  $E_{el}^2 = 19\,250\text{ cm}^{-1}$  is distinguished better from the noise. The anisotropy parameter  $\beta$  of the first peak at  $E_{el}^1 = 14\,250\text{ cm}^{-1}$  has a values of  $\approx 1.3(1)$  for all delay times, that of the second one is close to 0. The PEI results are summarized in Table 3.13

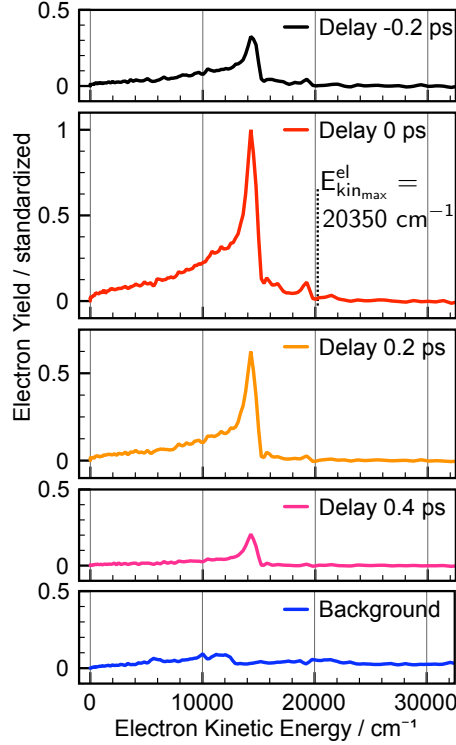


**Figure 3.45:** Photoelectron kinetic energy releases for different delay times  $\Delta t$ . The intensities are shown relative to the normalized distribution at  $\Delta t = 0\text{ ps}$ .

**Table 3.13:** Summary of the transient PEI results for *N*-methylpyrrole. The peak energies do not change with the delay time, neither do the anisotropy parameters.

Delay Time ps	Peak Energy			Peak Energy		
	$\text{cm}^{-1}$	Amplitude <sup>a</sup>	$\beta$ <sup>b</sup>	$\text{cm}^{-1}$	Amplitude	$\beta$
-0.2	14 266	0.88	1.21	19 240	0.12	0.03
0	14 266	0.90	1.23	19 240	0.10	-0.06
0.2	14 266	0.96	1.11	19 240	0.04	-0.18
0.4	14 266	0.97	1.23	19 240	0.03	-0.04

<sup>a</sup>given are normalized values

<sup>b</sup>Anisotropy Parameter

### 3.5.4 Results for 2,4- and 2,5-Dimethylpyrrole

#### 3.5.4.1 Time-Resolved ToF Mass Spectrometry

The pyrrole derivatives 2,4- and 2,5-dimethylpyrrole were investigated by transient ToF-MS by exciting at pump wavelengths of  $\lambda_{pump} = 217, 225,$  and  $230$  nm. The excited state dynamics were probed time delayed at  $\lambda_{probe} = 775$  nm.

The results obtained by the (1+3')-REMPI scheme are shown in Figure 3.46. The transient mass spectra were fitted with one decaying exponential function convoluted with a Gaussian IRF. The fits revealed decay times of  $\tau_1 \approx 0.1$  ps for 2,4-dimethylpyrrole and  $\tau_1 \approx 0.15$  ps for 2,5-dimethylpyrrole over the whole range of excitation wavelengths ( $217 \text{ nm} \leq \lambda_{pump} \leq 230 \text{ nm}$ ). The time-resolved results show a very fast deactivation, which is close to, but not below, the time resolution of the experiment ( $\sigma_{IRF} = 0.09$  ps). If the time resolution was lower than the investigated electronic decay, the transient signal should mirror the cross correlation between the pump and probe laser pulses, what would result in a symmetric (Gaussian) response. As one can see from Figure 3.46, this was not the case.

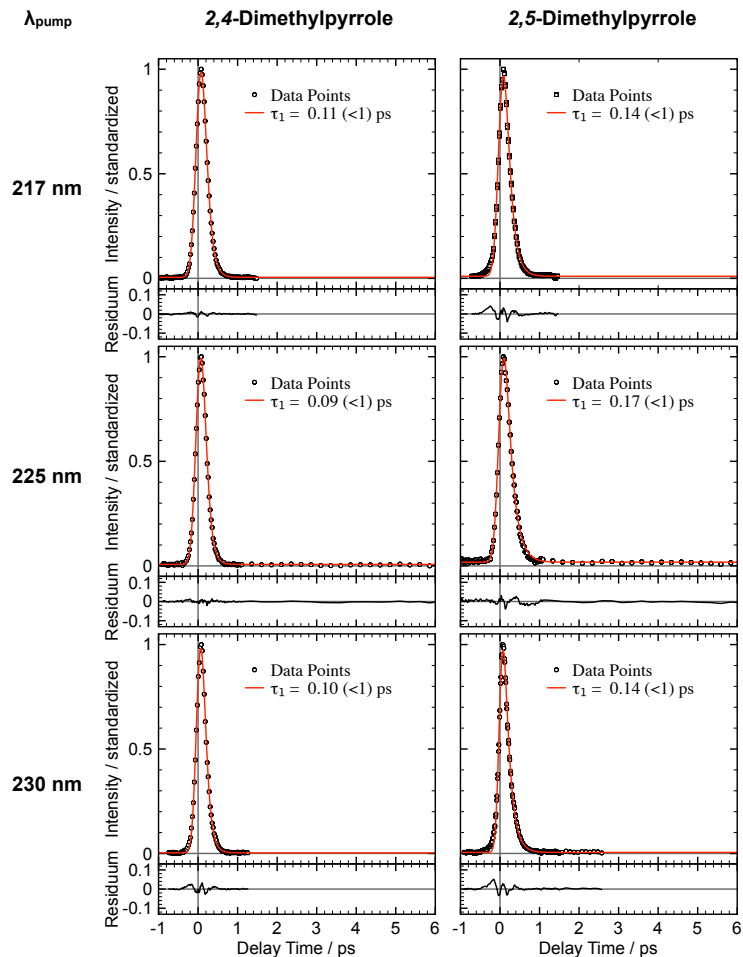


**Figure 3.46:** Transient ToF-MS results for 2,4- and 2,5-dimethylpyrrole pumping at  $\lambda_{pump} = 217, 225,$  and  $230$  nm.

### 3.5.5 Discussion

#### 3.5.5.1 *N*-Methylpyrrole

It can be clearly seen that the overall decay of the time-resolved ToF-MS measurements on *N*-methylpyrrole become faster with increasing pump energy. All measurements, at  $\lambda_{pump} = 217, 222,$  and  $230$  nm, show two decaying components with amplitude ratios that depend on the excitation wavelength. The non-linear fit results of the measurement at an excitation wavelength of  $\lambda_{pump} = 230$  nm revealed the decay times  $\tau_1 = 0.13$  ps and  $\tau_2 = 1.00$  ps with amplitudes of  $A_1 = 0.76$  and  $A_2 = 0.24$ , respectively. The measurements at higher energies exhibit slightly different values for  $\tau_1$  and  $\tau_2$ , but a larger difference is the very low amplitude of the slower component  $\tau_2$ , which contributes only with 0.11 ( $\lambda_{pump} = 217$  nm) and 0.05 ( $\lambda_{pump} = 222$  nm).

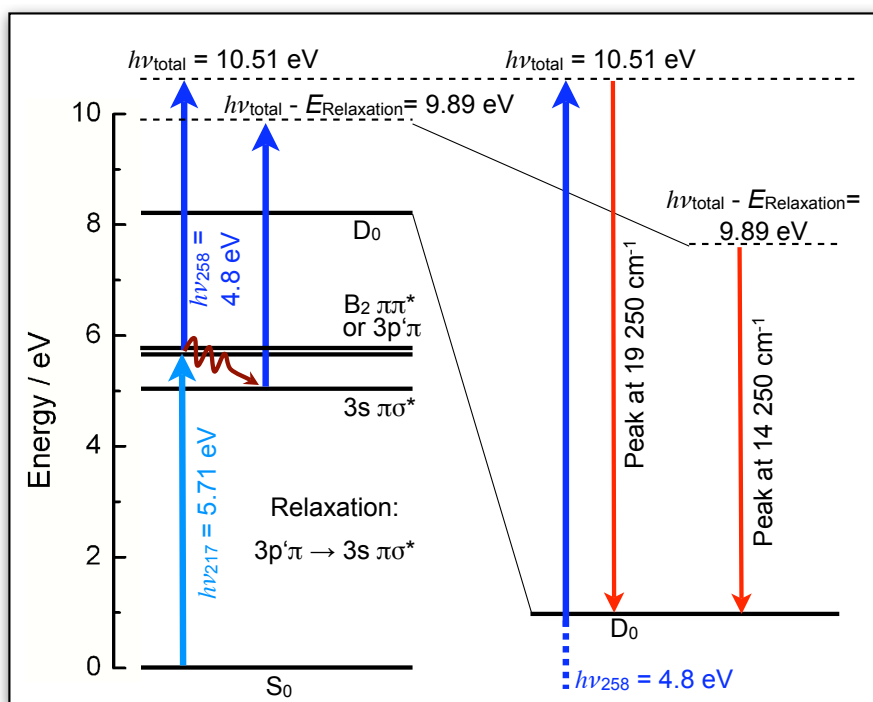


**Figure 3.47:** *N*-methylpyrrole excited to the  $3p'\pi$  state relaxes to the energetically lower  $3s(\pi\sigma^*)$  state. The time-delayed ionization pulse ionizes the molecules and depending on the excited electronic state, different total energies result ( $h\nu_{total} = 10.51$  eV and  $h\nu_{total} - E_{Relaxation} = 9.89$  eV), explaining the two peaks in the observed electron distributions of the PE images.

The one-photon absorption at  $\lambda_{pump} = 217$  nm ( $h\nu_{217} = 5.71$  eV) most probably excites *N*-methylpyrrole to the  $3p'\pi$  Rydberg state, which strongly absorbs at 5.71 eV. A  $\pi\pi^*$  state of  $B_2$  symmetry lies close by at 5.72 eV [174], but its absorption strength is much lower. At less energy ( $\lambda_{pump} > 217$  nm), an excitation to the



$3p\pi$  Rydberg state ( $5.41 \text{ eV} \hat{=} 229.08 \text{ nm}$ ) becomes more and more probable. With this information at hand, a correlation of the excited transitions with the observed electronic lifetimes gathered by the ToF-MS measurements could be observed. However, the PEI measurements provide additional important information, which, when taken into account, change the interpretation (see Figure 3.47). The PEI measurements show a peak at an electron kinetic energy of  $14\,250 \text{ cm}^{-1}$  and a second peak at  $19\,250 \text{ cm}^{-1}$ . The excitation at  $\lambda_{pump} = 217 \text{ nm}$  excites *N*-methylpyrrole to the  $3p'\pi$  ( $5.71 \text{ eV}$ ) state. According to the energy conservation law, a kinetic energy of  $20\,350 \text{ cm}^{-1}$  is maximally available for the photo-ejected electrons. Therefore, the peak at  $19\,250 \text{ cm}^{-1}$  corresponds to electrons ionized out of the excited  $3p'\pi$ . The peak at  $14\,250 \text{ cm}^{-1}$  corresponds to electrons released from an energetically lower electronic state. The energy difference of  $5\,000 \text{ cm}^{-1}$  ( $0.62 \text{ eV}$ ) between the observed photoelectron peaks equals exactly the energy difference between the  $3p'\pi$  and  $3s(\pi\sigma^*)$  states, which is  $0.61 \text{ eV}$  [174]. Consequently, the molecules relax to the energetically lower  $3s(\pi\sigma^*)$  state after excitation, from which the molecules are ionized by the time-delayed probe pulse. In the PEI distributions, one can see that the peak that is assigned to the  $3s$  state is much higher in intensity than the peak corresponding to the  $3p'\pi$  state. Already at  $t_0$  ( $\Delta t = 0 \text{ ps}$ ), the peak at  $19\,250 \text{ cm}^{-1}$  is only 10 % of the height of the peak at  $14\,250 \text{ cm}^{-1}$ . This shows the very fast relaxation of the  $3p'\pi$  state.

### 3.5.5.2 2,4- and 2,5-Dimethylpyrrole

The pyrrole derivatives 2,4- and 2,5-dimethylpyrrole have not been investigated by transient PEI, but only by time-resolved ToF-MS. The reasons are based on the ToF-MS results, which show exponential electronic decays of  $\tau_1 \approx 0.1 \text{ ps}$  for 2,4-DMP and  $\tau_1 \approx 0.15 \text{ ps}$  for 2,5-DMP, which is close to the time resolution ( $\sigma \approx 0.1 \text{ ps}$ ) of the experiment. Furthermore, the decay rates did not change within the excitation range of  $217 \text{ nm} \leq \lambda_{pump} \leq 230 \text{ nm}$ . PEI experiments would not deliver additional results.

### 3.5.6 Conclusion and Summary

Together with the time-resolved ToF-MS results for *N*-methylpyrrole this can be interpreted as follows. After excitation by the pump pulse, the  $3p'\pi$  state deactivates to the energetically lower  $3s(\pi\sigma^*)$  state through a conical intersection with a time constant faster than the time resolution and therefore it is not resolved by the MS nor the PEI experiment. Further, relaxation of the  $3s$  state is observed as decay component  $\tau_1 = 0.13 - 0.36 \text{ ps}$ .

The relaxation pathway of *N*-methylpyrrole in the  $3s$  state could be similar to the relaxation pathway of  $\pi\sigma^*$  state excited pyrrole. However, instead of *N-CH*<sub>3</sub> bond

dissociation, which represents an important analogous channel for pyrrole ( $N-H$ ), 3s state excited  $N$ -methylpyrrole exclusively relaxes to the ground state through a conical intersection formed by  $N - CH_3$  bond stretching, which represents the minor decay channel for  $\pi\sigma^*$  state excited pyrrole that was not observed in this thesis.

At lower excitation energies ( $\lambda_{pump} = 222$  and 230 nm), the  $3p\pi$  state (5.41 eV) becomes excited additionally (or instead of) to the  $3p'\pi$  state, which contributes to the transient mass spectra as the slow component ( $\tau_2 = 0.55 - 1.20$  ps). This channel is growing in intensity with decreasing excitation energy and may be involving a deactivation pathway that does not include the  $3s(\pi\sigma^*)$  state.

To fully understand the dynamics of  $N$ -methylpyrrole in its lowest electronically excited states, further investigations are necessary. In particular, PEI measurements with increased time resolution and at excitation wavelength between  $\lambda_{pump} = 240$  nm and 220 nm would shed more light on the involved electronic states.

The measurements on 2,4- and 2,5-dimethylpyrrole show that the substitution of two  $C$ -bonded H atoms increases the electronic deactivation dynamics by a factor of  $\approx 3$ , but no further information concerning the deactivation mechanisms of pyrrole-like molecules was obtained. This has been observed before, *e.g.*, for toluene, and is described in Section 3.2.

## 4 Summary

The electronic relaxation dynamics of several prototypical aromatic molecules, including benzene, toluene, xylenes, hexafluorobenzene, pyrrole and selected derivatives of pyrrole, were investigated by means of femtosecond time-resolved time-of-flight mass spectrometry (ToF-MS) and femtosecond time-resolved transient photoelectron imaging (PEI). These experiments were set up and characterized in this thesis. The time-resolved ToF mass spectrometer reaches a mass resolution of up to  $m/\Delta m = 1000$ , the time resolution of the femtosecond experiment was  $\Delta t = 40 - 100$  fs, depending on the pulses and wavelengths used. The PEI experiment has a similar time resolution and an electron kinetic energy resolution of  $\Delta E_{el} \approx 150 \text{ cm}^{-1} \approx 0.02 \text{ eV}$ .

In the experiment, benzene was excited by one-photon absorption to the  $S_1$  state at  $\lambda_{pump} = 258 \text{ nm}$  and to the  $S_2$  state by two-photon absorption at  $\lambda_{pump} = 387 \text{ nm}$ . The excited state decays were monitored by multi-photon ionization, probing with  $\lambda_{probe} = 775 \text{ nm}$ . Biexponential fits to the transient parent mass signals gave two decay constants, which were, respectively,

$$\tau_1 = 0.04 \text{ ps and } \tau_2 > 150 \text{ ps}$$

for  $S_1$  excited benzene and

$$\tau_1 = 0.02 \text{ ps and } \tau_2 > 1.12 \text{ ps}$$

for  $S_2$  excited benzene. Additional information on the vibronic dynamics was obtained by (1+1)- and (3+3)-PEI, where a vibrational progression originating from the  $\nu_1$  and  $\nu_6$  modes was observed. Benzene was used to calibrate the experimental setups. In particular, the PEI measurements benefited from its well known spectroscopic properties.

ToF-MS experiments on toluene and the three isomeric xylenes showed results similar to those of benzene. However, their dynamics were significantly faster due to a stronger coupling of the  $S_2$  states to their respective ground states. The results for benzene and toluene were found to be in good agreement with previous literature data.

The excited state decays of the  $S_2$  ( $\pi\pi^*$ ) and  $S_3$  ( $\pi\pi^*$ ) states of hexafluorobenzene were investigated using excitation wavelengths of  $265 \text{ nm} \geq \lambda_{pump} \geq 217 \text{ nm}$  and an

ionization wavelength at  $\lambda_{probe} = 775$  nm. The observed temporal profiles exhibit two decay times,

$$\tau_1 = 0.54 \text{ to } 0.10 \text{ ps} \quad \text{and} \quad \tau_2 = 493 \text{ to } 4.67 \text{ ps},$$

depending on the excitation wavelength. These were superimposed by a damped coherent oscillation with the following specifications:

$$\tau_D = 1.18 \text{ to } 0.36 \text{ ps} \quad \text{and} \quad \tilde{\nu}_{osc} = 94 \text{ to } 107 \text{ cm}^{-1}.$$

$\tau_1$  was assigned to the deactivation of the  $S_2$  state (and, at higher excitation, the  $S_3$  state) to the energetically lower and optically “dark”  $S_1$  state through a first conical intersection (CI).  $\tau_2$  mirrors the lifetime of the  $S_1$  state, which showed a strong dependence on the pump wavelength at  $\lambda_{pump} \geq 245$  nm. This was interpreted to be due to a threshold energy that is necessary to reach the second CI connecting the  $S_1$  state with the  $S_0$  state.  $\tau_2$  decreased over the whole excitation range by a factor of 100. The coherent oscillation originated from vibrational motion in the optically “dark”  $S_1$  state, reached from the  $S_2$  state within  $\tau_1 \leq 1$  ps.

The heteroaromatic molecule pyrrole was excited to the  $1^1B_2(\pi\pi^*)$  state by one-photon absorption at  $\lambda_{pump} = 219$  nm. The decay of this state was probed by multi-photon absorption at  $\lambda_{probe} = 775$  nm. A monoexponential fit revealed a decay time of

$$\tau_1 = 0.38 \text{ ps}.$$

This was assigned to an relaxation pathway involving a CI with the energetically lower  $\pi\sigma^*$  state of  $B_1$  symmetry. The  $1^1B_2(\pi\pi^*)$  state of pyrrole was also studied by PEI using a (1+1’)-REMPI scheme ( $\lambda_{pump} = 219$  nm and  $\lambda_{probe} = 258$  nm). Three electron bands were observed.

$$E_{el}^{\#1} = 3\,100 \text{ cm}^{-1}, \quad E_{el}^{\#2} = 12\,425 \text{ cm}^{-1}, \quad E_{el}^{\#3} = 17\,150 \text{ cm}^{-1}.$$

The latter two bands showed a vibronic progression with a band spacing of  $\approx 1000$   $\text{cm}^{-1}$ . Band #1 represented background noise. Band #2 and #3 were assigned to ionization of  $B_2$  excited pyrrole reaching the  $D_1$  and  $D_0$  states of the ion, respectively. The progressions were tentatively assigned to the normal mode  $\nu_{10}$ , which has  $a_2$  symmetry and is suggested as the main coupling mode for the  $B_2(\pi\pi^*) \rightarrow B_1(\pi\sigma^*)$  transition.

Several methyl-substituted derivatives of pyrrole gave similar time constants. However, PEI results for *N*-methylpyrrole showed interesting differences owing to the higher stability of its  $\pi\sigma^*$  state. To fully understand the dynamics of these molecules in their lowest excited states, further PEI investigations are necessary. In particular, measurements at excitation wavelengths lower than 240 nm would be of great interest.

## 5 Appendix

### 5.1 Technical Drawings and Photographs

#### 5.1.1 ToF Mass Spectrometry and Photoelectron Imaging Setup

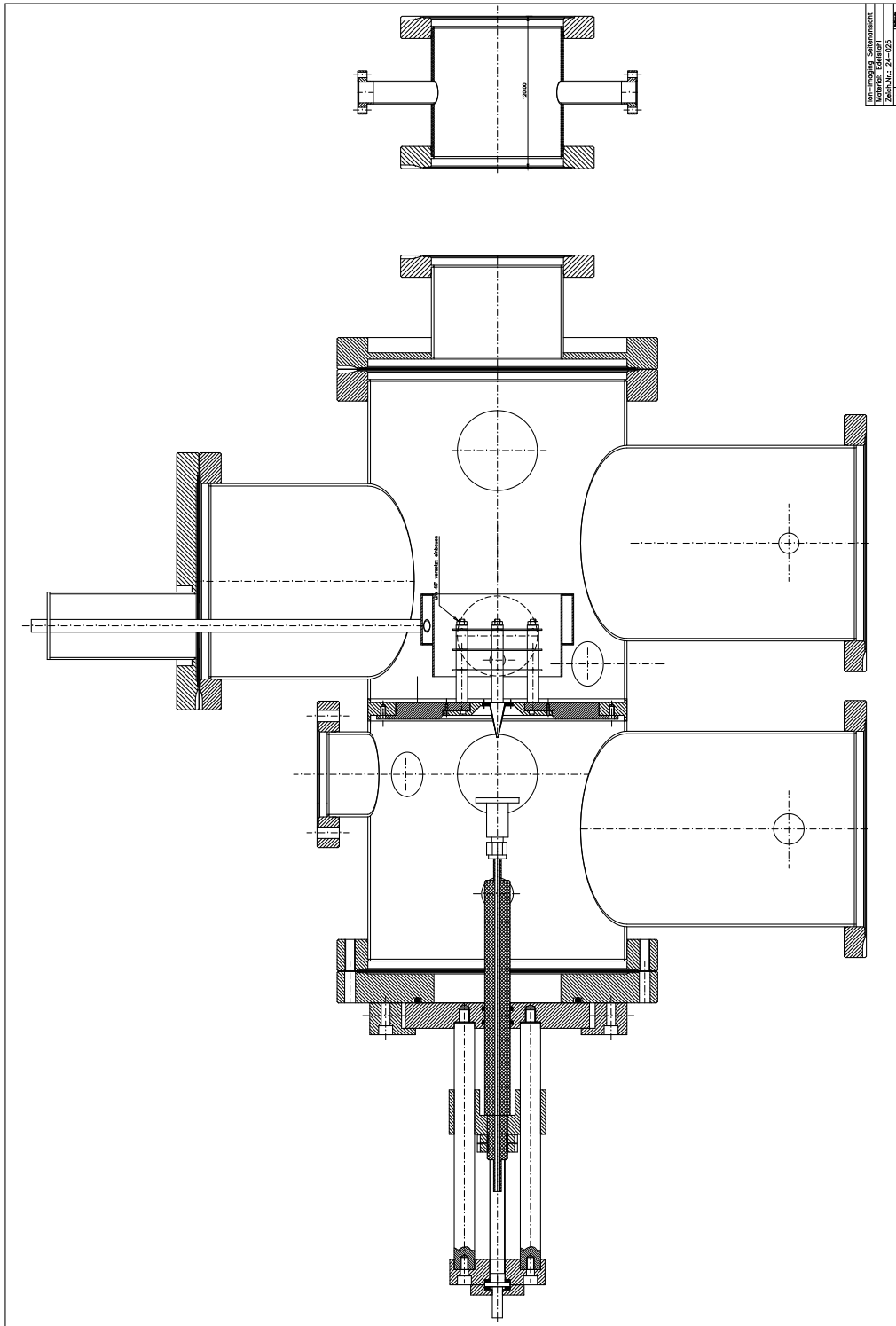


**Figure 5.1:** Assembled experiment chamber including nozzle mount, nozzle, ion lens assembly, cooling trap, and adapter flange

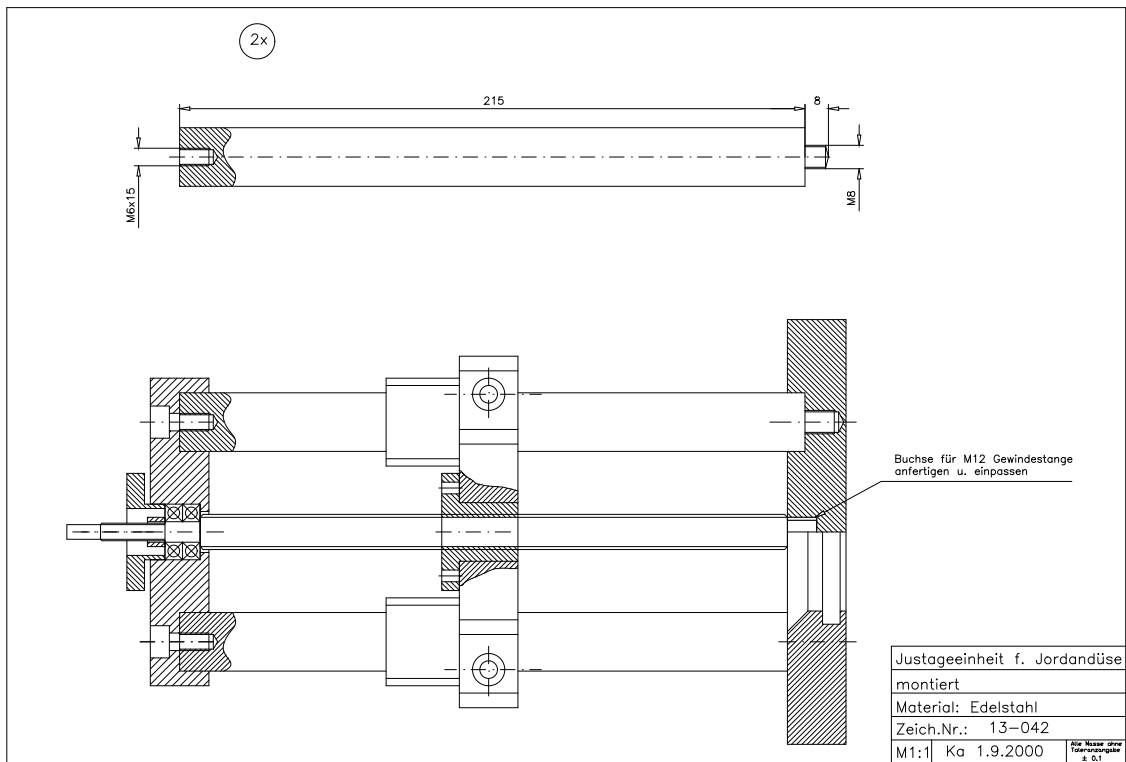


**Figure 5.2:** Adjustable General Valve nozzle mount.

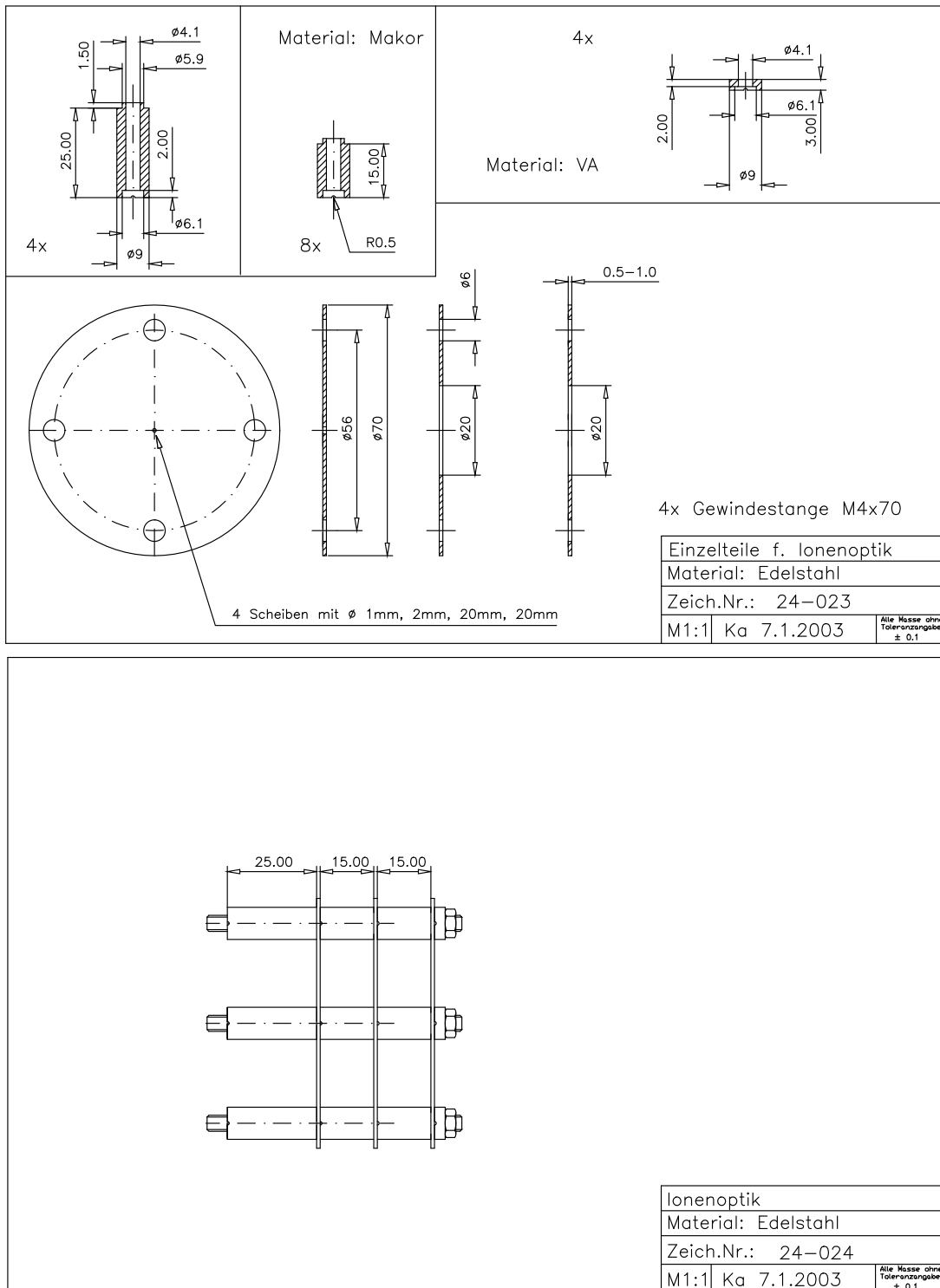


Figure 5.3: Ion lens assembly dimensioning.



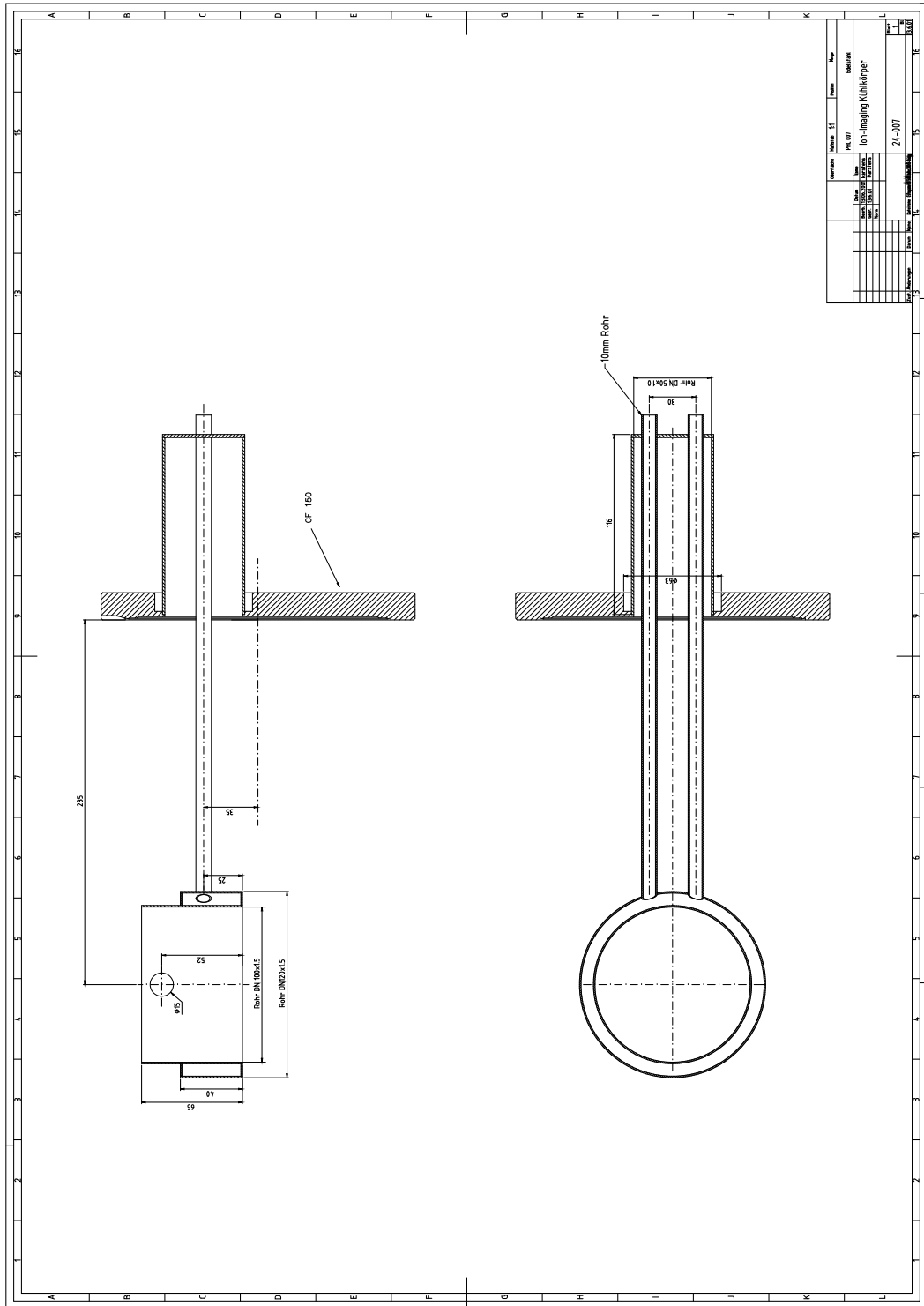


Figure 5.4: Drawing of the liquid nitrogen cooling trap.



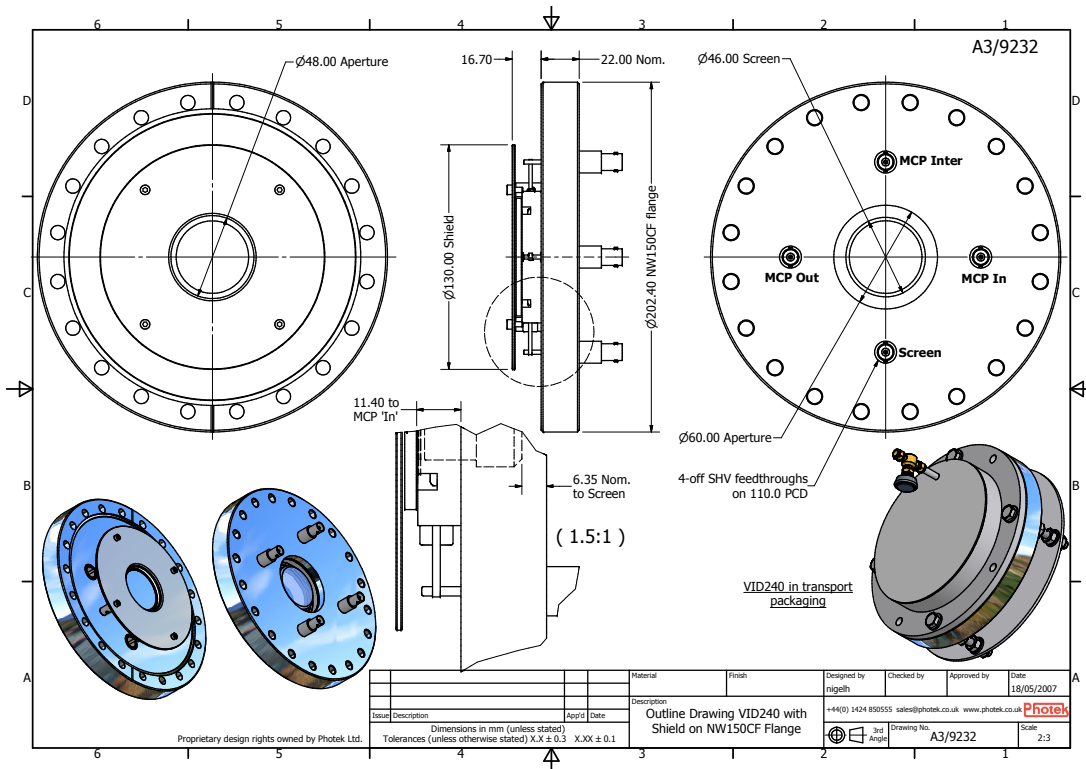
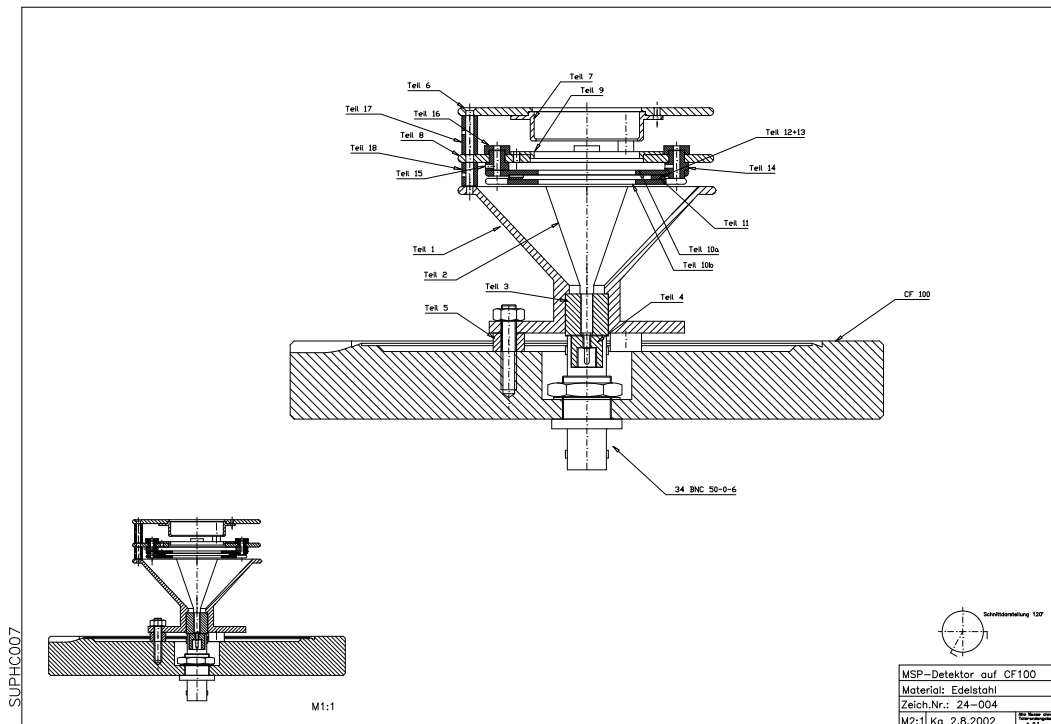


Figure 5.6: The upper drawing shows the ToF-MS MCP detector. In the bottom is illustrated the position sensitive imaging detector composed of two MCPs, and the phosphorescence screen.

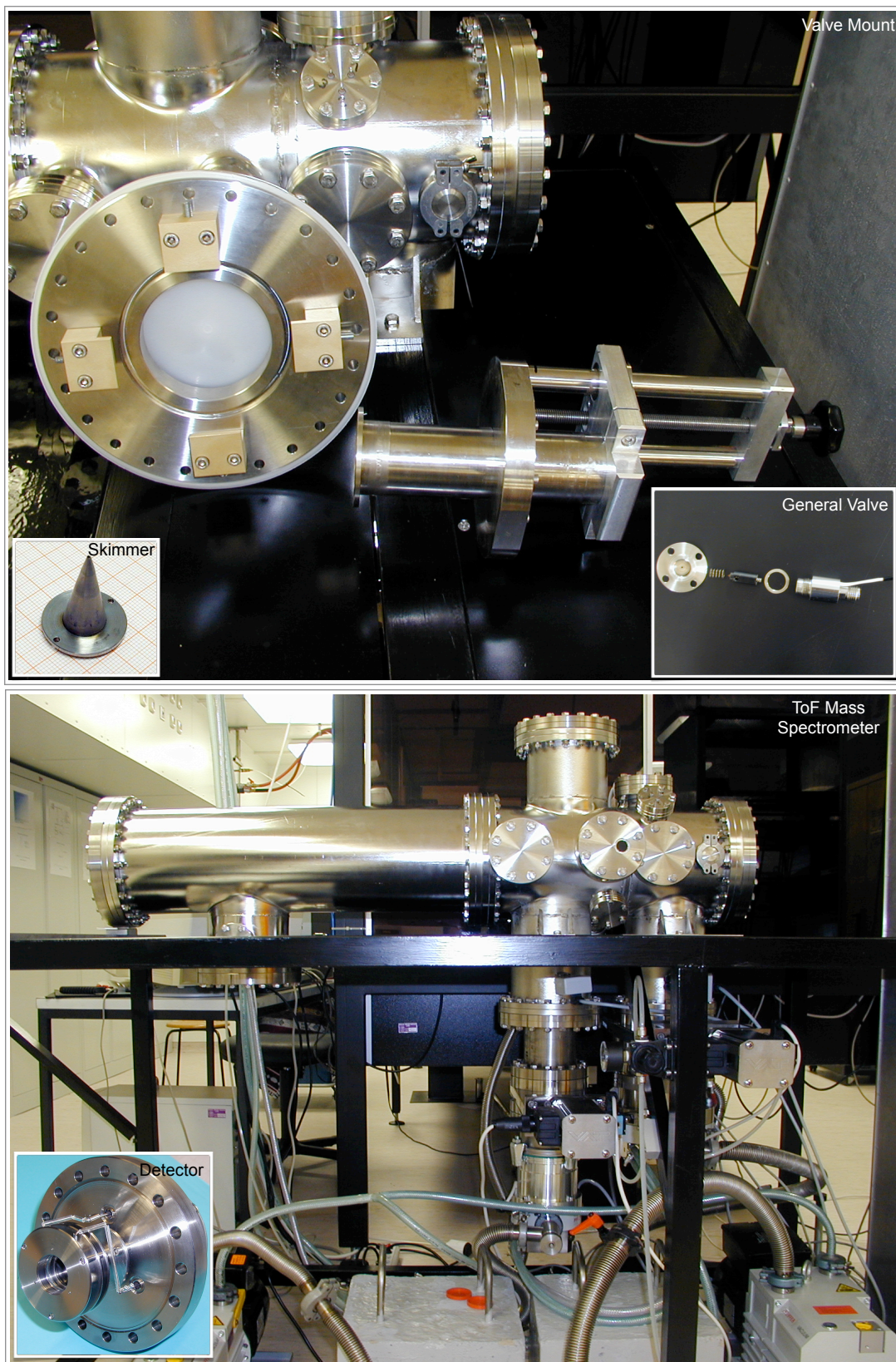
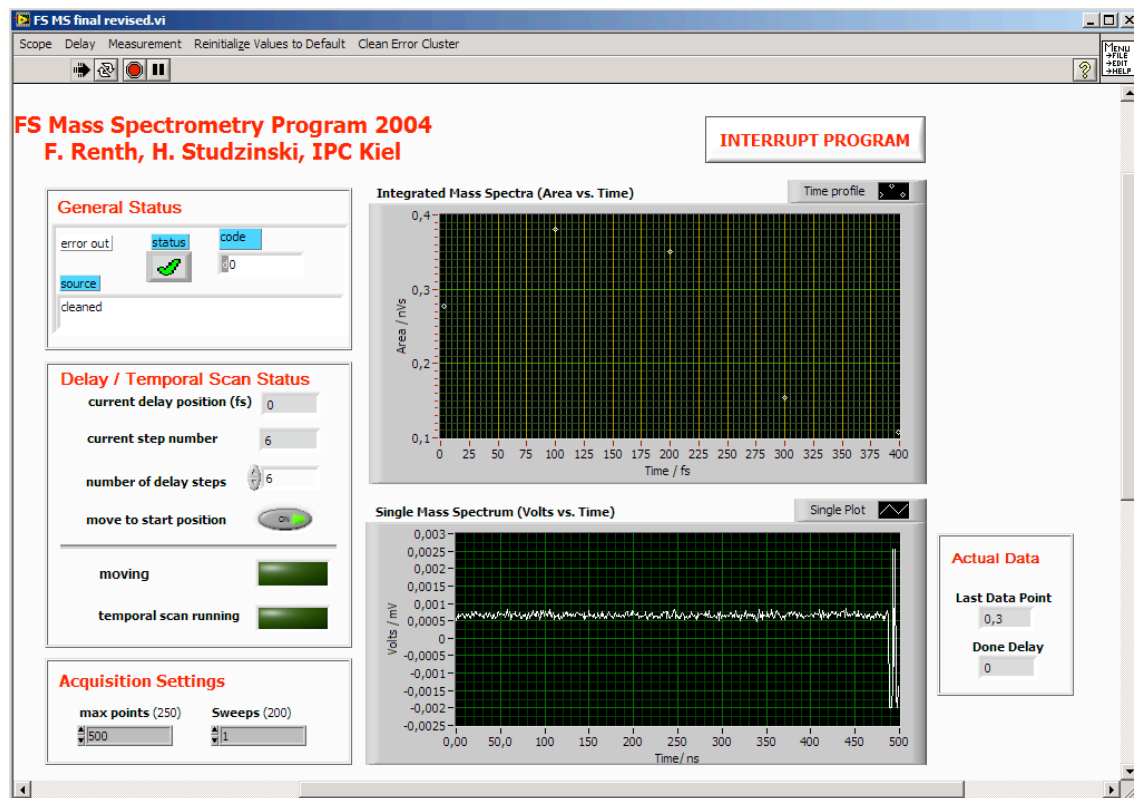


Figure 5.7: Photographs of the ToF mass spectrometer and some of its components.

## 5.2 Control Programs

The programs were designed in LabView 8.2. Their functionalities are shown in a series of screenshots, while explanatory notes are given in the labels.

### 5.2.1 Time-Resolved ToF Mass Spectrometry



**Figure 5.8:** The ToF-MS control program is adjusted by the menu points, “Scope”, “Delay”, and “Measurement”. Additionally, the acquisition settings are controlled directly on the front panel. The progress of running measurements can be observed on the displays and the indicator “current delay position”. The lower display panel shows the last recorded mass spectrum, while in the upper display the area of the mass signal is plotted versus the delay time.

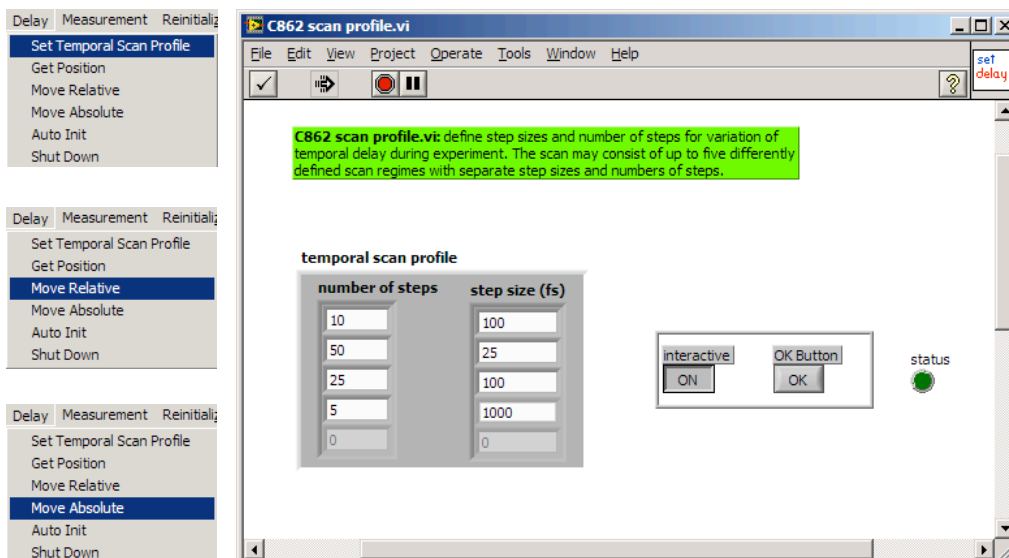


**Figure 5.9:** The “Delay” menu consists of several points. Important are “Set Temporal Scan Profile”, “Move Relative”, and “Move Absolute”. “Set Temporal Scan Profile” defines the number of delay steps and their spacings (in fs). By “Move Relative” the delay stage can be moved relatively to its initial position and by “Move Absolute” its moved to an absolute position.

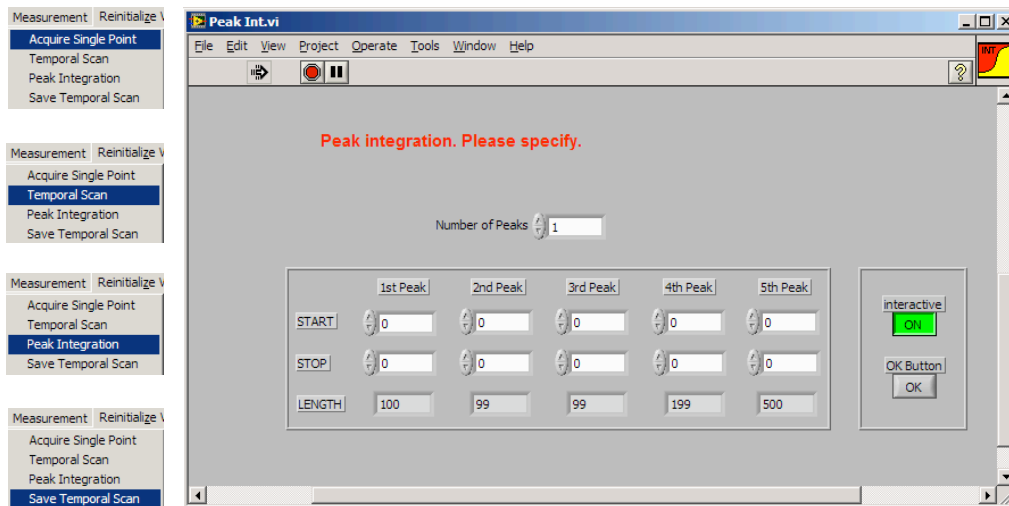


**Figure 5.10:** The “Measurement” menu consists of the points “Acquire Single Point”, “Temporal Scan”, “Peak Integration”, and “Save Temporal Scan”. “Acquire Single Point” takes a mass spectrum at the current time delay position and displays the peak area. By “Temporal Scan” a measurement is started, which records mass spectra following the defined step profile. With the menu point “Peak Integration” one can manually integrate over the measured mass peaks after a measurement has finished. And last, “Save Temporal Scan” stores the obtained data to the hard drive.

## 5.2.2 Transient Photoelectron Imaging

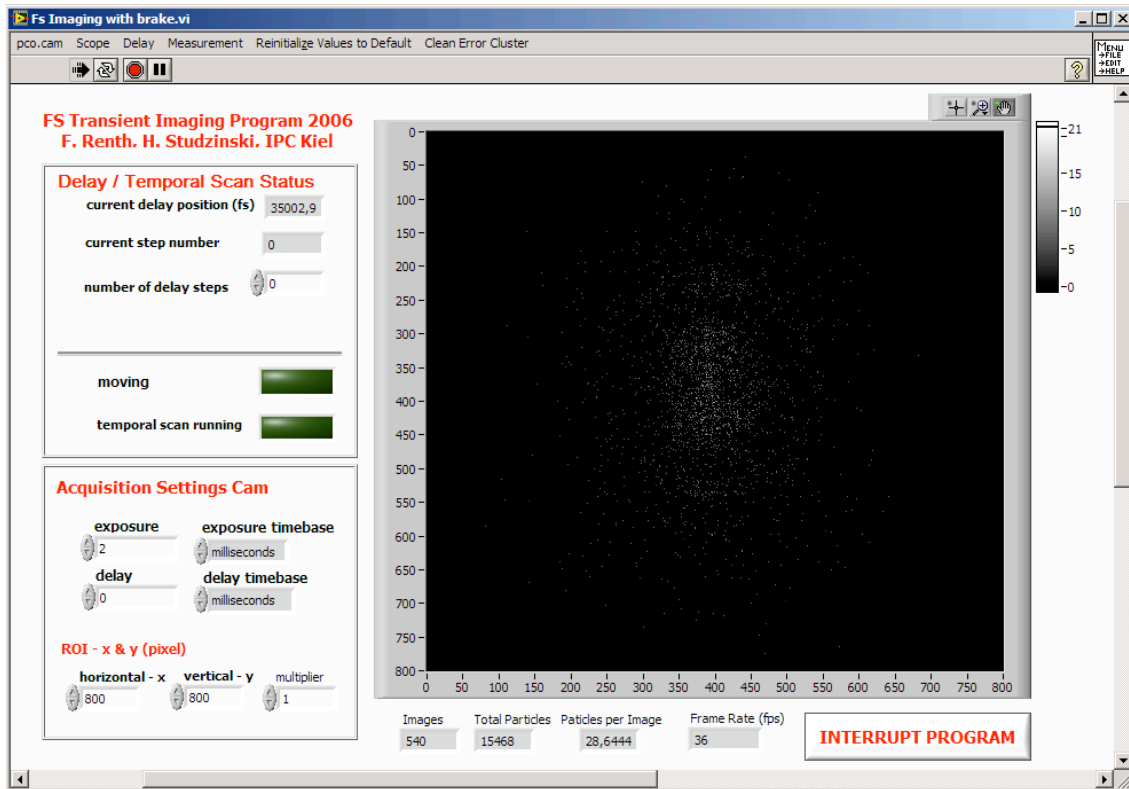


**Figure 5.11:** The PEI control program is operated by the menu points, “pco.cam” and “Delay”. All other menu points have not to be considered. The acquisition settings for the CCD camera are directly controlled from the front panel. Additionally, the region of interest (RoI) can be adjusted. Below the display are shown the statistics of the last measurement, respectively.

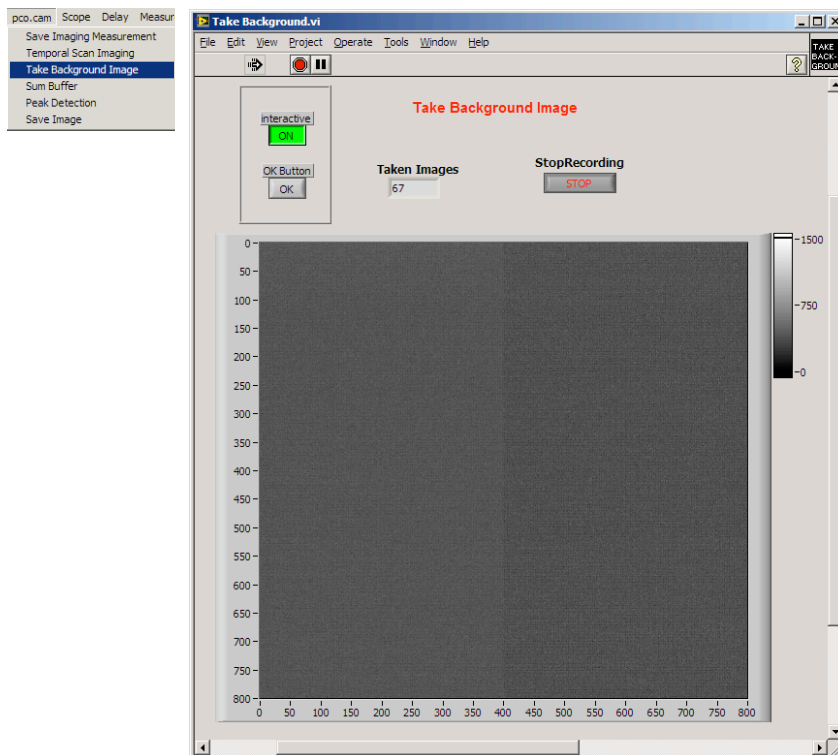


**Figure 5.12:** The menu point “pco.cam → Take Background Image” stores a background image, which can be subtracted from the images take while measuring.

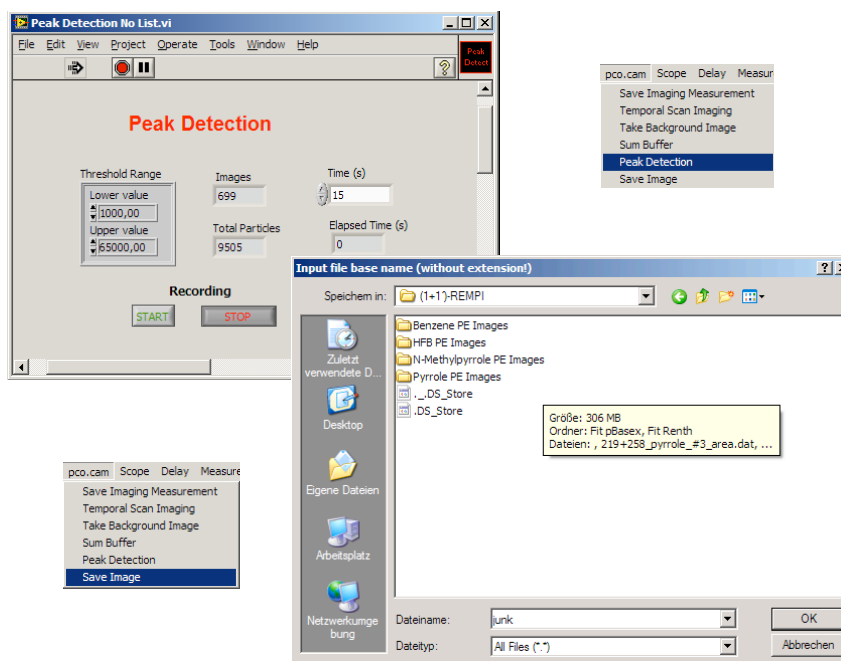


**Figure 5.13:** The menu point “pco.cam → Peak Detection” starts a measurement at a fixed delay position. “pco.cam → Save Image” stores the PE image.



## 5.3 Data Evaluation

The time-resolved mass spectra were fitted with a program written with Mathematica 6.0, while the photoelectron images were inverted with the pBASEX program. The energy distributions were calculated from the radial distributions using two different Mathematica 6.0 programs. The first simply correlated the edge of the most outer peak with the calculated maximum available electron kinetic energy. The second, used the distance between peaks that derived from an over threshold ionization. The programs are shown in a series of screenshots, explaining their functions in the figure labels.

### 5.3.1 Fit of Transient Mass Spectra with Mathematica

#### Data Fit with exponential and oscillating functions convoluted with IRF-gaussians

##### Initializing Functions

---

```
Needs["NonlinearRegression`"]
SetDirectory[
  "/Users/studzinski/Work/Mass/FS-MS/Daten/Pentafluorobenzene/Fit
  Mathematica/";
OscillatingDecay[x_, aCos_, decayCos_, phi_, T_] :=
  aCos Cos[ $\frac{2 \pi x}{T} + \frac{\pi \text{phi}}{180}$ ] e- $\frac{x}{\text{decayCos}}$ 
MonoExponentialDecay[x_, a_, decay_] := a e- $\frac{x}{\text{decay}}$ 
MonoExponentialRise[x_, b_, rise_] := b (1 - e- $\frac{x}{\text{rise}}$ )
SigmaGaussian[x_, x0_, sigma_] :=  $\frac{e^{-\frac{(x-x_0)^2}{2 \sigma^2}}}{\sqrt{2 \pi \sigma}}$ 
ConvolutedOscillatingDecay[x_, x0_, aCos_, decayCos_, phi_, T_, sigma_] :=
  Integrate[OscillatingDecay[t, aCos, decayCos, phi, T]
    SigmaGaussian[x - t, x0, sigma], {t, 0, infinity},
  Assumptions -> {T > 0, decayCos > 0, sigma > 0, x in Reals, t in Reals}]
ConvolutedMonoExponentialDecay[x_, x0_, a_, decay_, sigma_] :=
  Integrate[MonoExponentialDecay[t, a, decay] SigmaGaussian[x - t, x0, sigma],
  {t, 0, infinity}, Assumptions -> {sigma > 0, decay > 0}]
ConvolutedMonoExponentialRise[x_, x0_, b_, rise_, sigma_] :=
  Integrate[MonoExponentialRise[t, b, rise] SigmaGaussian[x - t, x0, sigma],
  {t, 0, infinity}, Assumptions -> {sigma > 0, rise > 0}]
```

**Figure 5.14:** In this cell all fitting functions are defined. After loading the program, they have to be initialized before the fitting can begin.

```

m[x_, x0_, aCos_, decayCos_, phi_, T_, a_, decay_, sigma_] :=
  ConvolutedOscillatingDecay[x, x0, aCos, decayCos, phi, T, sigma] +
  ConvolutedMonoExponentialDecay[x, x0, a, decay, sigma]
MonoExponentialDecayMonoExponentialRise[x_, x0_, a_, decay_, sigma_,
  b_, rise_] := ConvolutedMonoExponentialDecay[x, x0, a, decay, sigma] +
  ConvolutedMonoExponentialRise[x, x0, b, rise, sigma]
MultiExponential[x_, x0_, p_, sigma_] :=
  Sum[Length[p], i=1] ConvolutedMonoExponentialDecay[x, x0, p[[i, 1]], p[[i, 2]], sigma]
MultiOscillations[x_, x0_, q_, phi_, Time_, sigma_] :=
  Sum[Length[q], i=1] ConvolutedOscillatingDecay[x, x0, q[[i, 1]], q[[i, 2]], phi[[i, 1]],
  Time[[i, 1]], sigma]
MultiExponentialsMultiOscillations[x_, x0_, p_, sigma_, q_, phi_, Time_] :=
  Sum[Length[p], i=1] ConvolutedMonoExponentialDecay[x, x0, p[[i, 1]], p[[i, 2]], sigma] +
  Sum[Length[q], j=1] ConvolutedOscillatingDecay[x, x0, q[[j, 1]], q[[j, 2]], phi[[j, 1]],
  Time[[j, 1]], sigma]
MultiExponentialsMultiOscillationsRise[x_, x0_, p_, sigma_, q_, phi_,
  Time_, b_, rise_] :=
  Sum[Length[p], i=1] ConvolutedMonoExponentialDecay[x, x0, p[[i, 1]], p[[i, 2]], sigma] +
  Sum[Length[q], j=1] ConvolutedOscillatingDecay[x, x0, q[[j, 1]], q[[j, 2]], phi[[j, 1]],
  Time[[j, 1]], sigma] + ConvolutedMonoExponentialRise[x, x0, b, rise, sigma]
MultiExponentialRise[x_, x0_, p_, sigma_, b_, rise_] :=
  Sum[Length[p], i=1] ConvolutedMonoExponentialDecay[x, x0, p[[i, 1]], p[[i, 2]], sigma] +
  ConvolutedMonoExponentialRise[x, x0, b, rise, sigma]

```

Figure 5.15: Initializing Part 2

## Importing and Manipulating Data File

```

dtest = Import["PFB_224nm_a+b.dat"];
dtest[[All, 1]] = dtest[[All, 1]] - dtest[[1, 1]];
dtest[[All, 1]] =  $\frac{dtest[[All, 1]]}{1000}$ ;
dtest[[All, 2]] = dtest[[All, 2]]  $\times$  1;
dtest[[All, 2]] = dtest[[All, 2]] - Min[dtest[[All, 2]]];
dtest[[All, 2]] =  $\frac{dtest[[All, 2]]}{Max[dtest[[All, 2]]]}$ ;
DataGraph = ListPlot[dtest, Joined  $\rightarrow$  True,
  PlotRange  $\rightarrow$  {{0., 10.}, {0., 1.}}]

```

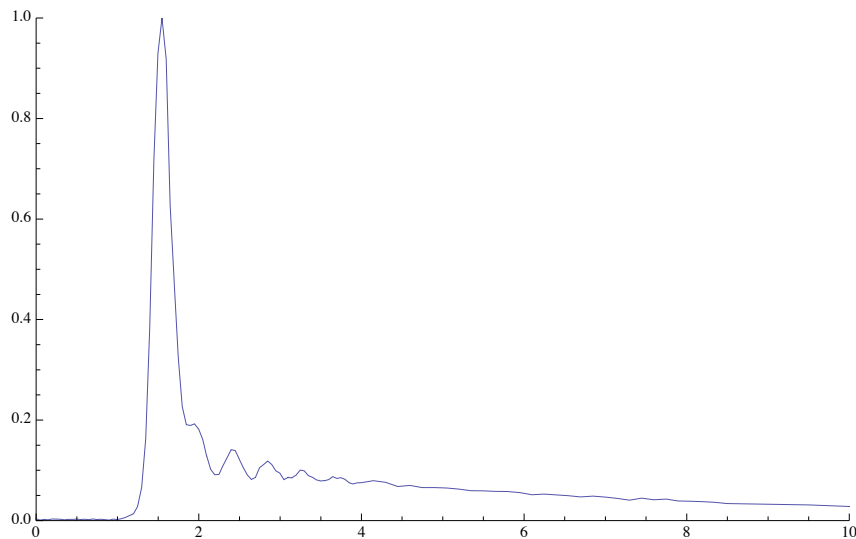


Figure 5.16: Data importing and normalization. The abscissa data should be in ps.

## Fitting the data with oscillations

```

f2 =
FindFit[dtest,
  background +
  Re[MultiExponentialsMultiOscillations[x, x0,
    {{a1, decay1}, {a2, decay2}},  $\sigma$ , {{aCos, decayCos}}, {{phi}}, {{T}}]],
  {{background, 0.01}, {x0, 1.5}, {a1, 2.1}, {decay1, 0.12}, {a2, 0.12},
  {decay2, 3.5}, { $\sigma$ , 0.09}, {aCos, 0.12}, {decayCos, 1.1}, {phi, -90.},
  {T, 0.45}}, x]
{background  $\rightarrow$  0.00301331, x0  $\rightarrow$  1.46177, a1  $\rightarrow$  2.23473,
  decay1  $\rightarrow$  0.112673, a2  $\rightarrow$  0.128495, decay2  $\rightarrow$  4.89246,  $\sigma$   $\rightarrow$  0.0856922,
  aCos  $\rightarrow$  0.146088, decayCos  $\rightarrow$  0.967135, phi  $\rightarrow$  -76.5763, T  $\rightarrow$  0.432052}

```

Figure 5.17: Before the fit can be initiated, starting parameters have to be defined.

## Plotting Fitted Data

```
SimMEMO =  
  Evaluate[  
    background + MultiExponentialsMultiOscillations[x, x0,  
      {{a1, decay1}, {a2, decay2}},  $\sigma$ , {{aCos, decayCos}}, {{phi}}, {{T}}] /.  
    f2];  
overview = Table[{x, Re[SimMEMO]}, {x, -1., 20., 0.03}];  
SimGraph = ListPlot[overview, Joined -> True,  
  PlotRange -> {{0., 20.}, {0., 1.1}},  
  PlotStyle -> RGBColor[1., 0., 0.]]  
Show[SimGraph, DataGraph]
```

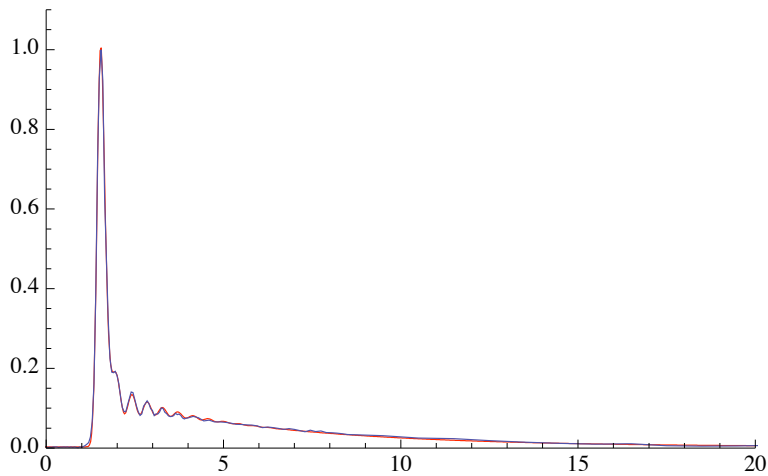
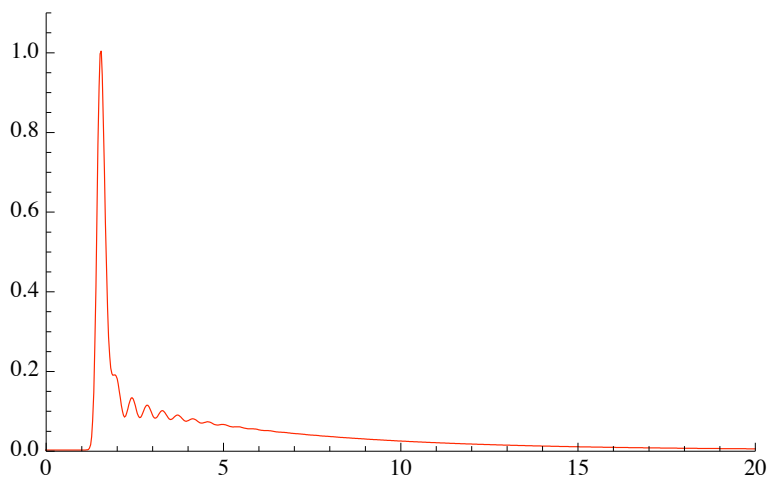


**Figure 5.18:** The fit results are examined by plotting. If the fit results are corrupt, the fit has to be repeated with better starting parameters.

### Creating Data Sheet of Fitted Data

```
SimME1 = Evaluate[background + MultiExponential[x, x0, {{a1, decay1}},  $\sigma$ ] /.  
  f2];  
SimME2 = Evaluate[background + MultiExponential[x, x0, {{a2, decay2}},  $\sigma$ ] /.  
  f2];  
SimOS1 =  
  Evaluate[  
    background + Re[MultiOscillations[x, x0, {{aCos, decayCos}},  
      {{phi}}, {{T}},  $\sigma$ ] /. f2];  
xkorr = x0 /. f2;  
dfit = Table[{x - xkorr, Re[SimMEMO],  
  SimME1, SimME2, SimOS1}, {x, -1., 100., 0.025}];
```

**Figure 5.19:** Decay curves for each component are generated with the fit results. The amount of points per ps and the total length in ps has to be chosen.

### Saving Fitted Data

```
Export["PFB224nm_fit.dat", dfit, "Table"];  
Export["PFB224nm_fit.res", f2, "List"];  
dtest[[All, 1]] = dtest[[All, 1]] - xkorr;  
Export["PFB224nm_raw.dat", dtest, "Table"];
```

**Figure 5.20:** The fit results are exported in text form and the generated curves as spreadsheets.

### 5.3.2 Inversion of 2D Projections with pBasex

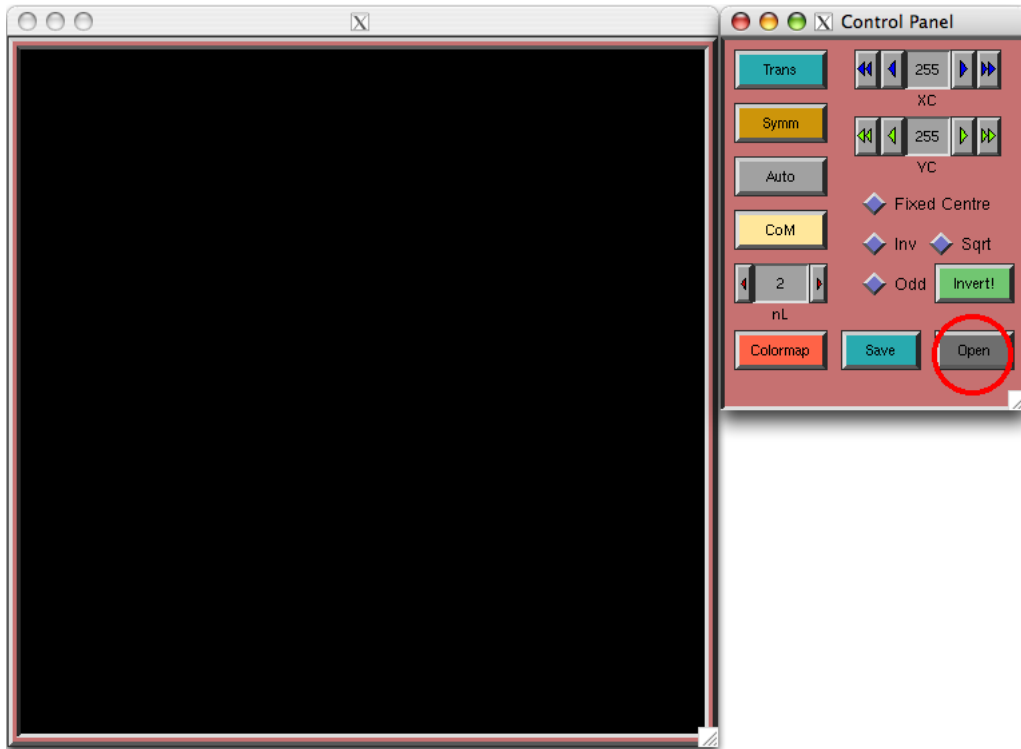


**Figure 5.21:** With the “Open” button, an image for inversion can be chosen.

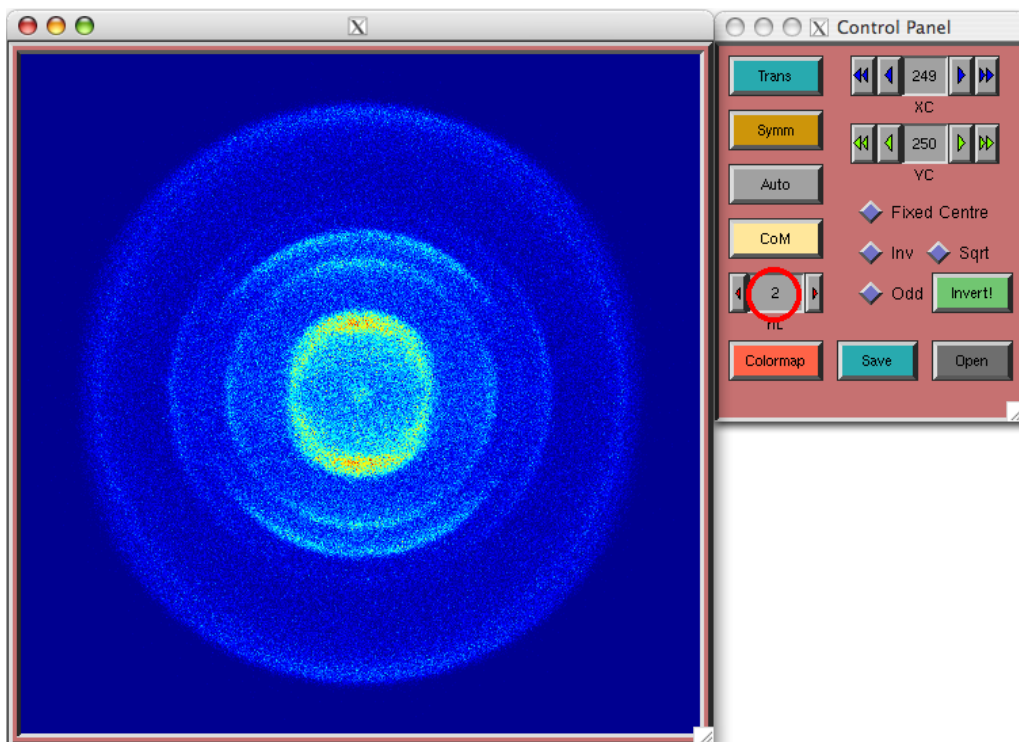


**Figure 5.22:** The order of the Legendre polynomial is selected by the slider “nL”. Odd polynomials can be included.

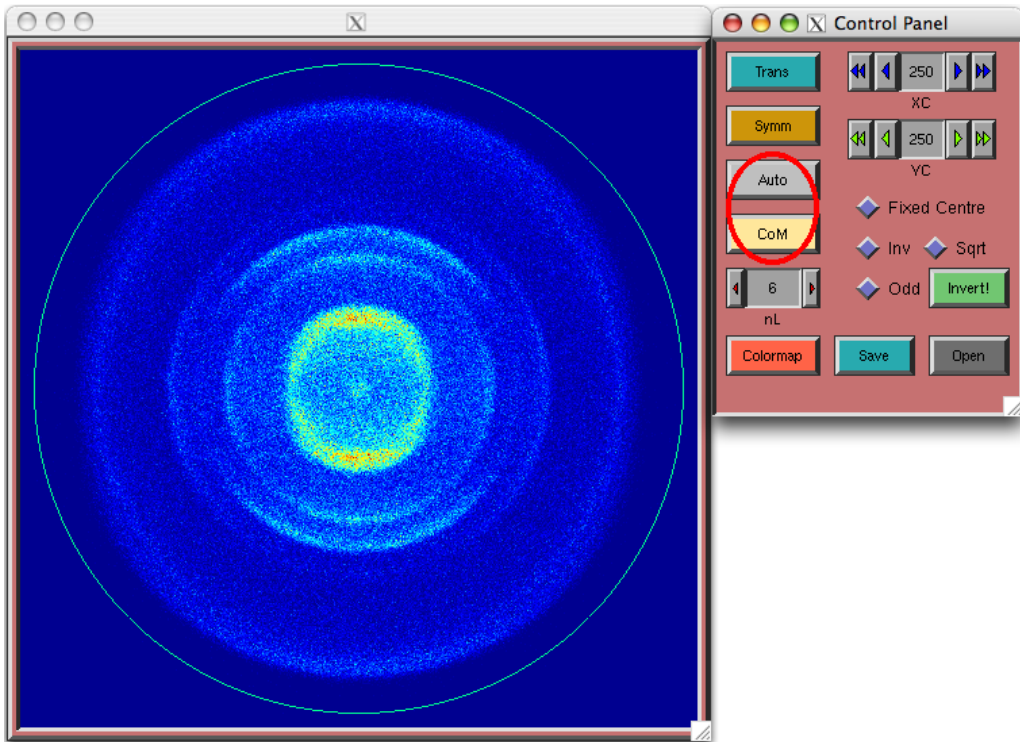


**Figure 5.23:** The image center is determined by the buttons “Auto” or “CoM”. The center position can be checked and adjusted by the sliders “XC” and “YC” in the upper right.

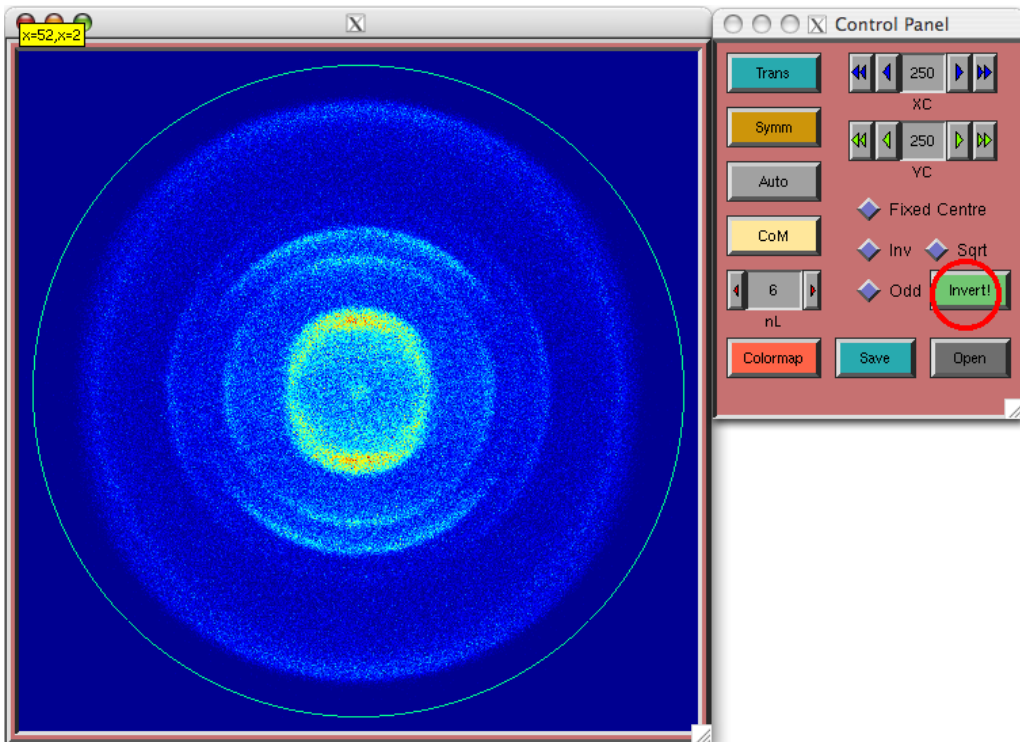


**Figure 5.24:** The image is inverted by the “Invert!” button.



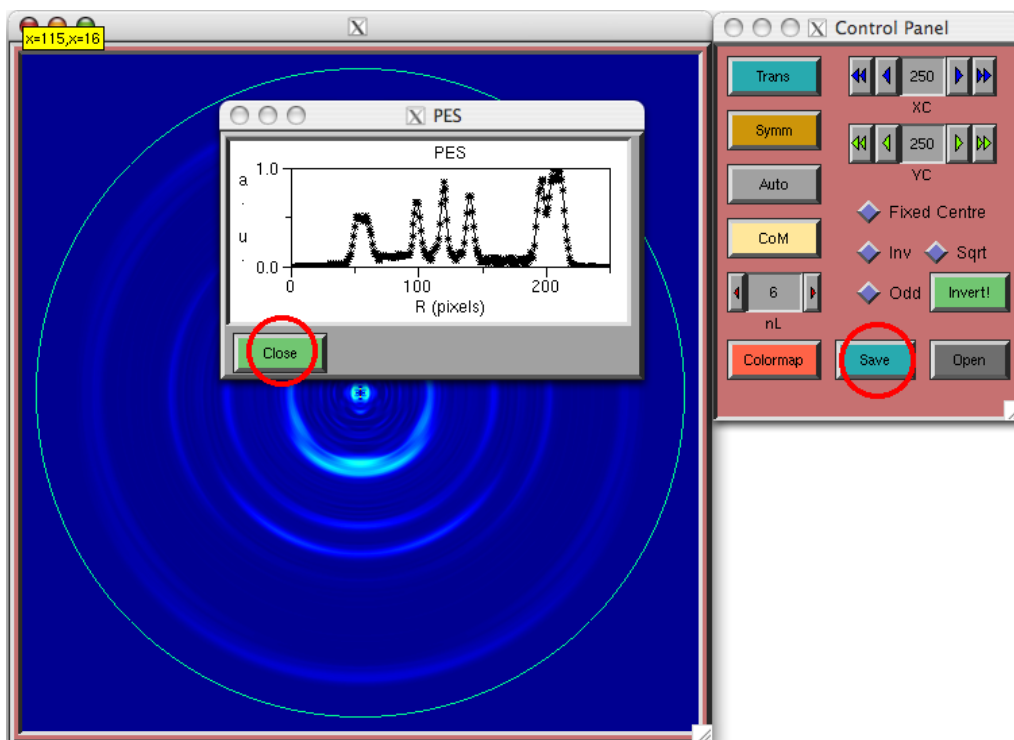


**Figure 5.25:** The inversion is done in  $\approx 1$  s. The “Save” button stores the results to the hard disk.

### 5.3.3 Energy Calibration of the PE Distributions

#### 5.3.3.1 By Maximum Electron Kinetic Energy

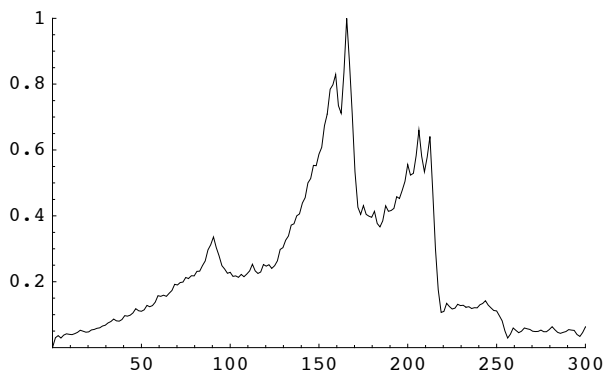
### Energy Calibration for PE Images

DEFINE EQUATIONS:

```
Needs["NonlinearRegression`"]
deltaE =  $\frac{1.599809509 \times 1.60219}{10^{19}}$ ;
me =  $\frac{9.10953}{10^{31}}$ ;
EnergyRingEndJoule :=  $\frac{\text{distance}^2 \text{me}}{2 \text{tof}^2}$ 
tof :=  $\sqrt{\frac{\text{me distance}^2}{2 \text{EnergyRingEndJoule}}}$ 
EnergyRingEndJoule :=  $\frac{1.60219 \text{ EnergyRingEnd}}{10^{19} 8065.5}$ 
distance :=  $\frac{0.05291 \text{ PixelRingEnd}}{1000}$ ;
```

SET DIRECTORY AND LOAD DATA:

```
SetDirectory[
"/Users/studzinski/Work/Mass/FS-IM/DATEN/(1+775
nm)-REMPI/Benzol/Messungen aug05 387_775/Eis&Wasser/qbasex/"];
pes = Import["IMG260805_h+i(TO)_p4even_pes.dat"];
ListPlot[pes, Joined -> True, PlotRange -> {{0., 300.}, {0., 1.}}]
```



USER INPUT OF RINGEND DIST.(PIXEL) and CORRELATED ENERGY(cm-1):

```
PixelRingEnd = 218.75;
EnergyRingEnd = 18 128.2319;
```

**Figure 5.26:** In this cells are the necessary functions initialized, the radial distributions are imported and the position of the calculated maximum available electron kinetic energy is defined.

### TIME OF FLIGHT (ns):

```
tof ÷ 10-9
```

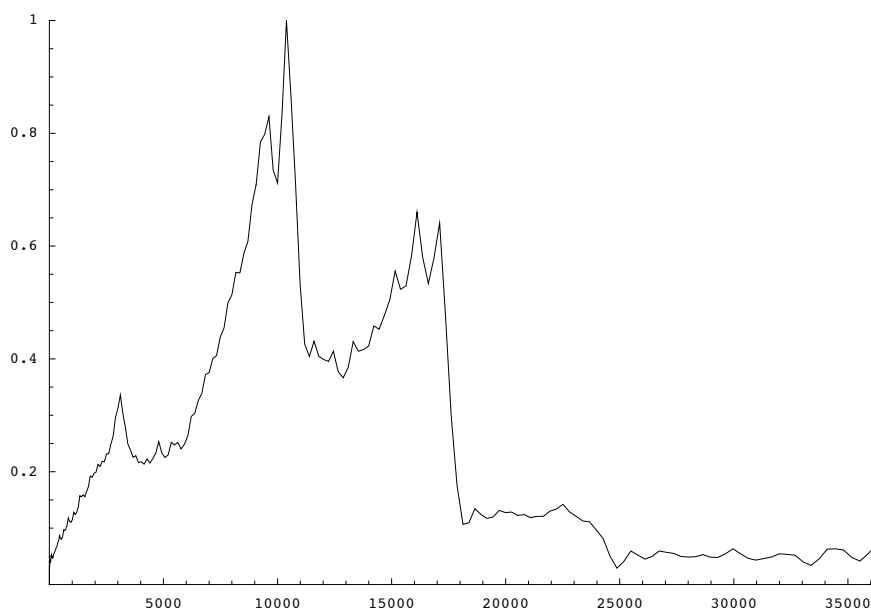
```
13.0167
```

CALCULATE ENERGY DISTRIBUTION ( $\text{cm}^{-1}$ ) :

```
pesWavenumbers = pes;
```

```
pesWavenumbers[[All, 1]] =  $\frac{\left( \text{me} \left( \frac{\text{pesWavenumbers}[[\text{All}, 1]] \cdot 0.05291}{1000} \right)^2 \right) \cdot 8065.5}{(2 \text{ tof}^2) \cdot 1.60219 \cdot 10^{19}};$ 
```

```
ListPlot[pesWavenumbers, Joined → True,  
PlotRange → {{0., 40000.}, {0., 1.}}]
```



EXPORT DATA FILE ( $\text{cm}^{-1}$  vs. intensity) :

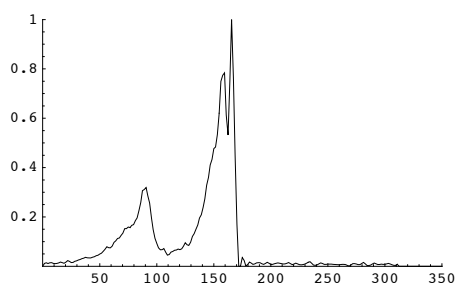
```
Export["pyrrole_219_258_260207_f_scaled_p4even_pes_cm-1.dat",  
pesWavenumbers, "Table"];
```

**Figure 5.27:** The ToF of the electrons and the energy distribution are calculated. Followed by the export of the resulting calibrated distribution.

## Apply Cablibration to Other Images, Pixel to Wavenumber Conversion

SET DIRECTORY AND LOAD DATA:

```
SetDirectory[
"/Users/studzinski/Desktop/Pyrrrole PE Images/Fit pBasex/Scaled/"];
pesOther =
Import[
"/Users/studzinski/Desktop/Pyrrrole PE Images/Fit
pBasex/Scaled/pyrrrole_background_258nm_260207_g_scaled_p4even_pes.dat"
ListPlot[pesOther, Joined → True, PlotRange → {{0., 350.}, {0., 1.}}]
```



CALCULATE ENERGY DISTRIBUTION ( $\text{cm}^{-1}$ ) :

```
pesWavenumbersOther = pesOther;
pesWavenumbersOther[[All, 1]] = 
$$\frac{\left( \text{me} \left( \frac{\text{pesWavenumbersOther}[[\text{All}, 1]] 0.05291}{1000} \right)^2 \right) 8065.5}{\frac{(2 \text{tof}^2) 1.60219}{10^{19}}}$$
;
ListPlot[pesWavenumbersOther, Joined → True,
PlotRange → {{0., 40000.}, {0., 1.}}]
```

EXPORT DATA FILE (intensity vs.  $\text{cm}^{-1}$ ) :

```
Export["pyrrrole_background_258nm_260207_g_scaled_p4even_pes_cm-1.dat",
pesWavenumbersOther, "Table"];
```

**Figure 5.28:** The calibration can be applied to radial distributions of different images/measurments.

### 5.3.3.2 By Over Threshold Ionization

## Energy Calibration for Images with Extra Rings Out of Over Threshold Ionization

DEFINE EQUATIONS:

```
Needs["NonlinearRegression`"]
deltaE =  $\frac{1.599809509 \times 1.60219}{10^{19}}$ ;
me =  $\frac{9.10953}{10^{31}}$ ;
E1 :=  $\frac{\text{distance1}^2 \text{ me}}{2 \text{ tof}^2}$ 
E2 :=  $\frac{\text{distance2}^2 \text{ me}}{2 \text{ tof}^2}$ 
tof :=  $\sqrt{\frac{\text{me} (\text{distance2}^2 - \text{distance1}^2)}{2 \text{ deltaE}}}$ 
distance1 :=  $\frac{0.05291 \text{ PixelRing1}}{1000}$ ;
(distance2 :=  $\frac{0.05291 \text{ PixelRing2}}{1000}$ );
```

SET DIRECTORY AND LOAD DATA:

```
SetDirectory["/Users/studzinski/Desktop/"];
pes = Import["benzene130207_775nm_d_pbasex_p6_pes.dat"];
ListPlot[pes, Joined -> True, PlotRange -> {{0., 300.}, {0., 1.}}]
```

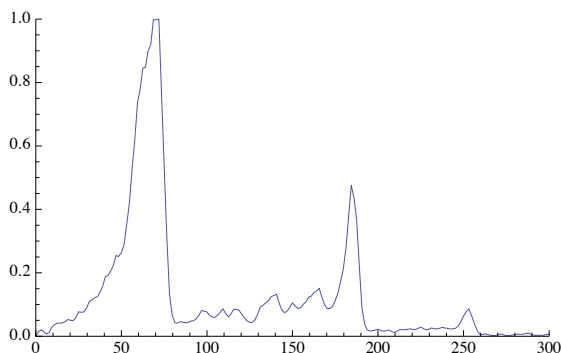


**Figure 5.29:** The energy calibration on rings that derive from “over threshold” ionization is more accurate, but not sempiternal possible.

USER INPUT OF RING DISTANCES IN PIXEL VALUES:

```
PixelRing1 = 65.625;
PixelRing2 = 184.375;
```

TIME OF FLIGHT (ns):

```
E1 ÷ (1.60219 × 10-19);
E2 ÷ (1.60219 × 10-19);
tof ÷ 10-9
```

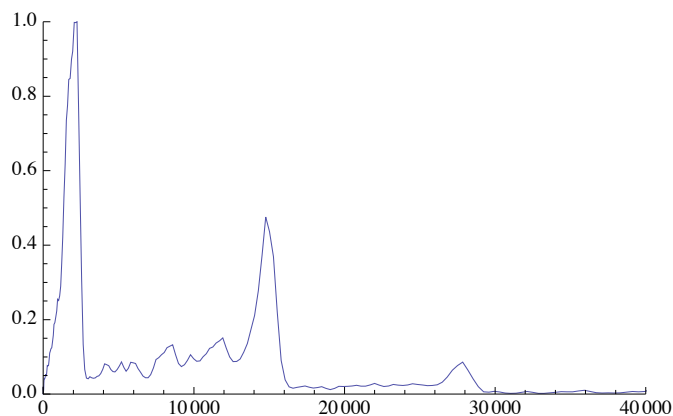
```
12.1525
```

CALCULATE ENERGY DISTRIBUTION ( $\text{cm}^{-1}$ ) :

```
pesWavenumbers = pes;
```

$$\text{pesWavenumbers}[\text{All}, 1] = \frac{\left( \text{me} \left( \frac{\text{pesWavenumbers}[\text{All}, 1] \cdot 0.05291}{1000} \right)^2 \right) \cdot 8065.5}{(2 \cdot \text{tof}^2) \cdot 1.60219 \cdot 10^{19}};$$

```
ListPlot[pesWavenumbers, Joined → True,
PlotRange → {{0., 40000.}, {0., 1.}}]
```



EXPORT DATA FILE ( $\text{cm}^{-1}$  vs. intensity) :

```
Export["benzene130207_775nm_d_pbasex_p6_pes_cm-1.dat", pesWavenumbers,
"Table"];
```

**Figure 5.30:** Defining the ring positions and their energy spacing. Export of the results.

## Bibliography

- [1] T. H. MAIMAN, Stimulated Optical Radiation in Ruby, *Nature* 187, 493 – 494 (1960).
- [2] E. P. IPPEN, C. V. SHANK, A. DIENES, Passive Mode Locking of the CW Dye Laser, *Appl. Phys. Lett.* 21, 348 – 350 (1972).
- [3] A. H. ZEWAIL, Femtochemistry: Atomic-Scale Dynamics of the Chemical Bond, *J. Phys. Chem.* 104, 5660 – 5694 (2000).
- [4] A. H. ZEWAIL, Femtochemistry: Atomic-Scale Dynamics of the Chemical Bond Using Ultrafast Lasers (Nobel Lecture), *Angew. Chem.-Int. Edn.* 39, 2587 – 2631 (2000).
- [5] A. H. ZEWAIL, Femtochemistry: Past, Present, and Future, *Pure Appl. Chem.* 72, 2219 – 2231 (2000).
- [6] J. CHESNOY, A. MOKHTARI, Resonant Impulsive-Stimulated Raman Scattering on Malachite Green, *Phys. Rev. A* 38, 3566 – 3576 (1988).
- [7] W. T. POLLARD, S. L. DEXHEIMER, W. W., L. A. PETEANU, C. V. SHANK, A. MATHIES, Theory of Dynamic Absorption Spectroscopy of Nonstationary States. 4. Application to 12-fs Resonant Impulsive Raman Spectroscopy of Bacteriorhodopsin, *J. Phys. Chem.* 96, 6147 – 6158 (1992).
- [8] E. T. J. NIBBERING, T. ELSAESSER, Ultrafast Vibrational Dynamics of Hydrogen Bonds in the Condensed Phase, *Chem. Rev.* 104, 1887 – 1914 (2004).
- [9] A. H. ZEWAIL, Femtochemistry, *J. Phys. Chem.* 97, 12427 – 12446 (1993).
- [10] N. PUGLIANO, D. K. PALIT, A. Z. SZARKA, R. M. HOCHSTRASSER, Wave Packet Dynamics of the HgI<sub>2</sub> Photodissociation Reaction in Solution, *J. Chem. Phys.* 99, 7273 – 7276 (1993).
- [11] U. BANIN, S. RUHMAN, Ultrafast Photodissociation of I<sub>3</sub>. Coherent Photochemistry in Solution, *J. Chem. Phys.* 98, 4391– 4403 (1993).
- [12] J. MANZ, *Femtosecond Chemistry*, VCH Verlagsgesellschaft, Weinheim (1995).
- [13] M. KLESSINGER, J. MICHL, *Excited States and Photochemistry of Organic Molecules*, VCH Verlagsgesellschaft, Weinheim (1995).
- [14] F. C. DE SCHRYVER, S. DE FEYTER, G. SCHWEITZER, *Femtochemistry*, VCH Verlagsgesellschaft, Weinheim (2001).
- [15] H. S. SON, P. KAMBHAMPATI, T. W. KEE, P. F. BARBARA, Femtosecond Multicolor Pump-Probe Study of Ultrafast Electron Transfer of [(NH<sub>3</sub>)<sub>5</sub>Ru(III)NCRu(II)(CN)<sub>5</sub>]- in Aqueous Solution, *J. Phys. Chem.* 106, 4591 – 4597 (2002).
- [16] Q. WANG, R. W. SCHOENLEIN, L. A. PETEANU, R. A. MATHIES, C. V. SHANK, Vibrationally Coherent Photochemistry in the Femtosecond Primary Event of Vision, *Science* 266, 422 – 424 (1994).
- [17] C. E. CRESPO-HERNANDEZ, B. COHEN, P. M. HARE, B. KOHLER, Ultrafast Excited-State Dynamics in Nucleic Acids, *Chem. Rev.* 104, 1977 – 2019 (2004).
- [18] D. R. YARKONY, Diabolical Conical Intersections, *Rev. Mod. Phys.* 68, 985 – 1013 (1996).
- [19] M. V. BERRY, M. WILKINSON, Diabolical Points in the Spectra of Triangles, *Proc. R. Soc. Lond. A* 392, 15 – 43 (1984).

- [20] F. HUND, Zur Deutung der Molekelspektren, *Z. Physik* 40, 742 – 764 (1927).
- [21] J. VON NEUMANN, E. P. WIGNER, Über das Verhalten von Eigenwerten bei adiabatischen Prozessen, *Z. Physik* 30, 467 (1929).
- [22] L. D. LANDAU, E. M. LIFSHITZ, J. B. SYKES, *Quantum Mechanics: Non-Relativistic Theory*, Mir Editions (1981).
- [23] M. BARBATTI, J. PAIER, H. LISCHKA, Photochemistry of Ethylene: A Multireference Configuration Interaction Investigation of the Excited-State Energy Surfaces, *J. Chem. Phys.* 121 (23), 11614 – 11624 (2004).
- [24] A. L. SOBOLEWSKI, W. DOMCKE, Conical Intersections Induced by Repulsive  $\pi\sigma^*$  States in Planar Organic Molecules: Malonaldehyde, Pyrrole and Chlorobenzene as Photochemical Model Systems, *Chem. Phys.* 259, 181–191 (2000).
- [25] A. L. SOBOLEWSKI, W. DOMCKE, C. DEDONDER-LARDEUX, C. JOUVET, Excited-State Hydrogen Detachment and Hydrogen Transfer Driven by Repulsive  $\pi\sigma^*$  States: A New Paradigm for Nonradiative Decay in Aromatic Biomolecules, *Phys. Chem. Chem. Phys.* 4, 1093–1100 (2002).
- [26] J. WEI, A. KUCZMANN, J. RIEDEL, F. RENTH, F. TEMPS, Photofragment Velocity Map Imaging of H Atom Elimination in the First Excited State of Pyrrole, *Phys. Chem. Chem. Phys.* 5, 315–320 (2003).
- [27] J. RIEDEL, Untersuchung photoinduzierter molekularer Zerfallsprozesse mittels Photofragment-Geschwindigkeitskartographie, Phd thesis, Christian-Albrechts Universität zu Kiel (2006).
- [28] J. PHILIS, A. BOLOVINOS, G. ANDRITSOPOULOS, E. PANTOS, P. TSEKERIS, A Comparison of the Absorption Spectra of the Fluorobenzenes and Benzene in the Region 4.5–9.5 eV, *J. Phys. B: At. Mol. Phys.* 14, 3621–3635 (1981).
- [29] D. PHILLIPS, Fluorescence and Triplet State of Hexafluorobenzene, *J. Chem. Phys.* 46 (12), 4679–4689 (1967).
- [30] G. L. LOPER, E. K. C. LEE, Fluorescence Decay and Radiative Lifetime of Fluorinated Aromatic Molecules, *Chem. Phys. Lett.* 13 (2), 140–143 (1972).
- [31] D. V. O'CONNOR, M. SUMITANI, J. M. MORRIS, K. YOSHIHARA, Non-Exponential Picosecond Fluorescence Decay in Isolated Pentafluorobenzene and Hexafluorobenzene, *Chem. Phys. Lett.* 93 (4), 350–354 (1982).
- [32] H. KANG, B. JUNG, K. S. KIM, Mechanism for Ultrafast Internal Conversion of Adenine, *J. Chem. Phys.* 118 (15), 6717–6719 (2003).
- [33] C. PLUETZER, I. HUENIG, K. KLEINERMANN, Pairing of the Nucleobase Adenine Studied by IR-UV Double-Resonance Spectroscopy and ab initio Calculations, *Phys. Chem. Chem. Phys.* 5, 1158–1163 (2003).
- [34] R. A. JONES, E. C. TAYLOR, A. WEISSBERGER, *Pyrroles: The Chemistry of Heterocyclic Compounds*, Wiley, New York (1990/92).
- [35] W. E. STEPHENS, A Pulsed Mass Spectrometer with Time Dispersion, *Phys. Rev.* 69, 691 (1946).
- [36] A. E. CAMERON, D. F. EGGERS JR., An Ion "Velocitron", *Rev. Sci. Instr.* 19 (9), 605–607 (1948).
- [37] B. A. MAMYRIN, Author's Abstract of Doctorate, Dissertation, A.F. Ioffe Physico-Technical Institute, Leningrad (1966).
- [38] B. A. MAMYRIN, Time-of-Flight Mass Spectrometry (Concepts, Achievements, and Prospects), *Int. J. Mass Spectrom.* 206, 251–266 (2001).
- [39] W. C. WILEY, I. H. MCLAREN, Time-of-Flight Mass Spectrometer with Improved Resolution, *Rev. Sci. Instr.* 26, 1150–1157 (1955).



- [40] C. P. SCHULZ, R. HAUGSTAETTER, H. U. TITTES, I. V. HERTEL, Free Sodium-Water Clusters, *Phys. Rev. Lett.* 57, 1703 – 1706 (1986).
- [41] W. R. GENTRY, C. F. GIESE, Resolved Single-Quantum Rotational Excitation in HD+He Collisions: First Results from a Unique Pulsed Molecular Beam Apparatus, *J. Chem. Phys.* 67, 5389 – 5391 (1977).
- [42] W. R. GENTRY, C. F. GIESE, Ten-Microsecond Pulsed Molecular Beam Source and a Fast Ionization Detector, *Rev. Sci. Instrum.* 49, 595 – 600 (1978).
- [43] P. R. BEVINGTON, D. K. ROBINSON, *Data Reduction and Error Analysis (Third Edition)*, Mc Graw-Hill Higher Education (2003).
- [44] I. V. HERTEL, W. RADLOFF, Ultrafast Dynamics in Isolated Molecules and Molecular Clusters, *Rep. Prog. Phys.* 69, 1897–2003 (2006).
- [45] T. BAUMERT, J. L. HEREK, A. H. ZEWEIL, Femtosecond Real-Time Probing of Reactions. XI. The Elementary OCIO Fragmentation, *J. Chem. Phys.* 99, 4433 – 4440 (1993).
- [46] D. R. CYR, C. C. HAYDEN, Femtosecond Time-Resolved Photoionization and Photoelectron Spectroscopy Studies of Ultrafast Internal Conversion in 1,3,5-Hexatriene, *J. Chem. Phys.* 104, 771 – 774 (1996).
- [47] P. KRUIT, F. H. READ, Magnetic Field Paralleliser  $2\pi$  Electron Spectrometer and Electron-Image Magnifier, *J. Phys. E: Sci. Instrum.* 16, 313 – 324 (1982).
- [48] S. LOCHBRUNNER, J. J. LARSEN, J. P. SHAFFER, M. SCHMITT, T. SCHULTZ, J. G. UNDERWOOD, A. STOLOW, Methods and Applications of Femtosecond Time-Resolved Photoelectron Spectroscopy, *J. Electron Spectrosc. Relat. Phenom.* 112, 183 – 198 (2000).
- [49] D. H. PAIK, T. M. BERNHARDT, N. J. KIM, A. H. ZEWEIL, Femtochemistry of Mass-Selective Negative-Ion Clusters of Dioxygen: Charge-Transfer and Solvation Dynamics, *J. Chem. Phys.* 115 (2), 612 – 616 (2001).
- [50] A. E. BRAGG, R. WESTER, A. DAVIS, A. KAMMRATH, D. M. NEUMARK, Excited-State Detachment Dynamics and Rotational Coherences of  $C_2^-$  via Time-Resolved Photoelectron Imaging, *Chem. Phys. Lett.* 376, 767 – 775 (2003).
- [51] A. STOLOW, Femtosecond Time-Resolved Photoelectron Spectroscopy of Polyatomic Molecules, *Annu. Rev. Phys. Chem.* 54, 89 – 119 (2003).
- [52] V. BLANCHET, M. Z. ZGIERSKI, T. SEIDMANN, A. STOLOW, Discerning Vibronic Molecular Dynamics Using Time-Resolved Photoelectron Spectroscopy, *Nature* 401, 52 – 54 (1999).
- [53] T. SEIDEMAN, Time-Resolved Photoelectron Angular Distributions as a Probe of Coupled Polyatomic Dynamics, *Phys. Rev. A* 64, 042504 – 042522 (2001).
- [54] K. L. REID, Photoelectron Angular Distributions, *Annu. Rev. Phys. Chem.* 54, 397 – 424 (2003).
- [55] T. SUZUKI, Femtosecond Time-Resolved Photoelectron Imaging, *Annu. Rev. Phys. Chem.* 57, 555 – 592 (2006).
- [56] B.-Y. CHANG, R. C. HOETZLEIN, J. A. MUELLER, J. D. GEISER, P. L. HOUSTON, Improved Two-Dimensional Product Imaging: The Real-Time Ion-Counting Method, *Rev. Sci. Instrum.* 69 (4), 1665 – 1670 (1998).
- [57] R. N. BRACEWELL, *The Fourier Transform and its Applications*, McGraw-Hill, 2. Aufl. (1986).
- [58] F. RENTH, J. RIEDEL, F. TEMPS, Inversion of Velocity Map Ion Images Using Iterative Regularization and Cross Validation, *Rev. Sci. Instrum.* 77, 033103 – 033112 (2006).

- [59] G. A. GARCIA, L. NAHON, I. POWIS, Two-Dimensional Charged Particle Image Inversion Using a Polar Basis Function Expansion, *Rev. Sci. Instrum.* 75 (11), 4989 – 4996 (2004).
- [60] D. W. CHANDLER, P. L. HOUSTON, Two-Dimensional Imaging of State-Selected Photodissociation Products Detected by multiphoton Ionization, *J. Chem. Phys.* 87, 1445 – 1447 (1987).
- [61] B. J. WHITAKER, *Imaging in Molecular Dynamics*, Cambridge University Press (2003).
- [62] A. LAFOSSE, M. LEBECH, J. C. BRENOT, P. M. GUYON, O. JAGUTZKI, L. SPIELBERGER, M. VERVLOET, J. C. HOUPER, D. DOWEK, Vector Correlations in Dissociative Photoionization of Diatomic Molecules in the VUV Range: Strong Anisotropies in Electron Emission from Spatially Oriented NO Molecules, *Phys. Rev. Lett.* 84(26), 5987 – 5990 (Jun 2000).
- [63] K. TONOKURA, T. SUZUKI, Slicing Photofragment Spacial Distribution by Laser Sheet Ionization, *Chem. Phys. Lett.* 224, 1 – 6 (1994).
- [64] D. TOWNSEND, M. P. MINITTI, A. G. SUITS, Direct Current Slice Imaging, *Rev. Sci. Instrum.* 74 (4), 2530 – 2539 (2003).
- [65] S. MANZHOS, H.-P. LOOCK, Photofragment Image Analysis Using the Onion-Peeling Algorithm, *Comput. Phys. Commun.* 154, 76 – 87 (2003).
- [66] C. BORDAS, F. PAULING, H. HELM, D. L. HUESTIS, Photoelectron Imaging Spectrometry: Principle and Inversion Method, *Rev. Sci. Instrum.* 67, 2257 – 2268 (1996).
- [67] K. ZHAO, T. COLVIN, W. T. HILL III, G. ZHANG, Deconvolving Two-Dimensional Images of Three-Dimensional Momentum Trajectories, *Rev. Sci. Instrum.* 73, 3044 – 3050 (2002).
- [68] J. WINTERHALTER, D. MAIER, J. HONERKAMP, V. SCHYJA, H. HELM, Imaging of Charged Atomic Reaction Products: Inversion by a Two-Dimensional Regularization Method, *J. Chem. Phys.* 110 (23), 11187 – 11196 (1999).
- [69] B. J. WHITAKER, *Imaging in Chemical Dynamics*, ACS Symposium Series 770, Oxford University Press (2000).
- [70] M. J. J. VRAKING, An Iterative Procedure for the Inversion of Two-Dimensional Ion/Photoelectron Imaging Experiments, *Rev. Sci. Instrum.* 72 (11), 4084 – 4089 (2001).
- [71] V. DRIBINSKI, A. OSSADTCHI, V. A. MANDELSTAM, H. REISLER, Reconstruction of Abel-Transformable Images: The Gaussian Basis-Set Expansion Abel Transform Method, *Rev. Sci. Instrum.* 73 (7), 2634 – 2642 (2002).
- [72] T. JAHNKE, T. WEBER, A. L. LANDERS, A. KNAPP, S. SCHÖSSLER, J. NICKLES, S. KAMMER, O. JAGUTZKI, L. SCHMIDT, A. CZASCH, T. OSIPOV, E. ARENHOLZ, A. T. YOUNG, R. DÍEZ MUIÑO, D. ROLLES, F. J. GARCÍA DE ABAJO, C. S. FADLEY, M. A. VAN HOVE, S. K. SEMENOV, N. A. CHEREPKOV, J. RÖSCH, M. H. PRIOR, H. SCHMIDT-BÖCKING, C. L. COCKE, R. DÖRNER, Circular Dichroism in *K*-Shell Ionization from Fixed-in-Space CO and N<sub>2</sub> Molecules, *Phys. Rev. Lett.* 88(7), 073002 – 073006 (2002).
- [73] M. LEBECH, J. C. HOUPER, A. LAFOSSE, D. DOWEK, C. ALCARAZ, L. NAHON, R. R. LUCCHESI, Complete Description of Linear Molecule Photoionization Achieved by Vector Correlations Using the Light of a Single Circular Polarization, *J. Chem. Phys.* 118 (21), 9653 – 9663 (2003).
- [74] K. L. REID, D. J. LEAHY, R. N. ZARE, Complete description of molecular photoionization from circular dichroism of rotationally resolved photoelectron angular distributions, *Phys. Rev. Lett.* 68(24), 3527 – 3530 (1992).

- [75] N. BOEWERING, T. LISCHKE, B. SCHMIDTKE, N. MÜLLER, T. KHALIL, U. HEINZMANN, Asymmetry in Photoelectron Emission from Chiral Molecules Induced by Circularly Polarized Light, *Phys. Rev. Lett.* 86(7), 1187 – 1190 (2001).
- [76] G. A. GARCIA, L. NAHON, M. LEBECH, J.-C. HOVER, D. DOWEK, Circular Dichroism in the Photoelectron Angular Distribution from Randomly Oriented Enantiomers of Camphor, *J. Chem. Phys.* 119 (17), 8781 – 8784 (2003).
- [77] W. H. PRESS, Hg., *Numerical Recipes in Fortran 90: The Art of Parallel Scientific Computing*, Cambridge University Press, 2. Aufl. (1996).
- [78] L. LANDWEBER, An Iterative Formula for Fredholm Integral Equations of the RST Kind, *Amer. J. Math.* 73, 615 – 624 (1951).
- [79] M. BERTERO, P. BOCCACCI, *Introduction to Inverse Problems in Imaging*, Institut of Physics, Bristol and Philadelphia (1998).
- [80] A. NEUMAIER, Solving Ill-Conditioned and Singular Linear Systems: A Tutorial on Regularization, *SIREV* 40 (3), 636 – 666 (1998).
- [81] C. VOGEL, *Computational Methods for Inverse Problems*, SIAM, Philadelphia (2002).
- [82] M. STONE, An Asymptotic Equivalence of Choice of Model by Cross-Validation and Akaike's Criterion, *JSTOR B* 39 (1), 44 – 47 (1977).
- [83] H. STUDZINSKI, Aufbau und Charakterisierung eines nicht-kollinearen optisch-parametrischen Verstärkers, Diplomarbeit, Universität Kiel (2002).
- [84] N. SCHWALB, Zeitaufgelöste Femtosekunden-Fluoreszenzspektroskopie an  $N^6, N^6$ -Dimethyladenin, Diplomarbeit, Universität Kiel (2005).
- [85] M. G. NIX, A. L. DEVIN, B. CRONIN, N. R. ASHFOLD, Ultraviolet Photolysis of Adenine: Dissociation via the  $^1\pi\sigma^*$  state, *Chem. Phys.* 126, 124312–124322 (2007).
- [86] J. H. CALLOMON, T. M. DUNN, I. M. MILLS, Rotational Analysis of the 2600 angstrom Absorption System of Benzene, *Phil. Trans. R. Soc. Lond. A.* 259, 499–532 (1996).
- [87] E. B. WILSON JR., The Normal Modes and Frequencies of Vibration of the Regular Plane Hexagon Model of the Benzene Molecule, *Phys. Rev.* 45, 706–714 (1934).
- [88] M. OLDANI, R. WIDMER, G. GRASSI, A. BOUDER, Pure Rotational Spectra of 1,2- and 1,3-Benzene- $d_2$  Observed by Microwave Fourier Transform Spectroscopy, *J. Molec. Struct.* 190, 31–40 (1988).
- [89] E. RIEDLE, E. KNITTEL, T. WEBER, H. J. NEUSSER, Rotationally Resolved Spectra of the  $6_{10}$  and  $6_{10} 1_{10}$  Band of Benzene in a Moderately Cold Molecular Beam: Spectral and Dynamical Analysis, *J. Chem. Phys.* 91, 4555–4563 (1989).
- [90] E. RIEDLE, A. BEIL, D. LUCKHAUS, M. QUACK, Sub-Doppler supersonic jet spectra of the coupled  $^6a$  and  $^6b_1$  vibronic bands of the  $S_1(^1B_{2u}) \leftarrow S_0(A_{1g})$  transition in monodeuterobenzene and their rovibrational analysis, *Molec. Phys.* 81, 1–15 (1994).
- [91] M. FORD, R. LINDNER, K. MUELLER-DETHLEFS, Fully Rotationally Resolved ZEKE Photoelectron Spectroscopy of  $C_6H_6$  and  $C_6D_6$ : Photoionization Dynamics and Geometry of the Benzene Cation, *Molec. Phys.* 101 (4-5), 705–716 (2002).
- [92] C. L. BRAUN, S. KATO, S. LIPSKY, Internal Conversion from Upper Electronic States to the First Excited Singlet State of Benzene, Toluene, *p*-Xylene, and Mesitylene, *J. Chem. Phys.* 39 (7), 1645–1652 (1963).
- [93] W. RADLOFF, T. FREUDENBERG, H.-H. RITZE, V. STERT, F. NOACK, I. V. HERTEL, Lifetime of the Benzene Dimer in the  $S_2$  Electronic State, *Chem. Phys. Lett.* 261, 301–306 (1996).

- [94] M. CLARA, T. HELLERER, H. J. NEUSSER, Fast Decay of High Vibronic  $S_1$  States in Gas-Phase Benzene, *Appl. Phys. B* 71, 431–437 (2000).
- [95] W. RADLOFF, V. STERT, T. FREUDENBERG, I. V. HERTEL, C. JOUVET, C. DEDONDER-LARDEUX, D. SOLGADI, Internal Conversion in Highly Excited Benzene and Benzene Dimer: Femtosecond Time-Resolved Photoelectron Spectroscopy, *Chem. Phys. Lett.* 281, 20–26 (1997).
- [96] A. L. SOBOLEWSKI, C. WOYWOD, W. DOMCKE, Ab initio Investigations of Potential-Energy Surfaces Involved in the Photophysics of Benzene and Pyrazine, *J. Chem. Phys.* 98 (7), 5627–5641 (1993).
- [97] S. KATO, A Theoretical Study on the Mechanism of Internal Conversion of  $S_1$  Benzene, *J. Chem. Phys.* 88 (5), 3045–3056 (1988).
- [98] B. R. SMITH, M. J. BEARPARK, M. A. ROBB, F. BERNARDI, M. OLIVUCCI, 'Classical Wavepacket' Dynamics Through a Conical Intersection. Application to the  $S_1/S_2$  Photochemistry of Benzene, *Chem. Phys. Lett.* 242, 27–32 (1995).
- [99] R. RAMIRES, M. C. BÖHM, J. SCHULTE, Feynman Path Integral - ab initio Investigations of the Excited-State Properties of Benzene, *J. Phys. B: At. Mol. Opt. Phys.* 35, 2583–2592 (2002).
- [100] G. K. SPEARS, S. RICE, Study of the Lifetimes of Individual Vibronic States of the Isolated Benzene Molecule, *J. Chem. Phys.* 55 (12), 5561–5581 (1971).
- [101] L. WUNSCH, H. J. NEUSSER, E. W. SCHLAG, Two-Photon Absorption in the Collisionless Gas Phase: Lifetime of New Vibrational Levels in Benzene, *Chem. Phys. Lett.* 210 (2), 210–216 (1975).
- [102] W. A. NOYES, W. A. MULAC, D. A. HARTER, Some Aspects of the Photochemistry of Benzene, *J. Chem. Phys.* 44 (5), 2100–2106 (1966).
- [103] A. E. W. KNIGHT, C. S. PARMENTER, M. W. SCHUYLER, An Extended View of the Benzene 260 nm Transition via Single Vibronic Level Fluorescence. I. General Aspects of Benzene Single Vibronic Level Fluorescence, *J. Am. Chem. Soc.* 97 (8), 1993–2005 (1975).
- [104] A. E. W. KNIGHT, C. S. PARMENTER, M. W. SCHUYLER, An Extended View of the Benzene 260 nm Transition via Single Vibronic Fluorescence. II. Single Vibronic Level Fluorescence as a Probe in the Assignment of the Absorption Spectrum, *J. Am. Chem. Soc.* 97 (8), 2005–2013 (1975).
- [105] S. G. GRUBB, R. L. WHETTEN, A. C. ALBRECHT, E. R. GRANT, A Precise Determination of the First Ionization Potential of Benzene, *Chem. Phys. Lett.* 108 (5), 420–424 (1984).
- [106] R. J. SENSION, R. J. BRUDZYNSKI, S. LI, S. HUDSON, F. ZERBETTO, M. Z. ZGIERSKI, Resonance Raman Spectroscopy of the  $B_{1u}$  Region of benzene: Analysis in Terms of pseudo-Jahn-Teller Distortion, *J. Chem. Phys.* 96 (4), 2617–2628 (1991).
- [107] A. GIUSTI-SUZOR, X. HE, O. ATABEK, Above-Threshold Dissociation of  $H_2^+$  in Intense Laser Fields, *Phys. Rev. Lett.* 64 (5), 515–518 (1990).
- [108] H. KRAUSE, H. J. NEUSSER, Dissociation of State-Selected Complex Ions Studied by Mass-Selective Pulsed Field Threshold Ionization Spectroscopy, *J. Chem. Phys.* 97 (8), 5923–5926 (1992).
- [109] H. KRAUSE, B. ERNSTBERGER, H. J. NEUSSER, Binding Energies of Small Benzene Cluster, *Chem. Phys. Lett.* 184, 411–417 (1991).
- [110] A. KIERMEIER, B. ERNSTBERGER, H. J. NEUSSER, E. W. SCHLAG, Multiphoton Mass Spectrometry of Clusters: Dissociation Kinetics of the Benzene, *J. Phys. Chem.* 92, 3785–3789 (1988).

- [111] H. HIPPLER, J. TROE, H. J. WENDELKEN, UV Absorption Spectra of Vibrationally Highly Excited Toluene Molecules, *J. Chem. Phys.* 78 (9), 5351–5357 (1983).
- [112] C. G. HICKMAN, J. R. GASCOOKE, W. D. LAWRANCE, The  $S_1$ - $S_0$  ( $^1B_2$ - $^1A_1$ ) Transition of Jet-Cooled Toluene: Excitation and Dispersed Fluorescence Spectra, Fluorescence Lifetimes, and Intramolecular Vibrational Energy Redistribution, *J. Chem. Phys.* 104 (13), 4887–4901 (1996).
- [113] N. GINSBURG, W. W. ROBERTSON, The Near Ultraviolet Absorption Spectrum of Toluene Vapor, *J. Chem. Phys.* 14 (9), 511–517 (1946).
- [114] J. B. HOPKINS, D. E. POWERS, R. E. SMALLEY, Vibrational Relaxation in Jet-Cooled Alkyl Benzenes. I Absorption Spectra, *J. Chem. Phys.* 72 (9), 5039–5048 (1980).
- [115] M. JACON, C. LARDEUX, R. LOPEZ-DELGADO, A. TRAMER, On the “Third Decay Channel” and Vibrational Redistribution Problems in Benzene Derivatives, *Chem. Phys.* 24 (2), 145–157 (1977).
- [116] C. S. PARMENTER, B. M. STONE, The Methyl Rotor as an Accelerating Functional Group for IVR, *J. Chem. Phys.* 84 (8), 4710–4711 (1986).
- [117] D. R. BORST, D. W. PRATT, Toluene: Structure, Dynamics, and Barrier to Methyl Group Rotation in its Electronically Excited State. A Route to IVR, *J. Chem. Phys.* 113 (9), 3658–3669 (2000).
- [118] P. T. WHITESIDE, A. K. KING, K. L. REID, Photoelectron Spectroscopy of  $S_1$  Toluene: I. Photoionization Propensities of Selected Vibrational Levels in  $S_1$  Toluene, *J. Chem. Phys.* 123, 202316–201322 (2005).
- [119] P. T. WHITESIDE, A. K. KING, K. L. REID, Photoelectron Spectroscopy of  $S_1$  Toluene: II. Intramolecular Dynamics of Selected Vibrational Levels in  $S_1$  Toluene Studied by Nanosecond and Picosecond Time-resolved Photoelectron Spectroscopies, *J. Chem. Phys.* 123, 204317–204322 (2005).
- [120] S. J. STRICKLER, R. A. BERG, Relationship Between Absorption Intensity and Fluorescence Lifetime of Molecules, *J. Chem. Phys.* 37 (4), 814–822 (1962).
- [121] P. FARMANARA, V. STERT, W. RADLOFF, I. V. HERTEL, Ultrafast Internal Conversion in Highly Excited Toluene Monomers and Dimers, *J. Phys. Chem. A* 105, 5613–5617 (2001).
- [122] O. E. POLANSKY, Zur Behandlung induktiv wirksamer Gruppen in der LCAO-MO-Methode (Hückelmethode), 1.Mitt: Allgemeine Theorie, *Mh. Chem.* 94, 39–42 (1963).
- [123] T. G. BLEASE, R. J. DONOVAN, P. R. R. LANGRIDGE-SMITH, T. RIDLEY, (2+2) Resonance Enhanced Multiphoton Ionization Spectra of Jet-Cooled *ortho*-, *meta*- and *para*-Xylene, *Laser Chem.* 9, 241–263 (1988).
- [124] W. D. GEPPERT, C. E. H. DESSENT, M. C. R. COCKETT, M. MUELLER-DETHLEFS, Evidence for Stable Rydberg States in the Presence of an Electron Scavenger: The ZEKE Spectrum of the Toluene  $SF_6$  Complex, *Chem. Phys. Lett.* 303, 194–200 (1999).
- [125] O. E. POLANSKY, Bestimmung des Parameters der Methylgruppe und *M*-Effekt der Methylgruppe, *Mh. Chem.* 94, 43–50 (1962).
- [126] C. S. BURTON, W. A. NOYES JR., Electronic Energy Relaxation in Toluene Vapor, *J. Chem. Phys.* 49 (4), 1705–1714 (1968).
- [127] K. C. INGHAM, S. J. STRICKLER, Hindered Rotation in the Ground and Excited Electronic States of *o*-Xylene, *J. Chem. Phys.* 53 (11), 4313–4318 (1970).

- [128] F. HIRAYAMA, T. A. GREGORY, S. LIPSKY, Fluorescence from Highly Excited States of Some Aromatic Molecules in Solution, *J. Chem. Phys.* 58 (10), 4696–4697 (1973).
- [129] E. MIGIRDICYAN, J. BAUDET, On the Electronic Spectra of *o*- and *m*-Xylenes and Their Methylated Derivatives. An Experimental and Theoretical Study, *J. Am. Chem. Soc.* 97 (26), 7400–7404 (1975).
- [130] T. G. DIETZ, M. A. DUNCAN, R. E. SMALLEY, Time Evolution Studies of Triplet Toluene by Two-Color Photoionization, *J. Chem. Phys.* 76 (3), 1227–1232 (1982).
- [131] R. L. WHETTEN, K.-J. FU, E. R. GRANT, High Rydberg States of Jet-Cooled Toluene Observed by Ultraviolet Two-Photon Absorption Spectroscopy: Ultrafast Radiationless Decay and Pseudo-Jahn-Teller Effects, *Chem. Phys.* 90, 155–165 (1985).
- [132] P. J. BREEN, J. A. WARREN, E. R. BERNSTEIN, A Study of Nonrigid Molecules by Supersonic Molecular Jet Spectroscopy. I. Toluene and the Xylenes, *J. Chem. Phys.* 87 (4), 1917–1926 (1987).
- [133] R. DISSELKAMP, E. R. BERNSTEIN, J. I. SEEMAN, H. V. SECOR, Minimum Energy Conformation of *ortho*-Xylene in its Ground and First Excited Electronic States, *J. Chem. Phys.* 97 (11), 8130–8136 (1992).
- [134] K. T. LU, G. C. EIDEN, J. C. WEISSHAAR, Toluene Cation: Nearly Free Rotation of the Methyl Group, *J. Phys. Chem.* 96 (24), 9742–9748 (1992).
- [135] B. TROST, J. STUTZ, U. PLATT, UV-Absorption Cross Section of a Series of Monocyclic Aromatic Compounds, *Atmos. Env.* 23, 3999–4008 (1997).
- [136] F. GUNZER, J. GROTEMEYER, New Features in the Mass Analysed Threshold Ionization (MATI) Spectra of Alkyl Benzenes, *Phys. Chem. Chem. Phys.* 24, 5966–5972 (2002).
- [137] H. LIPPERT, H.-H. RITZE, I. V. HERTEL, W. RADLOFF, Femtosecond Time-Resolved H Atom Elimination From Photoexcited Pyrrole Molecules, *ChemPhysChem* 5, 1423–1427 (2004).
- [138] M. Z. ZGIERSKI, T. FUJIWARA, E. C. LIM, Photophysics of Aromatic Molecules with Low-Lying  $\pi\sigma^*$  States: Fluorinated Benzenes, *J. Chem. Phys.* 122, 144312–14418 (2005).
- [139] R. P. FREUHOLZ, W. M. FLICKER, O. A. MOSHER, A. KUPPERMANN, Electronic Spectroscopy of Benzene and the Fluorobenzenes by Variable Angle Electron Impact, *J. Chem. Phys.* 70 (06), 3057–3070 (1979).
- [140] S. A. KOVALENKO, A. L. DOBRYAKOV, FARZTDINOV, Detecting Electronic Coherence in Excited-State Electron Transfer in Fluorinated Benzenes, *Phys. Rev. Lett.* 96, 068301–068304 (2006).
- [141] P. KIRCHMANN, Ultrakurzzeitdynamik von Elektronentransferprozessen im Adsorbatsystem  $C_6F_6/Cu(111)$ , Diplomarbeit, Freie Universität Berlin (2004).
- [142] P. S. KIRCHMANN, P. A. LOUKAKOS, U. BOVENSIEPEN, M. WOLF, Ultrafast Electron Dynamics Studied with Time-Resolved Two-Photon Photoemission: Intra- and Interband Scattering in  $C_6F_6/Cu(111)$ , *New J. Phys.* 7, 113 – 128 (2005).
- [143] T. J. V. FINDLAY, Vapor Pressure of Fluorobenzenes from 5° to 50°C, *J. Chem. Eng. Data* 14 (2), 229 (1969).
- [144] M. J. FRISCH, G. W. TRUCKS, H. B. SCHLEGEL, G. E. SCUSERIA, M. A. ROBB, J. R. CHEESEMAN, J. A. MONTGOMERY, JR., T. VREVEN, K. N. KUDIN, J. C. BURANT, J. M. MILLAM, S. S. IYENGAR, J. TOMASI, V. BARONE, B. MENNUCCI, M. COSSI, G. SCALMANI, N. REGA, G. A. PETERSSON, H. NAKATSUJI, M. HADA,

- M. EHARA, K. TOYOTA, R. FUKUDA, J. HASEGAWA, M. ISHIDA, T. NAKAJIMA, Y. HONDA, O. KITAO, H. NAKAI, M. KLENE, X. LI, J. E. KNOX, H. P. HRATCHIAN, J. B. CROSS, V. BAKKEN, C. ADAMO, J. JARAMILLO, R. GOMPERTS, R. E. STRATMANN, O. YAZYEV, A. J. AUSTIN, R. CAMMI, C. POMELLI, J. W. OCHTERSKI, P. Y. AYALA, K. MOROKUMA, G. A. VOTH, P. SALVADOR, J. J. DANNENBERG, V. G. ZAKRZEWSKI, S. DAPPRICH, A. D. DANIELS, M. C. STRAIN, O. FARKAS, D. K. MALICK, A. D. RABUCK, K. RAGHAVACHARI, J. B. FORESMAN, J. V. ORTIZ, Q. CUI, A. G. BABOUL, S. CLIFFORD, J. CIOSLOWSKI, B. B. STEFANOV, G. LIU, A. LIASHENKO, P. PISKORZ, I. KOMAROMI, R. L. MARTIN, D. J. FOX, T. KEITH, M. A. AL-LAHAM, C. Y. PENG, A. NANAYAKKARA, M. CHALLACOMBE, P. M. W. GILL, B. JOHNSON, W. CHEN, M. W. WONG, C. GONZALEZ, J. A. POPLE, Gaussian 03, Revision C.02. Gaussian, Inc., Wallingford, CT, 2004.
- [145] R. AHLRICH, M. BAER, M. HAESER, H. HORN, C. KOELMEL, Electronic structure calculations on workstation computers: The program system Turbomole, *Chem. Phys. Lett.* 162, 165–169 (1989).
- [146] H. L. FRAGNITO, J. Y. BIGOT, P. C. BECKER, C. V. SHANK, Evolution of the Vibronic Absorption Spectrum in a Molecule Following Impulsive Excitation with a 6 fs Optical Pulse, *Chem. Phys. Lett.* 160, 101 – 104 (1989).
- [147] K. OKUYAMA, T. KAKINUMA, M. FUJII, N. MIKAMI, M. ITO, Electronic Spectra of 1,2,4,5-Tetrafluorobenzene in a Supersonic Jet: Butterfly Tunneling in the Excited State, *J. Phys. Chem.* 90, 3948 – 3952 (1986).
- [148] P. A. MULLEN, M. K. ORLOFF, Ultraviolet Absorption Spectrum of Pyrrole Vapor Including the Observation of Low-Energy Transitions in the Far Ultraviolet, *J. Chem. Phys.* 51, 2276–2278 (1969).
- [149] M. BAVIA, F. BERTINELLI, C. TALIANI, C. ZAULI, The Electric Spectrum of Pyrrole in the Vapor and Crystal, *Mol. Chem.* 31 (2), 479–489 (1976).
- [150] E. E. RENNIE, C. A. F. JOHNSON, J. E. PARKER, R. FERGUSON, D. M. P. HOLLAND, D. A. SHAW, A Photoabsorption and Mass Spectrometry Study of Pyrroles, *Chem. Phys.* 250 (2), 217–236 (1999).
- [151] M. H. PALMER, I. C. WALKER, M. F. GUEST, The Electronic States of Pyrrole Studied by Optical (VUV) Absorption, Near-Threshold Electron Energy-Loss (EEL) Spectroscopy and ab initio Multi-Reference Configuration Interaction Calculations, *Chem. Phys.* 238, 179–199 (1998).
- [152] G. BIERI, L. ASBRINK, v. W. NIESSEN, 30.4 nm He (II) Photoelectron Spectra of Organic Molecules: Part VII. Miscellaneous Compounds, *J. Electron Spectrosc., Relat. Phenom.* 20, 129–78 (1980).
- [153] C. D. COOPER, A. D. WILLIAMSON, J. C. MILLER, R. N. COMPTON, Resonantly Enhanced Multiphoton Ionization of Pyrrole, *N*-Methylpyrrole and Furan, *J. Chem. Phys.* 73 (4), 1527–1537 (1980).
- [154] L. SERRANO-ANDRES, M. MERCHAN, I. NEBOT-GIL, B. O. ROOS, M. FÜLSCHER, Theoretical Study of the Electronic Spectra of Cyclopentadiene, Pyrrole and Furan, *J. Am. Chem. Soc.* 115, 6184–6197 (1993).
- [155] J. WAN, J. MELLER, M. HADA, M. EHARA, H. NAKATSUJI, Electronic Excitation Spectra of Furan and Pyrrole: Revisited by the Symmetry Adapted Cluster-Configuration Interaction Method, *J. Chem. Phys.* 113 (18), 7853–7866 (2000).
- [156] B. O. ROOS, P.-A. MALMQVIST, V. MOLINA, L. SERRANO-ANDRES, M. MERCHAN, Theoretical Characterization of the Lowest-Energy Absorption Band of Pyrrole, *J. Chem. Phys.* 116 (17), 7526–7536 (2002).

- [157] M. BARBATTI, M. VAZDAR, A. J. A. AQUINO, M. ECKERT-MAKSIC, H. LISCHKA, The Nonadiabatic Deactivation Path of Pyrrole, *J. Chem. Phys.* 125, 164323 – 164330 (2006).
- [158] H. KOEPEL, E. V. GROMOV, A. B. TROFIMOV, Multi-Mode-Multi-State Quantum Dynamics of Key Five-Membered Heterocycles: Spectroscopy and Ultrafast Internal Conversion, *Chem. Phys.* 304, 35 – 49 (2004).
- [159] Z. LAN, A. DUPAYS, V. VALLET, S. MAHAPATRA, W. DOMCKE, Photoinduced Multi-Mode Quantum Dynamics of Pyrrole at the  $^1\pi\sigma^*$ - $S_0$  Conical Intersection, *J. Photochem. Photobiol. A: Chemistry* 190, 177 – 189 (2007).
- [160] T. PANCUR, N. K. SCHWALB, F. RENTH, F. TEMPS, Femtosecond Fluorescence Up-Conversion Spectroscopy of Adenine and Adenosine: Experimental Evidence for the  $\pi\sigma^*$  state?, *Chem. Phys.* 313, 199 – 212 (2005).
- [161] M. N. R. ASHFOLD, B. CRONIN, A. L. DEVINE, R. N. DIXON, M. G. D. NIX, The Role of  $\pi\sigma^*$  Excited States in the Photodissociation of Heteroaromatic Molecules, *Science* 312, 1637–1640 (2006).
- [162] T. H. ELSAESSER, H. J. BAKKER, *Ultrafast Hydrogen Bonding Dynamics and Proton Transfer Processes in the Condensed Phase*, Kluwer Academic (2002).
- [163] M. GUTOWSKI, I. DABKOWSKA, J. RAK, S. XU, J. M. NILLES, D. RADISIC, K. H. BOWEN JR., Barrier-free Intermolecular Proton Transfer in the Uracil-Glycine Complex Induced by Excess Electron Attachment, *Eur. Phys. J. D.* 20, 431–439 (2002).
- [164] H. LIPPERT, V. STERT, I. HESSE, C. P. SCHULZ, W. RADLOFF, I. V. HERTTEL, Hydrogen Atom Transfer in Indole( $NH_3$ ) $_n$  Clusters: Formation Dynamics of ( $NH_3$ ) $_n$ - $NH_4$ ,  $n = 1-6$ , Fragments, *Eur. Phys. J. D.* 20, 445–448 (2002).
- [165] W. DOMCKE, A. L. SOBOLEWSKI, Unraveling the Molecular Mechanisms of Photoacidity, *Science* 302, 1693–1694 (2003).
- [166] C. TANNER, C. MANCA, S. LEUTWYLER, Probing the Threshold to H Atom Transfer Along a Hydrogen-Bonded Ammonia Wire, *Science* 302, 1736–1739 (2003).
- [167] N. K. SCHWALB, F. TEMPS, Ultrafast Electronic Relaxation in Guanosine is Promoted by Hydrogen Bonding with Cytidine, *J. Am. Chem. Soc.* 129, 9272 – 9273 (2007).
- [168] D. A. BLANK, S. W. NORTH, Y. T. LEE, The Ultraviolet Photodissociation Dynamics of Pyrrole, *Chem. Phys.* 187 (1-2), 35–47 (1994).
- [169] B. CRONIN, G. D. NIX, R. H. QADIRI, N. R. ASHFOLD, High Resolution Photofragment Translational Spectroscopy Studies of the Near Ultraviolet Photolysis of Pyrrole, *Phys. Chem. Chem. Phys.* 6, 5031 – 5041 (2004).
- [170] B. BAK, D. CHRISTENSEN, L. HANSEN, J. RASTRUP-ANDERSEN, Microwave Determination of the Structure of Pyrrole, *J. Chem. Phys.* 24 (4), 720 – 725 (1956).
- [171] P. CELANI, H. J. WERNER, Analytical Energy Gradients for Internally Contracted Second-Order Multireference Perturbation Theory, *J. Chem. Phys.* 119 (10), 5044 – 5057 (2003).
- [172] O. CHRISTIANSEN, J. GAUSS, J. F. STANTON, P. JORGENSEN, The Electric Spectrum of Pyrrole, *J. Chem. Phys.* 111 (2), 525 – 537 (1999).
- [173] D. J. TOZER, R. D. AMOS, N. C. HANDY, R. B. O., L. SERRANO-ANDRES, Does Density Functional Theory Contribute to the Understanding of Excited States of Unsaturated Organic Compounds?, *Mol. Phys.* 97 (7), 859 – 868 (1999).
- [174] R. MCDIARMID, X. XING, On the Energetics of the Lower Excited States of N-Methylpyrrole, *J. Chem. Phys.* 105, 867 – 873 (1996).



- [175] N. BISWAS, S. WATEGAONKAR, J. G. PHILIS, Geometry and Vibrations of *N*-Methylpyrrole in the  $S_0$  State Studied by Dispersed Fluorescence Spectroscopy and *ab initio* Calculations, *Chem. Phys.* 293, 99 – 109 (2003).
- [176] J. G. PHILIS, Internal Rotation of the Methyl Group in the  $S_0$  and  $S_1$  (3s Rydberg) Electronic States of *N*-Methylpyrrole, *Chem. Phys. Lett.* 353, 84 – 88 (2002).
- [177] N. KANAMARU, Description of the  $S_1(\pi\pi^*)$  State and the Reinterpretation of the (1+1) REMPI Spectra of *N*-methylpyrrole as Based on the *ab initio* Calculations: A Computational Spectroscopy, *J. Mol. Struct. (Theochem)* 686, 15 – 23 (2004).
- [178] J. G. PHILIS, Torsional Features in the (3s) $S_1 \leftarrow S_0$  Transition of *N*-Methylpyrrole and  $C_4D_4NCH_3$ , *J. Mol. Struct.* 651-653, 567 – 570 (2002).



# Acknowledgment

This dissertation has been extensive and exhausting, but in the first place, instructive and enlightening. Without help, support, and encouragement from several persons, I would never have been able to complete this work.

First of all, I would like to thank my doctoral advisor Prof. Friedrich Temps, for his inspiring way to guide me to a deeper understanding of the research field, and his invaluable comments during the whole time of the work with this thesis.

I thank Nina Schwalb, Ron Sievertsen, and Dr. Zhang Song for a wonderful collaboration in the “femto-lab”. In particular, Nina supported me by fruitful discussions and by reading the manuscript.

Very special thanks go to Siarhei Dziarzhyski, who is a great co-worker and friend, for his assistance with the “really heavy stuff”.

I am very grateful to Dr. Falk Renth, who supported me with his great programming knowledge and working experience, especially in the beginning of this work.

I am also very grateful to Dr. Joachim Gripp, who has been always to the spot, when something had to be done concerning vacuum affairs and further for the supply with UV absorption spectra.

Mr. Klaus Warns and Mr. Uwe Eggers as well as the whole workshop, I thank for the permanent cooperativeness even with short-term special requirements.

I thank the whole workgroup for the friendly atmosphere and the strong company.

At last I would like to thank my parents for their great encouragement, which has had an important positive influence on this work.



# Curriculum Vitae

## Harald Studzinski

### Personal Data

Date/Place of Birth: 17.07.1976 in Hamburg/Germany  
Adresse: Röntgenstr. 16  
25709 Marne  
+49-177/2723837  
E-Mail: studzinski@phc.uni-kiel.de

### Study

09/2002 - now **PhD (doctoral thesis):** Ultrafast Radiationless Dynamics of Selected Electronically Excited Aromatic Molecules by Femtosecond Time-resolved Mass Spectrometry and Photoelectron Imaging (Supervisor **Prof. F. Temps**, Institute of Physical Chemistry, University of Kiel). **Magna cum laude**

10/2002 **Final degree** (Dipl. Chem.): **very good/outstanding.**

10/2001 – 10/2002 **Diploma thesis:** Assembly and characterization of a non-collinear optical parametric amplifier (Supervisor **Prof. F. Temps**, Institute of Physical Chemistry, University of Kiel).

10/1999 – 10/2001 **Graduate student** of chemistry at the Christian-Albrechts-University Kiel, major field of study: Physical chemistry.

07/1999 – 10/1999 **Industrial Placement** at the **Bayer AG:** Development of a segregation unit for industrial scale.

05/1999 **Pre-degree** (Vordipl. Chem.): **very good/intermediate.**

10/1996 – 05/1999 **Undergraduate student** of chemistry at the Christian-Albrechts-University Kiel, major field of study: Physical chemistry.

### Education

06/1996 **A-Levels**, final result: **good.**

08/1987 – 06/1996 **Grammar School:** Gymnasium Marne.

02/1985 – 08/1987 **Elementary School:** Grundschule Marne.

08/1983 – 02/1985 **Elementary School:** Grundschule Hamburg-Finkenwerder.

### Activities & Skills

IT Word, Excel, Powerpoint, LaTeX, CorelDraw, Photoshop, Gaussian, Lab View, Origin, Turbomole, Mathematica, Pages, Keynote, Numbers, gnuPlot

Languages German (native), English (fluent), Latin (school knowledge).



# Eidesstattliche Erklärung

Hiermit erkläre ich an Eides Statt, daß die vorliegende Abhandlung - abgesehen von der Beratung durch meinen Betreuer Herrn Prof. Dr. F. Temps - nach Inhalt und Form meine eigene Arbeit ist.

Diese Arbeit hat weder in Auszügen noch in ganzer Form einer anderen Stelle im Rahmen eines Prüfungsverfahrens vorgelegen. Sie wurde nicht veröffentlicht und auch nicht zur Veröffentlichung eingereicht.

---

Harald Studzinski